RUHR-UNIVERSITÄT BOCHUM

Partial Wave Analysis of the Decay $J/\psi \rightarrow \gamma\omega\omega$ at BESIII and Developments for the Electromagnetic Calorimeter of the $\overline{\text{P}}$ANDA Detector

Dissertation zur Erlangung des Grades
eines Doktors der Naturwissenschaften
an der Fakultät für Physik und Astronomie
der Ruhr-Universität Bochum

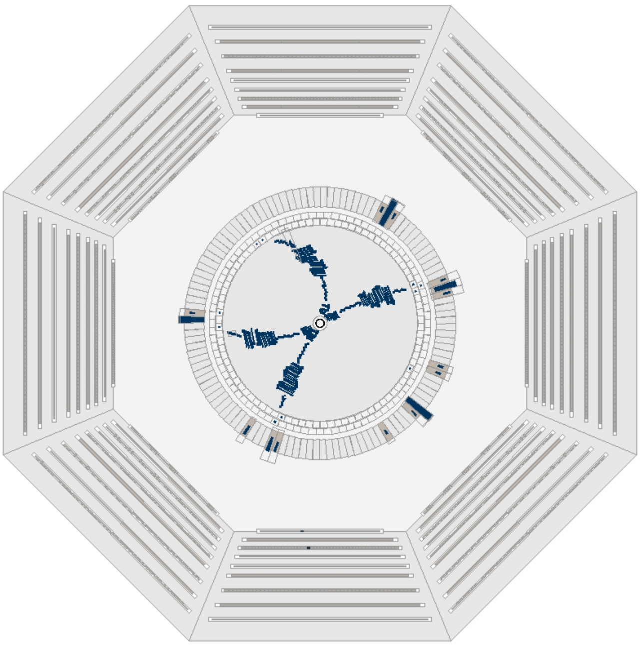

vorgelegt von
Malte Albrecht
geboren in Essen

Bochum, April 2016

1. Gutachter: Prof. Dr. Ulrich Wiedner
2. Gutachter: PD Dr. Fritz-Herbert Heinsius
Lehrstuhl für experimentelle Hadronenphysik, Ruhr-Universität Bochum

Tag der mündlichen Prüfung: 05. Juli 2016

The cover picture shows a visualization of the BESIII detector with hits in its subdetectors which are originating from a simulated $J/\psi \rightarrow \gamma\omega\omega$ event.

Abstract

The present thesis comprises two parts, the first of which deals with the analysis of data recorded by the BESIII experiment at the symmetric electron-positron collider BEPCII located in Beijing, China.
A data set of $1.31 \cdot 10^9$ recorded J/ψ events has been analyzed to study the radiative decay $J/\psi \to \gamma\omega\omega$. Both ω mesons were reconstructed via their decay into $\pi^+\pi^-\pi^0$. A clean sample of 75245 ± 274 events was retained after the application of an event-based background subtraction method. Prominent enhancements located at the $\omega\omega$ mass threshold and at the mass of the $\eta_c(1S)$ are observed in the invariant mass spectrum of the $\omega\omega$ system; no resonant structures are observed in the $\gamma\omega$ system. The selected data set was subjected to a full partial wave analysis, for which two strategies were employed: A model independent partial wave analysis in slices of the invariant $\omega\omega$ mass revealed that the $\omega\omega$ system is dominated by pseudoscalar (0^{-+}) contributions. This assignment also holds for both enhancements discussed above. Additionally, significant scalar (0^{++}) and tensor (2^{++}) contributions in the region below $2.3\,\mathrm{GeV}/c^2$ were found. Based on these results, three main contributions were considered in a model dependent analysis, where the K-matrix formalism was employed for the description of the decay dynamics. As the result of an iterative approach, a good description of the data was achieved using parameterizations containing five poles for the pseudoscalar ($\eta(1760), X(1835), \eta(2225), X(2500), \eta_c$), and two poles for each of the scalar ($f_0(1710), f_0(2020)$) and tensor ($f_2(1640), f_2(1950)$) contributions, respectively. The branching fraction for the decay $J/\psi \to \gamma\omega\omega$ was determined to be $\mathcal{B}(J/\psi \to \gamma\omega\omega) = (2.50 \pm 0.01_{\text{stat}} \pm 0.16_{\text{syst}}) \cdot 10^{-3}$. In a dedicated analysis step, the branching fraction of the decay $\eta_c \to \omega\omega$ was measured for the first time as a part of this thesis and amounts to $\mathcal{B}(\eta_c \to \omega\omega) = (1.88 \pm 0.09_{\text{stat.}} \pm 0.17_{\text{syst.}} \pm 0.44_{\text{ext.}}) \cdot 10^{-3}$.

In the second part, studies to facilitate the construction of the electromagnetic calorimeter of the $\overline{\mathrm{P}}$ANDA detector at the antiproton storage ring HESR are presented. The $\overline{\mathrm{P}}$ANDA experiment is to be built as a part of the future FAIR facility near Darmstadt, Germany. The production of close-to-final sub-modules for the forward endcap of the calorimeter is presented and the assembly of photodetector-preamplifier units is discussed. These units are equipped with a Vacuum Photo Tetrode or two Avalanche Photo Diodes, each, to detect scintillation light from lead tungstate crystals. The calorimeter modules were tested during various test beam times with a prototype setup, utilizing electron and tagged photon beams in the energy range between 23 and 15000 MeV. The energy resolution of symmetric crystal matrices was determined to be $\frac{\sigma_E}{E} = \frac{(2.41 \pm 0.02)\%}{\sqrt{E[GeV]}} \oplus (0.86 \pm 0.02)\%$ from the analysis of the test beam data.

Contents

1 Introduction and Motivation

Important steps towards the understanding of the building blocks of matter undoubtedly were the discovery of the electron by Thompson (1897), the first scattering experiments by Rutherford et. al. (1911) and finally the discovery of the neutron by Chadwick (1932), which led to a much deeper understanding of the structure of atoms. Together with the modifications that Bohr added to the model, a theoretical description of atoms was established. His findings led to the first theoretical description of the emission spectrum of hydrogen, which was only empirically known before. With the help of quantum theory, which evolved in the 1930s, the orbital model of atoms was established and finally the behavior of chemical elements could be explained: The *electromagnetic force* that acts between the positively charged protons in the atomic nuclei and the electrons in their shells was identified to be responsible for the macroscopically visible behavior of the elements. Since the atoms were no longer considered elementary particles, two questions quickly evolved: Do electrons, protons and neutrons have an inner structure themselves? What kind of force is responsible for keeping the neutrons and protons together on very small distances in the atomic nucleus? While no experimental evidence for an inner structure of the electron was found, more than a hundred new particles were discovered mainly by accelerator based experiments from the 1950s on. The variety of different particles, called hadrons (greek: *hadrós*, "thick"), suggested that these were not elementary particles, but had an inner structure themselves. In the 1970s Gell-Mann developed the so called *quark model*, in which hadrons consist of three quarks (baryons as e.g. proton and neutron), three antiquarks (antibaryons) or a quark and an antiquark (mesons). It was found that quarks are bound together to form hadrons due to the *strong interaction*, which is also responsible for binding protons and neutrons to atomic nuclei. However, many aspects of the strong interaction are not yet understood. A successful tool to tackle the open questions of hadron physics is the spectroscopical classification of hadrons, which is being pursued until today.
Advanced detector systems as well as sophisticated analysis methods are necessary to facilitate further progress in the field of hadron spectroscopy. Both fields are addressed within the scope of this thesis: On the one hand a partial wave analysis of data recorded by the BESIII experiment is discussed, while on the other hand hardware developments for the future hadron physics experiment $\overline{\text{P}}$ANDA are presented. Before going into detail, the fundamentals of hadron physics will be briefly introduced in the subsequent section.

1.1 The Standard Model of Particle Physics

The classification of the particles that were discovered - and especially their postulated inner structure - was the first step towards the emerging *Standard Model of Particle Physics*, which describes all elementary particles and the interactions between them in a unified way. All particles that are point-like and thus do not have an inner structure are considered to be elementary particles. In general elementary particles with half integer spin (*fermions*), and those with integer spin (*bosons*) are distinguished. Twelve different fermions are included in the standard model, namely six *quarks* and six *leptons*. Each of these two groups is sub-divided into three families. Additionally, for each of these twelve particles an antiparticle exists, for which some properties are identical (mass, spin), while e.g. the electrical charge is inverted. Table 1.1 lists the elementary particles and some of their basic properties.

Apart from the electron, two other charged elementary leptons with prominently higher mass were found. These are called *muon* and *tauon*; however both of these leptons are unstable and decay into other leptons. The three remaining leptons are the uncharged, extremely light and weakly interacting *neutrinos* (ν_e, ν_μ, ν_τ), one of which is associated to each charged lepton. Additionally to the properties given in Table 1.1, each lepton family is assigned a *lepton family number*, which is conserved in all interactions described by the standard model. Up to now, the only process which is known to violate the conservation of the lepton family number is the *neutrino oscillation*.

Quarks appear in six different flavors, which are called up, down, charm, strange, top and bottom. Similar to the classification scheme for leptons, three families can be defined containing one positively and one negatively charged quark each. When considering charge in connection with quarks, two features must be discussed: In constrast to the charged leptons, quarks carry a fractional electric charge of $+\frac{2}{3}e$ or $-\frac{1}{3}e$. Furthermore, each quark carries a so called *color charge*, which can be either red, green or blue and in case of antiquarks anti-red, anti-green or anti-blue, respectively. A unique feature of quarks is, that they do not exist as isolated particles but are always bound in hadrons, a property that is called the *confinement*. In fact, the phenomenon of confinement is not understood yet and requires a further spectroscopical classification of hadrons.

Free particles are neutral regarding the color charge. Thus, in analogy to additive color mixing, a meson always contains a quark carrying some specific color and an antiquark

	Family	Particle	Electrical charge [e]	Color charge	Flavor	Mass [MeV/c^2]
Leptons	1$^{\text{st}}$	e	-1	-	$L_e = +1$	0,511
		ν_e	0	-	$L_e = +1$	$< 2 \cdot 10^{-6}$
	2$^{\text{nd}}$	μ	-1	-	$L_\mu = +1$	105,66
		ν_μ	0	-	$L_\mu = +1$	$< 0{,}19$
	3$^{\text{rd}}$	τ	-1	-	$L_\tau = +1$	1777
		ν_τ	0	-	$L_\tau = +1$	$< 18{,}2$
Quarks	1$^{\text{st}}$	u	$+\frac{2}{3}$	r,g,b	$I_3 = +\frac{1}{2}$	1,7-3,3
		d	$-\frac{1}{3}$	r,g,b	$I_3 = -\frac{1}{2}$	4,1-5,8
	2$^{\text{nd}}$	c	$+\frac{2}{3}$	r,g,b	$C = +1$	$1{,}27 \cdot 10^3$
		s	$-\frac{1}{3}$	r,g,b	$S = -1$	101
	3$^{\text{rd}}$	t	$+\frac{2}{3}$	r,g,b	$T = +1$	$172 \cdot 10^3$
		b	$-\frac{1}{3}$	r,g,b	$B = -1$	$4{,}19 \cdot 10^3$

Table 1.1: Properties of the twelve elementary particles with half integer spin. The electrical charge is given in units of $e = 1{,}602 \cdot 10^{-19}$ C [1].

which carries the corresponding anticolor, while a baryon contains a quark of each color and an antibaryon an antiquark of each anticolor.

1.1.1 Fundamental Interactions

Since the standard model is a relativistic quantum field theory, all interactions between particles are described by the exchange of force-mediating particles, the *gauge bosons*. According to the standard model the *strong interaction* is mediated by eight gluons which themselves carry a color charge, the *electromagnetic interaction*, mediated by the *photon* and the *weak interaction* which is mediated by the heavy $W^{\pm}$ and Z^0 bosons. The *gravitation* is the last of the four fundamental forces of nature that are known today, which is possibly mediated by a particle called the *graviton*, however this has not been experimentally observed yet. The gravitation is not included in the standard model, since its relative strength compared to the other three forces for elementary particles at a distance of $\sim 10^{-15}$ m to each other is about 38 orders of magnitude smaller and thus can be neglected.

Due to the fact that the photon is massless and a direct coupling between two photons is not possible, the electromagnetic force acts on an infinite range. In contrast to that, the range of the weak interaction is limited to very small distances, due to the non-zero mass of its gauge bosons.

Despite these large differences between the interactions, Glashow, Weinberg and Salam were able to present a unified theory of the electroweak interaction, for which they were awarded the Nobel Prize in 1970. In this theory, gauge bosons that have a non-zero mass ($W^{\pm}$,Z^0) can only be described with an additional scalar field, to which they couple, the so-called Higgs field. The Higgs mechanism is also responsible for the generation of the mass of all other elementary particles. A consequence of the presence of the Higgs field is the existence of another observable elementary particle, the Higgs boson. In 2012, the two collaborations ATLAS (A Toroidal LHC Apparatus) and CMS (Compact Muon Solenoid) at the LHC (Large Hadron Collider) accelerator, located at the European nuclear research center CERN, reported the discovery of a new boson with a significance of $> 5\sigma$, which is assumed to be the long sought Higgs boson (Nobel Prize 2013). Its mass was determined to be $m_H = (125.09 \pm 0.24)\,\mathrm{GeV}/c^2$ [1]. With this discovery, the last elementary particle of the standard model was identified and the model is therefore completed.

In striking contrast to all other interactions, the gauge bosons of the strong interaction can couple to other gluons since they themselves carry a color charge. Due to this kind of gluon-gluon coupling, the range of the strong force is very limited, although gluons, like photons, are massless particles. The theoretical framework to describe the structure and dynamics of strongly interacting particles is called *Quantum Chromodynamics*. It is largely inspired by the successful theory of *Quantum Electrodynamics* that was developed to describe the electromagnetic interaction. When two electric charges are brought close to each other, the force between them gets stronger, while for larger distances the force weakens as $1/r$. The force between two quarks shows the same behavior at small distances, yet it unexpectedly gets stronger for larger distances. The $1/r$-type behavior is replaced with a linearly rising potential for distances larger than $r_0 \approx 0.5\,\mathrm{fm}$. The potential can be parameterized by

$$V(r) = -\frac{4}{3} \cdot \frac{\alpha_s(r)\hbar c}{r} + k \cdot r \quad \text{with} \quad \alpha_s(Q^2) = \frac{12\pi}{(33 - 2n_f) \cdot \ln(Q^2/\Lambda^2)}, \tag{1.1}$$

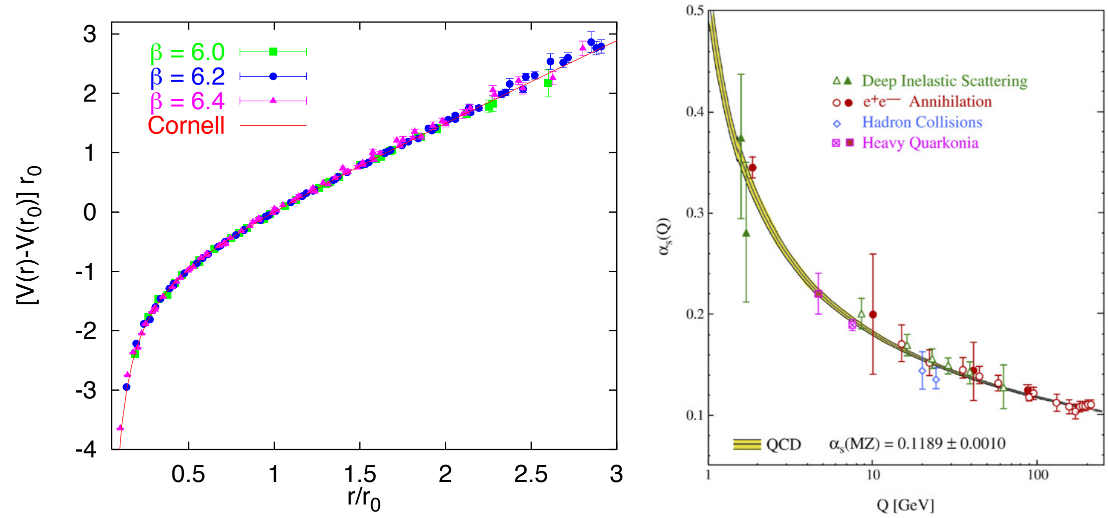

(a) **(b)**

Fig. 1.1: (a) Interaction potential of QCD in units of $r_0 \approx 0.5\,\mathrm{fm}$ for the *Cornell parameterization* (red line) and Lattice QCD calculations with three different lattice spacings (colored points). [2]
(b) Coupling constant of the strong interaction in dependence of the energy scale Q for theoretical predictions (filled symbols, yellow band) and measurements (open symbols) [3]

where n_f is the number of quark flavors and Λ is a scale parameter that has been experimentally determined to $\Lambda \approx 250\,\mathrm{MeV}/c^2$. The analytical form of the potential as well as calculations from Lattice QCD are shown in Figure 1.1a. It should be stressed here, that this is only an empirical parameterization of the *effective* potential and the true nature of the potential is yet to be discovered. Equation (1.1) shows, that the coupling constant of the strong interaction, α_s, unlike the one known for the electromagnetic interaction ($\alpha_{\mathrm{em}} = \frac{1}{137}$), depends heavily on the four-momentum transfer Q: For very large values of Q (corresponding to small distances), the strong coupling constant gets very small and the quarks can be regarded as quasi-free. This property is called *asymptotic freedom* of the quarks and can be reached at very high energies with accelerators such as the LHC. In this regime of QCD, perturbation theory (expansion in a small parameter) is applicable, while for small Q the strong coupling constant gets larger (non-perturbative regime). The behavior of α_s in dependence on the momentum transfer Q is shown for theoretical calculations as well as measurements in Figure 1.1b.

1.2 Hadron Spectroscopy

Applying the rules of QCD, many different hadrons consisting of quarks (and gluons) can be imagined. One goal of hadron spectroscopy is, to identify and precisely characterize these states and thus provide important tests for many aspects of QCD, especially in the non-perturbative regime. The findings must be compared to fundamental approaches, such as Lattice QCD calculations, or phenomenological expectations, e.g. from the "naive" quark model, QCD sum rules, and so on in order to verify or falsify a theoretical model.

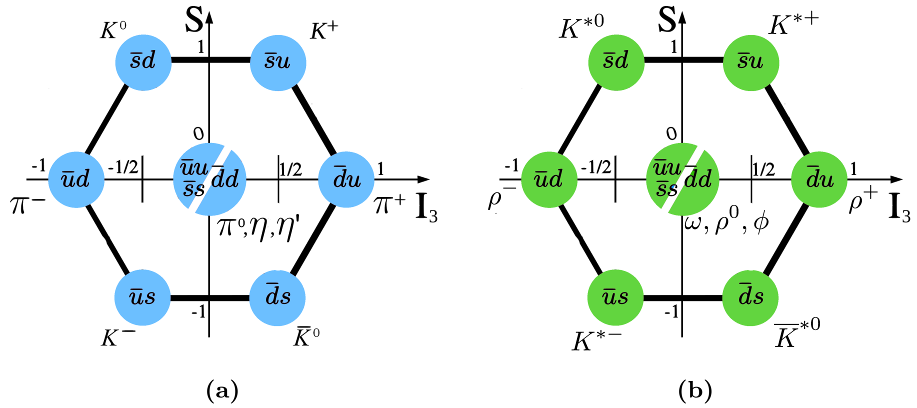

Fig. 1.2: Nonets of the *pseudoscalar* (a) and *vector* mesons (b). The colored circles represent the mesons and their quark content, depicted in a diagram showing strangeness (y-axis) versus the third component of the isospin (x-axis). The mesons that are located in the center of the diagrams contain a mixture of the three quark-antiquark combinations given in the label, indicated by the white diagonal line.

One distinguishes between mesons that are made up only of light quarks (up, down and strange), and those containing at least one heavy (charm or bottom) quark. Since the mass difference between the heavier quarks is quite large, it is easier to separate these states and identify their quark content than in the sector of the light quark hadrons. Additionally, the light states have similar masses and large widths, so that they largely overlap.

Mesons are usually classified using a spectroscopic notation, which contains information about the most important quantum numbers that characterize them. The naming schemes include the spin S of the quark-antiquark pair (0 or 1), the orbital angular momentum L between the two constituents, a quantum number describing a possible radial excitation n as well as the eigenvalues of the charge conjugation operator $C = (-1)^{L+S}$ and the parity operator $P = (-1)^{L+1}$. A state is either identified by the notation $n^{2S+1}L_J$, or J^{PC}, where the total spin is given by the vector sum $\vec{J} = \vec{L} + \vec{S}$. Therefore, the projection J is limited to the values given by $|L - S| \leq J \leq |L + S|$. Additionally, states can be distinguished by their quark content, where the number of up- and down-quarks determines their *isospin*, while for all other quark flavors an own quantum number was assigned (*strangeness, charm, bottomness, topness*). The spin-parity notation J^{PC} will be used throughout this thesis. Phenomenologically, in total nine different quark-antiquark states can be constructed, when only the three light quark flavors are considered. The nonets of the lightest mesons with $L = 0$, $S = 0$ and $L = 0$, $S = 1$ are shown in Figures 1.2a and 1.2b, respectively. These states are called *pseudoscalar* (0^{-+}) and *vector* mesons (1^{--}) and contain the π^+, π^-, π^0 as well as the ω mesons that are important for the analysis presented in the Chapters 3-5. Apart from the lightest mesons discussed up to now, many more states have been found which are characterized by different quantum numbers as e.g. higher spin, different parity, or which represent radial excitations of ground state mesons.

Due to the possibility of gluon-gluon interactions, the construction of *exotic* states that contain gluonic degrees of freedom is allowed in the framework of QCD. In principle, exotic states may carry conventional as well as exotic quantum numbers. The latter ones

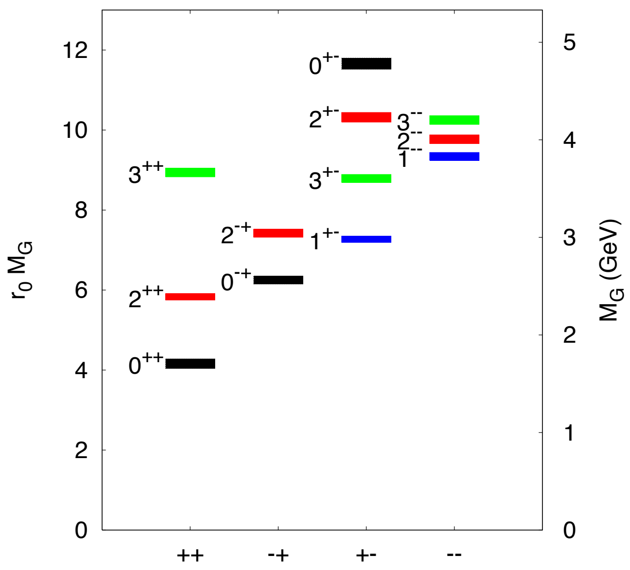

Fig. 1.3: Mass spectrum of glueball states predicted from Lattice QCD calculations. The vertical size of the boxes shows the uncertainty in the determined mass. The x-axis is labeled with the PC quantum numbers.[4]

are defined as J^{PC} combinations that can not be constructed for a quark-antiquark pair considering the selection rules discussed above, such as $0^{--}, 0^{+-}, 1^{-+}, 2^{+-}$, and so on. Particles that consist of quarks and antiquarks with additional "valence"-gluons ($q\bar{q}g$,...) are called hybrids, whereas objects that are solely consisting of gluons are called *glueballs* ($ggg, gg, ...$). The discovery of a particle with exotic quantum numbers would be a strong indication for its exotic nature. It is however a long standing discussion in the field of hadron physics, how glueballs that carry conventional J^{PC} quantum numbers could be experimentally identified and studied. The discovery of such states would be an enormous achievement for the understanding of the non-perturbative regime of QCD and also a strong argument for the correctness of this theory. Theoretical calculations in the non-perturbative energy regime are in most cases limited to numerical lattice calculations. These require large computing power and rely on a number of assumptions, e.g. on the masses of the light quarks, to perform estimations based on an arbitrarily discretized space-time grid. Despite these obstacles and limitations, several glueball-candidates have been predicted by Lattice QCD calculations, especially in the mass range between 1.5 and $\sim 4\,\mathrm{GeV}/c^2$ [4]. The results of these calculations are shown in Figure 1.3. Since this mass range is experimentally accessible for more than 50 years to date, the question arises, why no glueballs have been unambiguously identified yet. One reason for this is that a large number of the predicted glueball states carry non-exotic J^{PC} quantum numbers, and thus a clear, characteristic identification feature is missing. It is most important for a deeper understanding of the nature of hadrons and the interaction between their constituents, to finally classify all hadronic states. This does not only include the determination of quantum numbers ($J^{PC}, I, ...$), but also to study the production of hadrons in different processes and to cover as many decay modes as possible. A full understanding of the spectrum of conventional light hadrons is therefore essential for the identification of possible exotic states. This requires not only data sets with large statistics, but also sophisticated analysis tools, so that overlapping and interfering contributions can be extracted from the

observed intensity. The most sophisticated analysis tool at hand is a full partial wave analysis, which allows for a decomposition of the observed intensity into contributions of partial waves according to a model based on complex amplitudes (see Chapter 4).
In fact, glueball states might have shown up in the data of various experiments already, but their interpretation and unambiguous spectroscopic classification has not yet succeeded. Additionally, the expected states are located in a mass region, which is also populated by a variety of conventional mesons, some of which are broad and therefore overlapping states.
Likewise, also mesons containing heavier quarks have been spectroscopically analyzed. Of particular importance are the *charmonium* mesons, consisting of a charm and an anticharm quark, since they are suitable probes to investigate the transition region between the long and short distance regimes of QCD. The charmonium system is spectroscopically considered as a very clean environment. Two charmonia should be noted here, namely the J/ψ meson, which has the quantum numbers $J^{PC} = 1^{--}$ and therefore can be directly produced in e^+e^- annihilations via a virtual photon, and the ground state charmonium meson, the η_c ($J^{PC} = 0^{-+}$). The analysis presented in the following chapters is based on decays of the J/ψ. The η_c is one of the particles that is observed in its decay.

1.3 Motivation

1.3.1 Partial Wave Analysis of the Decay $J/\psi \to \gamma\omega\omega$ at BESIII

It is an obvious feature, that glueballs should strongly couple to gluons and thus should be produced to a larger fraction in QCD processes involving hard gluons, in contrast to e.g. electromagnetic processes. Already shortly after its discovery, the decay of the lightest vector charmonium state J/ψ was identified as a very rich environment for the study of the light hadron spectrum. Especially so-called radiative decays of the J/ψ, which in first order proceed via the diagram shown in the left part of Figure 1.4, are regarded as an ideal "laboratory" to search for states with gluonic excitations.
In this diagram, a photon is radiated off a quark line in the initial $c\bar{c}$ state. Two gluons are produced in the $c\bar{c}$ annihilation, which then hadronize into the object X under study. The right part of Figure 1.4 shows a diagram, where the photon is instead radiated off a final state quark line. This process is however strongly suppressed.
Extensive studies of various radiative decay modes of the J/ψ have been performed, including $J/\psi \to \gamma X$ with $X \to VV$, where V denotes any of the vector mesons ρ, ω or ϕ. MARKII first observed a large enhancement at threshold in the $J/\psi \to \gamma\rho\rho$ channel [6], which later was identified as a predominantly pseudoscalar structure by MARKIII [7]. A similar analysis was performed for the $\omega\omega$ channel, in which also a large pseudoscalar

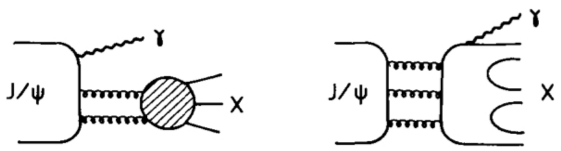

Fig. 1.4: Lowest order diagrams for the radiative decay of the J/ψ. The radiative photon is either emitted from the initial state (a) or final state (b) quark lines. The latter is considered to be strongly suppressed [5].

enhancement at threshold was observed by MARKIII [8]. The invariant mass of the $\omega\omega$ system as well as the results of a spin-parity analysis considering seven J^P waves by MARKIII are displayed in Figure 1.5(a) and (b). Apart from the pseudoscalar enhancement, significant activity is also observed in the scalar (0^+) and tensor (2^+) contributions. These findings were first confirmed by the DM2 experiment [9] with lower statistics, where also a spin-parity analysis was performed. Almost 20 years later the $\gamma\omega\omega$ decay of the J/ψ was also analyzed by the BESII [10] experiment, where a first partial wave analysis of the $\omega\omega$ system could be performed, the results of which are shown in Figure 1.6.
The enhancement at the $\omega\omega$ threshold was identified with the $\eta(1760)$ meson, which is the dominant contribution in the BESII result. Apart from this pseudoscalar contribution, 0^{++} as well as 2^{++} contributions were identified with the $f_0(1710)$, the $f_2(1640)$ and the $f_2(1910)$ mesons. It is not clear, however, if the description of the threshold enhancement with an $\eta(1760)$ component is sufficient and holds, when a much larger data sample is analyzed.
A similar near-threshold structure was also observed in the $\phi\phi$ system by DM2 [11] and later by MARKIII [12]. The unexpected presence of these dominant, broad pseudoscalar components in vector-vector systems, which was called the "pseudoscalar puzzle" [13] in the early days of accelerator based experiments, has not been satisfyingly explained up to now. To achieve a full understanding of the light hadron sector, it is most likely necessary to combine all information that are available and use the most advanced theoretical models and analysis tools. For example, it could be considered, that the pseudoscalar enhancement at threshold in the vector-vector systems, or at least a certain part of it, stems from a resonance that is located below the corresponding VV threshold. This attempt has been followed in a very early one-dimensional coupled channel analysis [13] using data from the MARKIII experiment. The interpretations of the analysis results however suffer from the comparably low statistics available in the MARKIII data set.
Another remarkable result is obtained by the Belle collaboration, where different VV systems including the $\omega\omega$ channel were studied in the process of two-photon fusion[1]: Belle reports an enhancement at threshold in the invariant $\omega\omega$ mass. A spin-parity analysis leads to the conclusion, that the enhancement is dominated by scalar (0^{++}) and tensor (2^{++}) contributions. This result blatantly contradicts the pseudoscalar character of the threshold enhancement found in radiative decays of the J/ψ. This is of special interest, since photons can not directly couple to gluons and thus resonances containing gluonic degrees of freedom should be strongly suppressed in two-photon fusion.[14]
In order to obtain a better understanding of the contributions to the $\omega\omega$ system, the large available BESIII data set (see Section 3.1) is used in Part I of this work and an exclusive reconstruction of events of the topology $J/\psi \to \gamma\omega\omega$ is performed. Both ω mesons are reconstructed via their decay into $\pi^+\pi^-\pi^0$ and both π^0 mesons in two photons, respectively (see Section 3.2). Different data- and Monte Carlo (MC) simulation-driven background studies are performed, to estimate the background level present in the selected data set (see Section 3.3). Due to the significant contamination of the selected sample by non-resonant, signal-mimicking background contributions, a background suppression based on probabilistic event weights is applied to the selected data set (see Section 3.4). After a detailed discussion on the performance of the background suppression method, based on studies employing toy MC samples (see Section 3.4.3), a model independent partial wave

[1] In the interaction region of an e^+e^- collider the two beam particles can both emit a photon when they are passing by close to each other. When the two photons collide, a resonance can be created.

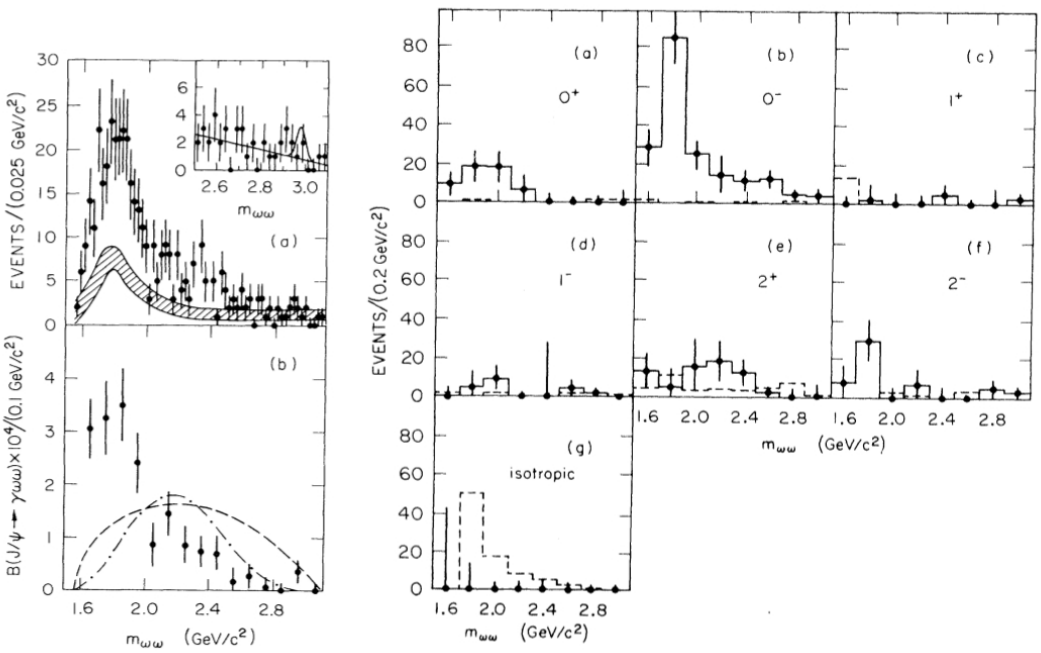

(a) **(b)**

Fig. 1.5: Invariant mass distribution of the $\omega\omega$ system from the previous analysis of the $J/\psi \to \gamma\omega\omega$ decay. (a) shows the invariant mass for reconstructed data as well as the background estimation (shaded band) in the upper, and $\mathcal{B}(J/\psi \to \omega\omega)$ vs. the $\omega\omega$ mass in the lower diagram from the MARKIII analysis. The diagrams in (b) show the results of the corresponding spin-parity analysis.[8]

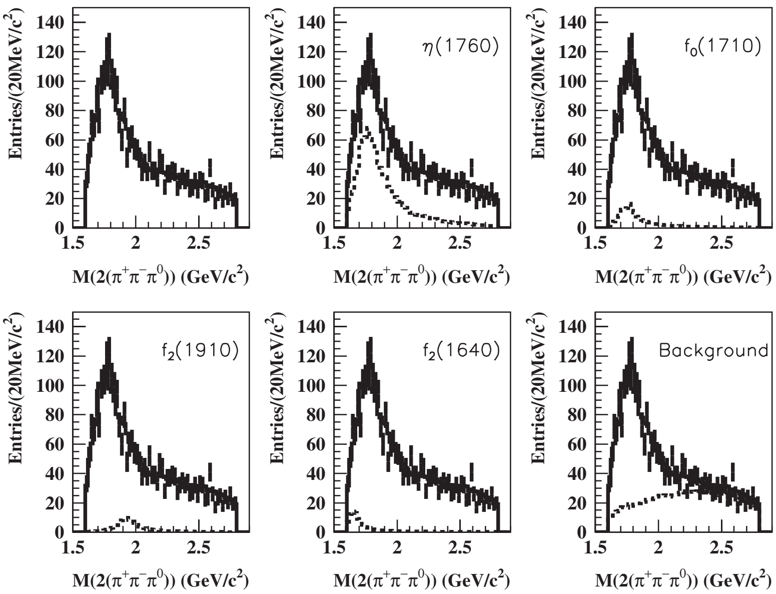

Fig. 1.6: Invariant mass distribution of the $\omega\omega$ system from the analysis of the BESII experiment (upper left plot) and the individual contributions of the result of a partial wave analysis.

analysis (PWA) in bins of the $\omega\omega$ mass is performed (see Section 4.7). The results of this study are used as a guidance for a model dependent PWA, which is presented in Chapter 4.8.

It is noteworthy that none of the previous experiments was sensitive enough to observe a signal of the $\eta_c(1S)$ in its decay into an ω-meson pair. Although it was discovered already in 1980, the properties of the η_c are still poorly known. Especially when considering the data available on the branching fractions of different decay modes of the η_c, it becomes obvious that this resonance is not fully understood yet. Several branching fractions listed e.g. in [1] are only measured with large statistical and/or systematic errors. The observed branching fractions sum up to only about 60%, meaning that major decay channels of this resonance are yet unobserved. Several peculiarities also arise when the resonance parameters of this meson are studied more closely. The observed mass and decay width seem to vary by a large fraction from experiment to experiment, and also seem to be dependent on the production and decay process in which they are observed. The mass is of particular interest, since the η_c-J/ψ hyperfine splitting provides an important test of theoretical predictions for the charmonium spectrum. The parameters reported in the most recent summary of the PDG [1] are dominated by high statistics measurements, while some of the earlier results are not taken into account for averaging any more, which causes frequent changes in the listed values.

The decay of the η_c into a pair of ω mesons is of special interest for this analysis: Only an upper limit for the branching fraction of this decay is listed by the PDG, although the decay $\eta_c \to 2(\pi^+\pi^-)\pi^0\pi^0$, which should implicitly also contain the $\omega\omega$ channel, has been determined to be one of the strongest decay modes of the η_c.

Predictions for the branching fractions of the η_c into a pair of vector mesons have been recently published [15]. However, the predicted branching fractions for the decay modes $\eta_c \to \phi\phi$ and $\eta_c \to \rho\rho$ are much smaller than those observed experimentally (see Table 1.2). The predictions are based on NLO perturbative QCD calculations and for the first time also include so-called higher-twist contributions. It was found that these contributions do have a major impact on the branching fractions and lead to much larger values than what was expected from pure perturbative QCD. However the effect is not strong enough to explain the experimentally determined branching fractions.

In the analysis presented in this thesis a strong signal at the mass of the $\eta_c(1S)$ meson is observed in its decay into $\omega\omega$. The extraction of the η_c resonance parameters and the

Decay mode	Measurement Γ_i/Γ	Prediction Γ_i/Γ
$\rho\rho$	$(1.8 \pm 0.5)\%$	$2.0 \cdot 10^{-4}$
$\phi\phi$	$(1.75 \pm 0.2) \cdot 10^{-3}$	$6.6 \cdot 10^{-4}$
$\omega\omega$	$< 3.1 \cdot 10^{-3}$ (CL: 90%)	$9.1 \cdot 10^{-5}$
$2(\pi^+\pi^-)\pi^0\pi^0$	$(17.4 \pm 3.3)\%$	

Table 1.2: Decay modes of the η_c and their corresponding branching fractions in terms of relative partial widths Γ_i/Γ [1]. Theoretical predictions for the decay modes $\eta_c \to VV$ with $V \in \{\rho, \omega, \phi\}$ from [15] are shown.

measurement of the branching fraction are discussed in detail in Chapter 5. With these measurements the current knowledge of the η_c will be improved.

1.3.2 Developments for the $\overline{\text{P}}$ANDA Electromagnetic Calorimeter

Apart from radiative decays of charmonia, the antiproton-proton annihilation process is known to be very gluon rich, which enables the study of exotic hadrons. Therefore, a new hadron physics experiment is currently being planned to be set up at the Facility for Antiproton and Ion Research (FAIR) near Darmstadt, Germany: The $\overline{\text{P}}$ANDA (AntiProton ANnihilations at DArmstadt) detector will be set up as a fixed target experiment in the beam line of a synchrotron ring, which is to deliver an antiproton beam with unprecedented momentum resolution. In contrast to the e^+e^- annihilation, where only states carrying the quantum numbers $J^{PC} = 1^{--}$ can be produced directly, at $\overline{\text{P}}$ANDA all states carrying non-exotic quantum numbers are directly accessible. To perform high precision measurements the $\overline{\text{P}}$ANDA detector must provide excellent capabilities for the reconstruction of charged and neutral final state particles. Therefore, an electromagnetic calorimeter with an excellent energy resolution and a low energy threshold is one of the key components of the detector. The *forward endcap* of the homogeneous crystal calorimeter, which is being constructed mainly at Ruhr-Universität Bochum, has to withstand the highest expected single crystal hit rates and radiation doses due to the Lorentz-boost in a fixed-target setup. After several tests have been performed in the past years, the first final crystal-photodetector-preamplifier units have been built and are presented in Chapter 9. Furthermore, calorimeter subunits were tested in a prototype setup at different accelerator centers providing test beams with different energies with the goal to determine the energy resolution of the calorimeter modules over the full $\overline{\text{P}}$ANDA energy range. The results of the two most recent test beam times are reported in Sections 10.3 and 10.4.

Part I

Partial Wave Analysis of the Decay $J/\psi \to \gamma\omega\omega$ at BESIII

2 Experimental Setup

The data set used for this work has been recorded with the BESIII detector located at the BEPCII electron-positron storage ring. Both, the detector and the accelerator will be discussed in more detail in the following sections.

2.1 The BEPCII Accelerator

The Chinese Academy of Sciences successfully operated a symmetrical, single ring electron-positron collider, called BEPC (Beijing Electron Positron Collider), in the years 1989 to 2004 at the Institute for High Energy Physics (IHEP) in Beijing, China. In the following years (2004 - 2006) this collider was upgraded and its successor, BEPCII, was installed in the same tunnel as BEPC. One major upgrade was the installation of a second beam pipe, so that electrons and positrons circulate in separate beam pipes until they are brought to collision at a defined point. The BESIII detector, which will be discussed in more detail in Section 2.2, is surrounding this so called *interaction point* (IP). Due to the design of the accelerator involving two distinct beam pipes, the electron and positron beams are colliding inside the BESIII detector under a small angle of 2×11 mrad (see Fig. 2.1b) [16]. Electrons as well as positrons are first accelerated in the BEPC injector, a linear accelerator with a length of 202 m, up to an energy of $E_{e^{\pm},\mathrm{inj}} = 1.89 - 2.5\,\mathrm{GeV}$. The pre-accelerated particles are then injected into the rings of BEPCII (see Fig. 2.1a). While the beam current in BEPC was only 35 mA using a single particle bunch per beam, beams are circulating in BEPCII at a design beam current of 910 mA, with 93 bunches per beam. These key parameters are necessary to achieve the high design luminosity of $\mathcal{L} = 1 \cdot 10^{33}\mathrm{cm}^{-2}\mathrm{s}^{-1}$ at a beam energy of 1.89 GeV, as required for the BESIII physics program. A summary of all relevant operational parameters of BEPC and BEPCII is given in Table 2.1.

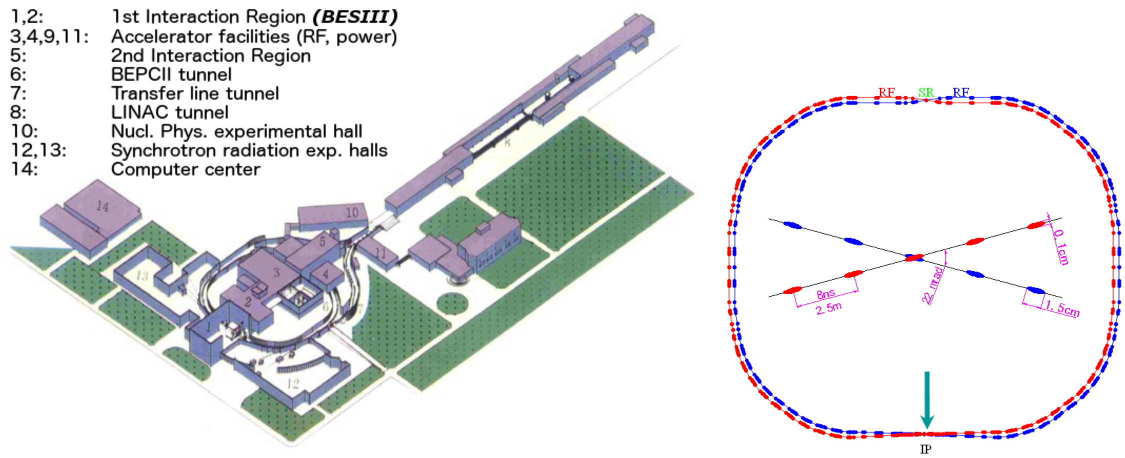

(a) (b)

Fig. 2.1: Schematic view of the BEPCII facility (a) and the collider itself (b) (cf. [17])

Parameter	Unit	BEPCII	BEPC
Center of mass energy	GeV	$2 - 4.6$	$2 - 5$
Circumference	m	237.5	240.4
Peak luminosity (at $2 \times 1.89\,\mathrm{GeV}$)	$\mathrm{cm}^{-2}\mathrm{s}^{-1}$	$\sim 10^{33}$	$\sim 10^{31}$
Number of bunches	–	2×93	2×1
Beam current	A	2×0.91	2×0.035
Bunch spacing	m/ns	2.4/8	–
Bunch length (σ_z)	cm	1.5	~ 5
Bunch size ($\sigma_x \times \sigma_y$)	µm×µm	$\sim 380 \times 5.7$	$\sim 840 \times 37$
Relative energy spread	–	$5 \cdot 10^{-4}$	$5 \cdot 10^{-4}$
Crossing angle	mrad	± 11	–

Table 2.1: Operational parameters of BEPCII and BEPC (cf. [18])

2.2 The BESIII Detector

During the runtime of the BEPC accelerator, the original BES (BEijing Spectrometer) detector recorded data from e^+e^- collisions produced at IHEP. In 1996 a major upgrade of the detector hardware was performed and the so called BESII experiment continued the successful data taking until its decommissioning in 2004, when BEPC was shut down. In order to fully exploit the advantages of the high luminosity of the BEPCII collider, a completely new detector utilizing advanced detector technology and knowledge gained with its predecessors BES and BESII, was built. Only four years after the decommissioning of BEPC and BESII, the BESIII detector recorded its first hadronic event from e^+e^- collisions in July, 2008 [17]. Since this day a large number of events at different beam energies have been recorded. An overview over the various BESIII data sets, and especially the ones used for this work, will be given in Sections 2.2.7 and 3.1.

Similar to many other detectors in high energy particle physics, BESIII is a cylindrically symmetrical detector, composed of various different subdetector systems. The goal is to precisely measure the momentum and energy of particles created in the e^+e^- annihilations. Additionally, the species of each particle must be identified. BESIII is equipped with a large solenoid magnet, which produces a 1 T magnetic field. Charged particles are forced onto curved tracks by this field, so that positively charged, negatively charged and neutral particles can be distinguished. Furthermore, the momentum of charged particles can be derived from the curvature of their tracks. The magnet coil and its iron flux return yoke are the mechanical core components of the detector (see Fig. 2.2: "SC-coil"). All subdetector systems apart from the muon counters, which are inserted into the layers of the iron flux return, are mounted inside the solenoid coil. In order to provide precisely focused beams exactly in the center of the detector, where positrons and electrons collide, two superconducting quadrupole magnets are placed as close as possible to the IP. The coils of these magnets are surrounding the beryllium beam pipe and are inserted into the volume of the BESIII detector, situated just outside the conically shaped end caps of the innermost detectors (see Fig. 2.2: "SCQ"). The main characteristics of the single subdetector systems will be explained in the following.

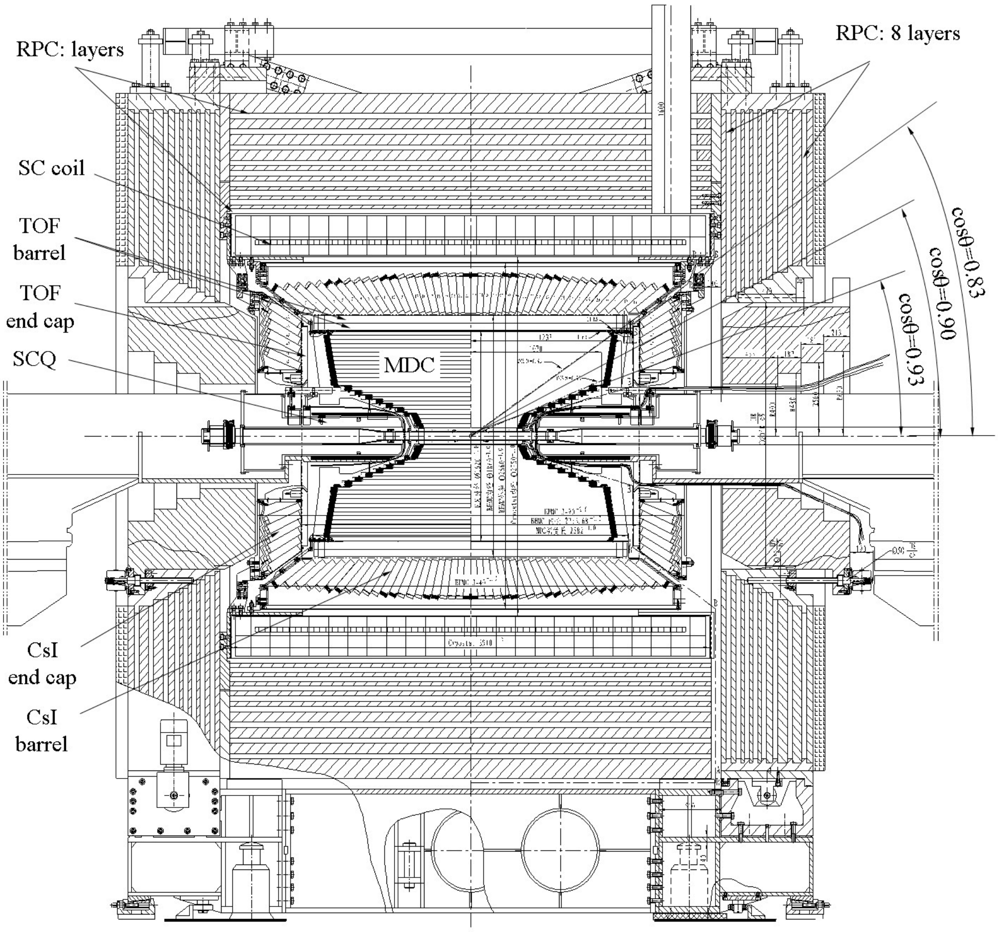

Fig. 2.2: Schematic drawing of the BESIII detector. The beam line runs horizontally through the detector, the interaction point is situated exactly at the geometrical center of the detector.[18]

2.2.1 The Multilayer Drift Chamber (MDC)

All particles originating from e^+e^- collisions which leave the beam pipe have to penetrate the first detector, a cylindrical wire drift chamber.

The inner radius of the chamber is only 59 mm, which leaves 2 mm between the beam pipe and the MDC, while the outer radius amounts to 810 mm. The end plates of the MDC have a stepped conical shape due to the space required for the beam focusing quadrupoles. For this reason the wires of the inner layers are much shorter than those of the outer layers. However, the polar angle coverage of the outermost and innermost wire layer is $|\cos(\theta)| \leq 0.83$ and $|\cos(\theta)| \leq 0.93$, respectively, so that a solid angle coverage of $\Delta\Omega/4\pi = 93\%$ is achieved.[18]

In total the MDC is equipped with 6796 sense wires arranged in 43 layers. All sense wires have a diameter of 25 µm and are made of gold plated tungsten-rhenium. Additional wires are needed to establish a homogeneous eletrical field in the MDC volume, but at the same time it is necessary to keep the material budget in the MDC as low as possible to avoid

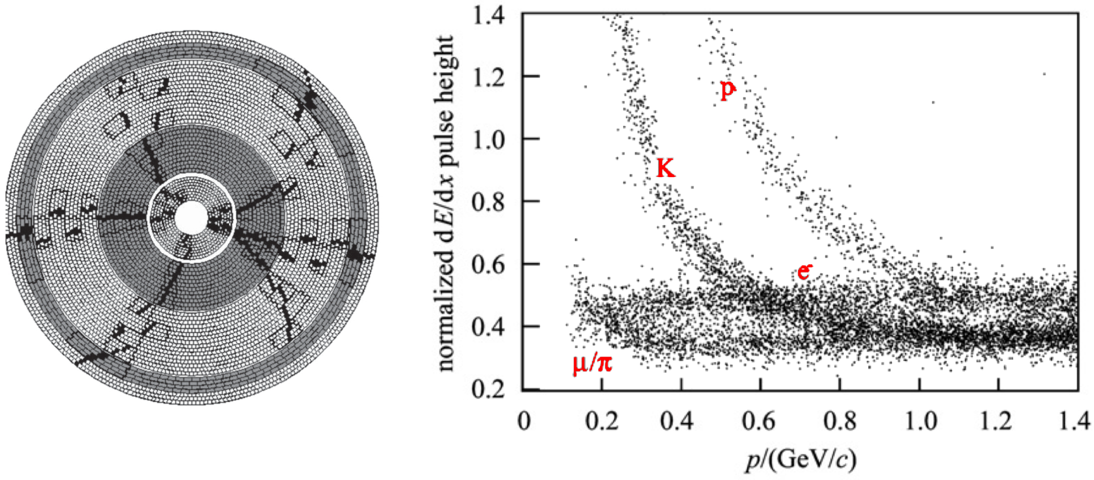

(a) **(b)**

Fig. 2.3: (a) Visualization of hits in the MDC (xy-projection shown)[18]
(b) Specific energy loss in the MDC vs. incident momentum for various particle species [19]
Both pictures show events from Monte Carlo detector simulation studies.

multiple Coulomb scattering. For this reason, the 21844 additional field wires are made of gold plated aluminium.

The complete volume of the MDC, which amounts to about $4\,\mathrm{m}^3$, is filled with a gas mixture of 60% helium and 40% propane (C_3H_8) gas at a pressure of 3 mbar above ambient atmospheric pressure.

When charged particles traverse the gas volume of the MDC, they can ionize the gas along their trajectory. The ions and electrons start drifting through the volume due to the high voltage which is applied to the MDC wires. This produces electrical signals at the corresponding wires, which are read out and digitized. Figure 2.3a shows a visualization of MDC hits in the xy-plane, perpendicular to the beam axis. Wires that delivered a signal above the detection threshold are marked in black. Multiple possible tracks can be seen in this example. Using the wire signals, a three-dimensional reconstruction of the particles' trajectories can be performed.

The expected single cell position resolution in the $r - \varphi$ plane is $\sim 130\,\mu\mathrm{m}$ and $\sim 2\,\mathrm{mm}$ in z-direction. The momentum of a particle is calculated from the curvature of its track. The momentum resolution is expected to be $\sigma_p/p \approx 0.5\%$ at $1\,\mathrm{GeV}/c$.

Furthermore, the measurement of the specific energy loss dE/dx of a particle traveling through the gas is used for the identification of the particle species. Figure 2.3b shows the normalized pulse heights of simulated MDC wire signals, which is proportional to the energy loss of a particle in the gas, versus the incident momentum of the particles. One can clearly see, that the e^--π separation works well down to a momentum of $\sim 0.2\,\mathrm{GeV}/c$, while the K-e^- separation only suffers beyond $0.6\,\mathrm{GeV}/c$. For this analysis, the K-π separation power is most important.

A 3σ K-π separation can be achieved up to $0.77\,\mathrm{GeV}/c$ using only the dE/dx measurement. Overall a dE/dx resolution of $\sim 6\%$ is expected.

When particles are created, which live long enough to leave the beam pipe and decay only in the gas volume (K_s^0, Λ), the MDC track information is used to determine the position of their decay vertex.
Signals from the MDC are analyzed online and valid tracks are identified using FPGA driven readout boards. Besides two other subdetectors, the information from the MDC is used as a fast Level-1 trigger for the data acquisition.

2.2.2 The Time-of-Flight System (TOF)

Apart from the specific energy loss and momentum of charged particles measured with the MDC, their time-of-flight is determined using a dedicated detector system, which is mounted directly to the outside carbon fibre hull of the MDC.
The TOF system is comprised of a barrel part and two endcaps, which are mounted directly adjacent to the MDC end plates. In the barrel part, two layers of plastic scintillator bars (Bicron BC-408) are arranged in a staggered configuration to avoid gaps between the detector elements and thus achieve a very high azimuthal acceptance. All bars have a length of 2300 mm, a thickness of 50 mm and a trapezoidal cross section. Fine mesh photomultiplier tubes are attached to both ends of each bar, to provide dual side readout of the scintillation light produced in the TOF segments. With the given length, the barrel TOF covers the polar angle region of $|\cos(\theta)| < 0.83$.
The TOF endcaps contain only a single layer of plastic scintillator bars (Bicron BC-404), that are arranged in a almost circular geometry, based on trapezoidally shaped single segments. The scintillator bars of the TOF endcaps are only read out at the outer side, farther away from the beamline, by a single photomultiplier tube per segment. Each scintillator segment has a length of 480 mm and a thickness of 50 mm. The polar angle coverage of the endcaps is about $0.85 < |\cos(\theta)| < 0.95$, which leaves a small acceptance gap between the barrel and the endcaps. This space is needed for the mechanical support structure of the MDC.
Due to the fact that momentum, velocity and mass of a particle are strongly correlated quantities, the knowledge of the momentum derived from the MDC tracks together with the velocity, calculated from the length of the MDC track and the time of flight measured with the TOF system, enables the identification of a particle by its mass.
The time resolution, which is crucial for particle identification, varies depending on the point of impact of a charged particle on the TOF scintillators. While in the barrel part a resolution of $\sigma_t \approx 100\,\text{ps}$ is achieved, the resolution in the endcaps is slightly worse, with a value of $\sigma_t \approx 110\,\text{ps}$. This resolution allows for a $K - \pi$ separation on the level of about 3σ up to a particle momentum of approximately $0.9\,\text{GeV}/c$.
Figure 2.4b shows the mass square calculated from the track parameters measured with the MDC and the time of flight for particles of different species versus the incident particle momentum (MC simulation). In simulation studies it was also shown, that the probability of misidentifying a kaon as a pion is well below 10% for $p < 0.9\,\text{GeV}/c$ and reaches 20% for momenta of $\sim 1.4\,\text{GeV}/c$ (see Fig. 2.4a). The fast signals from the TOF system also serve as an input for the L1-trigger of the full detector.

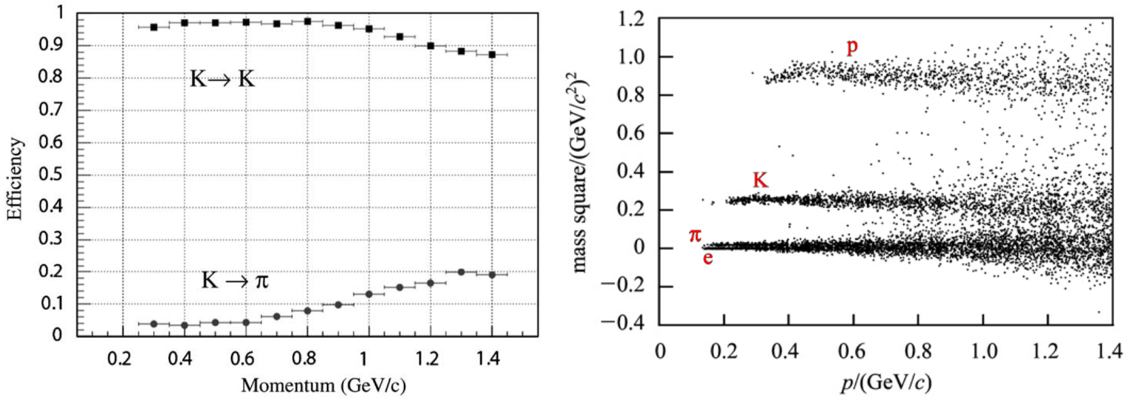

(a) (b)

Fig. 2.4: (a) Efficiency for positive identification of kaons (squares) as well as misidentification of kaons as pions (dots) [18]
(b) Extracted particle mass using MDC and TOF information for p, K, π, e vs. incident momentum [19]
Both distributions were extracted using Monte Carlo simulation studies.

2.2.3 The Electromagnetic Calorimeter (EMC)

The subdetector arrangement inside the coil of the superconducting solenoid magnet, and thus also inside its magnetic field, is concluded by a homogeneous crystal calorimeter. With this calorimeter the energy and flight direction of photons, electrons and positrons is measured.

Photons originating e.g. from radiative decays (as in $J/\psi \to \gamma\omega\omega$) have to be identified and distinguished from photons originating from the decay of neutral pions or η mesons. This imposes a strong requirement on the threshold for the detection of a photon, while at the same time the maximum energy that has to be measured is basically given by the beam energy. In the latter case processes like $e^+e^- \to \gamma\gamma$ are most important, due to the high energy photons produced in the given reaction. Thus, photons in the energy range of 20 MeV to $\sim$ 2.1 GeV are expected.

The low photon energy threshold requires a scintillator material with a comparably high light yield. For this reason the EMC is equipped with thallium doped caesium iodide (CsI(Tl)) crystals. Similar to the TOF detector, the EMC also consists of a cylindrical barrel part and two endcaps. The barrel EMC is composed of 44 ring sections, each containing 120 crystals, i.e. a total amount of 5280 crystals. All crystals are pointing to a region slightly off the interaction point (± 5 cm), to avoid loosing photons originating from the IP and passing through exactly between two crystals. Each endcap consists of 6 rings, containing 480 crystals in total, amounting to 6240 crystals for the whole EMC. While the sizes of the front and rear faces vary with the position of a crystal in the EMC, all crystals have a length of 28 cm, which corresponds to 15.1 radiation lengths (X_0) of CsI. The polar angle coverage of the barrel and the endcaps are $|\cos(\theta)| < 0.82$ and $0.83 < |\cos(\theta)| < 0.93$, respectively.

In the case of photons, the EMC is the only detector providing an information on the position, which requires an adequate granularity. Since hadrons also create a shower

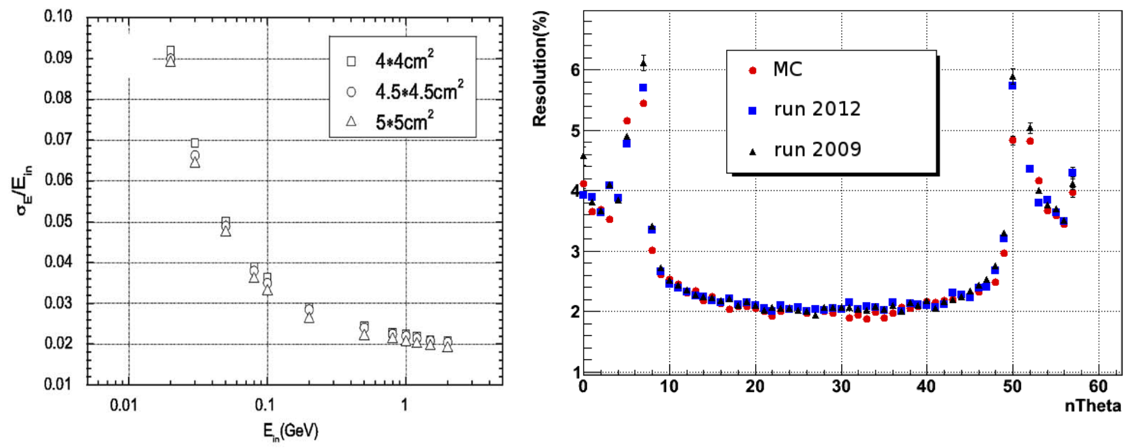

(a) **(b)**

Fig. 2.5: (a) Energy resolution vs. incident photon energy for different lateral crystal dimensions in the BESIII EMC (MC simulation) [18]
(b) Energy resolution vs. crystal ring number (polar angle θ) using 1.5 GeV Bhabha scattering events (MC data, 2009 and 2012 J/ψ runs) [20]

in the EMC crystals, which has a different lateral shape than showers created e.g. by electrons, the information from the EMC is used to support the other detectors for particle identification in the case of electron-hadron separation.
The design energy resolution of $\sigma_E/E \leq 2.5\%$ at a photon energy of 1 GeV and $\sigma_E/E \leq 4\%$ for photons with only 100 MeV of energy can be reached. Figure 2.5a shows the relative energy resolution for different lateral crystal shapes versus the energy of the incident photon derived from a Monte Carlo simulation study for comparison. The resolution of the calorimeter at a particle energy of 1.5 GeV after several years of operation was studied using Bhabha-scattering events at a center of mass energy of 3.097 GeV. The results are shown in Figure 2.5b in dependence of the crystal ring number, which corresponds to the polar angle θ. One can clearly see, that the performance of the BESIII EMC is very stable over more than three years and is in very good agreement with the Monte Carlo simulations. The resolution in the endcaps is about 4%, while in the barrel section a resolution of $\sim 2.3\%$ at the given energy is reached.

2.2.4 The Muon System (RPC)

All previously described subdetector systems (MDC, TOF, EMC) are mounted inside the coil of the superconducting solenoid magnet. An iron yoke surrounding the coil is used for the flux return of the magnetic field and for the mechanical support of the inner spectrometer components, which altogether have a weight of about 50 t. The massive yoke is made of steel plates and weighs a total of $\sim$ 500 t.
As can be seen in Fig. 2.3b, it is not possible to distinguish between pions and muons based on the measurement of the specific energy loss in the gas of the MDC. To solve this problem, the feature of muons to penetrate large amounts of heavy material can be exploited: the iron flux return yoke has been instrumented with resistive plate chambers (RPCs), which are triggered by a traversing muon. For that reason small gaps of $\sim$ 4 cm have been left

between layers of steel plates in the iron yoke. The barrel part of the yoke is equipped with 9 layers of RPCs, while the two endcaps contain only 8 RPC layers for reasons of spatial limitations in these regions. Together, a fraction of $\sim 89\%$ of the full solid angle is covered with the muon identification system. The active detector volume of the RPCs is filled with a gas mixture of Argon, a halocarbon gas and n-Butan ($Ar/C_2F_4H_2/C_4H_{10}$) with a mixing ratio of 50%/42%/8%. The minimum muon momentum from which the muon identifier system works effectively is $\sim 0.4\,\mathrm{GeV}/c$.
Most particles created in the e^+e^- collisions are stopped either in the calorimeter or in the coil of the solenoid. Muons however penetrate the whole detector and most of them even escape the 500 t iron yoke. Since muons are copiously produced in the reactions under study at the BESIII experiment (e.g. the di-lepton decay of the J/ψ into $\mu^+\mu^-$) and additionally have a mass that is very similar to the mass of the charged pion ($m_{\mu^\pm} \approx 105.6\,\mathrm{MeV}/c^2$, $m_{\pi^\pm} \approx 139.6\,\mathrm{MeV}/c^2$), it is of utmost importance to precisely identify muons and especially provide a measurement with a good muon-pion separation.

2.2.5 Trigger and Data Acquisition

The data acquisition of the BESIII experiment is based on a two-stage trigger system, where the first trigger level (L1 trigger) is realized as a hardware trigger utilizing FPGA (Field Programmable Gate Array) driven front-end boards, and the second level (L3 trigger) is a software trigger. Signals from the MDC, the TOF and the EMC are continously stored in a pipelined buffer and fed into the L1-trigger boards. The signals have to be buffered for at least 6.4 µs, since this is the time needed to obtain an L1-trigger decision. The main purpose of the L1-trigger is to reduce cosmic ray and beam background, originating from beam electrons or positrons, that are out of focus and e.g. hit the beam pipe before they reach the interaction region and thus create a signal in different subdetectors. The typical rates of cosmic ray events and beam background sources are given in Table 2.2. Running at a center of mass energy corresponding to the mass of the J/ψ, a physics event rate of about 2 kHz is expected. The rate of the different background sources should be suppressed at least to a rate lower than the physics event rate by the L1 trigger, so that the L1 trigger rate does not exceed its maximum value of ~ 4 kHz. Pre-scaled Bhabha scattering events are written to disk to allow for detector calibration and determination of the luminosity. Once an L1-accepted signal is generated, all frontend buffers are read out and the data is transferred to an online computing farm responsible for event building. At this stage tracks are reconstructed from the MDC data and clustering algorithms are running on the EMC data.
Based on various event filters an event is eventually accepted and permanently stored to disk. The L3-trigger reduces the remaining background event rate to a level acceptable for permanent storage and further offline filtering. During normal operation, the data rate stored to disk is approximately 42 Mb/s.

2.2.6 The BESIII Offline Software System (BOSS)

For data analysis and Monte Carlo simulation studies the object-oriented *C++* software framework "BES Offline Software System (BOSS)" is used. Core component of the framework is the GAUDI package [21], which provides tools for event simulation, data processing and also physics analysis. There are three different types of persistent event data accessible from within BOSS, namely raw data, reconstructed data and so called DST data ("Data

Process	Event rate (kHz)	After L1 [kHz]	After L3 [kHz]
Physics	2	2	2
Bhabha	0.8	Pre-scaled	Pre-scaled
Cosmic ray	< 2	~ 0.2	~ 0.1
Beam background	$> 10^4$	< 2	< 1
Total	$> \mathbf{10^4}$	**4**	**3**

Table 2.2: BESIII event rates for physics events and various background sources without any scaling, after the L1-trigger (hardware) and after the event-building L3-trigger (software) [18]

Summary Tape"). Analyses of beam data are usually performed on preprocessed and reconstructed DST data. BOSS provides services for access to run information and detector status, e.g. the magnetic field at any point within the detector volume. The geometry of the full BESIII detector is implemented using a markup language description. Interfaces to different event generators are foreseen, however the standard chain of generators is used for this work, as discussed in more detail in Section 3.1.

2.2.7 Datasets collected by the BESIII Experiment

Since the start of the first physics run in 2009, a large collection of different data sets has been recorded by the BESIII experiment. For this work, all available data recorded at the center of mass energy corresponding to the mass of the J/ψ is used. This data was recorded in the years 2009 ($\sim 225 \cdot 10^6$ J/ψ events on disk) and 2012 ($\sim 1 \cdot 10^9$ J/ψ events on disk). Apart from the J/ψ data set, also the collected data at the ψ' resonance represents the worlds largest data set of its kind. A comparison of the BESIII data sets with those of other experiments is shown in Table 2.3.

Resonance	MARKIII	Crystal Ball	BES	BESII	CLEO-c	BESIII
J/ψ	$5.8 \cdot 10^6$	$2.2 \cdot 10^6$	$7.8 \cdot 10^6$	$51 \cdot 10^6$	-	$1.31 \cdot 10^9$
ψ'	$0.3 \cdot 10^6$	$1.8 \cdot 10^6$	$3.8 \cdot 10^6$	$14 \cdot 10^6$	$27 \cdot 10^6$	$0.5 \cdot 10^9$

Table 2.3: Comparison of J/ψ and ψ' data sample sizes from various experiments

3 Event Selection

An exclusive reconstruction of events with the topology $J/\psi \to \gamma\omega\omega$ is performed, where both ω mesons are reconstructed via their decays to $\pi^+\pi^-\pi^0$ and subsequently both π^0s are reconstructed via their decay into two photons. In the following chapter, an overview over the data sets and the applied selection criteria is given.

3.1 Data Sets

The analysis presented in this work is based on the data sets recorded in the years 2009 and 2012 by the BESIII experiment at a beam energy corresponding to the mass of the J/ψ resonance. In total these data sets contain $(1.3106 \pm 0.0072) \cdot 10^9$ J/ψ decays [22]. Analyses of final states with a comparably high multiplicity of charged and neutral particles, as the one presented here, could be limited due to the sparse statistics remaining after the application of all selection criteria. While the early experiments MarkIII and DM2 recorded ~ 2.7M and ~ 8.6M J/ψ decays, respectively, the available statistics were remarkably improved by the BESII experiment, where 58M events could be recorded. The BESIII data available to date is about a factor of 22 larger than that of the BESII experiment and hence represents the worlds largest J/ψ data set, enabling detailed studies of rare decay channels or those with complex final states.
Apart from the beam data, a generic Monte Carlo (MC) sample consisting of $\sim 1.225 \cdot 10^9$ simulated J/ψ events is used for background estimation studies. This MC sample was generated using all known decay modes of the J/ψ, taking into account the corresponding branching fractions. Apart from that, a signal MC sample with the event topology

$$\begin{aligned} J/\psi &\to \gamma\omega\omega, \\ \omega &\to \pi^+\pi^-\pi^0, \\ \pi^0 &\to \gamma\gamma \end{aligned} \tag{3.1}$$

was generated. The MC simulation is carried out utilizing different software packages for the various stages of generating and reconstructing events of the topology listed above: The event generator package *KKMC*, which was specifically designed to provide precise predictions for the electroweak standard model process $e^+e^- \to f\bar{f}+n\gamma$, with $f \in \{\mu,\tau,d,u,s,c,b\}$, is used in the first stage of MC event production. This generator provides all calculations needed to simulate the production of the J/ψ, consisting of a $c\bar{c}$ fermion-antifermion pair, including effects due to photon emission of the initial beam particles, namely *Initial State Radiation* (ISR).[23] The subsequent decay of the J/ψ is then handled by the *BesEvtGen* package (see Fig. 3.1), which is an adaptation of the *EvtGen* package developed by the *BaBar* and *CLEO* collaborations for the study of B-meson decays [24][25]. The package provides a plain text file based configuration interface to allow users to generate events with an arbitrary chain of decays and intermediate resonances. While (*Bes-*)*EvtGen* offers a variety of models e.g. to simulate the decay of intermediate hadronic resonances

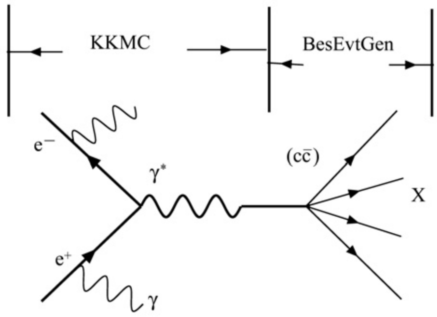

Fig. 3.1: Illustration of the stages of MC event generation. The e^+e^- annihilation and production of the J/ψ is handled by the *KKMC* package, while for the J/ψ decay *BesEvtGen* is used.[25]

including correct angular distributions, all events for the studies presented here have been generated without any particular model, so that pure phase space distributed events were obtained. These phase space distributed events are needed for the partial wave analysis (PWA) fits, which will be discussed in Chapter 4.
All information on the final state particles of the generated events is finally fed into the third software package called GEANT4 [26], which is responsible for the simulation of the BESIII detector and the interactions of the final state particles with the material inside the detector volume. The simulated signals generated in the active elements of the BESIII detector geometry model are then smeared to simulate the performance of the detector in terms of electronic noise and finally stored to disk. The obtained files are then processed by the same BOSS analysis module that is also used for the reconstruction of beam data. In total $2.4 \cdot 10^7$ phase space distributed events of the topology given in (3.2) were generated, in the following referred to as "signal MC". This sample is mainly needed for the PWA, where caution must be taken to ensure that a large enough number of phase space distributed MC events is available at any point in the phase space. The MC sample is also used for a simple one-dimensional estimation of the reconstruction and selection efficiency as well as for different studies for the optimization of selection criteria. The analysis presented here is performed using BOSS version 6.6.4.p01.

3.2 Selection of $\gamma\omega\omega$ Candidates

3.2.1 Track Selection and Particle Identification

Tracks of charged particles are reconstructed using the hit information from the MDC. A track is associated with a charged particle candidate, when the following requirements are fulfilled: The track must originate from a region close to the interaction point. That is, the distance of the track origin from the interaction point in the xy-plane (perpendicular to the beam) must be smaller than 1 cm. In z-direction (beam direction) the distance must be smaller than 10 cm. Furthermore, each track is required to be within the angular acceptance of the MDC, thus fulfilling the requirement $|\cos(\theta)| < 0.93$.
Pion candidates are selected from all valid tracks by exploiting the capabilities of particle identification of the different subdetector systems. Using the information on the specific energy loss dE/dx measured with the MDC, as well as the information from the TOF

system, a likelihood is calculated under the hypothesis, that the particle candidate under investigation is a pion ($\mathcal{L}(\pi)$), kaon ($\mathcal{L}(K)$) or proton ($\mathcal{L}(p)$). Only candidates fulfilling the criteria $\mathcal{L}(\pi) > \mathcal{L}(K)$ and $\mathcal{L}(\pi) > \mathcal{L}(p)$ are accepted and retained for further analysis. In summary, only events with exactly four reconstructed, oppositely charged tracks with positive pion identification are retained for further analysis.

3.2.2 Photon Candidate Selection

A photon entering the electromagnetic calorimeter can produce an electromagnetic shower, most likely in more than one crystal. Only if the reconstructed energy of such a cluster exceeds a value of 25 MeV in the EMC barrel region ($|\cos(\theta)| < 0.8$) or 50 MeV in the end caps ($0.86 < |\cos(\theta)| < 0.92$), the cluster is treated as a photon candidate. The threshold for the photon detection in the endcaps is set to a higher value than for the barrel part in order to reduce the mis-identification of beam background as low-energetic photons. Each shower must have been measured in a time window of $0 \leq t \leq 14$, with t in units of 50 ns since the time of the electron-positron collision (see Fig. 3.2b). This start time is deduced from the reconstructed tracks of charged particles. Additionally, the extrapolation of each reconstructed track into the volume of the EMC, using information from the MDC, must lie outside a cone with an opening angle of 20°, in order to accept a photon candidate. This cut ensures the rejection of clusters that originated from the (small) energy deposit of hadrons (e.g. pions) in the EMC. Only events with more than five surviving photon candidates are kept for further analysis, resembling the four photons originating from the decay of π^0 mesons, as well as the photon from the radiative J/ψ decay. Figure 3.2a shows the number of photons per event, after all selection criteria discussed in this chapter have been applied. In the distributions from beam data as well as the signal MC sample, the number of photons per event extends up to a value of about 15. A reasonable agreement between data and MC is observed for both distributions in Figure 3.2.

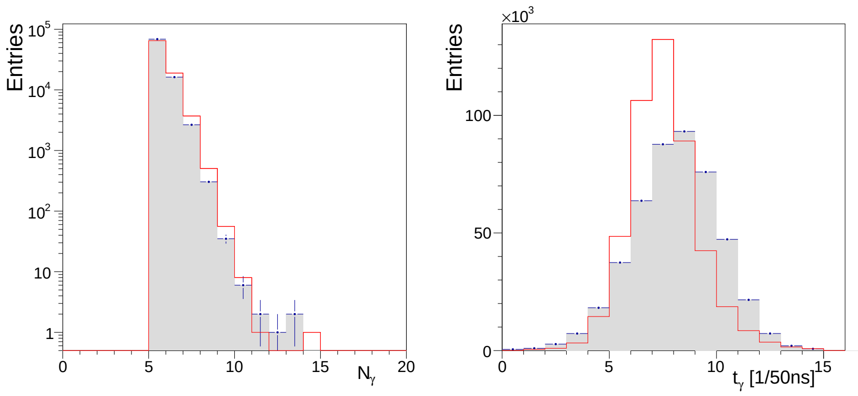

(a) (b)

Fig. 3.2: (a) Number of photons per event after all selection criteria described in this chapter were applied to data (blue dots with error bars) and signal MC (red). (b) Measured time for all photons for data (blue) and MC (red). The signal MC was scaled to the number of selected events from data.

3.2.3 Pre-selection and Combinatorics

After applying the cuts to the photon and pion candidate multiplicities, only events containing exactly four pion candidates and at least five photon candidates are left.
There are several possibilities to combine the photon candidates of a given event to π^0 candidates and subsequently to combine two pion candidates of opposite charge and a π^0 candidate to an ω candidate. All possible combinations to form $\gamma\omega\omega$ candidates, where each photon and pion candidate can only occur once in each combination, are considered. The next step in the selection procedure is the application of rough mass windows for the two π^0 candidates as well as both ω candidates for each $\gamma\omega\omega$ candidate. A π^0 candidate is required to have an invariant mass of $100\,\text{MeV} < m(\gamma\gamma) < 160\,\text{MeV}$, while an ω candidate must fulfill the requirement $580\,\text{MeV} < m(\pi^+\pi^-\pi^0) < 980\,\text{MeV}$. If a $\gamma\omega\omega$ candidate does not fulfill all mass window requirements, the current combination is rejected.

3.2.4 Vertex Fit

Since all intermediate resonances involved in the decay under study have an extremely short lifetime as it is typical for strong decays, it is expected that for a valid event the tracks of the four charged pions should originate from a common point. To ensure that this criterion is met a vertex fit is performed: The reconstructed track parameters of all four tracks are varied within their measured uncertainties, until the distance of the reconstructed point in space where all tracks have the closest distance to each other, and the nominal interaction point is minimized. The same principle is applied for the kinematic fit in the following selection step and will be explained in more detail in the next paragraph. The vertex fit is just used as a binary information on whether to discard an event or not. An event is retained for further analysis, if the vertex fit converges, which rejects events containing uncorrelated tracks e.g. from beam background or cosmic muons.

3.2.5 Kinematic Fit

General Principle

While the vertex fit is performed only once per event, more sophisticated fitting methods can be used to determine the correct combination of photons and pions to form two ω candidates, while at the same time the resolution of the measured four-vectors is improved, by means of kinematic fits. As for the vertex fit, the measured quantities - in this case the components of the reconstructed four-vectors of all particles - are varied within their measurement uncertainties, while at the same time an arbitrary number of predefined constraints must be fulfilled. A commonly used set of constraints is the conservation of the total energy and momentum: When an exclusive reconstruction of a decay chain is performed (i.e. no missing particles), the sum of the four-vectors of all final state particles must resemble the four-vector of the initial e^+e^- or J/ψ system, given by $\vec{p_4}_{J/\psi} = (0.0305, 0, 0, 3.097)$ in units of GeV.[1] The three components of the linear momentum and the energy hence represent four constraints. A fit using only these boundary

[1]The four-vector is given here in the convention, which specifies the three components of the linear momentum in the first three places of the vector, while the fourth contains the energy, i.e. $\vec{p_4} = (p_x, p_y, p_z, E)$. The p_x component of the initial four-vector of the e^+e^--system is chosen to be non-zero, to introduce a very small boost to the resonance created in the collision and thereby to allow heavy created particles to leave the interaction zone.

conditions is called a four-constraint or 4C-fit. Additional contraints can be imposed to the candidates by e.g. the invariant mass of a photon pair, which can be required to correspond to the mass of the π^0 meson.

The fit method applied in the BOSS software is based on the *least squares* method, utilizing Lagrange-multipliers. A detailed description of this method is given in [27], however the principle of the kinematic fit is briefly described in the following:

Consider a measurement of n distinct parameters, where the true values are given by $\vec{\eta} = (\eta_1,...,\eta_n)^T$, while the actually measured values are given as $\vec{y} = (y_1,...,y_n)^T$. The deviation from the true to the measured values is given by the uncertainties of the measurement, denoted as $\vec{\delta} = (\delta_1,...,\delta_n)^T$, so that

$$\vec{y} = \vec{\eta} + \vec{\delta}. \tag{3.2}$$

One important restriction is, that the uncertainties δ_i must be normally distributed. Furthermore, the dependencies of the measurable values $\vec{\eta}$ from a number of r unknown parameters $\vec{x} = (x_1,...,x_r)^T$ are given by m boundary conditions of the form

$$f_i(\vec{x},\vec{\eta}) = f_i(\vec{x},\vec{y} - \vec{\delta}) = 0, \;\; i = 1,...,m. \tag{3.3}$$

Now the equations $f_i = 0$ can be expanded around a point $(\vec{x}_0,\vec{\eta}_0)$, yielding

$$f_i(\vec{x},\vec{\eta}) \approx f_i(\vec{x}_0,\vec{\eta}_0) + \sum_{j=0...r} \left.\frac{\partial f_i}{\partial x_j}\right|_{(\vec{x}_0,\vec{\eta}_0)} (x_j - x_{j,0}) + \sum_{k=0...n} \left.\frac{\partial f_i}{\partial \eta_k}\right|_{(\vec{x}_0,\vec{\eta}_0)} (\eta_k - x_{k,0}). \tag{3.4}$$

Now we define the two matrices A and B, which contain the partial derivatives of the functions f_i with respect to the unknown parameters x_j and the values η_j, evaluated at the point $(\vec{x}_0,\vec{\eta}_0)$. These matrices can be written as

$$A_{ij} = \left.\frac{\partial f_i}{\partial x_j}\right|_{(\vec{x}_0,\vec{\eta}_0)} \quad \text{and} \quad B_{ij} = \left.\frac{\partial f_i}{\partial \eta_j}\right|_{(\vec{x}_0,\vec{\eta}_0)}, \tag{3.5}$$

with $i = 1,...,m$ and $j = 1,...,r$. Moreover, let $\vec{\xi} = \vec{x} - \vec{x}_0$, $\vec{\tau} = \vec{\eta} - \vec{\eta}_0$. With these definitions, the approximation from 3.4 can be written more conveniently as

$$\vec{f}(\vec{x},\vec{\eta}) \approx \vec{f}(\vec{x}_0,\vec{\eta}_0) + A\vec{\xi} + B\vec{\tau} = \vec{0}. \tag{3.6}$$

Minimizing the quadratic distance of the measured values to the true values while at the same time fulfilling equation 3.6 is called the *method of least squares*. The expression that is to be minimized is given as

$$\chi^2 = \vec{\tau}^T C_y^{-1} \vec{\tau}, \tag{3.7}$$

with C_y being the covariance matrix of the measured values $\vec{y}$. Finally, the method of *Lagrange multipliers* is applied, which states, that both conditions are met, when the expression

$$\begin{aligned} \mathcal{L} &= \chi^2 + 2\vec{\lambda}^T \cdot \vec{f}(\vec{x},\vec{\eta}) \\ &= \vec{\tau}^T C_y^{-1} \vec{\tau} + 2\vec{\lambda}^T \cdot [\vec{f}(\vec{x}_0,\vec{\eta}_0) + A\vec{\xi} + B\vec{\tau}] \\ &\overset{!}{=} 0, \end{aligned} \tag{3.8}$$

with the vector $\vec{\lambda} = (\lambda_1,...,\lambda_m)$ containing the *Lagrange-Multipliers*, is fulfilled.
From this, it can be shown that $\vec{\xi}$ and $\vec{\tau}$ can be written as

$$\vec{\xi} = -(A^T G_B A)^{-1} A^T G_B \vec{f}(\vec{x}_0,\vec{\eta}_0) \tag{3.9}$$

and

$$\vec{\tau} = -C_y B^T G_B(\vec{f}(\vec{x}_0,e\vec{t}a_0) + A\vec{\xi}), \tag{3.10}$$

with $G_B = (B^T C_y B)^{-1}$. The expression that is to be minimized follows a χ^2 distribution with $m - r$ degrees of freedom ($n.d.f.$). In the special case, where no additional free (unknown) parameters $\vec{x}$ are present, the $n.d.f.$ reduces to m and therefore is equal to the number of constraints applied. The χ^2 value is used to determine the goodness of the fit, whereas small values are expected for signal and large values for background events.

Application of the Kinematic Fit

Each $\gamma\omega\omega$ candidate is subjected to a kinematic fit involving two stages: The four-vector of each $\gamma\omega\omega$ candidate is first constrained to the four-momentum of the initial J/ψ system (4C kinematic fit), in order to ensure energy and momentum conservation for the exclusively reconstructed events. Only candidates yielding a χ^2 value of the 4C kinematic fit of less than 200 are retained. For $\gamma\omega\omega$ candidates that survive, a kinematic fit with 6 constraints (6C), including the four-vector of the initial J/ψ system, as well as a mass constraint to each of the two π^0 candidates, is performed. The 6C kinematic fit is performed to improve the mass resolution of the ω candidates and find the correct pairings of photon candidates.

Only candidates which yield a χ^2 value of the 6C kinematic fit of less than 25 are kept for further analysis. Different studies were performed to obtain a reasonable choice for this value: Since the measurement requires a partial wave analysis, a sample as clean as possible has to be selected. Thus it is more important to suppress as much background as possible, than to get the best signal to background ratio. Important criteria for the choice of the χ^2 cut value include the fraction of miscombined events as well as the background suppression power. However, before these criteria can be discussed, the final parameter, that is used to select the best combination per event has to be introduced. Figure 3.3a shows the χ^2 distributions for selected events from the data sample as well as the signal MC sample. Since the χ^2 distribution and any χ^2 value are only meaningful once the $n.d.f.$ is known, in statistics the p-value is commonly used. It can be calculated from a given χ^2 and $n.d.f.$-value by integrating the corresponding χ^2 distribution from the given

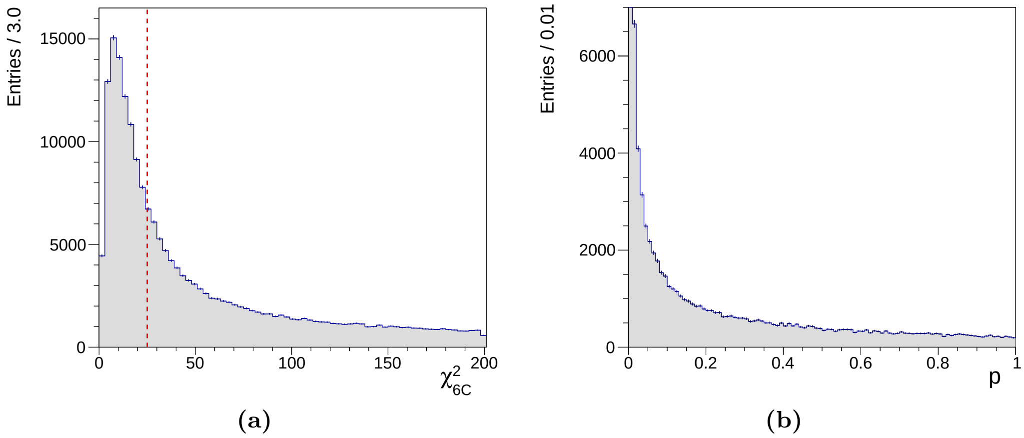

Fig. 3.3: (a) χ^2 distribution of the 6C-kinematic fit for data (gray shaded histogram). The red dashed line marks the χ^2 cut value of 25.
(b) p-value distribution corresponding to the χ^2 distribution shown in (a) (y-axis truncated)

χ^2 value to infinity[2]. The p-value represents the probability, that a signal event reaches a χ^2-value, which is at least as large as the given χ^2 value. While for signal events a flat p-value distribution is expected, background events lead to a peak at low p-values. Figure 3.3b shows the p-value distributions for beam data and signal MC.

3.2.6 Selection of the Best Signal Candidate

The 6C kinematic fit is not sensitive to the combination of pions to form ω candidates, so finally the best of all remaining candidates is selected by choosing the one, which yields the smallest Euclidean distance r of both ω candidates to the nominal ω mass given by the PDG. Namely, r can be written as

$$r = \sqrt{(m(\omega_1) - m(\omega)_{PDG})^2 + (m(\omega_2) - m(\omega)_{PDG})^2}, \tag{3.11}$$

where $m(\omega)_{PDG}$ denotes the nominal ω mass, as given in [1]. Figures 3.4a and 3.4b show the invariant mass distributions of two photons before performing any kinematic fit and that of three pions for all candidates as well as after the selection of the best candidate based on the r-value. There is a substantial background contribution visible under the chosen ω candidates (see 3.4b, red curve).
The invariant 3π versus 3π mass distribution is shown in Figure 3.5a for the best combination. For comparison, Figure 3.5b shows the same distribution for generated signal MC events (truth information). Two distinct bands are visible in the diagrams from data as well as MC-truth, indicating that they do not originate from the reconstruction procedure or candidate selection but reflect the true behavior of the pions. However, while the bands from pure ω decays (MC-truth) are weakening towards larger 3π masses, the bands get stronger for selected events from data. This indicates the presence of $\omega 3\pi$ background.

[2]This integral involves the complex error function, which in most cases can not be analytically solved. Here, an implementation based on the lower incomplete gamma function provided by the ROOT software is used to calculate p-values.

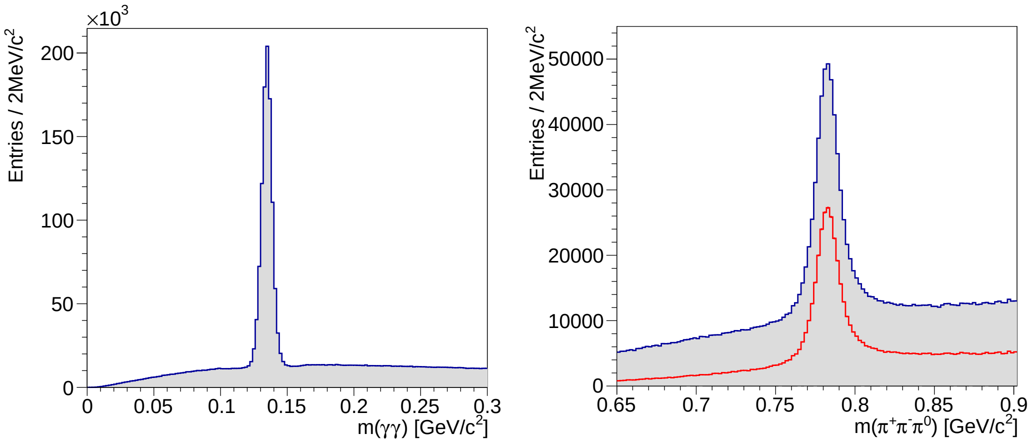

(a) **(b)**

Fig. 3.4: (a) Invariant mass for all possible combinations of two photons before application of any kinematic fit
(b) Invariant $\pi^+\pi^-\pi^0$ mass for all possible combinations (blue, eight entries per event) and for the chosen combination (red, two entries per event) after the 6C fit

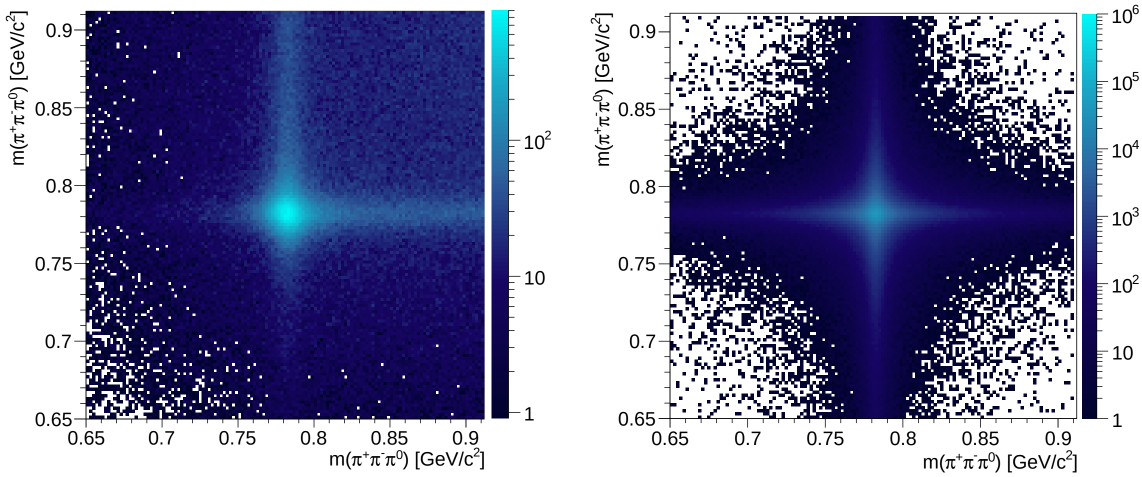

(a) **(b)**

Fig. 3.5: 3π versus 3π invariant mass for (a) the chosen combination of pions for data and (b) for generated signal MC events (generator output on MC truth level).

3.2.7 Veto of additional π^0 Candidates

After applying the cut to the χ^2_{6C} value, the remaining events might still contain more than five photons, whereas one is identified as the photon from the radiative J/ψ decay and in total four photons are assigned to the π^0 candidates. To exclude the possibility, that a residual photon forms a π^0 together with the candidate for the radiative photon, a cut to the invariant mass of the radiative photon (γ_{rad}) combined with any other leftover photon (γ_{unused}) is performed. Events, for which this invariant mass lies within a window of $(130-$

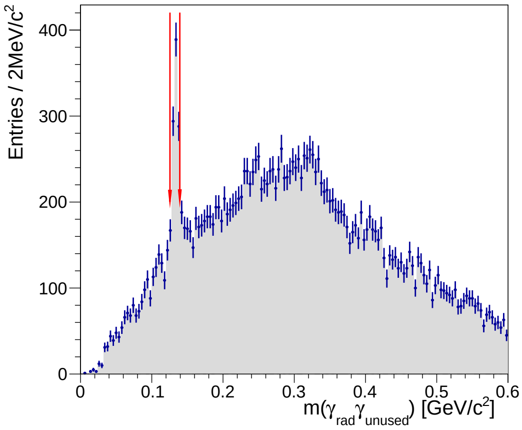

(a) **(b)**

Fig. 3.6: Invariant mass of the radiative photon combined with (a) one excess photon, which is not identified as a π^0 daughter photon in an event with more than five photons in total, and (b) one daughter photon of a π^0 candidate. All excess photons per event are considered in these plots. The red arrows indicate the mass range used for the π^0 veto.

140) MeV are vetoed. Figure 3.6a shows the corresponding invariant mass distribution as well as markers indicating the window for the applied π^0 veto. A clear peak at the π^0 mass can be seen. The cut removes 836 events, which corresponds to about 0.9% of the selected data set (88783 events, after veto 87947 events).

Additionally, the combination of all residual photon candidates with each of the photons assigned to π^0 candidates is shown in Figure 3.6b. No enhancements can be seen at the masses of the π^0 and η mesons.

3.2.8 Pion Mis-Combination and Selection Efficiency

After selecting only events which fulfill the condition $\chi^2 < 25$ and subsequently selecting one combination of pions for each leftover event based on the r value, it is still possible to obtain events with incorrectly combined pions. The fraction of mis-combined events was studied in dependence of the χ^2 cut using a truth-matched signal MC sample. For the chosen cut value an integral mis-combination fraction of about 0.7% after application of all selection criteria was found. Figure 3.7a shows the distribution of the mis-combined events in dependence of the invariant $\omega\omega$ mass (note logarithmic scale!). The events are distributed over the full $\omega\omega$ mass range, a slight overpopulation is observed at the beginning of the available phase space - however the contribution is well below 1% in every region of the invariant mass. Figure 3.7b shows the selection efficiency for MC events after application of the $\chi^2 < 25$ cut and selection of one combination. The selection efficiency is somewhat lower for small $\omega\omega$ masses and reaches a mean value of about 3.6% integrated over the whole mass range. The efficiency curve shows no significant structures or excesses.

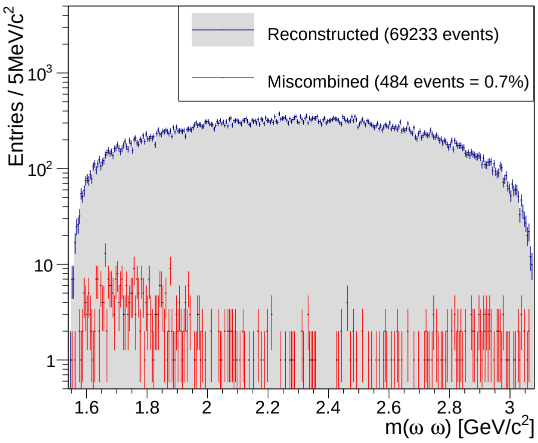

(a)

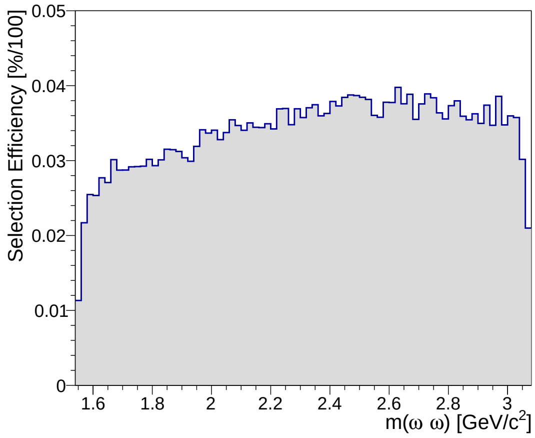

(b)

Fig. 3.7: Fraction of mis-combined events (a) and selection efficiency (b) as a function of $m(\omega\omega)$ for signal MC events.

3.2.9 A Glance at the Data: Signal and Sideband Regions

After applying all cuts discussed above, a significant background contribution was observed under the selected ω signals. As a first estimation, the two-dimensional sidebands in the 3π vs. 3π plane are studied. Figure 3.8c shows the invariant 3π vs. 3π mass. The signal region is defined as a circle around the nominal mass of the ω meson in both dimensions, with a radius of 26 MeV. The sideband regions are selected using the following cuts:

- Region B1: $759.65\,\text{MeV} < m_{\omega_1} < 805.65\,\text{MeV}$ and $850.00\,\text{MeV} < m_{\omega_2} < 896.00\,\text{MeV}$
- Region B2: $850.00\,\text{MeV} < m_{\omega_1} < 896.00\,\text{MeV}$ and $850.00\,\text{MeV} < m_{\omega_2} < 896.00\,\text{MeV}$
- Region B3: $850.00\,\text{MeV} < m_{\omega_1} < 896.00\,\text{MeV}$ and $759.65\,\text{MeV} < m_{\omega_2} < 805.65\,\text{MeV}$

The area of the sideband regions are chosen to match the area of the circle defining the signal region. The 6π invariant mass distribution for each of the sideband regions is shown in Figures 3.8a, 3.8b and 3.8d, respectively. The 3π vs. 3π invariant mass distribution shows the features of the background: Two bands are visible, which cross exactly at the $\omega\omega$ mass peak. These events originate from a mixture of $\gamma 3\pi\omega$ background channels as well as the signal channel (cf. Figure 3.5a and 3.5b). Apart from these contributions, 6π background events are distributed over the entire mass region. This type of background shows a rising slope towards higher 3π invariant masses.
As a very rough estimate of the background underneath the $\omega\omega$ peak, the events from the sideband regions $B1$, $B2$ and $B3$ were combined. The 6π invariant mass distributions of the events within the areas $B1$ and $B3$ were added, before the corresponding distribution from area $B2$ was subtracted. This is done to avoid overestimation due to the fact, that the 6π-type background is also present in the regions $B1$ and $B3$. The resulting distribution (dark blue) is shown together with the selected signal events (light blue) in Figure 3.8e. Although the background might be overestimated using this procedure, it is clear that further action needs to be taken to reduce the background as far as possible. For this reason a sophisticated event based background suppression method was applied to the data set, which is described in Section 3.4.

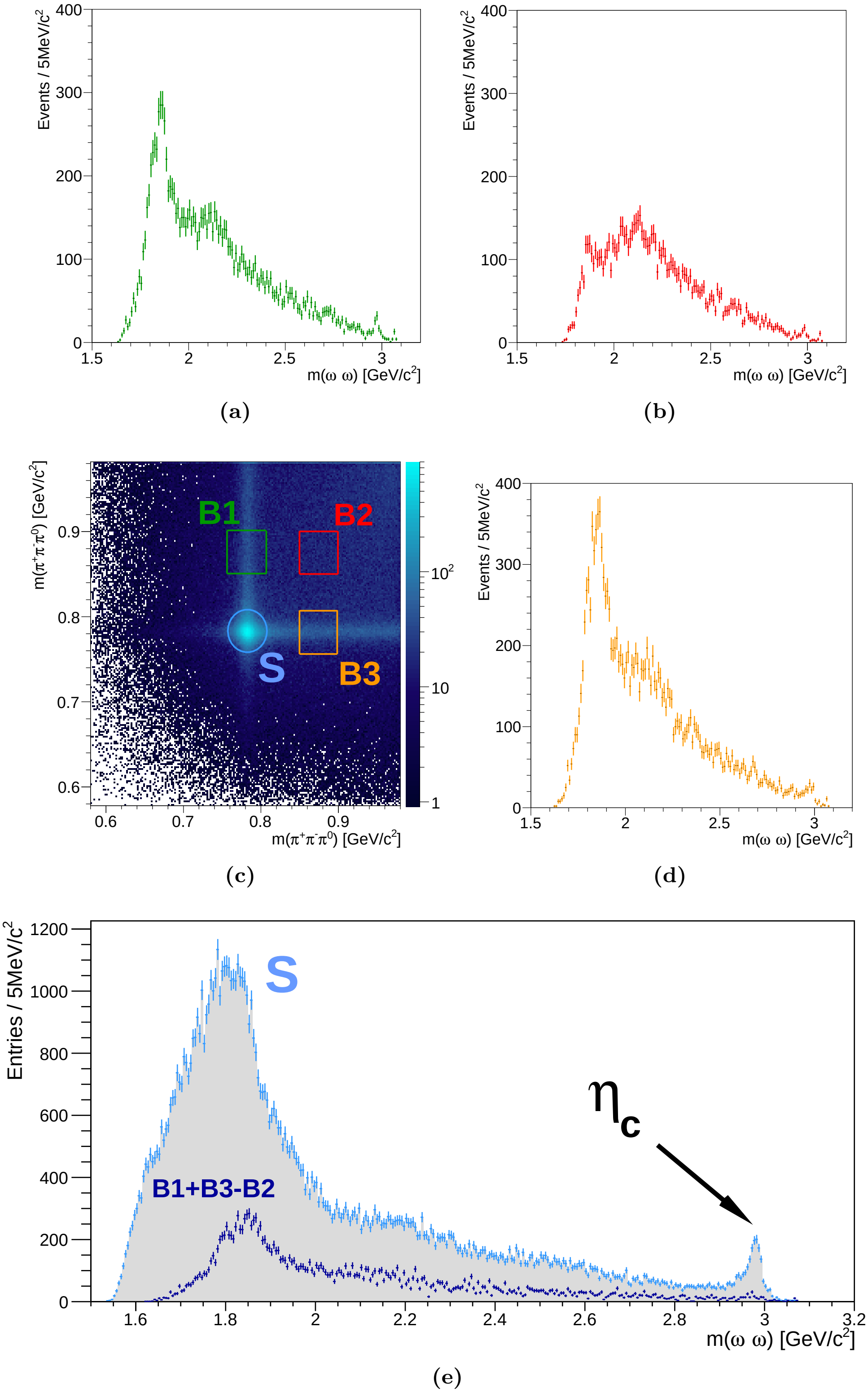

Fig. 3.8: Distribution of events in the 6π invariant mass ((a),(b),(d)) for different mass windows shown in (c).
(e): Invariant mass of the $\omega\omega$ candidates. The different distributions show the selected signal events (light blue) and events from the combined sideband regions $B1 + B3 - B2$ marked in Figure 3.8c.

3.3 Background Studies

A first look at the invariant mass spectra of the selected signal sample and the corresponding sideband distributions revealed a background pollution in the signal region in the order of about 17%, which shows a complex shape in the invariant $\omega\omega$ mass. Since it is to be expected, that the background behaves similarly complex directly below the prominent $\omega\omega$ peak, all efforts have to be taken to reduce this background as far as possible.

In this chapter data- and MC-driven background studies are presented, involving the analyses of a large generic MC sample as well as a data sample recorded at a center-of-mass energy slightly below the mass of the J/ψ to estimate contributions of non-resonant continuum processes.

Finally, an event-based background suppression method using probabilistic weights is studied with the help of toy MC samples and applied to the selected data set.

3.3.1 Analysis of a Generic Monte Carlo Sample

The generic MC sample that was introduced in Section 3.1 has been analyzed to estimate the composition of the background and to identify possible background sources. Table 3.1 shows the contributing J/ψ decay modes from the generic MC sample surviving all selection criteria, sorted by the number of events for the most contributing channels. The table contains signal as well as background channels.

The largest background contribution is due to the decay $J/\psi \to \rho^+\rho^-\omega$, which results in a final state containing two pairs of oppositely charged pions and three π^0. For these events most probably one photon was not reconstructed due to geometrical acceptance or thresholds, and the leftover photon was accidentally identified as the radiative photon. Since events with more than five photons are accepted, the radiative photon candidate could also originate from a π^0 together with one of the reconstructed excess photons apart from those identified as π^0 daughter candidates. Yet, this type of events is largely suppressed by the π^0 veto discussed in Section 3.2.3.

The second largest group of background events is of the type $J/\psi \to \gamma\rho^\pm b_1^\mp$, which result in the same final state as signal events and thus are not further rejectable. In total, only 3.6% of all events passing the selection are originating from background channels.

Figure 3.9 shows the $\omega\omega$ invariant mass for all selected events from the generic MC sample as well as the five largest contributing decay channels, three of which are signal channels. Although the generic MC sample is a very handy tool for identifying the most significant background contributions, the data set does not represent the beam data from the J/ψ data set very well for this decay channel. Figure 3.9 also shows the events selected from the signal region for beam data. Especially in the mass region above $m(\omega\omega) > 2.2\,\mathrm{GeV}/c^2$ a large deviation from the measured distribution can be observed. Since only an upper limit for the decay of the η_c into $\omega\omega$ is known, this resonance was also not included in the generic MC sample. Conclusively, the generic MC sample did not reveal any major background contributions, but fails to describe the data due to the absence of the $\gamma 3\pi\omega$ and $\gamma 6\pi$-type backgrounds. This type of background therefore has to be addressed utilizing data-driven methods.

Decay Chain: $J/\psi \to ...$	Final State	Number of Events
$\gamma\omega\omega,\ \omega \to \pi^+\pi^-\pi^0$	$\gamma\pi^+\pi^+\pi^0\pi^0\pi^-\pi^-$	56923
$\gamma\eta(1760),\ \eta(1760) \to \omega\omega,\ \omega \to \pi^+\pi^-\pi^0$	$\gamma\pi^+\pi^+\pi^0\pi^0\pi^-\pi^-$	31594
$\gamma f_0(1710),\ f_0(1710) \to \omega\omega,\ \omega \to \pi^+\pi^-\pi^0$	$\gamma\pi^+\pi^+\pi^0\pi^0\pi^-\pi^-$	7720
$\rho^-\rho^+\omega,\ \rho^\pm \to \pi^\pm\pi^0,\ \omega \to \pi^+\pi^-\pi^0$	$\pi^+\pi^+\pi^0\pi^0\pi^0\pi^-\pi^-$	669
$\gamma\rho^- b_1^+,\ \rho^- \to \pi^-\pi^0,\ b_1^+ \to \omega\pi^+,\ \omega \to \pi^+\pi^-\pi^0$	$\gamma\pi^+\pi^+\pi^0\pi^0\pi^-\pi^-$	234
$\gamma\rho^+ b_1^-,\ \rho^+ \to \pi^+\pi^0,\ b_1^- \to \omega\pi^-,\ \omega \to \pi^+\pi^-\pi^0$	$\gamma\pi^+\pi^+\pi^0\pi^0\pi^-\pi^-$	215
$\omega f_2(1270),\ \omega \to \pi^+\pi^-\pi^0,\ f_2(1270) \to \pi^+\pi^-\pi^0\pi^0$	$\pi^+\pi^0\pi^0\pi^0\pi^-\pi^-$	149
$\omega\eta',\ \eta' \to \gamma\omega,\ \omega \to \pi^+\pi^-\pi^0$	$\gamma\pi^+\pi^+\pi^0\pi^-\pi^-$	137
$\omega a_0^0,\ \omega \to \pi^-\pi^0\pi^+,\ a_0^0 \to \pi^0\eta,\ \eta \to \gamma\pi^+\pi^-$	$\gamma\pi^+\pi^+\pi^0\pi^0\pi^-\pi^-$	136
$\gamma\rho^0 b_1^0,\ \rho^0 \to \pi^-\pi^+,\ b_1^0 \to \pi^0\omega,\ \omega \to \pi^+\pi^-\pi^0$	$\gamma\pi^+\pi^+\pi^0\pi^0\pi^-\pi^-$	122
$\pi^-\pi^0\pi^+\omega,\ \omega \to \pi^+\pi^-\pi^0$	$\pi^+\pi^+\pi^0\pi^0\pi^-\pi^-$	100
$\rho^-\gamma\pi^+\omega,\ \rho^- \to \pi^-\pi^0,\ \omega \to \pi^-\pi^0\pi^+$	$\gamma\pi^+\pi^+\pi^0\pi^0\pi^-\pi^-$	89
$\pi^-\gamma\rho^+\omega,\ \rho^+ \to \pi^0\pi^+,\ \omega \to \pi^-\pi^0\pi^+$	$\gamma\pi^+\pi^+\pi^0\pi^0\pi^-\pi^-$	86
$b_1^-\pi^+ f_2(1270),\ b_1^- \to \pi^-\omega,\ f_2(1270) \to \pi^0\pi^0,\ \omega \to \pi^+\pi^-\pi^0$	$\pi^+\pi^+\pi^0\pi^0\pi^0\pi^-\pi^-$	53
$\pi^- f_2(1270) b_1^+,\ f_2(1270) \to \pi^0\pi^0,\ b_1^+ \to \pi^+\omega,\ \omega \to \pi^+\pi^-\pi^0$	$\pi^+\pi^+\pi^0\pi^0\pi^0\pi^-\pi^-$	53
$\pi^-\pi^0 a_2^+,\ a_2^+ \to \pi^0\pi^+\omega,\ \omega \to \pi^-\pi^0\pi^+$	$\pi^+\pi^+\pi^0\pi^0\pi^0\pi^-\pi^-$	51
$\pi^-\gamma\pi^+ b_1^0,\ b_1^0 \to \pi^0\omega,\ \omega \to \pi^-\pi^0\pi^+$	$\gamma\pi^+\pi^+\pi^0\pi^0\pi^-\pi^-$	50
$a_2^-\pi^0\pi^+,\ a_2^- \to \pi^-\pi^0\omega,\ \omega \to \pi^-\pi^0\pi^+$	$\pi^+\pi^+\pi^0\pi^0\pi^0\pi^-\pi^-$	46
$\omega a_0^0,\ \omega \to \pi^-\pi^0\pi^+,\ a_0^0 \to \pi^0\eta,\ \eta \to \pi^+\pi^-\pi^0$	$\pi^+\pi^+\pi^0\pi^0\pi^0\pi^-\pi^-$	44
$\pi^0\omega a_1^0,\ \omega \to \pi^-\pi^0\pi^+,\ a_1^0 \to \pi^-\rho^+,\ \rho^+ \to \pi^+\pi^0$	$\pi^+\pi^+\pi^0\pi^0\pi^0\pi^-\pi^-$	43
$\gamma f_4(2050),\ f_4(2050) \to \omega\omega,\ \omega \to \pi^+\pi^-\pi^0$	$\gamma\pi^+\pi^+\pi^0\pi^0\pi^-\pi^-$	43

Table 3.1: Topology of events selected from the generic MC sample, that are surviving all selection criteria. The decay channels are ordered by frequency of their occurrence in the data set. Signal, as well as background channels are shown.

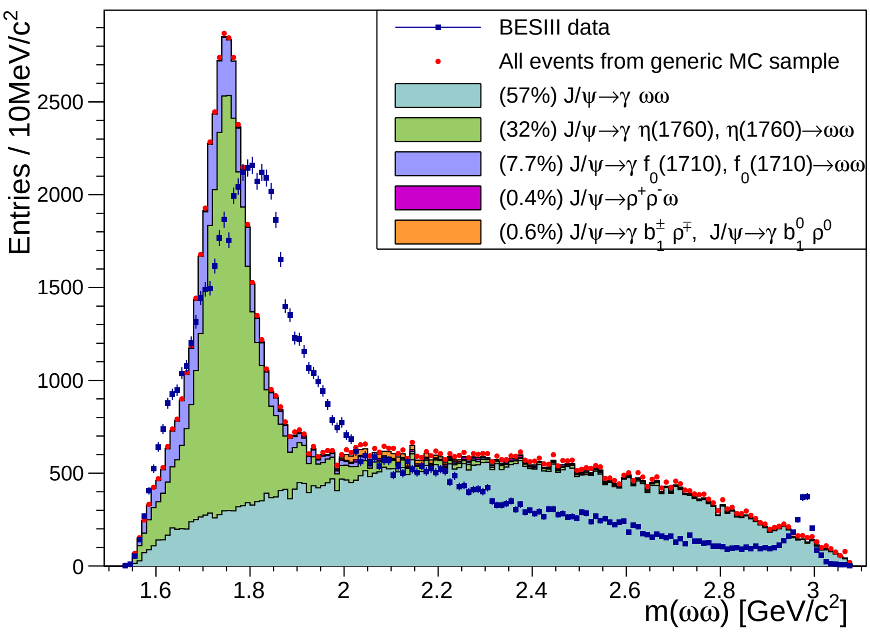

Fig. 3.9: Invariant mass of the $\omega\omega$ system for events passing the selection from the generic MC sample and from beam data. The colored distributions show the largest components of the events from the generic MC sample drawn on top of each other (cumulative).

3.3.2 Background from Continuum Processes

Background originating from continuum processes is studied using a data sample which was recorded at a center of mass energy of 3.08 GeV, slightly below the J/ψ mass. This data set contains in total 29.14 pb^{-1}, which is roughly a factor of 15 less than the J/ψ data sample. The same selection criteria as for data are applied to the full continuum data set and only 30 events survive when no restriction on the 3π invariant masses is applied (see Figure 3.10). After applying a cut to the $\omega\omega$ signal region marked with a blue circle, only one single event is left. By scaling the luminosity of this data set to that of the J/ψ data set, in total 15 events from continuum background processes are expected, which corresponds to less than 0.02% of the full selected data set and thus will be neglected for the following analysis steps.

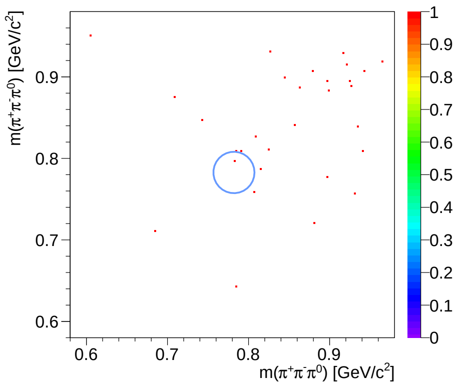

Fig. 3.10: Events surviving all selection criteria from the continuum data sample, recorded at $E_{\mathrm{c.m.}} = 3.08\,\mathrm{GeV}$

3.4 Event Based Background Suppression

The studies of the two-dimensional ω sidebands in Section 3.2.9 have shown, that a background contribution to the selected sample in the order of $\sim 17\%$ is to be expected in the signal region, originating from different sorts of non-resonant background sources. This kind of background is irreducible by simple cuts on kinematic variables. One possibility to deal with this kind of background is a so called *sideband-subtraction*, which in this case could also be applied in two dimensions (3π vs. 3π). For this method, events from different regions of a particular distribution (mostly from a kind of histogram) are selected, which correspond to signal- as well as possibly different background-regions. The resulting distributions are combined, to obtain a distribution which should represent the background present in the signal region underneath the signal of interest. Finally, the obtained background distribution is subtracted from the distribution obtained from the selection of the signal region and a background-subtracted version of the distribution under investigation can be used for further analysis. It should be stressed here, that the sideband-subtraction is only applied to a sub-set of the phase space coordinates and therefore all possible correlations between other phase space coordinates can not be considered. The main drawback of this method is, that it is not event based. This means that for a given event no information about the origin of this particular event (signal or background) can be derived. Only

a global information, i.e. the total number of signal events, or the shape of the corrected distribution, is obtained. Since the goal is to perform an event-based partial wave analysis, this method is not applicable here. Another possibility, which overcomes some of the restrictions of a simple sideband subtraction, is to use the events from sideband regions to construct an amplitude model of the contributing background channels. By including this background model in the calculation of the likelihood for events in a partial wave analysis, the background can be subtracted directly while the partial wave fit is performed. However, this method requires a detailed understanding of the origin of the background.
In this analysis, a relatively new, event based background subtraction method is employed, which is based on probabilistic event weights. The so called *Q-factor method* has been developed for and successfully applied to photoproduction data from the CLAS experiment [28], as well as $\bar{p}p$ annihilation data from the Crystal Barrel LEAR experiment [29]. All studies related to the Q-factor method presented in this work have been carried out with the *WiBaS* software package, that was developed at Ruhr-Universität Bochum [30].

3.4.1 The Q-Factor Method

Many methods have been developed to separate signal from background samples, in which known features of the corresponding distributions are used to optimize the signal to background ratio. These methods require detailed knowledge about the signal and background and are most likely only applicable in a limited number of cases. For the method described here, only very little about these distributions must be known and it is explicitly designed to be able to deal with *irreducible* background, which is mimicking the signal topology and has the same final state. The method will be briefly described in this section, a detailed explanation and examples from application can be found in [28].
Consider a sample of n events, which consists of n_B background events, and n_S signal events. A set of coordinates $\vec{\xi}$ must be chosen, so that each event can be assigned to a point in the phase space defined by the relevant reaction to be studied. These coordinates can be decay or production angles, invariant masses or other parameters, which can be calculated from the measured four-vectors of any event. One of these coordinates is selected as the *reference coordinate*, ξ_r. This is the only coordinate, for which a functional dependence of the signal and background distributions must be known. Additionally, these functions may also depend on a set of unknown variables, $\vec{\alpha}$. The distributions of the chosen reference coordinates should show a clear difference between signal and background events and at the same time should be easily expressible with analytic functions. In previous analyses (see [28],[29]), one-dimensional invariant masses were used as the reference, since the background (polynomial function) and signal shapes (Breit-Wigner or Voigt function, ...) could be deduced from the data. In this analysis a similar approach was chosen with the two-dimensional invariant mass of the two three-pion systems as the reference coordinates.
The final goal of this method is, to assign a so called Q-factor to each event, representing the probability, that this event is originating from the signal sample. Therefore, a metric must be defined, which can be used to measure distances in the relevant phase space spanned by the $\vec{\xi}$ coordinates. Here, a modified Euclidean metric was chosen, for which the distance between two events i and j is given by

$$d_{i,j}^2 = \sum_{k \neq r} \left[\frac{\xi_k^i - \xi_k^j}{\Delta_k} \right]^2 , \tag{3.12}$$

where the sum runs over all coordinates ξ_k, excluding the reference coordinate ξ_r. The normalization Δ_k by default is set to the largest possible distance between two events in the coordinate ξ_k. Considering an angular distribution of the form $\xi_k = \cos(\theta)$ as an example, the values of ξ_k can vary between -1 and 1. Thus, the corresponding normalization would be chosen to be $\Delta_k = 2$ by default. By normalizing all coordinates to their range, an equal weighting is achieved. It is possible, that one or more coordinates require a larger weight, so that fine structures present in the distributions of the corresponding coordinates can be accounted for. This could e.g. be necessary for an invariant mass, in which a resonance is visible as a peak, leading to a large rising gradient. In this case, the normalization can be modified to give more weight to this coordinate. The effect of this over-weighting has to be carefully studied using MC simulations.
The idea is, that each event can be assigned a probability to originate from the signal sample. Apart from the reference coordinate, a number of n_c nearest neighbors around a considered seed event are contained in a phase space cell that is so small, that they can not be distinguished any more. Thus, it is reasonable to interpret the signal-to-background ratio in this cell as the local probability density. Finally, a fit to the distribution of the reference coordinate for the selected n_c neighbor events is performed, using the previously selected functional dependencies. Technically, an unbinned maximum-likelihood fit is chosen due to the low number of events in each fit, to estimate the unknown parameters $\vec{\alpha}$ of the signal ($F_s(\xi_r,\vec{\alpha})$) and background ($F_b(\xi_r,\vec{\alpha})$) functions. In the last step, the Q-factor for each event i is calculated as

$$Q_i = \frac{F_s(\xi_r^i,\hat{\alpha}_i)}{F_s(\xi_r^i,\hat{\alpha}_i) + F_b(\xi_r^i,\hat{\alpha}_i)}. \tag{3.13}$$

This procedure is repeated for all events, and the obtained Q_i values are used as event weights for further analysis steps.

3.4.2 Application to this Analysis

As described in the previous section, a two-dimensional fit to the 3π versus 3π invariant mass distribution (reference coordinate) must be performed for each event. To be able, to fit a function to this distribution, which describes not only the signal, but also the background shape, the narrow cut to the signal region (light blue circle in Figure 3.8e) must be temporarily removed. Instead, a region defined by

$$|m(\pi_1^+\pi_1^-\pi_1^0) - m(\omega_{\mathrm{PDG}})| \leq 80\,\mathrm{MeV}/c^2 \tag{3.14}$$

$$|m(\pi_2^+\pi_2^-\pi_2^0) - m(\omega_{\mathrm{PDG}})| \leq 80\,\mathrm{MeV}/c^2 \tag{3.15}$$

is selected from the data. The same narrow cut as used before, namely a circle with a radius of $26\,\mathrm{MeV}/c^2$, will be re-introduced, after all Q-factors have been calculated. To determine the functional dependencies of the signal and background from the reference coordinate, different phase space distributed MC samples have been generated and analyzed. The upper row of plots in Figure 3.11 shows the 3π versus 3π invariant mass for different MC samples after all selection criteria have been applied. The left plot shows the distribution of events from a phase space distributed MC sample generated with the topology $J/\psi \to \gamma\pi^+\pi^-\pi^0\pi^+\pi^-\pi^0$. This type of background is rising linearly along both 3π mass axes. To parametrize this distribution, two linear functions, one for each 3π axis, forming a plane have been chosen. One free parameter per linear function, the slope, is allowed. For

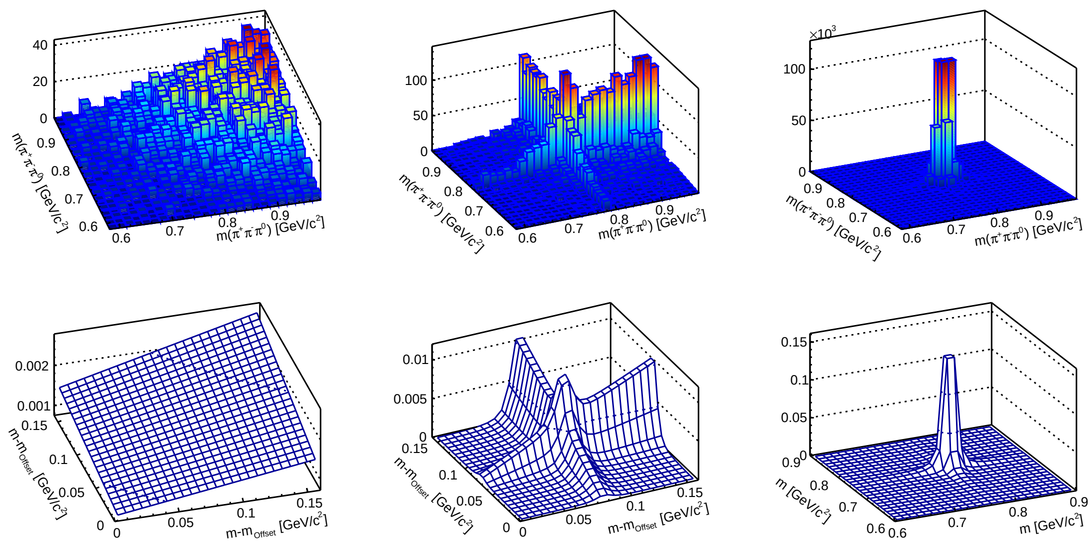

Fig. 3.11: Upper row: 3π vs. 3π invariant mass distribution for MC events with the topologies: $J/\psi \to \gamma 6\pi$ (left), $J/\psi \to \gamma 3\pi\omega$ (center) and $J/\psi \to \gamma\omega\omega$ (right). Lower row: Visualizations of the analytical functions used to describe the distributions shown in the upper row.

comparison, the left plot in the lower row of Figure 3.11 shows an example of this part of the background fit function.

A more sophisticated function is needed to describe background of the type $3\pi\omega$. A MC sample containing $J/\psi \to \gamma\omega\pi^+\pi^-\pi^0$ events has been studied. The 3π versus 3π mass distribution of the reconstructed and selected events clearly shows two narrow bands at the ω mass, which are intersecting, where both 3π systems are close to the nominal ω mass (see central plot in upper row of Figure 3.11). Additionally, the amplitude of the ω bands is increasing towards larger 3π masses. This behavior can be described by a Voigt function in one, and a linear function in the other of the two 3π dimensions for each of the two bands. Again, the slopes of the linear functions are free parameters. The Voigt function is a convolution of a non-relativistic Breit-Wigner function, describing the natural mass shape of the resonance, and a Gaussian function, modeling the detector resolution.

The Voigt function is defined as

$$V(m,\mu,\sigma,\Gamma) = \frac{1}{\sqrt{2\pi}\sigma}\Re\left[W\left(\frac{1}{2\sqrt{\sigma}}(m-\mu)+i\frac{\Gamma}{2\sqrt{2}\sigma}\right)\right], \tag{3.16}$$

where W symbolizes the complex error-function, μ and Γ are the fixed nominal mass and width of the ω meson, as listed in [1]. The width of the Gaussian function, σ, is kept as a free parameter. The central plot in the lower row of Figure 3.11 shows an example of this background function. Due to the intersection of the two narrow ω bands, an enhancement in the center of the plot, the $\omega\omega$ signal region, can be seen. This overlap will lead to a peak in the one-dimensional projections of each of the two 3π systems originating from the discussed background, not from misidentified $\omega\omega$ signal events. The sum of the functions for the 6π and $3\pi\omega$-type backgrounds is used to construct a total probability density function for background contributions.

For the description of signal events, a two-dimensional Voigt function is used. As described before, the common mean value of the Gaussian and Breit-Wigner part of this function, is set to the nominal mass of the ω, as well as the width Γ, which is set to the ωs natural decay width. Again, the width of the Gaussian part of the distribution is a free parameter. A dedicated MC sample was studied, the right plot in the upper row of Figure 3.11 shows the reconstructed and selected events. A plot of the analytical function used to describe the signal distribution is shown in the right plot of the lower row in Figure 3.11.

The metric includes different decay angular distributions and especially the squared invariant mass of the $\omega\omega$ system, which is the only coordinate not normalized to its range. This coordinate has been weighted more strongly, so that the structures in the $\omega\omega$ mass, like the enhancement at threshold or the peak of the η_c can be accounted for. The best value for the normalization of this phase space coordinate has been determined using the toy MC sample discussed in the subsequent section. Furthermore, the metric contains the angle between the normal vectors of the ω decay planes transformed into the $\omega\omega$ helicity system and the so called λ-parameter of both ω mesons. This parameter is the slope of the $\omega \to \pi^+\pi^-\pi^0$ Dalitz-plot, which is a characteristic property of the ω decay pattern and therefore a coordinate with a strong separation power. The λ parameter is defined as

$$\lambda = |(\vec{p}_{\pi^+} \times \vec{p}_{\pi^-})|^2, \tag{3.17}$$

where $\vec{p}_{\pi^\pm}$ describes the linear momentum of the corresponding pion in the helicity frame of the ω. This parameter assumes its maximum value $\lambda_{\max}$ for exactly symmetric decays (120° between any pion pair) in the center of the Dalitz-plot. The distribution of interest is the normalized λ-distribution, $\lambda/\lambda_{\max}$, which ranges from 0 to 1. While this distribution rises linearly with a fixed slope for ω signal events, it is assumed to be flat for non-ω background events. A summary of all coordinates entering the metric and their normalizations is given in Table 3.2.

The parameters that are considered in the metric have been deliberately chosen to represent all parameters entering the construction of the partial wave amplitudes (see Chapter

Coordinate	Description	Δ_k
$\cos(\vartheta_\gamma)$	Polar angle of the radiative photon	2
$\chi_{\omega\omega}$	Angle between the normal vectors of the ω decay planes in the $\omega\omega$ helicity system	$\pi/2$
$m^2(\omega\omega)$	Squared invariant mass of the $\omega\omega$ system	$0.254\,\mathrm{GeV}^2/c^4$
$\cos(\vartheta^{\omega\omega}_{\omega_1})$	Polar decay angle of ω_1	2
$\varphi^{\omega\omega}_{\omega_1}$	Azimuthal decay angle of ω_1	π
$\cos(\vartheta^{\omega\omega}_{\omega_2})$	Polar decay angle of ω_2	2
$\varphi^{\omega\omega}_{\omega_2}$	Azimuthal decay angle of ω_2	π
$\lambda_{\omega_1}/\lambda_{\max}$	Normalized slope parameter of the ω_1 Dalitz plot	1
$\lambda_{\omega_2}/\lambda_{\max}$	Normalized slope parameter of the ω_2 Dalitz plot	1

Table 3.2: Coordinates of the metric used for the Q-factor method and their normalizations. The upper right index indicates the relevant helicity system of the coordinate, if applicable.

4), so that they span the complete phase space of the reaction. Apart from the metric, the number of nearest neighbors n_c has to be set. If n_c is chosen too small, the fits for the single events are not converging well due to the small number of entries considered, while for too large values the phase space cell under consideration becomes too large. This can lead to the situation, that the density of the background contribution within the considered cell fluctuates too much and the obtained Q-factors might be systematically wrong. After tests with n_c between 25 and 1000 have been performed, a number of 200 nearest neighbors was chosen.

3.4.3 Validation of the Q-Factor Method using a Toy MC Sample

Since the performance of the presented method is very sensitive to the choice of parameters like the number of nearest neighbors or the normalization of all considered coordinates in the metric, a means to effectively test the method is necessary. Two different toy MC samples have been generated according to very rough amplitude models obtained from mass dependent fits to the selected data in signal and sideband regions. The Q-factor method was then applied to the combined generated data set, and the difference between the generated and reconstructed signal and background samples was studied. This rather complex method of testing had to be chosen, in order to ensure that the toy sample contains all angular production and decay distributions, which are exploited by the chosen metric. For this test, the selected data sample (light blue distribution in Figure 3.8e) was fitted using a mass dependent PWA fit containing three Breit-Wigner shaped resonances. The fitting procedure, amplitude construction and minimization technique will be discussed in Chapter 4. This PWA fit is only used as a tool to obtain a reasonable amplitude model for signal generation. It is explicitly not claimed here, that this fit can well describe the data, but it gives a reasonable representation of all angular distributions and especially the $\lambda/\lambda_{\text{max}}$ distributions and the invariant mass spectra under consideration. Similarly, a fit to the data selected from the $3\pi\omega$ sideband (Box B1 in Fig. 3.8e) was performed, using two resonances parametrized with Breit-Wigner line shapes. While for the fit in the signal region all resonances decay into an ω meson pair, in the sideband it is assumed that the resonances decay into one ω as well as an associated 3π system, to create the signal's final state. The partial wave analysis software PAWIAN (see [31]) can use a fitted model, namely the values of fit parameters like amplitudes, phases, masses or widths to generate events according to the model. The software was used to generate a data set from the signal model, as well as the sideband model. Additionally, a set of phase space distributed $J/\psi \to 6\pi$ events was generated. Finally, the two generated samples for the $3\pi\omega$ and the 6π events were mixed and are employed as the background sample. Table 3.3 lists the relevant contributions and decays for the signal and background sample, respectively.

Signal model	Background model
$\eta(1760) \to \omega\omega$	$0^{++} \to \omega\pi^+\pi^-\pi^0$
$f_2(1910) \to \omega\omega$	$2^{-+} \to \omega\pi^+\pi^-\pi^0$
$\eta_c \to \omega\omega$	$2(\pi^+\pi^-\pi^0)$ (phase space distributed)

Table 3.3: Components of PWA fits in the signal and sideband regions. The obtained models were used to generate toy MC samples.

The obtained signal and background samples are mixed and subsequently the Q-factor method is applied using this combined MC data set. Access to the MC truth information on the origin of each single event (signal or background sample) is preserved throughout the procedure, so that after all Q-factors have been determined, the performance of the method can be checked by comparing the generated with the Q-weighted (for background: $(1-Q)$-weighted) distributions. Figure 3.12a shows the angular decay distributions, the $\lambda/\lambda_{\mathrm{max}}$ distribution and the 3π invariant mass for the ω candidates, while in Figure 3.12b the invariant mass of the $\omega\omega$ system, the χ-angle between the ω decay planes and the angular distribution of the radiative photon are shown.

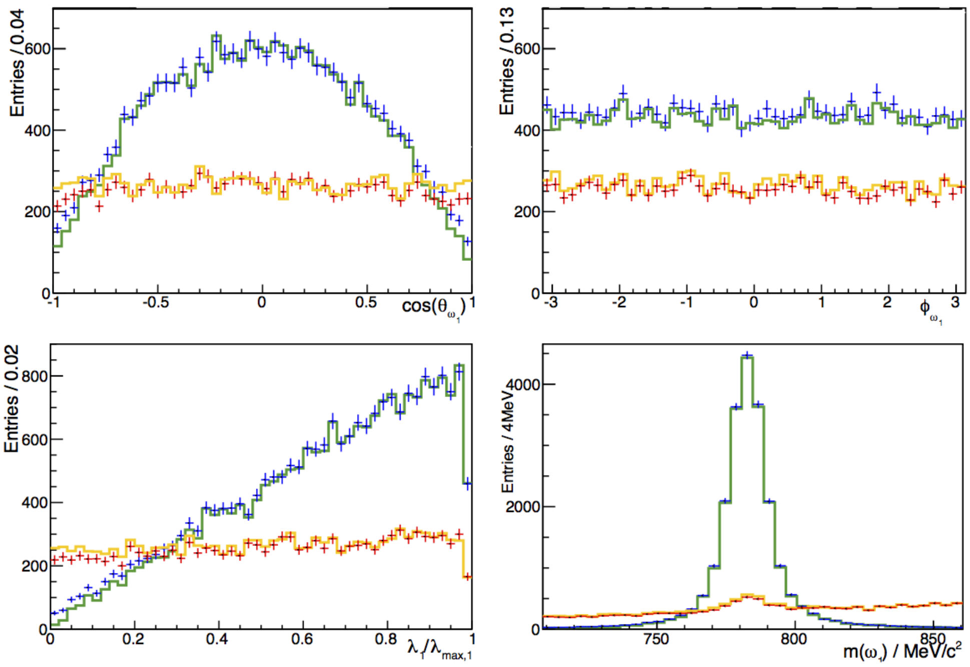

(a)

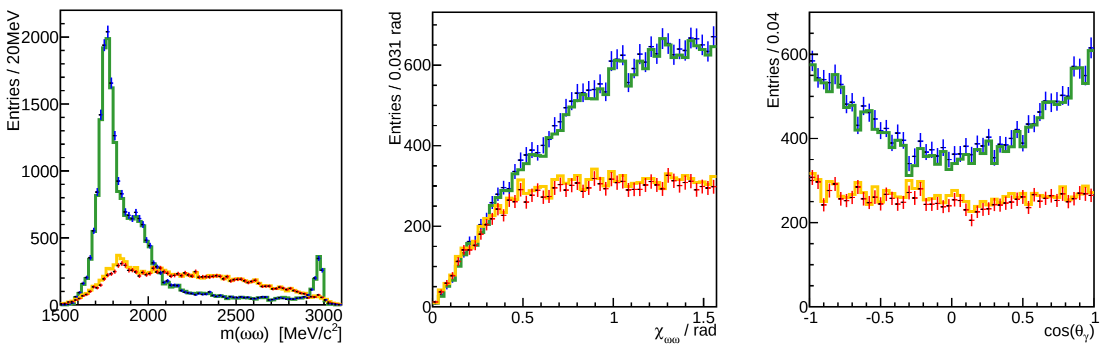

(b)

Fig. 3.12: Various angular and invariant mass distributions for events from a toy MC sample. The generated signal (green) and background (orange) distributions are overlayed with the Q-weighted (blue) and $(1-Q)$-weighted (red) results of the Q-factor method.

The figures show the generated distributions for signal (green) and background (orange), overlayed with the result of the Q-factor method. The full MC data set was weighted with the obtained Q-factors, which shows the identified signal component (blue), as well as the $(1-Q)$-weighted MC data set interpreted as background contribution (red). It should be noted here, that the cut to the $\omega\omega$ signal region (blue circle in 3.8e) has not yet been re-introduced, so that all distributions show the results for the complete kinematic range.

A very good agreement between the MC truth distributions and the identified signal and background contributions can be recognized. The deviations of the blue to the green, as well as the orange to the red curve are almost negligible within statistical uncertainties. This holds even for the non-smooth $\omega\omega$ invariant mass distribution. In the course of the studies leading to this result, the weighting of the $\omega\omega$ invariant mass was varied in a large range ($1-100$, where 1 indicates a normalization to its full range), until the value for the best agreement between MC truth and Q-factor identification was reached.

Figure 3.13 shows the calculated Q-factors for the generated signal (green) and background events (orange). One can clearly see, that the Q-factors for signal events show a sharp peak around $Q = 1$, while most of the background events are assigned with a weight near zero, which demonstrates the separation power of the method performed for this toy MC sample.

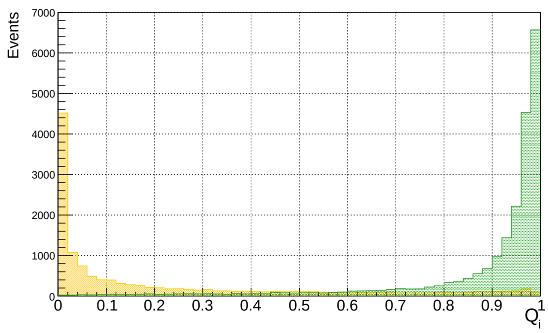

Fig. 3.13: Calculated Q-factors for events originating from the generated signal sample (green) and the background sample (orange)

Finally, the cut around the $\omega\omega$ peak in the 3π vs. 3π mass is re-introduced. Figures 3.14a and 3.14b show again the distributions for all coordinates entering the metric to check, how well the method performs for background events situated directly under the $\omega\omega$ peak. The cut on the two-dimensional 3π mass is indicated by the red arrows in Figure 3.14a. Note, that the invariant mass of the $\omega\omega$ system is shown in the left plot in Figure 3.14b on a logarithmic scale, so that the differences between the generated and Q-factor weighted distributions can be seen more clearly. Even here, a very good agreement is observed. Quantitatively, the numbers of the generated signal and background events are compared to the sums of the Q- and $(1-Q)$-factors in Table 3.4. The errors of the individual Q-factors were found to be negligible using the error estimation described in [28], so the errors quoted in the table are purely statistical (rough estimation). Within the signal region, the deviation between the generated signal events and the sum of the Q-factors amounts to less than one sigma of the statistical error.

Selected region	Generated signal events	$\sum_i Q_i$	Generated background events	$\sum_i (1-Q_i)$
Full sample	21527	22101 ± 149	13327	12743 ± 113
Signal region	18316	18433 ± 136	1585	1467 ± 38

Table 3.4: Number of generated signal and background events, in comparison with the sums of all Q- and $(1-Q)$-factors

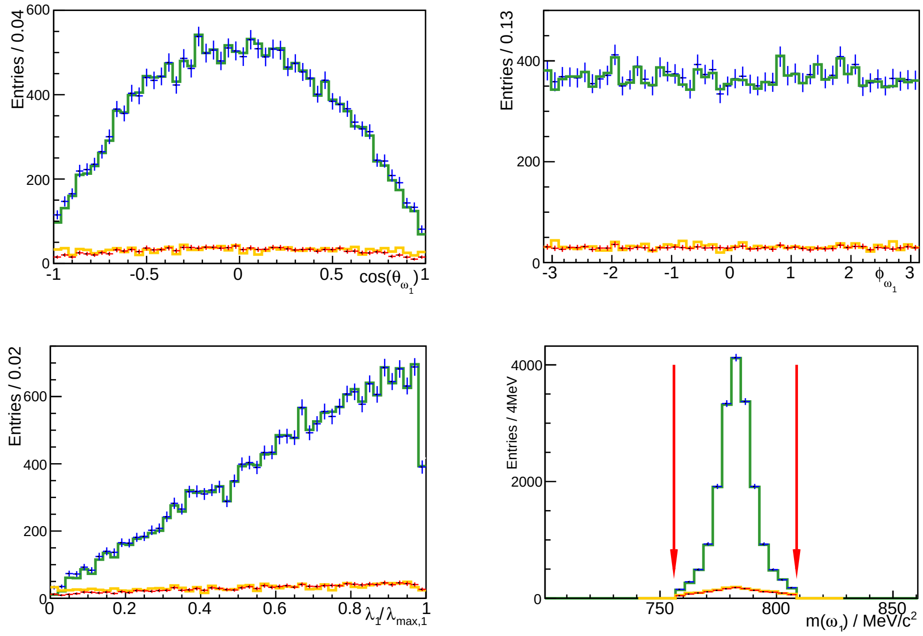

(a)

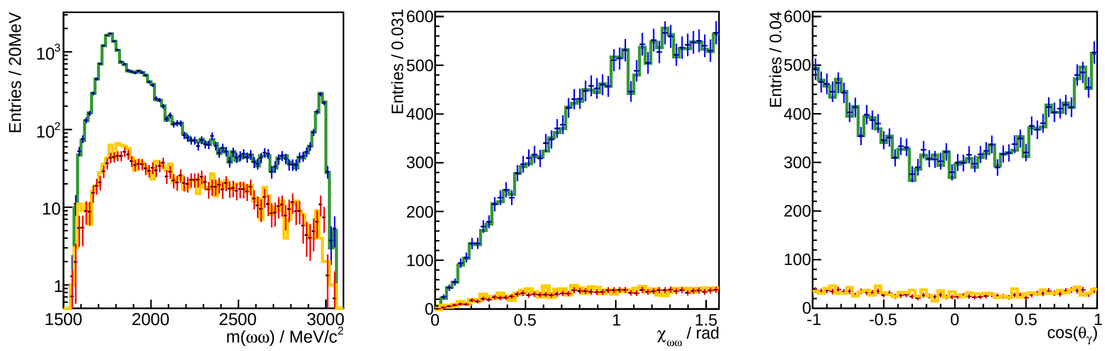

(b)

Fig. 3.14: Various angular and invariant mass distributions for events from a toy MC sample that are located in the $\omega\omega$ signal region (red arrows). The generated signal (green) and background (orange) distributions are overlayed with the Q-weighted (blue) and $(1-Q)$-weighted (red) results of the Q-factor method.

3.4.4 Application to the Selected Data Set

Finally, the Q-factor method is applied to the selected data. After the initial event selection (light blue distribution in Figure 3.8e) a sample of 87947 events was retained from the full 2009 and 2012 J/ψ data sample. Figure 3.15 shows a fit for the 200 nearest neighbors of one single seed event as an example. Depicted are the two-dimensional mass distributions which are subjected to the fit, as well as the single components of the fit function and the composite fit function. To be able to compare fit and data for this example, the projections of data and fit to both 3π axes are displayed as well.

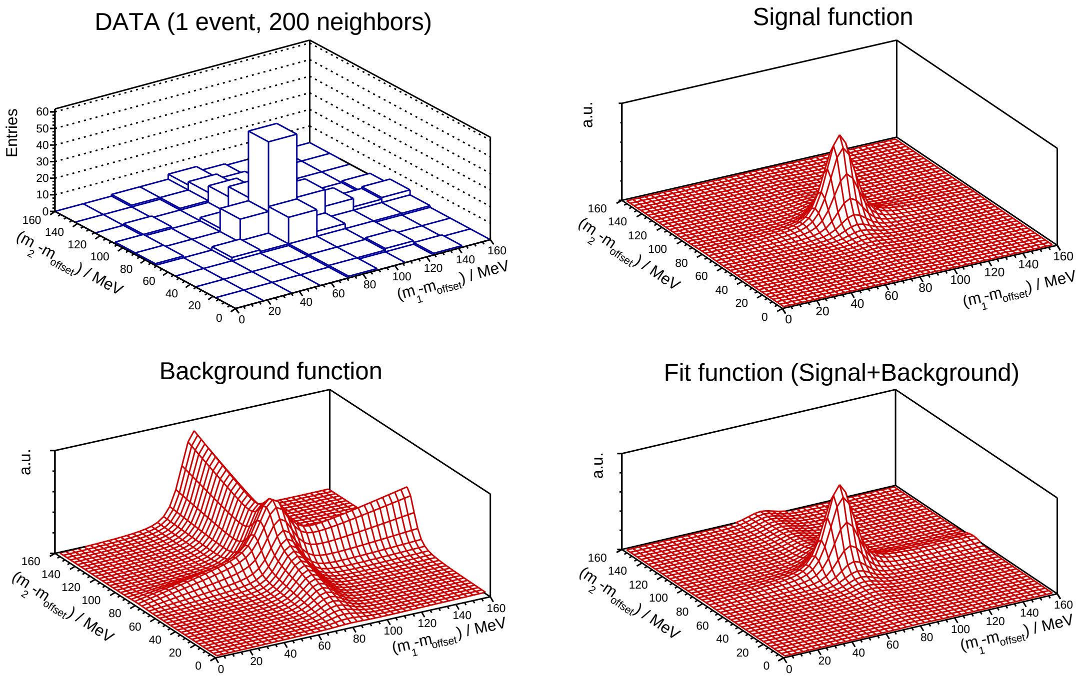

(a)

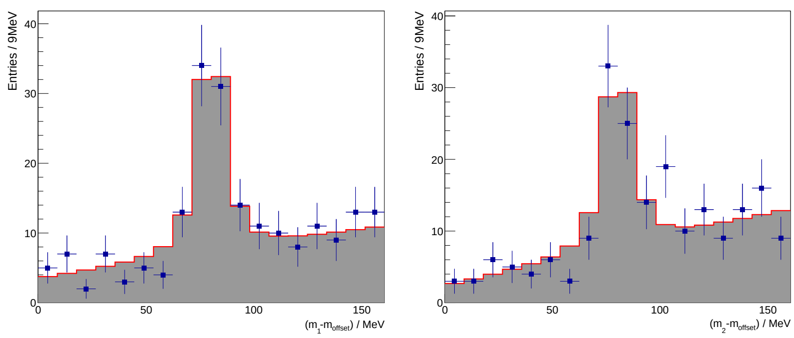

(b)

Fig. 3.15: Example fit for the 200 nearest neighbors of one seed event. (a) shows the 3π vs. 3π mass distribution for data (upper left), the signal function (upper right), the background function (lower left) and the complete fit function (lower right). Projections of data (blue symbols) and the fit function (red shaded) are shown in (b) for comparison.

The sum of all obtained Q-factors is treated as the number of signal events in the selected sample, yielding a number of $\sum_i Q_i = 75245$ signal events. Thus, a number of 12702 background events was identified and removed. This corresponds to a background fraction of $\sim 14.4\%$ in the selected sample, which is in very good agreement with the estimations from the two-dimensional sidebands. Figures 3.17 and 3.16c show the angular distributions, normalized λ distributions and different invariant mass spectra for the Q-weighted and $(1-Q)$-weighted data. The gray shaded histograms show the distributions from the sidebands, scaled to the integral of the $(1-Q)$-weighted distributions. Also here, a good agreement between expectations from sideband selections and $(1-Q)$-weighted data is observed. Figures 3.16a and 3.16b show the Q-weighted $\gamma\omega\omega$ and 3π Dalitz plots. While the 3π Dalitz plot shows a smooth distribution which peaks in the center, two structures can be clearly seen in the $\gamma\omega\omega$ Dalitz plot. The narrow diagonal band at low invariant mass squares corresponds to the η_c, while the broad band in the upper right corner represents the enhancement at the $\omega\omega$ threshold. In general, the Q-factor method presented and applied in this work can be seen as a multidimensional generalization of a sideband-subtraction, in which as many variables as needed can be considered simultaneously.

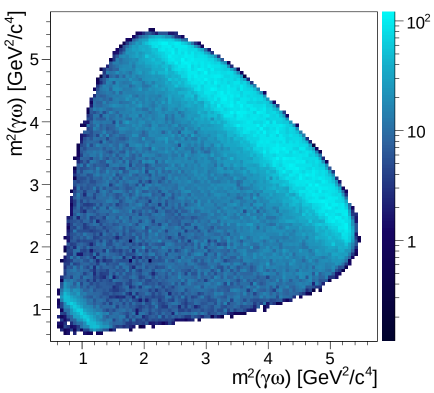

(a)

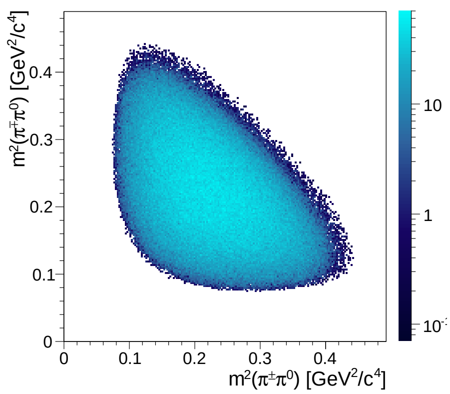

(b)

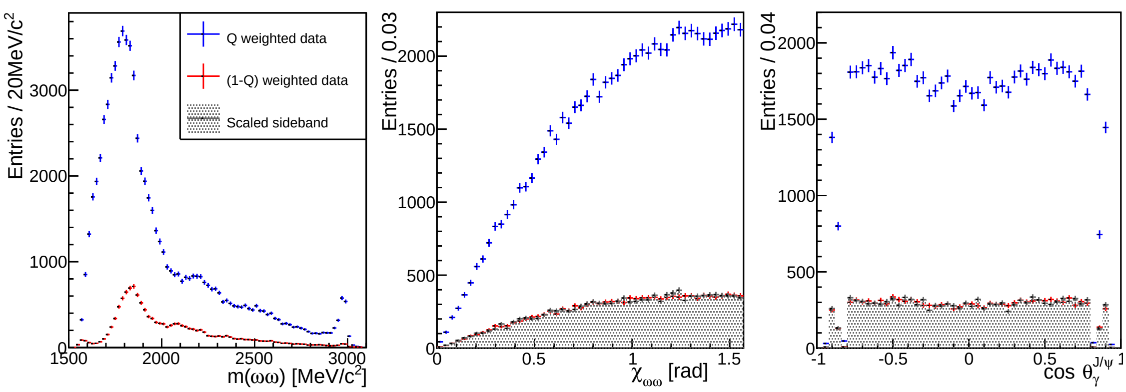

(c)

Fig. 3.16: Dalitz plots of the $\gamma\omega\omega$ (a) and $\pi^+\pi^-\pi^0$ (b) systems after application of all cuts and including Q-factor weights. (c) shows the invariant $\omega\omega$ mass, χ angle between the ω decay planes and $\cos(\vartheta)$ distribution of the radiative photon for events within the region marked with red arrows in Fig. 3.17 from data.

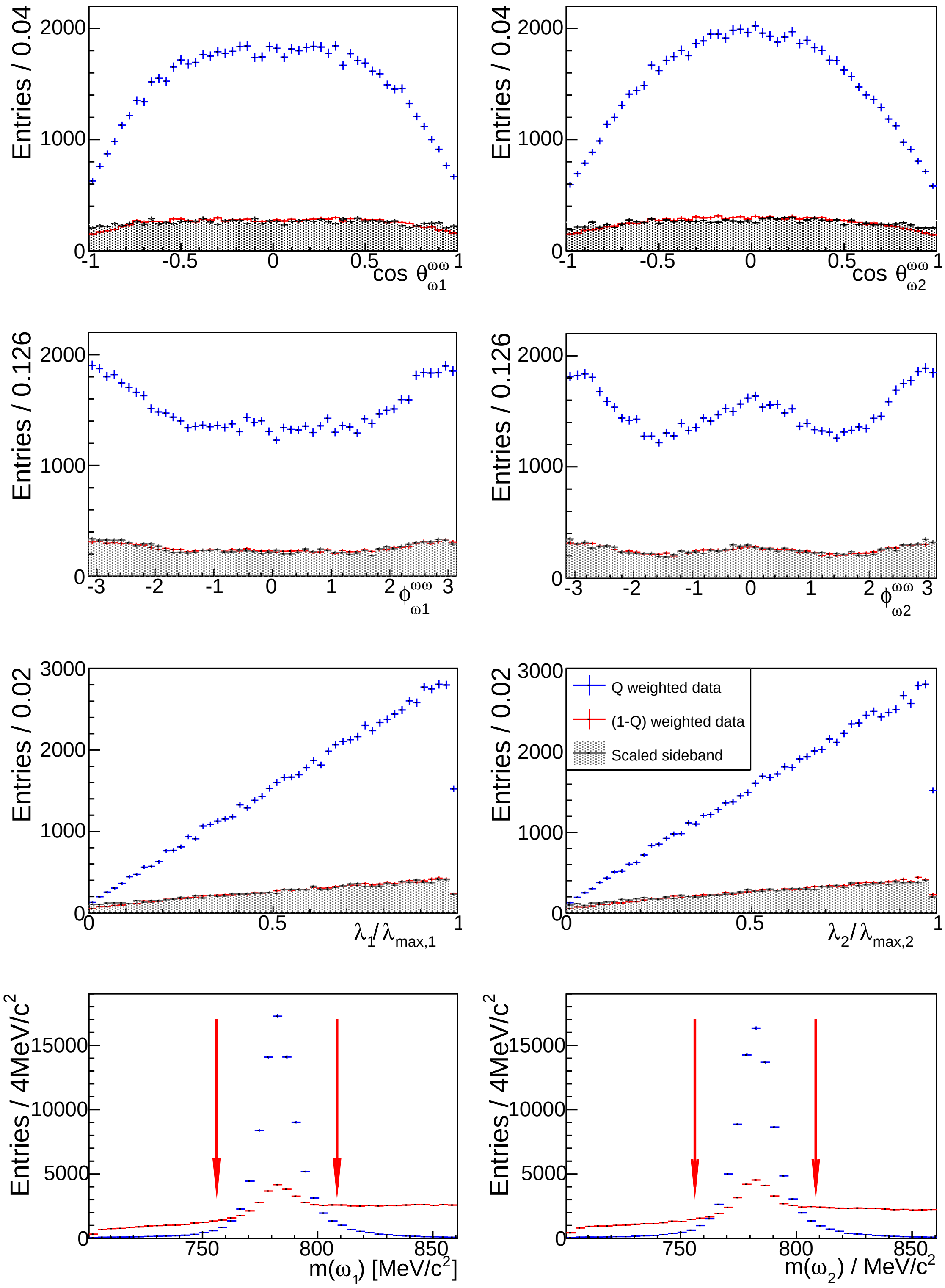

Fig. 3.17: Decay angular distributions, $\lambda/\lambda_{\text{max}}$ and 3π invariant mass distributions for the two ω candidates (left and right) for events within the region marked with red arrows from data.

4 Partial Wave Analysis

The decay of a particle into a specific final state in most cases can proceed via a number of intermediate states. In the simplest case, the identification and determination of the properties of intermediate resonances can be performed by analyzing one-dimensional (mass) distributions, or by performing Dalitz-Plot analyses. In this analysis, the decay $J/\psi \to \gamma\omega\omega$ was selected, but a Dalitz-Plot analysis is not applicable here, since the J/ψ as well as all three daughter particles exhibit a spin $J = 1$. The invariant mass of the $\omega\omega$ system shows a clear and isolated peak at a mass of about $2.98\,\mathrm{GeV}/c^2$, which is assumed to be identified with the charmonium ground state, the η_c, according to its mass and width. However, to verify this assumption, it is necessary to also identify the J^{PC} quantum numbers of the resonance. Access to these properties can be gained by the analysis of the angular distributions, since these show a characteristic behaviour depending on the spin-parity of the resonance under study. Therefore a simple *spin-parity analysis*, which has been applied by various experiments in the past, can be performed by one-dimensional fits to the corresponding angular distributions. However, difficulties arise when one has to deal with very broad, overlapping or weakly contributing resonances, that can not easily be identified in an invariant mass spectrum. Additionally, overlapping resonances may interfere with each other, which requires a more sophisticated description of the decay. In these cases, a decomposition of the different contributions is virtually impossible, when only one- or two-dimensional projections of the phasespace are interpreted. Therefore a full partial wave decomposition is required, which provides the possibility to simultaneously describe all dimensions of the phasespace and allows for interference between different components. The method is based on a concept from scattering theory, in which the quantum mechanical state of a particle can be interpreted as a plane wave. The scattering of such a plane wave off a given potential can be solved by expanding the scattering amplitude into partial wave amplitudes according to the contributing orbital angular momentum [32].

A similar procedure is applied in partial wave analyses: Here, the observed intensity is given by the absolute square of a (coherent) sum of partial wave amplitudes, which corresponds to the differential cross section of the reaction. The contributing partial wave amplitudes are identified with sets of different quantum numbers. The definition of the amplitude in this framework requires a description of the decay pattern (see Section 4.2), a formalism to describe the particles' spins (see Section 4.3) and finally the dynamical part of the amplitude for each corresponding resonance. In the easiest case this can be a parametrization of the observed line shape visible in the invariant mass spectrum of the daughter particles of the corresponding resonances (cf. Section 4.4.2).

The partial wave analysis (PWA) presented in this work has been carried out with the software package *PAWIAN* (*Pa*rtial *W*ave *I*nteractive *AN*alysis), which is being developed at Institut für Experimentalphysik I, Ruhr-Universität Bochum. *PAWIAN* is a user-friendly and highly modular PWA software package written in $C++$, which provides a framework for the generic construction of production and decay amplitudes in different spin-formalisms (covariant, helicity or covariant tensor formalism), based on plain-text configuration files as the user input [31]. The data is fitted using an event-based maximum likelihood fit, for which the minimization is carried out with the external MINUIT2 package.

In this chapter the construction of the amplitudes relevant for this analysis and the results of a model independent as well as a model dependent PWA will be discussed.

4.1 Analysis Strategy

One goal of this analysis is, to identify the contributions to the observed intensity in the complete $\omega\omega$ system from the large enhancement at the $\omega\omega$ mass threshold up to the mass of the η_c. Since it is not a priori clear, which resonances or partial waves contribute, in a first step a *model independent*, sometimes also called *mass independent* analysis is performed. In this case the dynamical part of the amplitudes, corresponding to the parametrization of the line shape, is omitted from the description. The data is then analyzed in bins of the invariant $\omega\omega$ mass. These bins must be narrow enough so that it is a valid assumption to approximate the mass dependence of the amplitude to be constant, but not narrower than the mass resolution. To ensure this, the mass resolution over the full $\omega\omega$ invariant mass range has been studied (see Section 4.7.1). For the model independent PWA, each bin is treated individually.

The results of the model independent analysis finally provide a guidance for the *model dependent* analysis discussed in Section 4.8. The *K-matrix formalism* [33] is used for the description of the dynamical parts of the amplitudes in this part of the analysis. The goal is, to identify the dominant contributions while at the same time a good description of the data over the full $\omega\omega$ mass range should be achieved. Additionally, the data in the mass region of the η_c is analyzed separately to study the η_c production mechanism and extract the $\eta_c \to \omega\omega$ branching fraction, without the need to obtain a good description over the full mass range. Here, the line shape of the η_c is parametrized with a relativistic Breit-Wigner function with two modifications to account for the distortion of the η_c line shape in the pure magnetic dipole transition $J/\psi \to \gamma\eta_c$ (cf. Chapter 5).

4.2 The Isobar Model

The description of decay chains in this PWA is based on the *isobar model*, in which each decay of a particle is described by a sequence of two-body decays. This holds true for the decay of most short-lived resonances, while there are some exceptions to this empiric rule as for the three-body decays of mostly light mesons like the ω or η decaying e.g. into $\pi^+\pi^-\pi^0$. The decay chain of the analysis presented here contains two of the two-body decays discussed above, namely

$$J/\psi \to \gamma X \quad \text{and} \quad X \to \omega\omega,$$

as well as the three-body decays of both ω mesons. To correctly describe the full decay tree in the PWA software without the need to parameterize the resonance line-shapes of the ω mesons, their decays into three pions are included in the phase space distributed

MC sample with the correct line shape. An intermediate resonance X decaying into $\omega\omega$, which is produced in a radiative decay of the J/ψ, may have the quantum numbers

$$\begin{array}{rcccccc} I^G(J^{PC}) \in & \{0^+(0^{-+}), & 0^+(0^{++}), & 0^+(1^{++}), & 0^+(2^{-+}), & 0^+(2^{++})\}, \\ \text{Naming convention:} & \eta & f_0 & f_1 & \eta_2 & f_2 \end{array} \tag{4.1}$$

when restricting the analysis to resonances with a total angular momentum of $J \leq 2$. Additionally, the possible contribution of a spin-exotic component with the quantum numbers $I^G(J^{PC}) = 0^+(1^{-+})$ was included in all studies for completeness.

4.3 The Helicity Formalism

The amplitudes of all two-body decays in this analysis are described in the *helicity formalism*, which is one possible choice of a *spin formalism*. One feature of the helicity formalism is, that particles with and without rest mass can be treated equally, which simplifies calculations. An even more advanced spin-formalism is given by the Lorentz invariant *Rarita-Schwinger formalism*, which was also implemented into the PWA software PAWIAN, but not fully tested and verified at the time of this analysis.

Some amplitudes are finally transformed into different coordinate systems to simplify the interpretation of the fit parameters or to exploit properties, known for special types of decays, such as the radiative decay of the J/ψ. The decay amplitudes of the radiative decay are transformed to the *radiative multipole basis*, while all other decay amplitudes are finally expanded in the LS basis (see [34]). This expansion is used, since L and S are meaningful quantum numbers for the system under study, e.g. due to the L dependence of the centrifugal barrier factors. Conservation laws lead to a reduction of the number of free parameters for the minimization, which will be discussed in more detail in Section 4.3.2.

4.3.1 Canonical and Helicity States

A single particle at rest can be described by its total spin j, as well as the projection m of the spin to a fixed quantization axis, e.g. the z-axis, yielding the state vector $|j,m\rangle$. These state vectors are called *canonical base vectors*, which represent a complete set of orthogonal states, thus fulfillinig the relations

$$\sum_{j,m} |j,m\rangle\langle j,m| = \mathbb{1} \quad \text{ and } \langle j',m'|j,m\rangle = \delta_{j'j}\delta_{m'm} \quad . \tag{4.2}$$

Each state may now be expressed in the helicity base, in which the direction of movement of the particle is the quantization axis. However, to transform any state into the helicity frame, it is necessary to first define an arbitrary rotation of a canonical angular momentum eigenstate. Consider a unitary operator $\hat{r}(\alpha,\beta,\gamma)$, where α, β and γ denote the Euler angles, which acts on the states $|j,m\rangle$ and provides the means of rotating this state into any direction. It is shown in [35], that the rotation can be written as

$$\hat{r}(\alpha,\beta,\gamma)|j,m\rangle = \sum_{m'} |j,m'\rangle D^j_{mm'}(\alpha,\beta,\gamma), \tag{4.3}$$

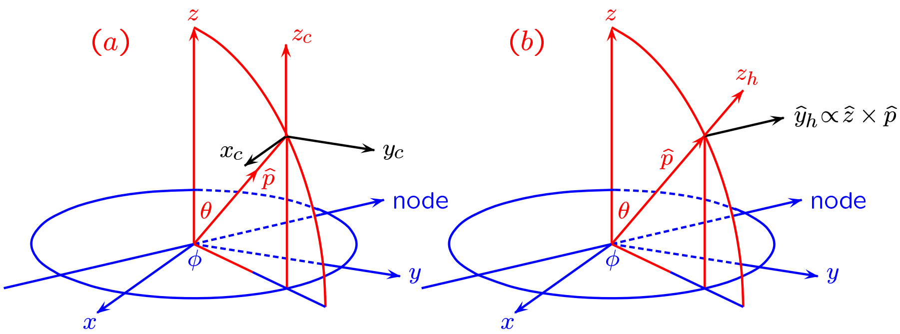

Fig. 4.1: Illustration of the coordinate systems of the canonical system (left) as well as the helicity system (right). [35]

where $D^j_{mm'}$ denotes the Wigner-D-matrices. These matrices are given by [35]

$$D^j_{mm'}(\alpha,\beta,\gamma) = \langle jm'|\hat{r}(\alpha,\beta,\gamma)|j,m\rangle \tag{4.4}$$
$$= e^{-im'\alpha} d^j_{m'm}(\beta) e^{-im\gamma}, \tag{4.5}$$

whereas the Wigner-(small)-d-matrices can be found tabulated e.g. in [1].

To transform a state at rest into any other reference frame, in which the particle may have the linear momentum $\vec{p}$, a Lorentz transformation is used, which can be factorized into rotations using the operator $\hat{r}$ introduced above, and a Lorentz boost $\hat{l}$ along a defined axis. It is a common choice to use $\alpha = \varphi$, $\beta = \vartheta$ and $\gamma = 0$, and to choose the Lorentz boost to act along the z-axis. Since γ describes a rotation around the z-axis, and this is the axis chosen for quantization, the choice $\gamma = 0$ is valid without loss of generality. A state is transformed into the *canonical reference system* by first applying a rotation, so that the z-axis is rotated to match the axis of the particles momentum $\vec{p}$, then applying a Lorentz-boost along the z-axis and finally rotating the state back, so that all axes have the same orientation as before the first operation. This system is illustrated in the left part of Figure 4.1. In terms of the defined operators this operation can be written as

$$|\vec{p},j,m\rangle = \hat{r}^{-1}(\varphi,\vartheta,0)\hat{l}_z(\vec{p})\hat{r}(\varphi,\vartheta,0)|j,m\rangle. \tag{4.6}$$

Analogously, a state can also be described by its *helicity*, instead of the quantity m. The helicity is defined as the projection of a particles' spin onto its direction of movement given by $\lambda = \vec{s}\cdot\vec{p}$, and a state $|j,\lambda\rangle$ therefore is an eigenstate of the helicity operator. A transformation into the helicity frame is achieved by performing an operation very similar to the transformation into the canonical system, only that the last rotation is omitted. Thus, the transformed z-axis stays parallel to the direction of motion of the particle. This can be expressed using the rotation and boost operators as

$$|\vec{p},j,\lambda\rangle = \hat{l}_z(\vec{p})\hat{r}(\varphi,\vartheta,0)|j,\lambda\rangle. \tag{4.7}$$

The new y-axis in the helicity system, called y_h, is then defined to be perpendicular to both the old z-axis as well as the direction of motion, which defines the new z-axis ($\hat{y}_h \propto \hat{z}\times\hat{p}$). The orientation of the axes in the helicity system is illustrated in the right part of Figure 4.1.

4.3.2 Helicity Amplitudes

Now the transition amplitude for the decay of a particle a with total angular momentum J_a and the projection of the spin onto an arbitrarily defined axis given as M_a, into two daughter particles b and c can be constructed. It is shown in detail in [35] and [36] that the transition amplitude for this decay in general can be written as

$$A^{J_a,M_a}_{\lambda_b\lambda_c}(a \to b + c) = \sqrt{\frac{2J_a+1}{4\pi}} D^{J_a*}_{M_a\lambda}(\varphi,\vartheta,0) F^{J_a}_{\lambda_b\lambda_c}, \tag{4.8}$$

with λ_b and λ_c being the helicities of the daughter particles and $\lambda = \lambda_b - \lambda_c$. The last term, $F^{J_a}_{\lambda_b\lambda_c}$, represents the (complex) fit parameter which is optimized in the PWA fit. However, depending on symmetry relations or conservation laws, some of these amplitudes may vanish and therefore reduce the number of free parameters in the fit. If for the decay $a \to b + c$ parity is conserved, the parameters $F^{J_a}_{\lambda_b\lambda_c}$ and $F^{J_a}_{-\lambda_b-\lambda_c}$ are correlated by the relation

$$F^{J_a}_{\lambda_b\lambda_c} = P_a \cdot P_b \cdot P_c \cdot (-1)^{-J_a+J_b+J_c} F^{J_a}_{-\lambda_b-\lambda_c}, \tag{4.9}$$

where P_i with $i \in \{a,b,c\}$ denotes the intrinsic parity of the corresponding particle and J_i its total angular momentum. Due to this relation, the number of independent helicity amplitudes is almost reduced by a factor of two [36]. If the initial state is not identified by the quantity M_a, but instead by its helicity, M_a is replaced with λ_a in the formula above. Due to the different transformations and expansions, from here on the radiative decay of the J/ψ, and the subsequent decays are treated separately.

Radiative Decay of the J/ψ

For the radiative decay $J/\psi \to \gamma X$, the initial state ($a = J/\psi$) is described by its total angular momentum $J_a = J_{J/\psi}$ and the projection of the spin onto the axis of the beam (z-axis), $M_a = M_{J/\psi}$. In this case, the initial state can not be described in the helicity system. For the spin projection of the J/ψ only the values $M_{J/\psi} = \pm 1$ are allowed. This restriction is caused by the QED interaction $e^+e^- \to \gamma^*$ at energies large compared to the electron mass, since in this case electrons only couple to positrons of the opposite helicity (cf. [36]). Another consequence is that the radiative photon can only carry the helicities $\lambda_\gamma = \pm 1$.

As long as the electron and positron beams are unpolarized, the dependence on the polar angle φ vanishes. The amplitude given in 4.8 therefore reduces to

$$A^{J_{J/\psi},M_{J/\psi}}_{\lambda_\gamma\lambda_X}(J/\psi \to \gamma + X) = \sqrt{\frac{2J_{J/\psi}+1}{4\pi}} d^{J_{J/\psi}}_{M_{J/\psi}\lambda}(\vartheta) F^{J_{J/\psi}}_{\lambda_\gamma\lambda_X} \tag{4.10}$$

$$= \sqrt{\frac{3}{4\pi}} d^{1}_{M_{J/\psi}\lambda}(\vartheta) F^{1}_{\lambda_\gamma\lambda_X}. \tag{4.11}$$

Note, that especially the Wigner-D matrices have been replaced by the Wigner-(small)-d matrices, due to the omitted dependence on φ. For this radiative decay, an expansion in the radiative multipoles related to the corresponding final state photon is meaningful. An example is the decay $J/\psi \to \gamma\eta_c$, which is a pure magnetic dipole transition, so the fit parameters of the amplitudes in the radiative multipole basis have a physical interpretation

J^{PC} of resonance X	Allowed multipole transitions	Corresponding (L,S) combinations
0^{-+}	$M1$	(1,1)
1^{-+}	$M1$,$E2$	(1,0), (1,1), (1,2)
2^{-+}	$M1$,$E2$,$M3$	(1,1), (1,2), (3,2), (3,3)
0^{++}	$E1$	(0,1), (2,1)
1^{++}	$E1$,$M2$	(0,1), (2,1), (2,2)
2^{++}	$E1$,$M2$,$E3$	(0,1), (2,1), (2,2), (2,3), (4,3)

Table 4.1: Allowed multipole transitions in dependence of the J^{PC} quantum numbers of a resonance X in the radiative decay $J/\psi \to \gamma X$

in this case. The transformation from the helicity amplitude to the radiative multipole basis is given by [37] [38] [39]

$$F^{J_{J/\psi}}_{\lambda_\gamma \lambda_X} = \sum_{J_\gamma} \sqrt{\frac{2J_\gamma + 1}{2J_{J/\psi} + 1}} \langle J_\gamma, \lambda_\gamma; J_{J/\psi}, \lambda_X - \lambda_\gamma | J_X, \lambda_X \rangle a^{J_{J/\psi}}_{J_\gamma}. \tag{4.12}$$

Here, J_γ denotes the angular momentum carried by the radiative photon, which is limited to $|J_{J/\psi} - J_X| \leq J_\gamma \leq |J_{J/\psi} + J_X|$. The single terms of this expansion can be identified with magnetic or electric dipole ($M1/E1$), quadrupole ($M2/E2$) and octupole ($M3/E3$) transitions, depending on the spin and parity of both the initial state (in this case the J/ψ) and the resonance X. Since the photon carries the quantum numbers 1^{--}, radiative transitions can only occur between two states of different C-parity. If the product of the parities of the initial ($P_{J/\psi}$) and the final state (P_X) is equal to $(-1)^{J_\gamma}$, one speaks of an E_{J_γ} transition, while processes for which $P_{J/\psi} \cdot P_X = (-1)^{J_\gamma + 1}$ are called M_{J_γ} transitions. In general, when more than one multipole transition is allowed, only the lowest one ($M1$ or $E1$) shows a dominant contribution, however higher order multipole contributions have also been observed for certain transitions [39]. Table 4.1 shows the multipole amplitudes considered in this analysis in dependence on the J^{PC} of the resonance X, each of which is represented by one (complex) fit parameter. In this case, an expansion in the LS-basis would lead to a larger number of amplitudes, which are also listed in Table 4.1.

Subsequent Decay of a Resonance into a Pair of ω Mesons

For the decay of intermediate resonances $X \to \omega\omega$, the "initial" state X may be described in the helicity system, and therefore the quantity M_a in equation 4.8 is replaced by the helicity $\lambda_a = \lambda_X$ of X with respect to the quantization axis of the helicity system. The helicity amplitudes for this decay are transformed into the so called LS basis, as the angular momentum between the daughter particles and the spin are meaningful quantum numbers for the systems under study. In general it is desirable to have fit parameters directly associated to these quantities. The transformation of the amplitude writes as [34]

$$F^{J_X}_{\lambda_{\omega_1} \lambda_{\omega_2}} = \sum_{L,S} \sqrt{\frac{2L+1}{2J_X + 1}} \langle L, 0; S, \lambda | J_X, \lambda \rangle \langle s_{\omega_1}, \lambda_{\omega_1}; s_{\omega_2}, -\lambda_{\omega_2} | S, \lambda \rangle \cdot \alpha^{J_X}_{LS}, \tag{4.13}$$

J^{PC} of resonance X	Allowed LS-combinations
0^{-+}	$L = 1,\ S = 1$
1^{-+}	$L = 1,\ S = 1$
2^{-+}	$L = 1,\ S = 1$
	$L = 3,\ S = 1$
0^{++}	$L = 0,\ S = 0$
	$L = 2,\ S = 2$
1^{++}	$L = 2,\ S = 2$
2^{++}	$L = 0,\ S = 2$
	$L = 2,\ S = 0$
	$L = 2,\ S = 2$
	$L = 4,\ S = 2$

Table 4.2: Allowed LS combinations for various J^{PC} quantum numbers of a resonance X decaying into a pair of ω mesons.

where the possible values for L and S are limited by $|J_{\omega_1} - J_{\omega_2}| \leq S \leq |J_{\omega_1} + J_{\omega_2}|$ and $|L - S| \leq J_X \leq |L + S|$. Also in this case, the selection rule due to parity conservation, which can be written as $P_X = P_{\omega_1} \cdot P_{\omega_2} \cdot (-1)^L$ for mesons, must be satisfied. Since in this decay the two daughter particles are identical, as an effect of symmetrization, the relation $L + S = even$ must be observed, which again reduces the number of allowed LS-combinations and thereby also the number of fit parameters [35]. Table 4.2 gives an overview over the allowed LS-combinations in dependence of the J^{PC} quantum numbers of the resonance X.

Both transformations (4.12) and (4.13) contain Clebsch-Gordon coefficients, which are noted as $\langle j_1{,}s_1; j_2{,}s_2|JS\rangle$ and can be found tabulated e.g. in [1].

The $\omega \rightarrow \pi^+\pi^-\pi^0$ Decay

The three-body decays of the two ω resonances must be treated separately. To formulate this special decay amplitude, one makes use of the λ-parameter, the characteristic slope of the $\omega \rightarrow \pi^+\pi^-\pi^0$ Dalitz plot, again (compare equation (3.17) in Section 3.4.2). In order to distinguish this quantity from the helicities appearing in this context, the Dalitz plot slope will be denoted as $\tilde{\lambda}$ in the following formula. A single decay plane for all daughter particles of the ω decay can be defined. The normal vector to this decay plane, $\vec{n}$, is described in terms of the Euler angles ϑ_n, φ_n and $\gamma_n := 0$ in the helicity frame of the ω. With $\mu = \vec{J}_\omega \cdot \vec{n}$ being the projection of the ω mesons spin to the direction of $\vec{n}$, the amplitude reads as

$$A^{J_\omega}_{\lambda_\omega}(\omega \rightarrow \pi^+\pi^-\pi^0) = \sqrt{\frac{3}{4\pi}} \cdot D^{1*}_{\lambda_\omega \mu}(\varphi_n{,}\vartheta_n{,}0) \cdot \tilde{\lambda}_\mu, \tag{4.14}$$

where only the case $\mu = 0$ is allowed for this decay [29].

4.4 The Dynamical Part of the Amplitude

While for the model independent analysis the dynamical (or energy dependent) part of the amplitudes was omitted, the K-matrix formalism was employed for the model dependent analysis. A relativistic Breit-Wigner parametrization was used for tests of the model dependent PWA, as well as for the measurement of the $\eta_c \to \omega\omega$ branching fraction. Both will be presented briefly in this section.

4.4.1 Centrifugal Barrier Factors

The invariant mass of the ω meson pair extends from the $\omega\omega$ production threshold up to approximately the mass of the J/ψ, because the energy of the radiative photon is not limited to a minimal value[1]. The observed line shape of a resonance is known to be distorted for small invariant masses at the beginning of the phase space, which here corresponds to small momenta of the ω mesons in the rest frame of the decaying resonance. The distortion originates from a limitation of the maximum contributing angular momentum L for slowly moving daughter particles. It is described in [1], that the decay particles can not generate sufficient angular momentum to conserve the spin of the decaying resonance, when the impact parameter is close to or smaller than the "meson radius" denoted as R. When dealing with decays of (light) mesons, this radius is usually chosen to be $R = 1\,\mathrm{fm}$, while for the decays of heavier resonances like charmonia, a somewhat smaller value of $\approx 0.3\,\mathrm{fm}$ is commonly used [40][41]. The latter value has also been used in this analysis, however [41] reports, that the distortion of the resonances line shape does not strongly depend on the parameter R.
The L-dependent distortion of the line shape is described by the *Blatt-Weisskopf barrier factors* (BWK factors), which depend on the linear momentum q of the daughter particles, as well as the scale parameter $q_R = \frac{\hbar c}{R}$. Using the definition $z = (q/q_R)^2$, the BWK factors of the form $b_L(z)$ are listed in Table 4.3 for angular momenta up to $L = 4$, which is the maximum value of L occuring in this analysis. The barrier factors are normalized to 1, when q reaches the value q_R. Furthermore, for a resonance with a given pole mass m_0, the nominal momentum q_0 of the daughter particles in the rest frame of the resonance can be calculated, so that barrier factors of the form

$$B_L(q,q_0) = \frac{b_L(q)}{b_L(q_0)} \tag{4.15}$$

are finally used. Apart from the distortion of a resonance (X) line shape due to its decay BWK factors, also the barrier factors relevant for the decay of the mother resonance (J/ψ), in which the resonance X is produced, have an influence on the line shape. However, this effect is important for large invariant masses of the $\omega\omega$ system, where the momentum of X gets small. For these production BWK factors, the breakup momentum q_0 is chosen to coincide with the $\omega\omega$ mass threshold.
The BWK barrier factors are needed to describe the varying shape of the "object" under study, thus they are related closely to the *form factor*. For the study of the η_c (see Section 5), a different description of the line shape was used, due to the knowledge on the transition form factor relevant for the radiative decay of the J/ψ, in which the η_c

[1] However, the energy threshold of the electromagnetic calorimeter presents a technical limitation on the photon energy of $E_{\gamma,\mathrm{min.}} = 25$ MeV (valid for the barrel part of the EMC)

L	$b_L(z)$
0	1
1	$\sqrt{\frac{2z}{z+1}}$
2	$\sqrt{\frac{13z^2}{(z-3)^2+9z}}$
3	$\sqrt{\frac{277z^3}{z(z-15)^2+9(2z-5)^2}}$
4	$\sqrt{\frac{12746z^4}{(z^2-45z+105)^2+25z(2z-21)^2}}$

Table 4.3: Blatt-Weisskopf barrier factors for angular momenta up to $L = 4$ [42]

is produced. The energy dependence of this transition form factor however also shows a strong q^L dependence, which underlines the similarity to the BWK factors.
Both, the BWK factors for the decay as well as the production of resonances are implemented into the *PAWIAN* software. The decay barrier factors are incorporated into the parameterization of the dynamical part of the amplitude (e.g. the Breit-Wigner function, see next paragraph).

4.4.2 Breit-Wigner Parametrization

A simple form to parameterize the line shape of a resonance is given by the relativistic Breit-Wigner function, which can be written as

$$BW(m) = \frac{m_0 \Gamma B_L(q,q_0)}{m_0^2 - m^2 - i(\rho/\rho_0) m_0 \Gamma B_L^2(q,q_0)}. \tag{4.16}$$

The parameters m_0 and Γ denote the nominal mass and width of the resonance, the $B_L(q,q_0)$ stand for the normalized barrier factors introduced in Section 4.4.1 and ρ as well as ρ_0 describe the phase space factors, which are defined as

$$\rho(m) = \sqrt{\left(1 - \left(\frac{m_b + m_c}{m}\right)^2\right) \cdot \left(1 - \left(\frac{m_b - m_c}{m}\right)^2\right)} \tag{4.17}$$

and $\rho_0 = \rho(m_0)$, respectively. Here m_b and m_c are the masses of the two daughter particles of the resonance to be described. This parameterization in principle is only valid for isolated, non-overlapping resonances far from the thresholds of additional decay channels.
While for the model independent PWA no parametrization for the energy dependence of the amplitudes is necessary, the η_c resonance is described with a relativistic Breit-Wigner function for the extraction of the $\eta_c \to \omega\omega$ branching fraction. For these model dependent fits some modifications to the relativistic Breit-Wigner were used, to account for the radiative $M1$-transition. This parametrization is discussed in detail in Chapter 5.

4.4.3 K-Matrix Formalism

The situation for the model dependent analysis covering the full $\omega\omega$ mass range is somewhat more complicated. Here it is to be expected that multiple overlapping resonances occur, and maybe even contributions to the observed intensity which originate from resonances below the $\omega\omega$ mass threshold. In this case, a description with multiple Breit-Wigner functions is not appropriate and a more complex formalism must be used. The K-matrix formalism provides sufficient features to describe overlapping resonances and even accounts for rescattering while at the same time unitarity is maintained. However, in practice the application of this formalism can be demanding, e.g. due to unknown coupling strengths of resonances to various final states. The strategy employed in this analysis will be discussed after a brief overview over the general principle of the K-matrix formalism and the necessary definitions. A detailed description of the K-matrix formalism can be found in [33] and [43].

The K-matrix formalism was originally developed to describe resonances in nuclear interactions, but its applicability in meson spectroscopy was quickly recognized. In general, the formalism describes two-body scattering processes of the form $a + b \to c + d$. The transition amplitude to find an initial state $|i\rangle$ in a specific final state $|f\rangle$ can be written as

$$S_{fi} = \langle f|S|i\rangle, \tag{4.18}$$

where S denotes the scattering operator. Since the incoming and outgoing intensity must be conserved (*conservation of probability*), one can deduce that the scattering operator is *unitary*, thus fulfilling the relation $SS^\dagger = S^\dagger S = \mathbb{1}$, with $\mathbb{1}$ being the identity operator. One may now separate the S matrix into a part that describes the probability that the initial and the final state do not interact at all ($\mathbb{1}$), and a term that describes the interaction (T) as

$$S = \mathbb{1} + 2iT. \tag{4.19}$$

To obtain a simple unitary parameterization of the S matrix, one can now introduce the K-operator, or the *K-matrix*, defined as

$$K^{-1} = T^{-1} + i\mathbb{1}. \tag{4.20}$$

This newly defined operator is hermitian ($K = K^\dagger$) and from time reversal invariance of S and T one can conclude, that the K-operator must be symmetric and the corresponding K-matrix can be chosen to be real and symmetric (cf. [33]). The T- and K- operators are a priori not Lorentz invariant due to their dependence on the phase space factors $\rho(m)$ (cf. equation 4.17) of the two-body initial and final states. To obtain Lorentz invariant operators, the phase space factors may be separated from T and K as

$$T_{ij} = \sqrt{\rho_i}\hat{T}_{ij}\sqrt{\rho_j} \quad \text{and} \quad K_{ij} = \sqrt{\rho_i}\hat{K}_{ij}\sqrt{\rho_j}. \tag{4.21}$$

The ρ_i denote here the diagonal elements of a $n \times n$ matrix for n open channels, which contains the phase space factors of the form given in equation (4.17). Considering a number of resonances (referred to with the index α) that should be described in a K-matrix, with the nominal masses m_α, the elements of the K-matrix can be written as

$$\hat{K}_{ij} = \sum_\alpha \frac{g_{\alpha i} g_{\alpha j} B_L^{\alpha i}(q_i,q_{\alpha i}) B_L^{\alpha j}(q_j,q_{\alpha j})}{m_\alpha^2 - m^2} + c_{ij}. \tag{4.22}$$

The indices i and j represent the different channels of the initial and final state, $B_L(...)$ denotes the normalized BWK barrier factor as defined in equation (4.15) and the so called g-factors, $g_{\alpha i}$ describe the coupling strength of the resonance α to the channel i. It is allowed to add a polynomial term c_{ij} to every K-matrix element without violating unitarity, which represents non-resonant background (not experimental background!). The g-factors can be expressed in terms of the partial widths $\Gamma_{\alpha i}$ of a resonance α in the channel i and its mass m_α as

$$g_{\alpha i} = \sqrt{\frac{m_\alpha \Gamma_{\alpha i}}{\rho_i(m_\alpha)}}. \tag{4.23}$$

To be applicable for analyses like the one presented here, the K-matrix formalism must be extended from a description of two-body scattering to the production of resonances. This procedure is reported in [43] and is based on the replacement of the scattering amplitude $\hat{T}$ by the Lorentz invariant transition amplitude

$$\hat{F} = (\mathbb{1} - i\rho\hat{K})^{-1}\hat{P}. \tag{4.24}$$

In this approach the production vector $\hat{P}$ is defined as

$$\hat{P} = \sum_\alpha \frac{\beta_\alpha g_{\alpha i} B_L^{\alpha i}(q,q_{\alpha i})}{m_\alpha^2 - m^2}, \tag{4.25}$$

with $\beta_\alpha = \tilde{\beta}_\alpha \sqrt{m_\alpha \Gamma_\alpha}$. The parameter $\tilde{\beta}_\alpha$ represents the production strength of a resonance α and is in general a (complex) free parameter in the fit. When only a single resonance and its decay into a single final state are considered, the parameterization reduces to a simple relativistic Breit-Wigner function.

4.4.4 Determination of T-Matrix Pole Parameters

It is of practical importance to mention here, that the poles of the K-matrix are not identical with those of the T-matrix, which represent the physically observable poles of resonances in terms of their mass and width. The pole parameters (m_α and Γ_α) of the K-matrix can not easily be transformed into T-matrix pole parameters, instead a numerical solution was employed here: For given K-matrix parameters, the corresponding T-matrix is evaluated at various points of the complex energy plane, based on the definition of the complex energy as $E = m - i(\Gamma/2)$. [44] The *PAWIAN* package provides a tool, with which this complex plane is scanned with a given step size, and pole positions m and corresponding widths Γ of found T-matrix poles are reported. This method was used for all K-matrix parameterizations discussed in Section 4.8.

While a description utilizing the K-matrix is in general to be preferred over a parameterization based on multiple Breit-Wigner functions, various difficulties arise while performing the analysis: It is not easily possible to release the pole masses and widths of single resonances as free fit parameters when the K-matrix parameters are chosen, since both the position of the pole, as well as its g-factor can possibly influence the corresponding T-matrix pole positions and widths of all other resonances described in the same K-matrix. Similarly, when fixing the K-matrix pole mass of a resonance while at the same time the g-factor is varied, the corresponding T-matrix pole might be shifted. The same argument is valid for the case, when an additional resonance should be considered or is dropped from an existing K-matrix parameterization. This circumstance requires an iterative approach to obtain a reasonable description of the data and is much more time consuming than the handling of various Breit-Wigner functions. Additionally, most resonances couple to a number of different final states, which in principle all must be considered in the corresponding K-matrix parameterization, to maintain unitarity and conserve the total width of the resonance. Here the problem arises, that for poorly measured states neither the total width, nor most (or all) of the g-factors are known. Due to this severe limitation, in this analysis a coupling only to the $\omega\omega$ channel is considered. Although this description is not fully correct, it is feasible and at least provides a much better representation of the distorted line shapes for overlapping resonances, than a description using Breit-Wigner functions.

4.5 Differential Cross Section and Likelihood Function

Taking into account the full decay tree, starting from the J/ψ down to the final state pions, the differential cross section must contain the decay amplitudes of the processes $J/\psi \to \gamma X$, $X \to \omega\omega$ and finally the three-body decays of both ω mesons into $\pi^+\pi^-\pi^0$. The differential cross section is given by

$$\frac{d\sigma}{d\Omega} \propto w = \sum_{\lambda_\gamma=-1,1} \sum_{M=-1,1} \left| \sum_X \left[\sum_{\lambda_X} \tilde{A}^{J_X M}_{\lambda_\gamma \lambda_X}(J/\psi \to \gamma X) \cdot \sum_{\lambda_{\omega_1}\lambda_{\omega 2}} \tilde{A}^{J_X \lambda_X}_{\lambda_{\omega_1}\lambda_{\omega_2}}(X \to \omega_1\omega_2) \right.\right.$$
$$\left.\left. \cdot A^{J_{\omega_1}}_{\lambda_{\omega_1}}(\omega_1 \to \pi_1^+\pi_1^-\pi_1^0) \cdot A^{J_{\omega_2}}_{\lambda_{\omega_2}}(\omega_2 \to \pi_2^+\pi_2^-\pi_2^0) \right] \right|^2 . \tag{4.26}$$

Here, $d\Omega$ denotes an infinitesimally small element of the phase-space, and the function w is the transition probability from the initial to the final state. The outer (incoherent) sum runs over the helicities of all final state particles as well as the alignment of the initial state particle, but since all pions are spin zero particles, the corresponding helicities are not defined and do therefore not appear in the incoherent summation. The leftover summation indices are the helicity of the radiative photon, λ_γ, as well as the z-component of the spin of the J/ψ. Furthermore, for all intermediate resonances X, a coherent summation over the helicities of the resonance (λ_X) as well as its daughter particles (λ_{ω_1},λ_{ω_2}) is performed. Special attention must be payed to the decay amplitudes of the J/ψ and those of an intermediate resonance X, denoted with $\tilde{A}^{J_X M}_{\lambda_\gamma\lambda_X}$ and $\tilde{A}^{J_X\lambda_X}_{\lambda_{\omega_1}\lambda_{\omega_2}}$ in equation (4.26): The placeholder $\tilde{A}$ is in the first case replaced with the helicity amplitude for the radiative decay of the J/ψ as defined in equation (4.11), and an expansion into the radiative multipole schema is performed according to equation (4.12). Additionally, the BWK-factor for the production of the resonance X is added. This BWK-factor is in principle dependent on the orbital angular momentum L, which is not defined in the radiative multipole schema. Therefore, the minimum value $L_{\min}$ of the orbital angular momentum for a given resonance X was chosen here. In case of a pseudoscalar resonance, this would be $L_{\min}(0^{-+}) = 1$ for example. The placeholder $\tilde{A}$ for the decay amplitudes of the resonance X is first replaced with the generic helicity amplitude defined in equation (4.8), before an expansion into the LS-system according to equation (4.13) is performed. In the case of a model dependent PWA fit, the dynamical part of the amplitude, here denoted with $\tilde{F}_L$, has to be considered here as well. $\tilde{F}_L$ can be replaced either with a Breit-Wigner function, or with the F-vector in case the K-matrix formalism is used for the description of the decay dynamics. In both cases, an explicit dependency on the orbital angular momentum L is apparent, since both parameterizations include the L-dependent BWK-factors for the decay of the resonance X. The decay amplitudes of the two ω mesons are inserted as defined in equation (4.14). After performing all replacements and expansions, the function w reads as

$$\begin{aligned} w = \frac{3}{(4\pi)^2} \sum_{\lambda_\gamma=-1,1} \quad \sum_{M=-1,1} \Bigg| \sum_X \\ & \Bigg[\sum_{\lambda_X} \sum_{J_\gamma} \sqrt{2J_\gamma+1} d^1_{M,\lambda_\gamma-\lambda_X}(\vartheta) \\ & \quad \langle J_\gamma,\lambda_\gamma;1,\lambda_X-\lambda_\gamma|J_X,\lambda_X\rangle a^1_{J_\gamma} B_{L_{\min}}(q_X,q_{X,0}) \\ & \cdot \sum_{\lambda_{\omega_1}\lambda_{\omega_2}} \sum_{L,S} \sqrt{2L+1} D^{J_X *}_{\lambda_X,\lambda_{\omega_1}-\lambda_{\omega_2}}(\varphi,\vartheta,0) \\ & \quad \langle L,0;S,\lambda_{\omega_1}-\lambda_{\omega_2}|J_X,\lambda_{\omega_1}-\lambda_{\omega_2}\rangle \\ & \quad \langle s_{\omega_1},\lambda_{\omega_1};s_{\omega_2},-\lambda_{\omega_2}|S\lambda_{\omega_1}-\lambda_{\omega_2}\rangle \cdot \alpha^{J_X}_{LS} \cdot \tilde{F}_L \\ & \cdot D^{1*}_{\lambda_{\omega_1},0}(\varphi_{n_1},\vartheta_{n_1},0) \cdot \tilde{\lambda}_{\mu_1} \\ & \cdot D^{1*}_{\lambda_{\omega_2},0}(\varphi_{n_2},\vartheta_{n_2},0) \cdot \tilde{\lambda}_{\mu_2} \;\Bigg]\Bigg|^2 . \end{aligned} \tag{4.27}$$

The goal is, to fit the probability function w to the selected data, by varying the free parameters given by the complex amplitudes $a^1_{J_\gamma}$, $\alpha^{J_X}_{LS}$ and $\tilde{\lambda}_\mu$, as well as g-factors/widths and pole masses, if applicable. Each one of these amplitudes can be expressed by a real magnitude and a phase, yielding two distinct fit parameters per amplitude. In fact, some of these parameters, especially phases, can be fixed by applying dependency relations. For all hypotheses *unbinned maximum likelihood* fits were performed. The likelihood function is given by [29]

$$\mathcal{L} \propto n_{\text{data}}! \cdot \exp\left(-\frac{(n_{\text{data}}-\overline{n})^2}{2n_{\text{data}}}\right) \prod_{i=1}^{n_{\text{data}}} \frac{w(\vec{\Omega}_i,\vec{\alpha})}{\int w(\vec{\Omega},\vec{\alpha})\epsilon(\vec{\Omega})d\Omega}. \tag{4.28}$$

In this formula, n_{data} denotes the number of data events, $\vec{\Omega}$ are the phase-space coordinates and $\vec{\alpha}$ the complex fit parameters. The function $w(\vec{\Omega},\vec{\alpha})$ is the transition probability function given in equation (4.26) and $\epsilon(\vec{\alpha})$ is the acceptance and reconstruction efficiency at the position $\vec{\Omega}$. Furthermore, $\overline{n}$ is defined as

$$\overline{n} = n_{\text{data}} \cdot \frac{\int w(\vec{\Omega},\vec{\alpha})\epsilon(\vec{\Omega})d\Omega}{\int \epsilon(\vec{\Omega})d\Omega}. \tag{4.29}$$

Due to the exponential term, in which $\overline{n}$ appears, this likelihood function a so called *extended likelihood* function. Using this form, a normalization is achieved, so that the mean weight of one event is approximately 1 after the likelihood has been maximized. The function w is interpreted here as a probability density function and the corresponding probabilities for all events are multiplied to obtain the total probability. The denominator in the product in equation (4.28) contains a phase-space integral for normalization, which is approximated using the phase space distributed MC sample. For this procedure it is important that the MC sample, which was introduced in Section 3.1, is propagated through the BESIII detector, reconstructed and selected with the same cuts as the data sample. This way the geometrical acceptance and selection efficiency is correctly considered in the normalization integrals within in the likelihood-function in all dimensions of the phase-space simultaneously.

The best description of the data sample is reached upon maximization of the likelihood $\mathcal{L}$. For technical reasons, eqn.(4.28) is logarithmized, so that the product is transformed into a sum that can be handled more easily numerically. Finally, the event weights Q_i obtained from the Q-factor method are also included in the likelihood function and a negative sign is added to the logarithmized function, so that commonly used minimizers and algorithms, in this case MINUIT2, can be used.

The negative log-likelihood function, that is actually minimized, now reads as

$$-\ln\mathcal{L} = -\sum_{i=1}^{n_{\mathrm{data}}} \ln(w(\vec{\Omega},\vec{\alpha})\cdot Q_i) + \left(\sum_{i=1}^{n_{\mathrm{data}}} Q_i\right)\cdot \ln\left(\frac{\sum_{j=1}^{n_{\mathrm{MC}}} w(\vec{\Omega},\vec{\alpha})}{n_{\mathrm{MC}}}\right) + \frac{1}{2}\cdot\left(\sum_{i=1}^{n_{\mathrm{data}}} Q_i\right)\cdot\left(\frac{\sum_{j=1}^{n_{\mathrm{MC}}} w(\vec{\Omega},\vec{\alpha})}{n_{\mathrm{MC}}} - 1\right)^2 . \tag{4.30}$$

4.6 Spin Alignment of the ω Mesons

In this section the spin alignment of the ω mesons in the decay $X \to \omega\omega$ is studied as a motivation for performing a full partial wave analysis, including the decay of the ω mesons. The goal of the partial wave analysis is, to extract the contributions to the $\omega\omega$ system and to possibly identify these contributions with resonances. Apart from the observed intensity and the angular distributions of intermediate resonances, the polarization observables of the ω mesons contain valuable information on their production process as well. The polarization observables can be described by the spin density matrix (SDM) ρ, which is Hermitian and has a trace of $\mathrm{Tr}(\rho) = 1$. A detailed description of the SDM and its features is given e.g. in [45]. For the purpose of this thesis, only the most important information on the SDM of the ω mesons shall be briefly noted.

The spin density matrix for a spin 1 particle, like the ω meson, contains 3×3 complex elements, which are denoted as $\rho_{\lambda_i\lambda_j}$. Here, λ_i and λ_j represent possible helicities of the particle. Now the two distinct properties *polarization* and *alignment* of the particle under study can be defined: The ω meson is said to be *polarized*, when $\rho_{11} \neq \rho_{-1-1}$, while it is called *aligned* when $\rho_{11} = \rho_{-1-1} \neq \rho_{00}$. Since the trace of the matrix must be equal to one, the ω meson is said to be *fully aligned* when ρ_{00} vanishes, while a value of $\rho_{00} = \frac{1}{3}$ means no alignment. In general, the values of the nine elements of the SDM depend on the chosen decay frame. Here, the helicity system of the corresponding ω meson is used. Due to the fact that the intermediate resonances decaying to $\omega\omega$ are expected to be unpolarized and additionally the decay channel under study is parity conserving, the complete SDM can be expressed by only four parameters (three real parts and one imaginary part). In this case, three of the four parameters can be obtained from the azimuthal and polar angular decay distributions of the corresponding ω meson. An analytical form of the dependence between the three parameters and the ϑ and φ decay angles is given in [45]. The ρ_{00} element, and in the case of zero polarization also the ρ_{11} and ρ_{-1-1} elements[2], only depend on ϑ, thus the relation

$$W(\cos(\vartheta)) = \frac{3}{4}\left((1-\rho_{00}) + (3\rho_{00}-1)\cdot\cos^2(\vartheta)\right) \tag{4.31}$$

is obtained after integration over φ.
The motivation for this study is the astonishingly different behavior of the ω alignment depending on the properties of the resonance from which it is produced. One can conclude the following restrictions on the possible alignment of the ω mesons from parity conservation and symmetry relations for identical particles in the decay $X \to \omega\omega$:

- $0^{-+} \to \omega\omega$: Both ω mesons are *fully aligned* (e.g. $\rho_{00} = 0$).
- $1^{-+} \to \omega\omega$: Both ω mesons show an alignment of $\rho_{00} = 0.5$.
- $0^{++} \to \omega\omega$: Both ω mesons are *not aligned* (e.g. $\rho_{00} = \frac{1}{3}$).

Figure 4.3a shows the angular distributions of the ω decay for the three cases listed above, extracted from the PAWIAN amplitude models for these three specific cases. One can clearly see the different shapes of the angular distributions, depending on the spin-parity of X. Fits to the generated distributions delivered exactly the expected values of ρ_{00} as listed above. For resonances of higher spin (e.g. 2^{-+}, 2^{++}), the situation quickly becomes much more complicated due to the larger number of possible amplitudes and therefore also possible helicities of the ω mesons. In these more complicated cases, no fixed value for the alignment can be derived and a mixture of various spin alignments might contribute. Of course the quantum numbers of an intermediate resonance X cannot be unambiguously deduced from the shape of the decay angular distribution. However this study shows clearly, that the ω decay contains important information concerning the quantum numbers of X and thus should definitely be considered in the PWA.
Finally, the ρ_{00} element of the SDM was extracted for the ω mesons in 75 MeV wide bins of the invariant $\omega\omega$ mass by fitting the function given in equation 4.31 to the efficiency corrected angular decay distributions. Figure 4.2 shows the angular distribution for one ω meson in four different mass bins as an example. The shape of the distribution, and therefore the alignment of the ω meson, is quite different in these four mass bins: All distributions show a non-zero alignment, while the alignment in the distribution corresponding to the mass of the η_c (Figure 4.2, lower right plot) is even compatible with $\rho_{00} = 0$ (=*fully aligned*).
The value of ρ_{00} is shown in dependence of $m(\omega\omega)$ in Figure 4.3b. Due to the fact that the two ω mesons are identical particles the extracted alignment must be the same for both particles. Since the errors in Figure 4.3b are derived from the one-dimensional fits and therefore are purely statistical, the obvious difference between the red ("ω_1") and blue ("ω_2") can be regarded as a systematical error due to differences in the efficiency correction based on signal MC data.
The spin alignment of the ω mesons evolves with increasing mass of the $\omega\omega$ system: The alignment gets stronger around $m(\omega\omega) \sim 1.8\,\mathrm{GeV}/c^2$, which corresponds to the large enhancement visible in the $m(\omega\omega)$ mass. This could be a hint to the dominantly pseudoscalar character, which has already been observed by previous experiments [8], [9], [10]. Already

[2]This is given due to the relation $\rho_{11} = \rho_{-1-1}$ and together with $\mathrm{Tr}(\rho) = 1$ follows $\rho_{11} = \rho_{-1-1} = 1/2(1-\rho_0 0)$.

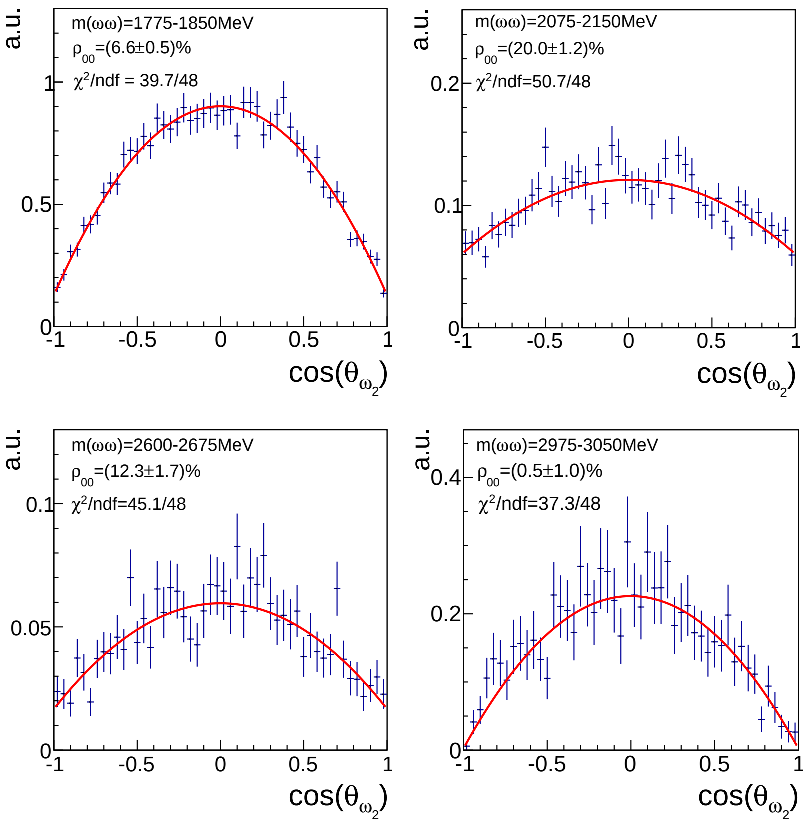

Fig. 4.2: Efficiency corrected angular decay distribution of one of the two ω mesons for four different bins of the invariant $\omega\omega$ mass. The red lines show the fits used to extract the ρ_{00} element of the spin density matrix.

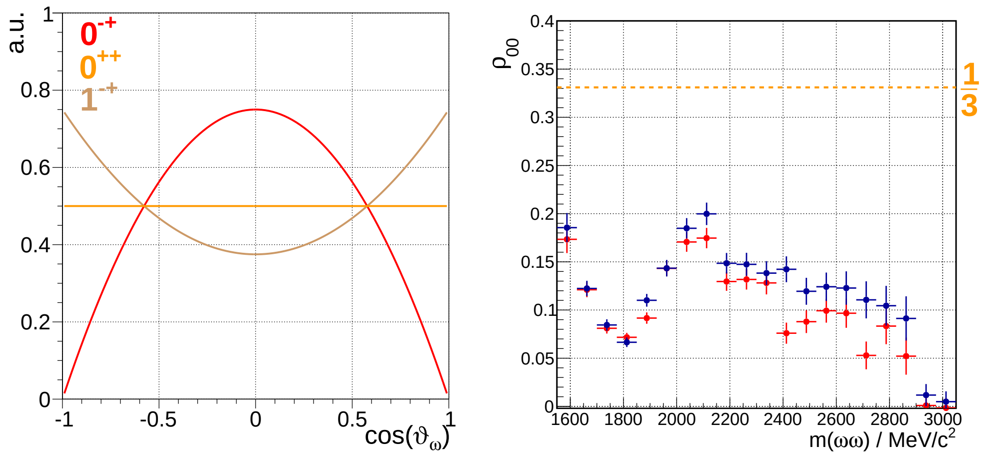

(a) (b)

Fig. 4.3: (a) Shapes of the ω decay angular distribution for decays of resonances with different J^{PC} quantum numbers into two ω mesons.
(b) ρ_{00} element of the spin density matrix for both ω mesons (red and blue markers) versus the invariant mass of the $\omega\omega$ system.

at this stage one can conclude, that a possible contribution of e.g. 1^{-+} waves should be small, since otherwise an alignment $\rho_{00} > \frac{1}{3}$ would be expected. It is also evident, that the ω mesons are fully aligned in the mass region of the η_c, which was expected for the reaction $0^{-+} \to \omega\omega$ and suggests a very small level of additional contributions in this mass region.

4.7 Model Independent PWA

To perform a full partial wave analysis, some reasonable assumptions about possibly contributing resonances have to be made and is is common practice to choose a base hypothesis as a starting point. In general this implies the choice of a model for the description of resonances. In some special cases, however it is possible to perform studies that are *model independent*: The decay $J/\psi \to \gamma\omega\omega$ is well suited for a model independent analysis, since intermediate resonances are expected to occur only in the $\omega\omega$ and not in the $\gamma\omega$ system. Therefore, the data can be divided into equally sized bins of the invariant $\omega\omega$ mass (see Section 4.7.1) in this case. Partial wave fits using several different hypotheses are performed for each mass bin individually, whereas the dynamical (mass dependent) parts of the amplitudes are omitted from all hypotheses. The hypothesis which yields the best result is identified for each bin using criteria from model selection theory (see Section 4.7.2). The intensity of the contributions from different J^{PC}-partial waves is finally extracted for the best hypothesis in each bin. The resulting $\omega\omega$ mass spectrum serves as an input for the choice of a base hypothesis for model dependent PWA fits.
In total 63 different hypotheses were considered for each mass bin. These hypotheses include combinations of one, up to a maximum of six different contributions (cf. equation (4.1) plus the 1^{-+} contribution) according to the possible quantum numbers of a resonance decaying into a pair of ω mesons. The simplest hypothesis contains just one 0^{-+} contribution, for which only one single parameter is subject to be fitted. For the most complex hypothesis with all six different J^{PC} contributions, the number of fit parameters increases to 33. In total 3843 single fits had to be performed for the full mass range which was subdivided into 61 individual bins.

4.7.1 Mass Binning

In order to determine the optimal size of the $\omega\omega$ mass bins, different boundary conditions must be observed: In principle the goal is, to choose the bins as fine as possible, so that the dynamical part of the amplitudes can be omitted. However, it is not useful to choose bins that are smaller than the mass resolution. Another limiting factor is the number of events, that are remaining in the single bins. The bins across the full $\omega\omega$ invariant mass are not equally populated, so the bin with the lowest content should still not contain less than a few hundred events to reach reasonable fit results. The $\omega\omega$ mass resolution was determined from the difference between generated and reconstructed phase space distributed MC events. This distribution is then fitted with a Crystal Ball function convoluted with a Gaussian function. Figure 4.4 shows the fitted mass difference distributions for three different regions of the invariant $\omega\omega$ mass. Since these distributions exhibit an asymmetric shape, the resolution was determined by two parameters, the full width at half maximum (FWHM) and the width of the Gaussian part (σ) of the single fits.

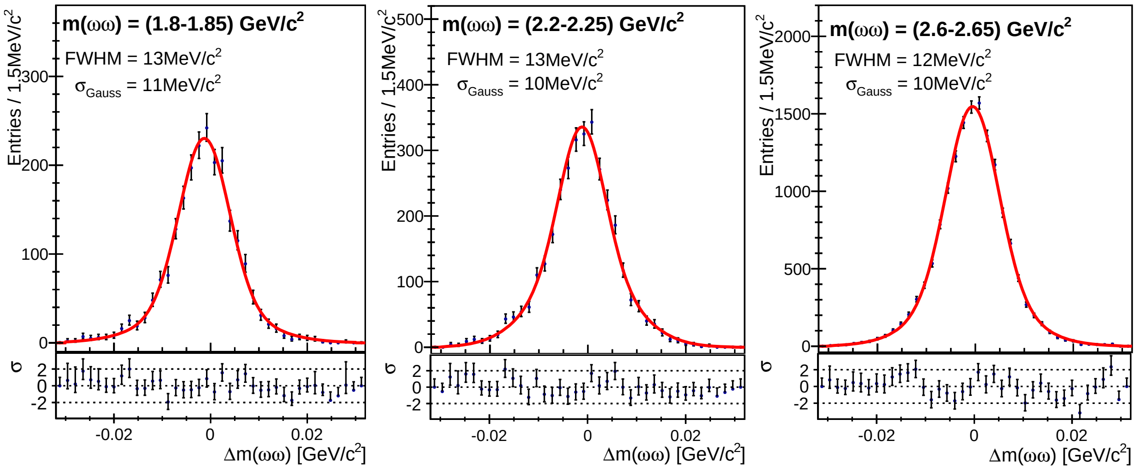

Fig. 4.4: Resolution of the $\omega\omega$ invariant mass for small, medium and large values of $m(\omega\omega)$ (left to right, exact values are given in the plots). The blue points in the large plots show the difference between generated and reconstructed $\omega\omega$ mass ($\Delta m(\omega\omega)$) fitted with a convolution of a Crystal Ball function with a Gaussian (red curve). The residuals of the corresponding fit are shown below each plot in units of the statistical error (σ).

The determined mass resolution varies slightly between approximately 10 and 13 MeV/c^2 over the full range of the $\omega\omega$ mass. The width of the mass bins has been chosen as 25 MeV/c^2. This ensures a sufficient number of events in each bin and at the same time is significantly larger than the mass resolution. Additionally, the chosen bin width is in the order of the width of the η_c meson, which is the most narrow structure that is visible in the $\omega\omega$ mass spectrum.

4.7.2 Selection of Hypothesis

In order to introduce as little bias as possible, each bin of the $\omega\omega$ mass is analyzed individually, without imposing any condition concerning the continuity of the solution. From all 63 hypotheses, one has to be selected, which best describes the data in the corresponding bin. Since the resulting likelihood is strongly correlated to the number of free parameters, its value is not a suitable quality factor to perform an absolute ranking of hypotheses. In most cases a better likelihood can be achieved by increasing the number of free parameters, i.e. choosing a more complex model. This effect potentially leads to *over-fitting* of the data and must be avoided.

Usually two fits with different hypotheses can be compared utilizing the *likelihood-ratio test*. This test provides the possibility, to calculate the significance of the improvement, that the more complex hypothesis gives in comparison to the simpler one. However, this implies, that one deals with so called *nested hypotheses*, i.e. the simple hypothesis is a subset of the more complex one. This assumption is not true for most of the cases considered here. To overcome this limitation, two different information criteria from model selection theory are used in this work. In general, these criteria are designed to balance the goodness-of-fit with the complexity of the selected model. In both cases, the criterion is dependent on the likelihood with an additional penalty term for the number of free parameters.

The first criterion is the *Bayesian Information Criterion* (BIC) and apart from the maximized value of the likelihood, $\mathcal{L}$, and the number of free parameters k, its value also depends on the number of data points n. It is defined as

$$BIC = -2 \cdot \ln(\mathcal{L}) + k \cdot \ln(n). \tag{4.32}$$

The penalty term rises logarithmically with the number of data points and therefore it can be expected, that this criterion in principle favors hypotheses with less parameters for large data samples. The BIC, as it is given in (4.32), is based on two additional assumptions. Firstly, the number of data points n must be much larger than the number of free parameters k as shown in [46]. This assumption can be fulfilled for all fits performed in this study. Secondly, the definition of the criterion is based on the assumption, that the *true* model (or at least some sort of *quasi-true* model) is among the collection of models that are tested against each other. The BIC criterion will asymptotically (with a probability of 1) select this *true* model [46]. Since we do not know the composition of the data in terms of contributing partial waves beforehand, this information is in general never available and thus cannot be taken into account. When testing different models with this criterion, the one with the lowest BIC value is preferred.

The second criterion is the *Akaike Information Criterion*, and the main difference to the BIC is a different penalty factor. It is defined as

$$AIC = -2 \cdot \ln(\mathcal{L}) + 2 \cdot k, \tag{4.33}$$

which is independent from the sample size n. In comparison to the BIC, the penalty term is much weaker, which increases the probability of over-fitting. In this work a slight modification of the AIC, denoted as $AICc$ is used. This incorporates an additional term that accounts for finite sample sizes and at the same time increases the penalty for additional parameters. In general, $AICc$ is preferred over AIC, since it delivers more realistic results and it converges towards AIC in the limit of large sample sizes. The $AICc$ is defined as

$$AICc = AIC + \frac{2k(k+1)}{n-k-1} = -2 \cdot \ln(\mathcal{L}) + 2 \cdot k + \frac{2k(k+1)}{n-k-1} \tag{4.34}$$

Even for this modified version, the penalty term is weaker than the one that is used in the BIC formula. Theoretical considerations show [46], that in general $AIC(c)$ should be preferred over BIC due to reasons of accurateness as well as practical performance. Moreover, the $AICc$ is *asymptotically optimal*, meaning that the model which gives the best representation of the data yields the lowest $AICc$ value. This implies, that the *true* model is not required to be within the set of considered hypotheses. In contrast to this, the BIC is *asymptotically true*, as it was mentioned above.

Given the strengths and weaknesses of the two criteria, the sum of both ($AICc$+BIC) was finally used to select the best hypothesis throughout this thesis. Since the absolute values of the information criteria cannot be interpreted easily, the differences of both criteria from the corresponding best values, namely $\Delta AICc_i + \Delta BIC_i = (AICc_i - AICc_{\text{best}}) + (BIC_i - BIC_{\text{best}})$ are presented (see e.g. Chapter 5) as proposed in [46].

4.7.3 Test of the Fitting Method Using a Toy MC Sample

To verify the performance of the model independent PWA approach, studies were performed using a toy MC sample. The same MC sample that served as the signal sample for the test of the *Q-factor* method described in Section 3.4.3 was utilized. As stated in Table 3.3, three resonances were included in a rough mass dependent PWA fit to the $\omega\omega$ signal region, namely $\eta(1760)$, η_c and $f_2(1910)$. In addition to the construction of the amplitudes shown above, the dynamical part of the amplitude, i.e. the mass dependent line shape, was parametrized using Breit-Wigner functions. In total 32000 events were generated with the amplitudes obtained from the fit. The generated sample contains correct angular distributions, which is an indispensable feature for a test of the model independent PWA (see Figure 4.5). The events were divided into bins of $40\,\mathrm{MeV}/c^2$ for this study. All 63 hypotheses containing one up to six different contributions with the J^{PC} quantum numbers listed in equation (4.1) plus the 1^{-+} contribution, were fitted to each of the 38 bins. It should be emphasized again, that no measures are taken to ensure the continuity of the obtained solution across the borders of the chosen bins to introduce as little bias a possible.

Figure 4.5 shows the decay angular distribution of the radiative photon, as well as the invariant mass of the $\omega\omega$ system of the generated toy MC sample. In this toy sample a large overlap between the f_2 meson and the dominant 0^{-+} component ($\eta(1760)$) was produced, to test the ability to separate the two waves. As an example, the decay angular distribution of the radiative photon is depicted, where a clear difference in shape between the spin zero and spin two contributions can be seen.

After performing all fits for each mass bin, the best hypothesis was selected using the BIC and the $AICc$ criterion alone, as well as the combined criterion. Figure 4.6 shows the obtained solutions, displayed in the invariant mass of the $\omega\omega$ system. It is clearly visible, that the main features of the MC sample are correctly identified by all three criteria. However, in the low-statistics bins as well as the tails of the f_2 resonance, the weaknesses of some of the ranking criteria become obvious. Figure 4.6a shows the components, when a ranking based on the BIC is used. The tails of the f_2 resonance are wrongly identified as 0^{++} contributions. This corresponds to the expected behavior, since the 0^{++} and 2^{++}

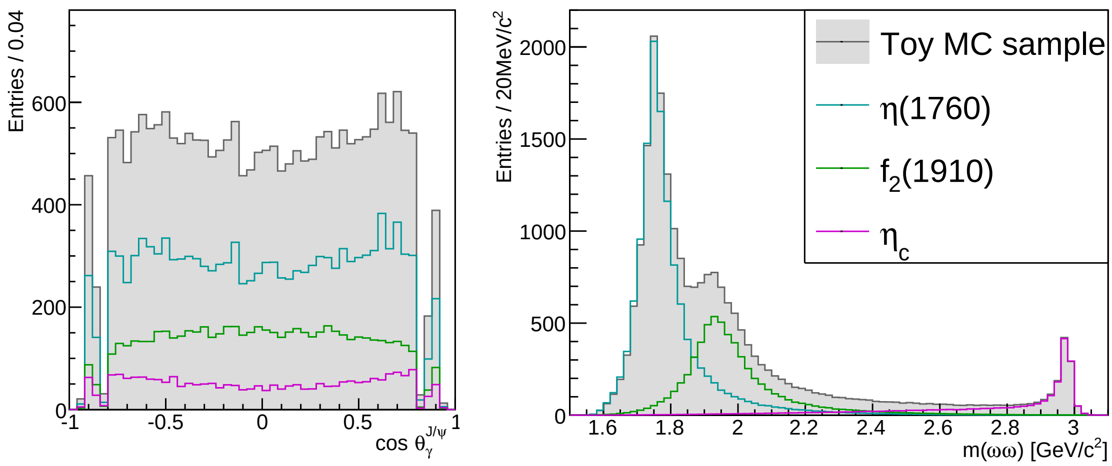

Fig. 4.5: Decay angular distribution of the radiative photon and $\omega\omega$ invariant mass of the generated toy MC sample.

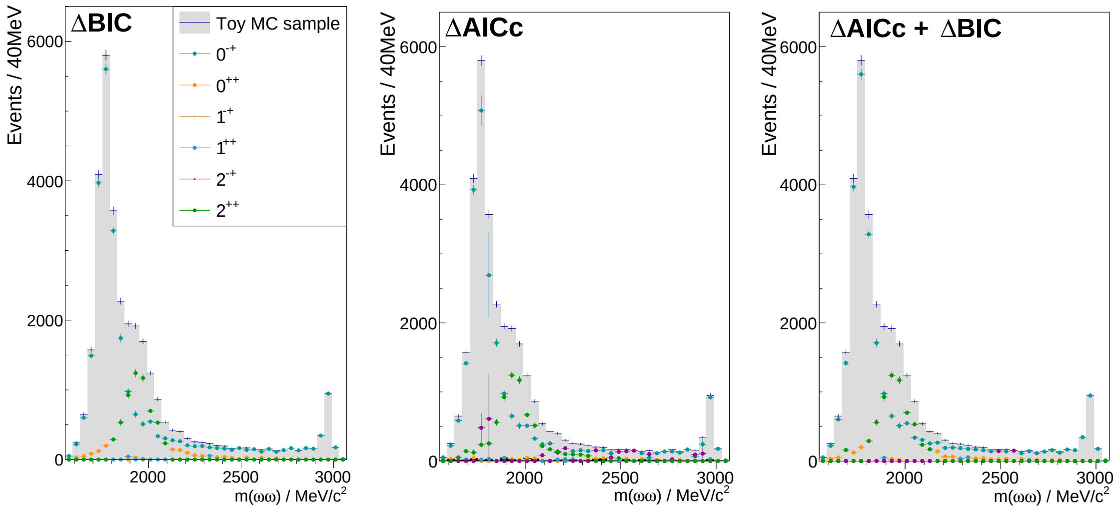

(a) (b) (c)

Fig. 4.6: Result of the model independent PWA applied to the generated toy MC sample. The three plots show the identified contributions in the $\omega\omega$ invariant mass, using a ranking of the hypotheses based on the ΔBIC (a), $\Delta AICc$ (b) or the combined criterion $\Delta AICc + \Delta BIC$ (c).

waves share a part of their amplitudes and the BIC favors hypotheses with a smaller number of free parameters. The opposite is the case for the $AICc$: Figure 4.6b shows the solution based on this ranking. Here, the f_2 resonance is identified almost perfectly, while a part of the dominant 0^{-+} wave is wrongly identified as a 2^{-+} contribution. Here, especially the low-statistics bins at $m(\omega\omega) \approx 2500\,\mathrm{MeV}/c^2$ suffer from this mismatch. The result confirms the expectation, that in general a more complex hypothesis is favored by the $AICc$.

Figure 4.6c shows the obtained solution using the combination of the two criteria. Mismatches in single bins can still be seen, but the solution is not any more biased in a single direction in terms of complexity of the hypotheses and the observed fluctuations are much less frequent then for the single criteria. Thus, the combination of both criteria was chosen to be applied to the selected data. For comparison, the contributions of all considered partial waves are displayed in single histograms in Figure 4.7 when a ranking by the combined $\Delta BIC + \Delta AICc$ criterion is applied.

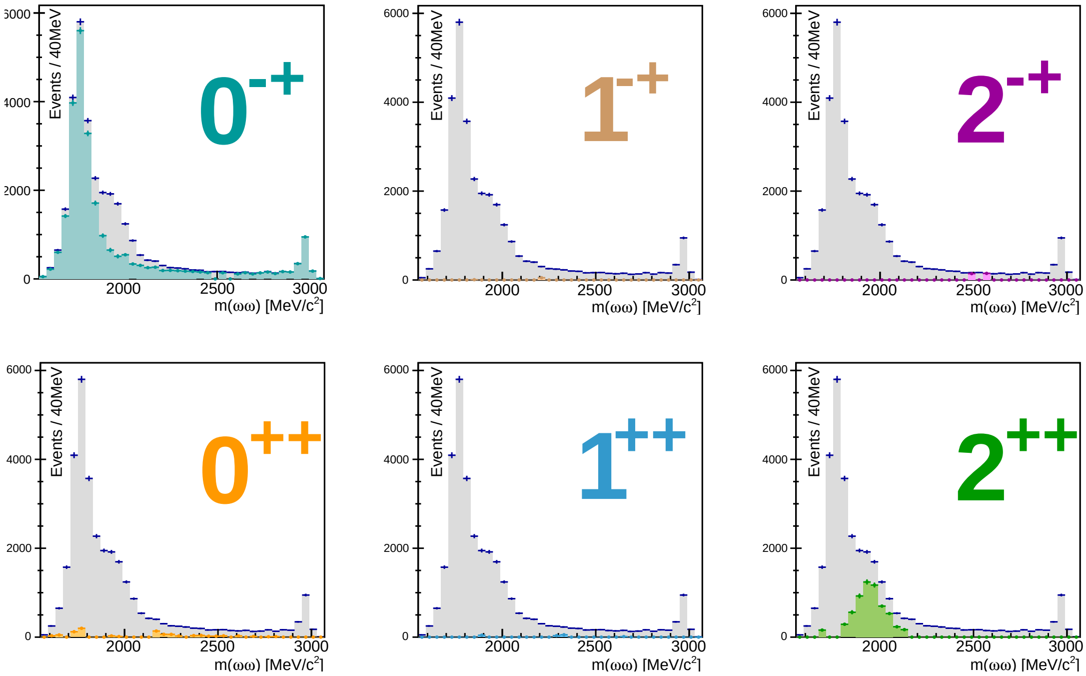

Fig. 4.7: Contributions of different partial waves obtained from the model independent PWA of a toy MC sample. Each plot shows the full generated $\omega\omega$ mass spectrum (gray shaded histogram with blue data points) as well as the contribution of one J^{PC} contribution in each of the $40\,\mathrm{MeV}/c^2$ wide bins after decomposition.

4.7.4 Results of the Model Independent PWA

All fits were performed for the selected and Q-weighted events. In the following, the result of the best fit for an arbitrarily chosen bin will be presented, to show the quality of the fit in a single bin. The results of the model independent PWA for the full $\omega\omega$ mass range are discussed and additionally examples from systematic studies concerning the reproducibility and stability of the fit results are presented.

Example: Fit of Data in a Single Mass Bin

The following results are presented for data in the mass bin $2000\,\mathrm{MeV}/c^2 < m(\omega\omega) < 2025\,\mathrm{MeV}/c^2$. After evaluating the results of all hypotheses using the $\Delta AICc + \Delta BIC$ criterion, the hypothesis containing a 0^{-+}, 0^{++} and a 2^{++} contribution was selected as the best one. The chosen bin contains 1357 events and is situated in the falling edge of the enhancement at threshold in the $\omega\omega$ mass. The largest contributions are given by the 0^{-+} and 2^{++} partial waves with each about 40 % of the total observed intensity. Furthermore, the 0^{++} partial wave yields a contribution of $\sim$ 20 %. Figure 4.8 shows angular distributions of both ωs, the characteristic λ distributions, as well as the azimuthal angle of the radiative photon and the invariant mass of the $\omega\omega$-system, in which the size of the chosen bin can be seen. The differences between the distributions for the two ω candidates are merely due to an arbitrary sorting of the reconstructed pions by their momentum and are thereby only an effect of the reconstruction.

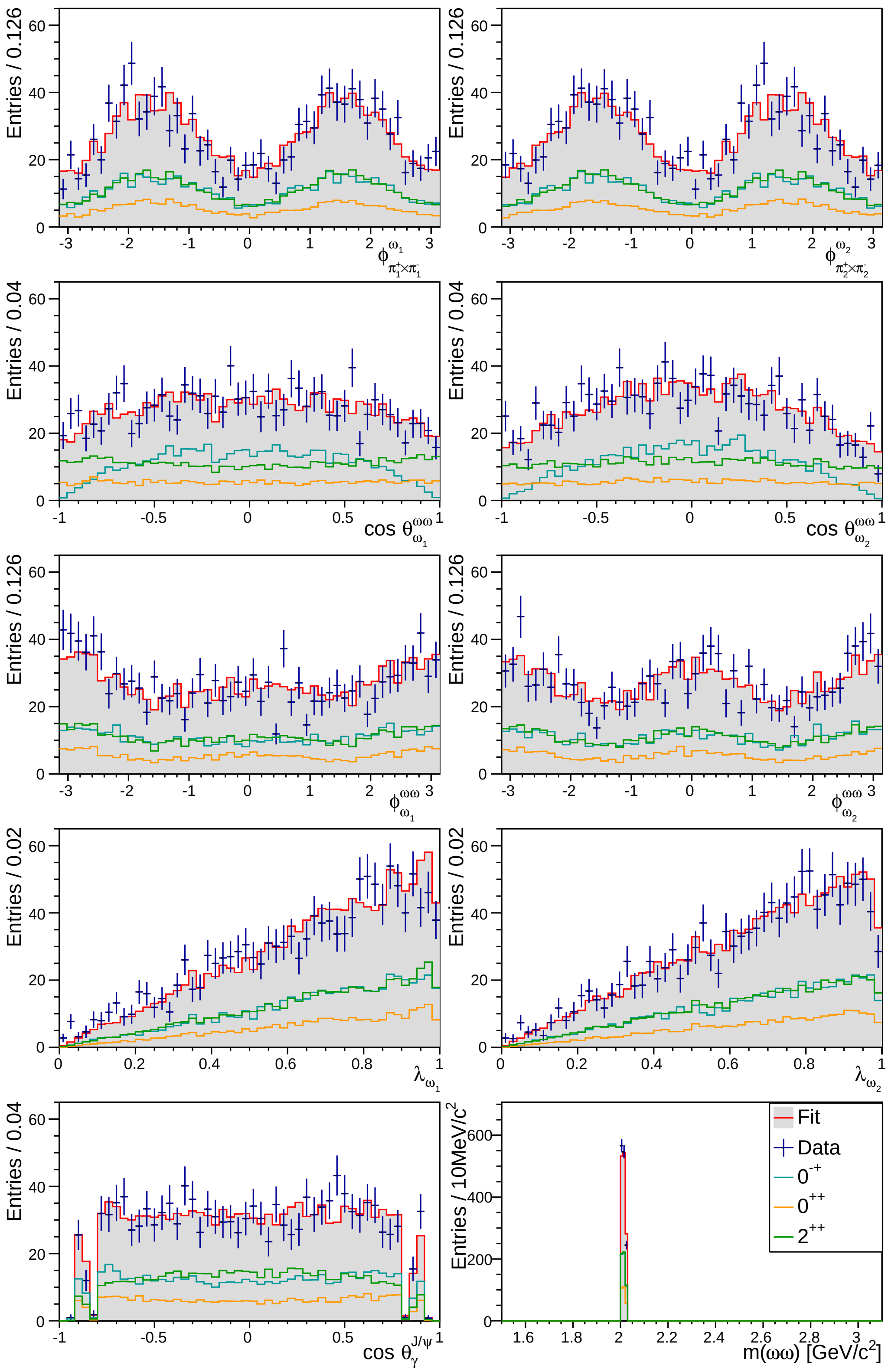

Fig. 4.8: Angular distributions of the production and decay of both ωs, $\cos(\theta)$ of the radiative photon and invariant mass of the $\omega\omega$ system. All plots show data in the mass bin $2000\,\mathrm{MeV}/c^2 < m(\omega\omega) < 2025\,\mathrm{MeV}/c^2$ together with the fit result and its decomposition into three contributing partial waves. The color code is given in the legend of the lower right plot.

A good agreement between fit and data is observed in all distributions. It should be noted here, that the fit projections shown in Figure 4.8 represent only a subset of the phase space dimensions and for the fit itself, the full decay tree from the initial (J/ψ) to the final state $(\gamma 6\pi)$, is considered. The hypothesis for this particular fit contains in total 17 free parameters.

Application to the Full Data Set

The data in all bins of the invariant $\omega\omega$ mass, which extends from 1550 MeV/c^2 up to 3050 MeV/c^2, was fitted with all 63 hypotheses, each. Afterwards, the selection of the best hypothesis based on the $\Delta AICc + \Delta BIC$ criterion was performed for each bin, as it was done for the toy MC sample before. The result, separated into single histograms for the contributions with different J^{PC} quantum numbers, is shown in Figure 4.9. The result allows for several different observations and interpretations. Firstly, single-bin-fluctuations are indeed observed, as it was expected from the study of the toy MC sample. However, in spite of the fluctuations, a strong, dominant pseudo-scalar contribution is observed over the complete $\omega\omega$ invariant mass range. Especially the enhancement at the $\omega\omega$ threshold is confirmed to have a predominantly pseudo-scalar character, as found by the earlier experiments [8] [9] [10]. The peak of this structure is located in the mass bin between 1775 MeV/c^2 and 1800 MeV/c^2,which is in accordance with the previous observations. The enhancement at $m(\omega\omega) \approx 2980$ MeV/c^2 is clearly identified as a $J^{PC} = 0^{-+}$ contribution. Further activity in the 0^{-+} partial wave is observed at ~ 2200 MeV/c^2 and in the higher mass region, where the fraction of the pseudo-scalar contribution with respect to the total observed intensity rises towards the end of the phase space.

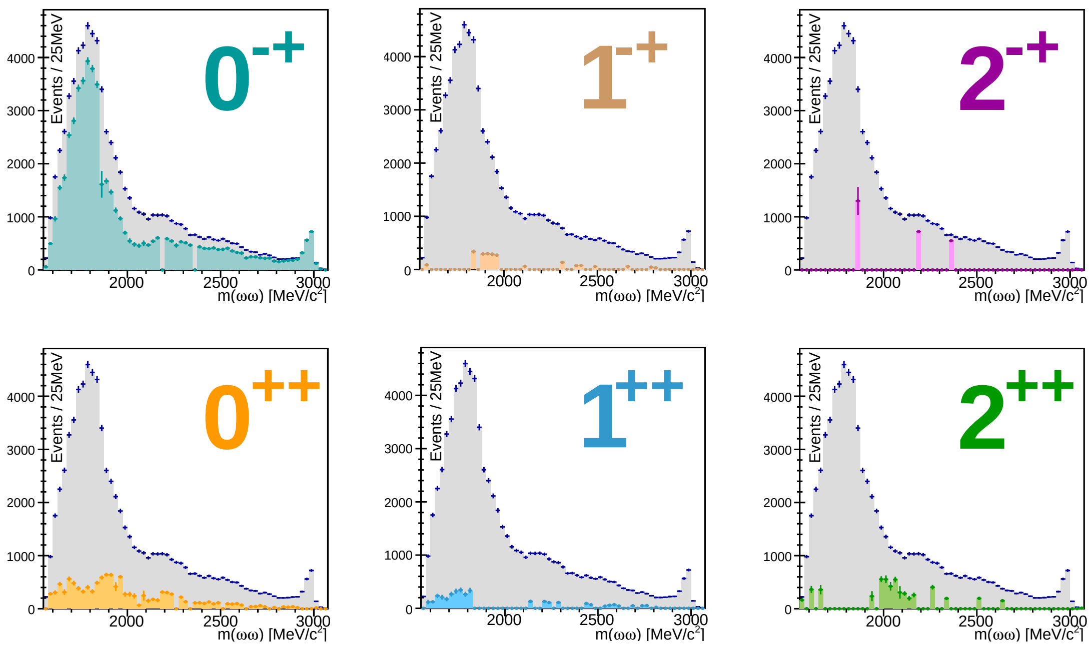

Fig. 4.9: Nominal result of the model independent PWA for the full selected data set. Blue dots with error bars represent the selected data, while the single colored histograms show the intensity of the corresponding partial waves.

The second largest contribution, which also shows an almost continuous behavior across the $\omega\omega$ mass range, is the scalar (0^{++}) component. Possible enhancements are observed at masses of about $1700\,\mathrm{MeV}/c^2$ and $1900\,\mathrm{MeV}/c^2$.

In several bins, a significant amount of the total intensity is identified to be originating from a tensor (2^{++}) component. The nominal fit result presented in Figure 4.9 shows only two disconnected bins at about $\sim 1600\,\mathrm{MeV}/c^2$ with a large 2^{++} contribution, the neighboring bins do not show any tensor component. At higher $\omega\omega$ masses ($\sim 2000\,\mathrm{MeV}/c^2$), a clear and broad tensor contribution is identified.

The nominal fit result shows a contribution of the 1^{++} partial wave in several of the bins in the lower mass region, which however abruptly drops to zero at a mass of about $1900\,\mathrm{MeV}/c^2$.

Very small contributions are observed in the spectrum of the spin-exotic 1^{-+} component, which could be explained by fluctuations due to the selection of the hypothesis. Furthermore, the pseudo-tensor component ($J^{PC} = 2^{-+}$) only shows contributions in single, isolated bins which could also be explained by fluctuations. Especially the bin $2175\,\mathrm{MeV}/c^2 < m(\omega\omega) < 2200\,\mathrm{MeV}/c^2$ shows a large 2^{-+} contribution, while at the same mass the 0^{-+} contribution unexpectedly drops to a very small value. Apart from this, only two other bins shows a significant 2^{-+} contribution, so that in total the pseudo-tensor component can be neglected.

Systematic Checks of the Model Independent PWA

To study possible numerical ambiguities, selected fits were performed multiple times with randomized start parameters. It was found, that all fits converge towards the same minimum and thus the same results are obtained. Especially the minimized negative likelihood and the most important observable for this study, the relative intensity of each partial wave in the $\omega\omega$ invariant mass, are not dependent on the choice of the start parameters and no numerical ambiguities are found. In this analysis it turns out, that the real difficulty lies in the selection of the correct hypothesis, rather than the performance of a single fit.

In order to determine, which of the features described in the previous paragraph may be accounted to fluctuations due to the hypothesis selection procedure, the borders of the mass bins have been shifted by half of the bin width and all fits were repeated. The result of this systematic test is shown in Figure 4.10. One can clearly see, that the contributions in the 1^{-+} and 2^{-+} spectra have changed drastically, while the global behavior of the other partial wave contributions remain stable and can still be identified. Completely different bins in the 2^{-+} distribution show a large contribution and the intensity in the corresponding bin of the 0^{-+} distribution drops to an unexpectedly low level.

As a last step, the two partial waves 1^{-+} and 2^{-+} were therefore removed from the set of considered contributions, which reduces the set of hypotheses from 63 to 15 per bin. Again, all fits were repeated and a ranking of the remaining hypotheses was performed using the $\Delta AICc + \Delta BIC$ criterion for each bin. The result (Figure 4.11) clearly shows, that by eliminating the 1^{-+} and 2^{-+} components, a continuous description of the 0^{-+} wave is achieved and no obvious fluctuations can be identified any more. Since the structures in the remaining partial waves are not significantly affected from this reduction of the set of considered partial waves, the 1^{-+} and 2^{-+} components will not be considered any further.

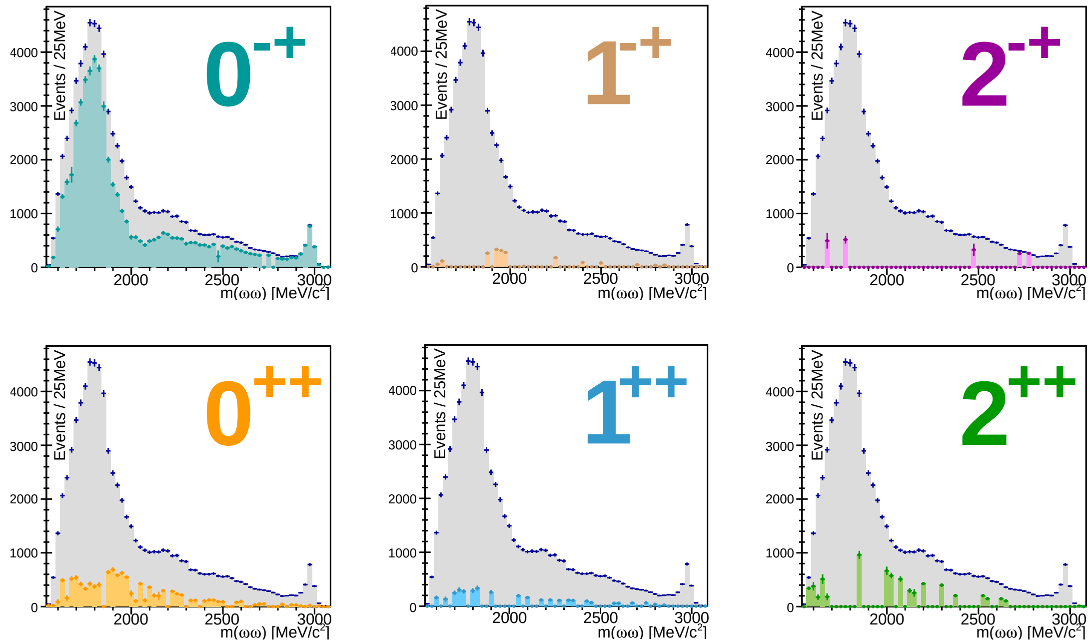

Fig. 4.10: Result of the model independent PWA for the full selected data set. Here the borders of all bins have been shifted by half the bin width to demonstrate the effect of single bin fluctuations.

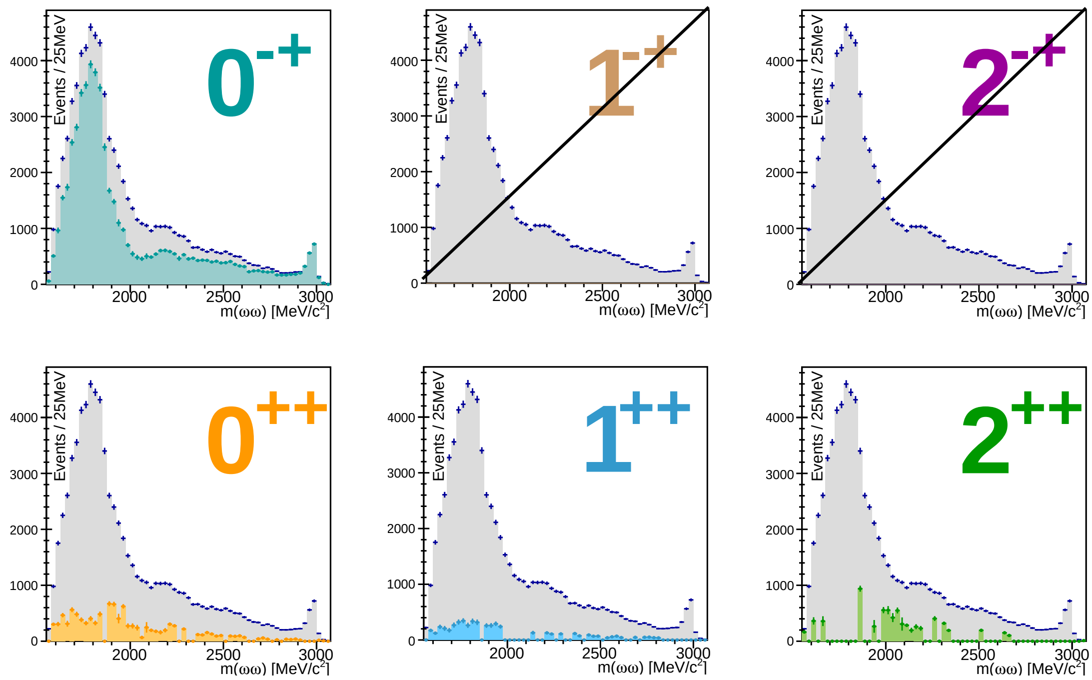

Fig. 4.11: Result of the model independent PWA for the full selected data set after reduction of the set of considered partial waves by two (1^{-+} and 2^{-+} are not considered any more).

Interpretation of the Results

The dominant pseudo-scalar enhancement at the $\omega\omega$ mass threshold was identified with the $\eta(1760)$ meson in earlier analyses. However, due to the large statistics available in this analysis, an asymmetry in the shape of the enhancement emerges. The asymmetry is characterized by a steep drop of the intensity at a mass of $m(\omega\omega) \approx 1850\,\mathrm{MeV}/c^2$, which surprisingly coincides with the $\overline{p}p$ mass threshold. It is not a priori clear, if a contribution of the $\eta(1760)$ is sufficient to describe the structure at the threshold, or if an additional contribution has to be considered to account for the asymmetric shape. Additionally, it is possible that the opening of the $\overline{p}p$ threshold is (partly) responsible for the observed shape of the structure. Another enhancement, which is visible in the 0^{-+} contribution at around $m(\omega\omega) \approx 2200\,\mathrm{MeV}/c^2$, may be associated with the $\eta(2225)$ meson. This state has previously only been observed in the $\phi\phi$ system, produced in radiative J/ψ decays [12],[47],[48]. Furthermore, the clear resonant structure at $m(\omega\omega) \approx 2980\,\mathrm{MeV}/c^2$ can be safely identified with the lowest lying charmonium state, the η_c, due to the absolutely dominant 0^{-+} contribution in the corresponding mass range. In general, the pseudo-scalar contribution exhibits a very complex behavior and it is possible that even more contributing resonances or threshold effects are responsible for the observed structures.

In previous analyses, also scalar contributions were found in the $\omega\omega$ system produced in radiative J/ψ decays. BESII found a significant contribution of the $f_0(1710)$ meson [10], which could be identified with the structure visible in the 0^{++} contribution located at $m(\omega\omega) \approx 1700\,\mathrm{MeV}/c^2$. Furthermore, the poorly known $f_0(2020)$ state was observed in the $\omega\omega$ system produced in central pp-collisions. This state has a large width of several hundred MeV and could explain a part of the structures around $2000\,\mathrm{MeV}/c^2$. Also the small structure at $\sim 2200\,\mathrm{MeV}/c^2$ could possibly be explained by a less established state, called $f_0(2200)$, which was observed in radiative J/ψ decays to K^+K^-, $K_s^0K_s^0$ and $\eta\eta$, as well as in pion-nucleon scattering.

The bins which show a significant 2^{++} contribution at $\sim 1650\,\mathrm{MeV}/c^2$ could be accounted to the presence of the $f_2(1640)$, which was also observed in the previous BESII analysis [10]. In the same analysis BESII also observed a large contribution of the $f_2(1910)$, which can not be directly identified here. However, the structure between $\sim 2000\,\mathrm{MeV}/c^2$ and $\sim 2200\,\mathrm{MeV}/c^2$ could be identified with a number of different f_2 states listed by the PDG. Candidates to be named here are the $f_2(2010)$, which was observed in its decays into a ϕ meson pair produced in pion-nucleon scattering, and the $f_2(1950)$, which has a large width of approximately $\sim 400\,\mathrm{MeV}/c^2$. One or more of these states could be identified with the bump visible at $\sim 2050\,\mathrm{MeV}/c^2$ in the 2^{++} contribution.

According to the PDG, no f_1 state is known in the mass region $> 1600\,\mathrm{MeV}/c^2$. It should be considered here, that a relatively broad resonance directly below the $\omega\omega$ threshold could, with a small branching fraction, decay into an ω meson pair, once the threshold opens up. This could explain the behavior of the 1^{++} contribution, but it is also possible that the intensity was wrongly accounted to this wave due to the difficulties in separating the three J^{++} contributions. In general, sub-threshold contributions should also be considered for all other partial waves.

In principle it is also desirable to extract the phases of the contributing partial waves together with their intensity per bin. The observation of phase-motions could be an additional indication for the presence of resonances and would be helpful for the interpretation of the results. Since only differences between phases for single amplitudes are meaningful, the need for a stable and omnipresent reference phase becomes apparent. In this case however, the only omnipresent contribution is the 0^{-+} wave, which shows a complex structure and most likely exhibits strong phase motions itself. Therefore, the interpretation of phase differences between other amplitudes and the 0^{-+} phase is not straight-forward.

4.8 Model Dependent PWA

The data was finally fitted in the full $\omega\omega$ mass range using a model dependent approach. As a first step, a series of fits was performed in which all possibly contributing resonances were parameterized using relativistic Breit-Wigner functions. It was found, that it is necessary to have strongly overlapping contributions especially from several 0^{-+} and 0^{++} resonances. Additionally, the fits required large interferences between the single contributions to adequately describe the data. Since in principle parameterizations using Breit-Wigner functions are only valid for isolated resonances, a more advanced formalism was employed for this analysis.

A description utilizing the K-matrix formalism with simplified assumptions was chosen. In a full K-matrix parameterization the coupling of all contributing resonances to all relevant final states has to be considered. Since only data corresponding to one final state is analyzed here, all other couplings (g-factors) have to be known for a full parameterization, which is unfortunately not the case for most of the resonances to be considered here. An additional benefit of a full parameterization is the correct description of the behavior at thresholds. For this analysis all K-matrix parameterizations were reduced to the g-factors responsible for the coupling to the $\omega\omega$ channel for simplification. This restriction in principle does not ensure unitarity, if the corresponding resonance can also couple strongly to other channels. However, this approach is still superior to the usage of simple Breit-Wigner functions. In order to obtain a better parameterization, a coupled channel analysis including all relevant decay channels would be necessary. The K-matrix pole masses and g-factors were chosen with the goal, to obtain T-matrix pole positions and widths close to the parameters listed in [1]. To achieve this, the T-matrix was scanned in the complex energy plane (see Section 4.4.4) and the corresponding pole positions were manually optimized.

4.8.1 Systematic Survey

A common procedure to start a model dependent PWA is to define a fixed base hypothesis, which does not describe the data perfectly, but serves as a reasonable starting point. Additional contributions are then added and removed from the hypothesis, while the changes of the fit quality are observed. If the new contribution leads to a significant improvement of the fit, it is kept and the hypothesis is extended. In this analysis however, the definition of such a base hypothesis has proven to be very difficult, since no obvious resonance shapes are visible, other than the η_c and some dominant 0^{-+} contribution at the beginning of the phase space. Any further contribution would have to be guessed, so in conclusion the hypothesis containing just the two pseudoscalar components $\eta(1760)$ and η_c was selected as a very basic hypothesis. Table 4.4 lists the likelihood and the values of the information criteria for this base hypothesis, Figure 4.12 shows the invariant mass of the $\omega\omega$ system and the corresponding fit projection. Already with this simple hypothesis the global shape of the spectrum can be fairly well reproduced, due to the usage of a

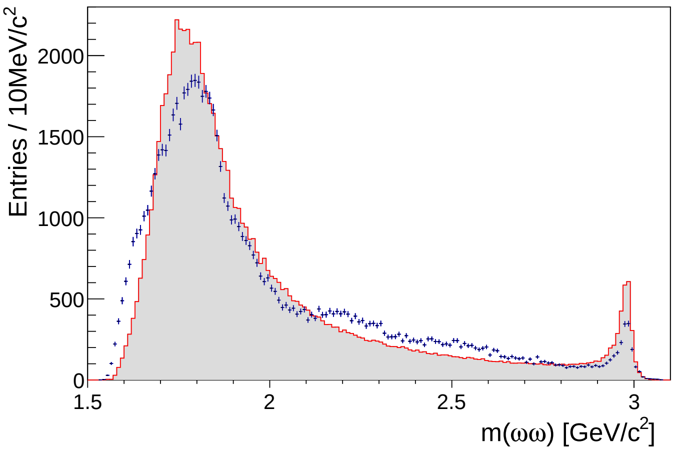

Fig. 4.12: Invariant $\omega\omega$ mass for data (blue) and the fit result (gray shaded) for the base hypothesis.

Hypothesis	log(LH)	$n.d.f.$	BIC	$AICc$
$\eta(1760)$,η_c	-51703.7	3	-103374	-103401

Table 4.4: Determined likelihood, $AICc$ and BIC values for the base hypothesis

K-matrix parameterization and the barrier factors for the production and decay of the two resonances.

Starting from this hypothesis, an iterative process for the identification of additional main contributions was started. It is to be expected, that in this preliminary stage, many additional contributions lead to a significant improvement of the fit result.

For the first set of hypotheses of the form $\eta(1760) + \eta_c + R$ in total 18 different resonances R with the quantum numbers $J^{PC} = 0^{-+}, 0^{++}, 1^{++}$ and 2^{++} were considered. These resonances were chosen based on the findings from the model independent PWA. Table 4.5 lists all of the considered resonances and the two base hypothesis components together with their nominal masses and full widths according to [1]. Several of the listed resonances have been observed in their decays into a vector meson pair before, some of them even in the $\omega\omega$ channel (cf. Table 4.5). In this analysis the poorly known $X(1835)$ state is treated as a pseudoscalar resonance, as it was determined in [49]. A maximum of three best candidates per set of J^{PC} quantum numbers were selected to be considered in the second iteration step (see Table B.1 in the Appendix). Due to possible interference effects between the contributing resonances it is not possible to deduce the performance of a fit with a complex hypothesis from that of its individual components. In combination the two additional contributions might perform much better (or worse) than expected, which is the reason to proceed here with this cumbersome analysis procedure.

All possible combinations of two of the contributions identified in the first iteration were considered in the next step. This leads to a total number of 28 hypotheses of the type $\eta(1760) + \eta_c + R_1 + R_2$. The two hypotheses yielding the best results at this stage are both comprised of one f_0, and one f_2 resonance in addition to the base hypothesis, namely the combinations $f_0(2020) + f_2(1565)$ and $f_0(1500) + f_2(1810)$. It is obvious, that the activities in the 0^{++} and 2^{++} partial waves play an important role for the description of the $\omega\omega$

J^{PC}	Name	m_{PDG} [MeV/c^2]	Γ_{PDG} [MeV/c^2]	Observed in VV?	Sub-threshold?
0^{-+}	$\eta(1405)$	1408.8 ± 1.8	51.0 ± 2.9	$\rho\rho, \gamma\gamma, \phi\gamma$	Yes
	$\eta(1475)$	1476 ± 4	85 ± 9	$\gamma\gamma$	Yes
	$\eta(1760)$	1751 ± 15	240 ± 30	$\rho\rho, \gamma\gamma, \omega\omega$	
	$\eta(2225)$	2226 ± 16	185^{+70}_{-40}	$\phi\phi$	
	η_c	2983.6 ± 0.6	31.8 ± 0.8	$\rho\rho, \phi\phi, \gamma\gamma$	
$?^{-+}$	$X(1835)$	$1835.7^{+5.0}_{-3.2}$	99 ± 50	$\gamma\gamma$	
0^{++}	$f_0(1500)$	1504 ± 6	109 ± 7	$\gamma\gamma, \rho\rho$	Yes
	$f_0(1710)$	1723^{+6}_{-5}	139 ± 8	$\gamma\gamma, \omega\omega$	
	$f_0(2020)$	1992 ± 16	442 ± 60	$\rho\rho, \omega\omega$	
	$f_0(2100)$	2101 ± 7	224^{+23}_{-21}	–	
	$f_0(2200)$	2189 ± 13	238 ± 50	–	
1^{++}	$f_1(1510)$	1518 ± 5	73 ± 25	–	
2^{++}	$f_2(1565)$	1562 ± 13	134 ± 8	$\rho\rho, \gamma\gamma, \omega\omega$	(Yes)
	$f_2(1640)$	1639 ± 6	99^{+60}_{-40}	$\omega\omega$	
	$f_2(1810)$	1815 ± 12	197 ± 22	$\gamma\gamma$	
	$f_2(1910)$	1903 ± 9	196 ± 31	$\rho\rho, \omega\omega$	
	$f_2(2010)$	2011^{+60}_{-80}	202 ± 60	$\phi\phi$	
	$f_2(2150)$	2157 ± 12	152 ± 30	–	
	$f_2(2300)$	2297 ± 28	149 ± 40	$\phi\phi, \gamma\gamma$	
	$f_2(2340)$	2345^{+50}_{-40}	322^{+70}_{-60}	$\phi\phi$	

Table 4.5: Resonances listed in [1] that are considered in the model dependent analysis

system, apart from the dominant 0^{-+} contribution. The results of all fits from the second iteration are listed in Table B.2 in the Appendix. After applying a second iteration, large differences between the hypotheses in terms of the likelihood and information criteria were still observed, so that the iterative approach was continued.

The Tables B.3 and B.4 in the Appendix list the results of all 56 hypotheses with three components additionally to the base hypothesis. The best hypothesis at this stage contains the $\eta(2225)$ together with the $f_0(2020)$ and the $f_2(1565)$. It was observed, that *all six* best three-component fits contain the best two-component hypothesis. With this result it can be concluded, that an f_0 contribution around $2\,\text{GeV}/c^2$ as well as an f_2 contribution at the beginning of the phase space are necessary to describe the data and thus a new base hypothesis comprised of the components $\eta(1760) + \eta_c + f_0(2020) + f_2(1565)$ was chosen and the iteration process was continued. All 15 possible combinations of the six best hypotheses with three components, namely $\eta(1760) + \eta_c + f_0(2020) + f_2(1565) + R_1 + R_2$, were fitted to the data and are listed in Table B.5 in the Appendix. It was found that only those fits, which are based on the best three-component hypothesis including the $\eta(2225)$ yield comparably good results, while all other fits can be discarded.

Hypothesis $\eta(1760)+\eta_c+\eta(2225)$ $+f_0(2020)+f_2(1565)+...$		$\log(LH)$	$n.d.f.$	BIC	$AICc$
$\boldsymbol{f_0(1710)}$	$\boldsymbol{+f_2(1810)}$	**−76794.6**	**25**	**−153308**	**−153539**
	$+f_2(2150)$	−76319.0	25	−152359	−152590
	$+f_1(1510)$	−75376.5	27	−150450	−150699
	$+f_0(1500)$	−75907.1	25	−151534	−151764
$f_2(1810)$	$+f_1(1510)$	−76734.1	27	−153165	−153414
	$+f_0(1500)$	−76531.8	25	−152783	−153014
$f_1(1510)$	$+f_2(2150)$	−76443.6	27	−152584	−152833
	$+f_0(1500)$	−76118.5	27	−151934	−152183
$f_2(2150)$	$+f_0(1500)$	−76054.3	25	−151828	−152059

Table 4.6: Results of fits from the last stage of the iterative approach to identify dominantly contributing resonances

The identification of the best hypothesis is ambiguous at this stage, since two fits yield very similar results: According to the BIC the hypothesis with an additional $f_0(1710)$ is preferred, while $AICc$ prefers the presence of the $f_1(1510)$ sub-threshold resonance.
Therefore, as a last step of the systematic survey all hypotheses of the type $\eta(1760)+\eta_c+f_0(2020)+f_2(1565)+\eta(2225)+R_1+R_2$ were considered, whereas $R_{1,2}$ denote either one of the residual contributions of the six best three-component hypotheses. Finally, the ambiguity could be resolved and one best hypothesis could be clearly identified. Table 4.6 lists the results of this iteration step, where the best hypothesis is given by

$$\mathcal{H}_0 := \{\eta(1760), \eta(2225), \eta_c, f_0(2020), f_0(1710), f_2(1565), f_2(1810)\}. \tag{4.35}$$

Up to this point, individual K-matrix parameterizations were used depending on the number of contributing resonances, but all pole positions were fixed according to the values listed in [1] in all fits. For this purpose the corresponding K-matrix properties have been determined beforehand. Table 4.7 lists all K- and T-matrix parameters for all contributions of the $\mathcal{H}_0$ hypothesis.

Resonance	K-matrix m [GeV/c^2]	K-matrix g factor	T-matrix m [GeV/c^2]	T-matrix Γ [MeV/c^2]
$\eta(1760)$	1.758	0.91	1.751	243.3
$\eta(2225)$	2.258	0.78	2.227	187.3
η_c	2.987	0.33	2.983	29.2
$f_0(1710)$	1.706	0.73	1.726	139.3
$f_0(2020)$	2.075	1.14	1.994	438.3
$f_2(1565)$	1.610	0.87	1.561	133.8
$f_2(1810)$	1.877	0.86	1.814	169.8

Table 4.7: K- and T-matrix parameters for all contributions of the best hypothesis ($\mathcal{H}_0$). All pole positions and g-factors were fixed in all fits.

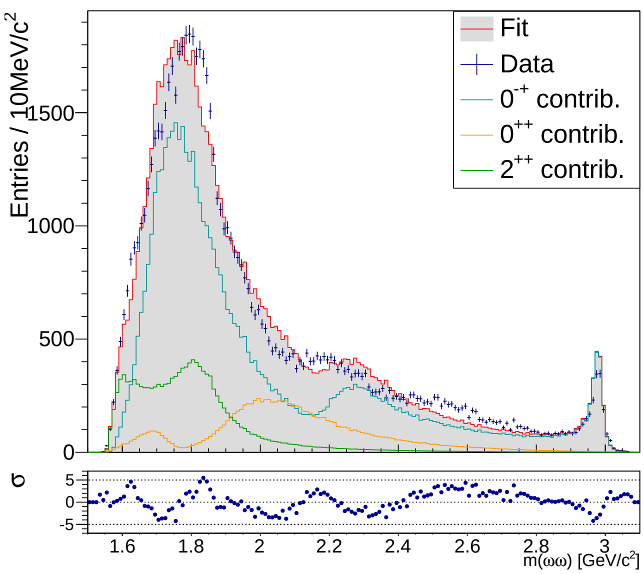

(a)

Component	Contribution [%]
0^{-+} contrib.	68.2 ± 0.4
0^{++} contrib.	14.2 ± 0.3
2^{++} contrib.	16.9 ± 0.3
Sum	$\mathbf{99.4 \pm 0.4}$

$\log LH$	-76794.6
$n.d.f.$	25
BIC	-153308
$AICc$	-153539

(b)

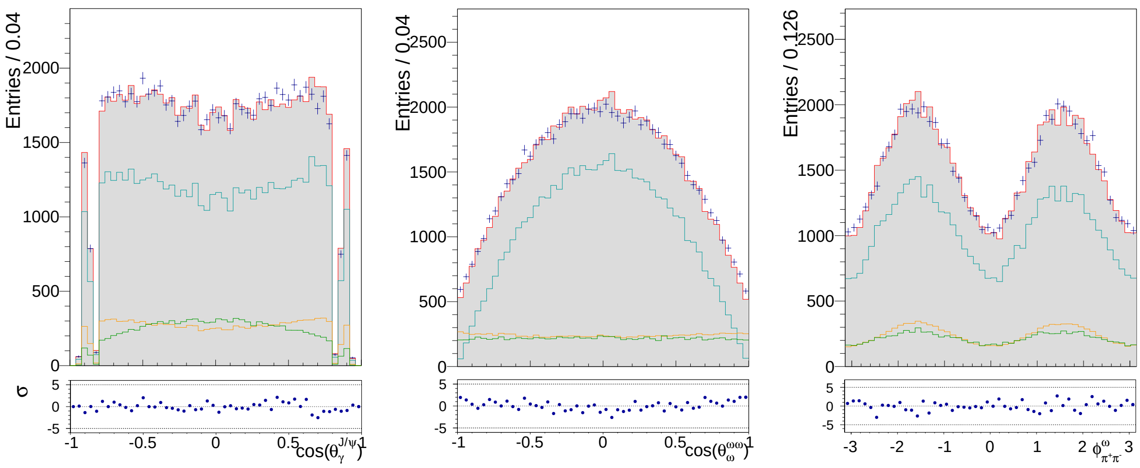

(c) (d) (e)

Fig. 4.13: Q-weighted data (blue dots), fit projection (red/gray shaded) and contributing resonances (colored lines) of the fit with the hypothesis $\mathcal{H}_0$. The individual subfigures show (a) $m(\omega\omega)$, (b) parameters of the fit, (c) azimuthal angle of the radiative photon, (d) azimuthal decay angle of an ω meson and (e) polar production angle of an ω meson.

All T-matrix poles are close to the nominal values on a level of a few MeV. Figure 4.13a shows the invariant mass of the $\omega\omega$ system, the fit projection and the resulting 0^{-+}, 0^{++} and 2^{++} components. Large systematic deviations between the fit and data can be seen across the full $\omega\omega$ mass range. Structures with a width of about $100\,\mathrm{MeV}/c^2$ are prominently visible also in the distribution of the residuals and are located at invariant masses of the $\omega\omega$ system of approximately 1.62, 1.83 and $2.15\,\mathrm{GeV}/c^2$, respectively.

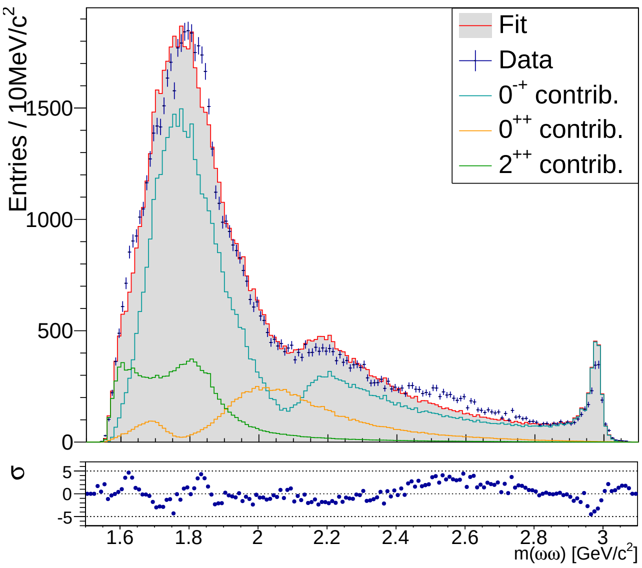

(a)

Component	Contribution [%]
0^{-+} contrib.	68.5 ± 0.4
0^{++} contrib.	14.8 ± 0.3
2^{++} contrib.	16.1 ± 0.3
Sum	$\mathbf{99.4 \pm 0.4}$
$\log LH$	-76976.3
$n.d.f.$	27
BIC	-153649
$AICc$	-153899

(b)

Fig. 4.14: Invariant mass of the $\omega\omega$ system (a) and fit results (b) after optimizing the masses of the $\eta(1760)$ and $\eta(2225)$ using hypothesis $\mathcal{H}_0$

Resonance	K-matrix		T-matrix	
	m [GeV/c^2]	g factor	m [GeV/c^2]	Γ [MeV/c^2]
$\eta(1760)$	1.765 ± 0.001	0.91 (*fixed*)	1.764	255.3
$\eta(2225)$	2.160 ± 0.005	0.78 (*fixed*)	2.121	179.8
η_c	2.987 (*fixed*)	0.33 (*fixed*)	2.983	29.3

Table 4.8: K- and T-matrix parameters after optimizing the masses of the $\eta(1760)$ and $\eta(2225)$ using hypothesis $\mathcal{H}_0$

Furthermore, a very broad structure centered around $m(\omega\omega) \approx 2.5\,\text{GeV}/c^2$ is visible, together with a (narrow) systematic deviation at the mass of the η_c (see Figure 4.13a). However, in the fit projections of the angular distributions, as e.g. the polar angle of the radiative photon (4.13c), the polar decay angle (4.13d) and the azimuthal production angle of the ω mesons (4.13e), a very good agreement between fit and data can already be observed. All other angular distributions show a good agreement as well and are not displayed here but only presented for the final fit result.

To further optimize the solution, the masses of the two lowest 0^{-+} resonances, the $\eta(1760)$ and the $\eta(2225)$, were released. While the $\eta(1760)$ pole position stays almost stable, the $\eta(2225)$ moves by about 100 MeV towards lower masses. The likelihood of the fit improves by about 190 counts due to this measure. Figure 4.14a shows the resulting fit projection of the $\omega\omega$ mass. The fit is able to describe the data much better at $\sim 2.15\,\text{GeV}/c^2$. The corresponding K- and T-matrix parameters after optimization are given in Table 4.8.

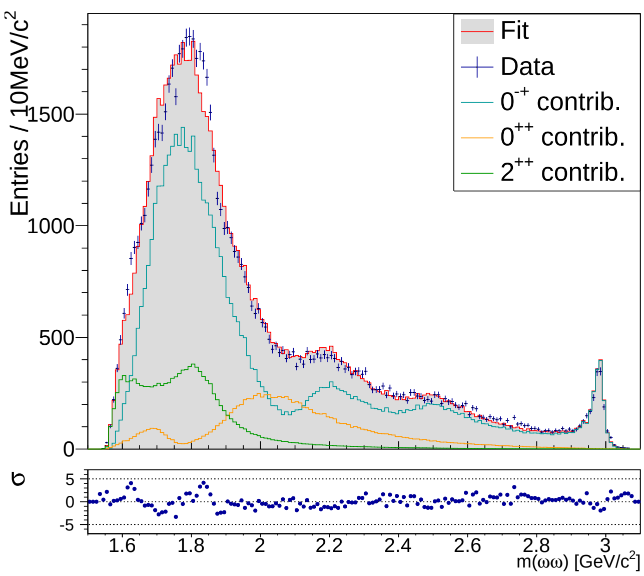

(a)

Component	Contribution [%]
0^{-+} contrib.	68.9 ± 0.4
0^{++} contrib.	14.7 ± 0.3
2^{++} contrib.	15.74 ± 0.3
Sum	$\mathbf{99.36 \pm 0.4}$
$\log LH$	-77267.8
$n.d.f.$	32
BIC	-154176
$AICc$	-154472

(b)

Fig. 4.15: Invariant mass of the $\omega\omega$ system (a) and fit results (b) after adding the $X(2500)$ pole to the 0^{-+} K-matrix and re-optimizing all 0^{-+} pole masses and g-factors

Resonance	K-matrix		T-matrix	
	m [GeV/c^2]	g factor	m [GeV/c^2]	Γ [MeV/c^2]
$\eta(1760)$	1.762 ± 0.001	0.930 ± 0.006	1.780	279.3
$\eta(2225)$	2.158 ± 0.002	0.75 (*fixed*)	2.145	219.8
$X(2500)$	2.532 ± 0.011	0.90 (*fixed*)	2.472	227.8
η_c	2.993 ± 0.0005	0.36 (*fixed*)	2.985	29.3

Table 4.9: K- and T-matrix parameters after adding the $X(2500)$ pole to the 0^{-+} K-matrix and re-optimizing all 0^{-+} pole masses and g-factors

4.8.2 Contribution of a Resonance at 2.5 GeV/c^2

The deviations observed in the high mass region ($m(\omega\omega) > 2.4\,\text{GeV}/c^2$) can not be resolved with the resonances considered up to now. To test for a possible additional contribution, a resonance with a pole mass of $m(X(2500)) = 2.47\,\text{GeV}/c^2$ and a width of $\Gamma(X(2500)) = 230\,\text{MeV}/c^2$ was added. Four different sets of J^{PC} quantum numbers were assumed for the $X(2500)$, namely $0^{-+}, 0^{++}, 1^{++}$ and 2^{++}. The 0^{-+} hypothesis was clearly preferred over all other J^{PC} assignments. Therefore, the $X(2500)$ was added as a new pole to the K-matrix of the 0^{-+} contribution and the fit was performed again, while all masses and g-factors of the new 0^{-+} K-matrix were left free in the fit (see Table 4.9). Figure 4.15a shows the fit result for the invariant mass of the $\omega\omega$ system after re-optimization. The addition of the $X(2500)$ resonance has greatly improved (cf. Table 4.15b) the fit in the complete high-mass region and the only remaining discrepancies are located in the mass range $m(\omega\omega) < 2\,\text{GeV}/c^2$. It should be noted here, that the resulting T-matrix parameters, which represent the physical poles, deliver reasonable values for all resonances of the 0^{-+} contribution, while the corresponding K-matrix pole masses and g-factors were released in the fit.

4.8.3 Final Optimizations

Several tests were performed to check for a possible additional contribution in the mass range $m(\omega\omega) < 2\,\mathrm{GeV}/c^2$, which could resolve the discrepancies between fit and data. It was found that the shape of the enhancement that is centered at around $1.8\,\mathrm{GeV}/c^2$ can neither be exactly reproduced by leaving the resonance parameters of the dominant $\eta(1760)$ contribution floating in the fit, nor by adding an additional resonance with a $J^{PC} = 0^{++}$ or 2^{++} assignment. However a test using an additional pseudoscalar resonance yielded a significant improvement of the fit, if it was combined with a different parameterization of the 2^{++} contributions.

During these studies it was found, that the fit is not very sensitive to the parameters of the contributing 2^{++} resonances: Since both the 0^{++} and 2^{++} K-matrix parameters can not be left free in the fit due to their relatively small contribution, the two poles of the 2^{++} K-matrix were systematically tested against other possible f_2 contributions. While for the scenario presented in the last section and in Figure 4.15a a description with two poles corresponding to the $f_2(1565)$ and the $f_2(1810)$ resonances yields the best results, the assignment changes when the additional pseudoscalar resonance is added to the fit. As a result of the systematic test considering the candidates $f_2(1565), f_2(1640), f_2(1810), f_2(1910), f_2(1950), f_2(2010)$ and $f_2(2150)$ the solution containing the two poles of the $f_2(1640)$ and $f_2(1950)$ yielded the best fit results. In contrast to the 2^{++} and 0^{++} contributions, several parameters of the dominant 0^{-+} K-matrix could be optimized in the fit. The T-matrix pole of the additional pseudoscalar contribution is located at $m = (1826 \pm 4)\,\mathrm{MeV}/c^2$ with a width of $98.9^{+1.5}_{-2.6}\,\mathrm{MeV}/c^2$. Thus, this resonance could be identified with the $X(1835)$. Figure 4.16 exemplary shows the complex energy plane which is scanned to determine the pole parameters of the 0^{-+} T-matrix as described in Section 4.4.4.

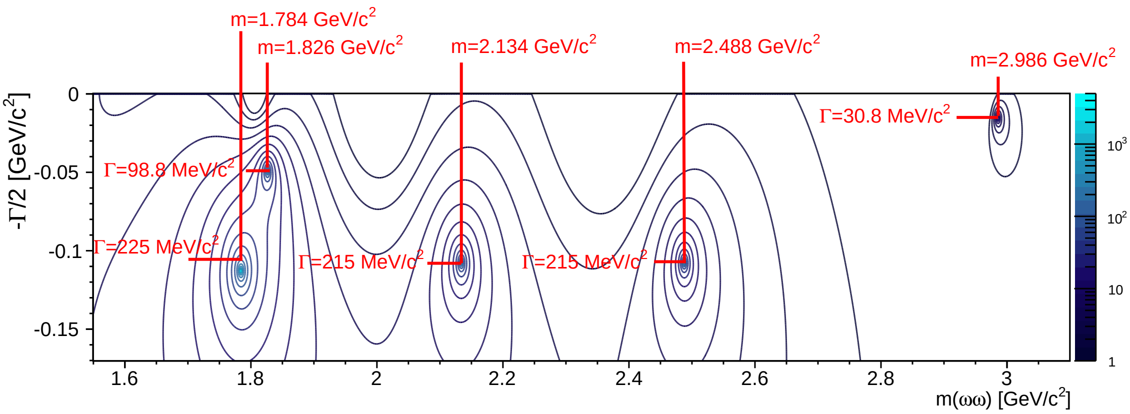

Fig. 4.16: Visualization of the complex energy plane with poles of the 0^{-+} T-matrix for the result of the final fit

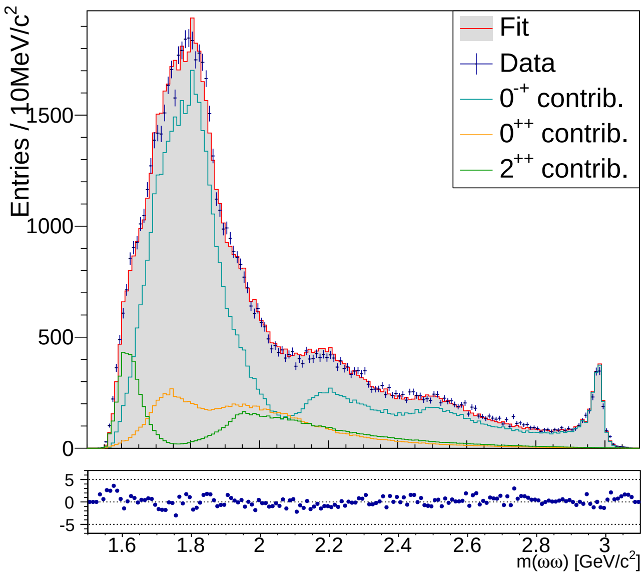

(a)

Component	Contribution [%]
0^{-+} contrib.	70.3 ± 0.4
0^{++} contrib.	15.2 ± 0.5
2^{++} contrib.	13.9 ± 0.6
Sum	$\mathbf{99.5 \pm 0.5}$
$\log LH$	-77294.2
$n.d.f.$	34
BIC	-154207
$AICc$	-154520

(b)

Fig. 4.17: Invariant mass of the $\omega\omega$ system (a) and fit results (b) after adding the $X(1835)$ and re-optimization of the f_2 components (Hypothesis: $\mathcal{H}_1$)

Resonance	K-matrix		T-matrix		PDG [1]	
	m [MeV/c^2]	g factor	m [MeV/c^2]	Γ [MeV/c^2]	m [MeV/c^2]	Γ [MeV/c^2]
$\eta(1760)$	1725 (*fixed*)	0.8 (*fixed*)	1784	225.3	1751 ± 15	240 ± 30
$X(1835)$	1864 ± 3	0.57 ± 0.01	1826 ± 4	$98.8^{+1.5}_{-2.6}$	$1835.7^{+5.0}_{-3.2}$	99 ± 50
$\eta(2225)$	2160 (*fixed*)	0.75 (*fixed*)	2134	215.3	2226 ± 16	185^{+70}_{-40}
$X(2500)$	2546 ± 12	0.86 ± 0.03	2488^{+13}_{-14}	215 ± 15	-	-
η_c	2993.9 ± 0.5	0.370 ± 0.007	2985.6 ± 0.2	30.8 ± 1.0	2983.6 ± 0.6	31.8 ± 0.8
$f_2(1640)$	1.622 (*fixed*)	0.70 (*fixed*)	1.621	100.3	1639 ± 6	99^{+60}_{-40}
$f_2(1950)$	2.030 (*fixed*)	1.20 (*fixed*)	1.944	478.3	1944 ± 12	472 ± 18
$f_0(1710)$	1.706(*fixed*)	0.73(*fixed*)	1.726	139.3	1723^{+6}_{-5}	139 ± 8
$f_0(2020)$	2.075(*fixed*)	1.14(*fixed*)	1.994	438.3	1992 ± 16	442 ± 60

Table 4.10: K- and T-matrix parameters for the fit with the final hypothesis $\mathcal{H}_1$

The resulting fit hypothesis is therefore given by

$$\mathcal{H}_1 = \{\eta(1760), X(1835), \eta(2225), \eta(2500), \eta_c, f_0(1710), f_0(2020), f_2(1640), f_2(1950)\}.$$

The projection of this fit to the invariant $\omega\omega$ mass and its decomposition into the different contributions is shown in Figure 4.17a, while a collection of angular distributions is displayed in Figure 4.18. In general a very good agreement between fit and data can be observed, apart from minor systematic deviations that are noticeable in both λ distributions. Table 4.10 lists the K- and T-matrix parameters that were obtained for the fit using

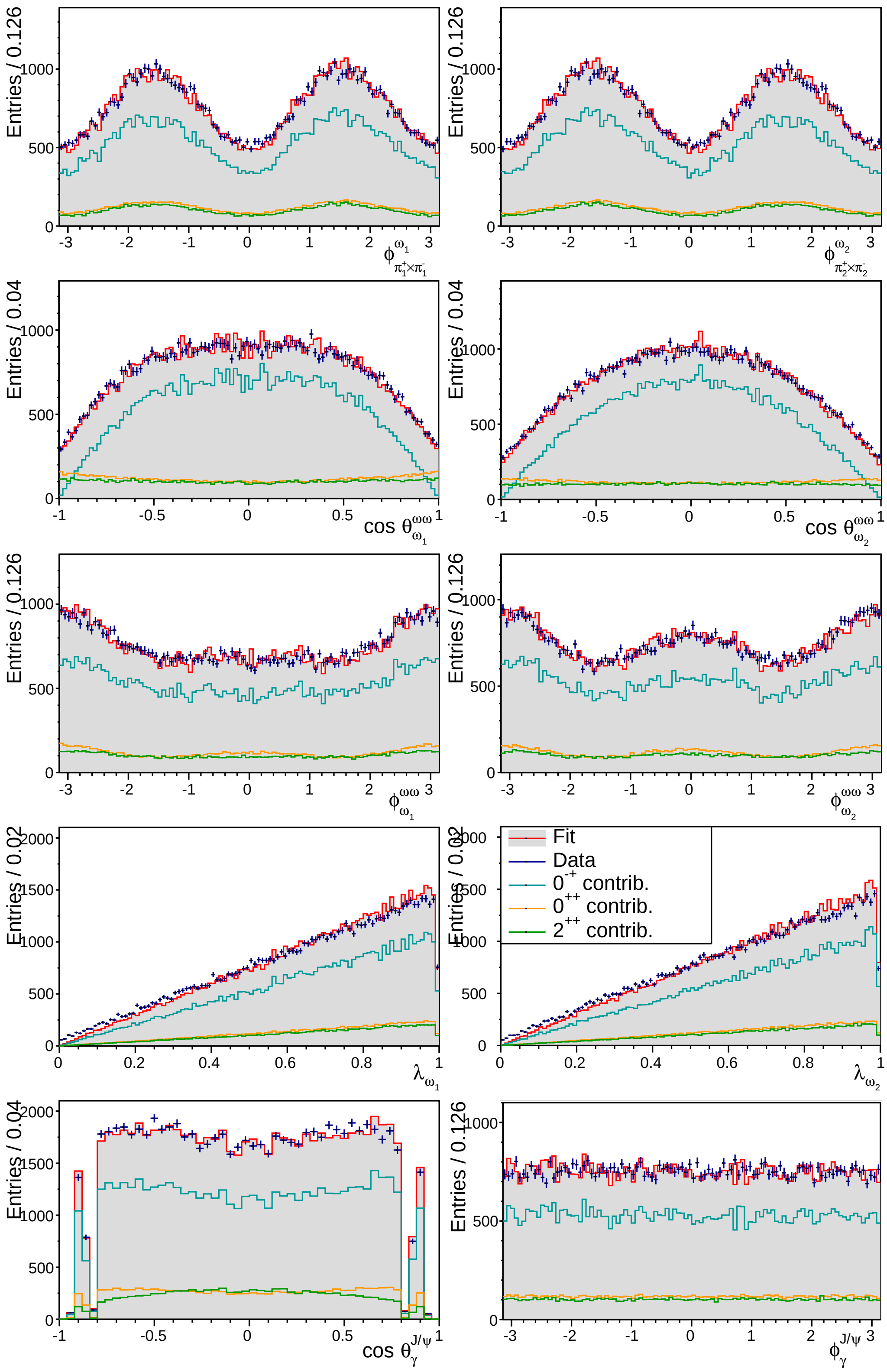

Fig. 4.18: Angular distributions of both ω mesons and corresponding λ distributions for the fit using the final hypothesis ($\mathcal{H}_1$).

hypothesis $\mathcal{H}_1$. In contrast to the T-matrix parameters given for all previous fit results, the statistical uncertainties for the T-matrix pole masses and widths were determined for this final fit. For this purpose the corresponding K-matrix parameters were varied, while for each variation step the remaining free parameters were re-optimized so that the correlations between all parameters are taken into account. This way, the corresponding T-matrix parameter variation for a likelihood change of 0.5 points could be evaluated and was taken as the statistical uncertainty.

4.8.4 Interpretation of the Results

In this analysis, the $\eta(1760)$ was identified as the main contribution to the enhancement at the $\omega\omega$ mass threshold. The T-matrix pole position of this resonance is however found to be $20 - 30\,\mathrm{MeV}/c^2$ ($\approx 2\sigma$) larger than what is currently listed by the PDG [1], while its width is compatible with the PDG value. The discrepancy between the T-matrix pole position and the PDG value is observed for both hypotheses, the one presented in Section 4.8.2 and the final one ($\mathcal{H}_1$), and thus is not introduced by the additional pseudoscalar component at $m(\omega\omega) \sim 1.83\mathrm{GeV}/c^2$. The parameters of this additional resonance are compatible with the values listed for the $X(1835)$, however the nature of this particle is somewhat unclear:
A very narrow threshold enhancement was observed in the decay $J/\psi \to \gamma\overline{p}p$, while a resonance with a width of $\sim 190\,\mathrm{MeV}/c^2$ was observed at about the same mass in the $\eta'\pi\pi$ channel [50][51]. The PDG interprets these two findings as one state, the $X(1835)$, but a superposition of two states is also discussed as a possible explanation [1]. In the $\omega\omega$ mass spectrum presented in this analysis, a rather sharp drop of the intensity is observed at a mass slightly above $1850\,\mathrm{MeV}/c^2$, which perfectly coincides with the opening of the $\overline{p}p$ threshold. This behavior could in principle be explained by a coupling of the $\eta(1760)$ meson to the $\overline{p}p$ channel. The K-matrix formalism used in this analysis provides the possibility to describe the coupling of resonances to multiple final states, thus the effect of opening the $\overline{p}p$ channel for the $\eta(1760)$ could be studied here. The effect is visible, but the drop of the intensity was found to be orders of magnitude too small. For studies like this, the g-factors responsible for the coupling to both final states must be left free in the fit, since none of these values - or at least ratios between them - have been measured before. This can lead to unphysical results, since the behavior of the contributions in the additionally opened channel is not controlled. This shortcoming could be overcome in a coupled channel analysis, where data in the $\overline{p}p$ final state can be fitted simultaneously. This example also holds true for (most) other contributions that are appearing in the parameterization presented here, and also for many more mass thresholds that are present in the region between 1.5 and $\sim 2.5\,\mathrm{GeV}/c^2$.
The $\eta(2225)$ was only observed in the $\phi\phi$ system produced in radiative decays of the J/ψ before [12],[47],[48]. The enhancement at $\sim 2.2\,\mathrm{GeV}/c^2$ is also clearly visible in the 0^{-+} contribution that was extracted using the model independent PWA and thus was identified with the $\eta(2225)$. The corresponding T-matrix pole mass was found to be $\sim 100\,\mathrm{MeV}/c^2$ smaller than what is known from the $\phi\phi$ system, while the width is compatible with the PDG average value. It should be noted here, that the width of this state is only poorly known and given with large uncertainties in [1].
The deviation between the fit and data in the mass region $m(\omega\omega) > 2.2\,\mathrm{GeV}/c^2$ could be resolved by adding a new state to the parameterization, called the $X(2500)$. Despite the finding that also the high mass region of the $\omega\omega$ system is dominated by a pseudoscalar

component, the data can be well reproduced by adding a resonance with a T-matrix pole position of $m = 2488^{+13}_{-14}\,\mathrm{MeV}/c^2$ and a width of $(215 \pm 15)\,\mathrm{MeV}/c^2$. No compatible state is listed by the PDG with a 0^{-+} assignment up to now, however in a very recent partial wave analysis of the decay $J/\psi \to \gamma\phi\phi$ [52] a similar structure was observed. There, an additional contribution was needed to adequately describe the $\phi\phi$ system which is located at a mass of $m = 2470^{+15+101}_{-19-23}\,\mathrm{MeV}/c^2$ with a width of $\Gamma = 230^{+64+56}_{-35-33}\,\mathrm{MeV}/c^2$. Both, mass and width, are compatible within their errors with the resonance parameters of the $X(2500)$ observed in this analysis. It should be noted here, that the existence of this state is rather unclear and should be considered with caution.

However, it can be concluded that significant pseudoscalar production is observed over the complete $\omega\omega$ mass spectrum, which may contain more resonances than what is known up to now.

The resonance parameters of the η_c are very close to the PDG values, however a detailed study utilizing a sophisticated description of the line shape of this charmonium state will be presented in Chapter 5 for the measurement of the $\eta_c \to \omega\omega$ branching fraction, which is measured for the first time within the scope of this work.

A significant 2^{++} contribution in the direct vicinity of the $\omega\omega$ mass threshold was identified with the $f_2(1640)$ meson, which was already observed by the BESII experiment in the $\omega\omega$ channel [10]. Both the T-matrix mass and width are compatible with the values reported by BESII.

The parameters of all remaining contributions, namely the $f_2(1950)$, the $f_0(1710)$ and the $f_0(2020)$ were not optimized in this study due to their small relative contributions and the difficulties that arise in the clear differentiation between 0^{++} and 2^{++} contributions. All T-matrix pole positions and widths of these resonances were chosen to be coinciding with the PDG values.

In general, the data can be well described with the solution presented in this analysis. Figure 4.19 shows a comparison of the contributions to the 0^{-+}, 0^{++} and 2^{++} waves extracted from the model independent PWA presented in Section 4.7, together with the projection of the corresponding 0^{-+}, 0^{++} or 2^{++} K-matrix components. A very good agreement is observed for the pseudoscalar contribution. The behaviour of the 0^{++} wave is represented fairly well, while the largest differences are visible for the 2^{++} component. It should be stressed here, that the contributions to the 0^{++} and especially the 2^{++} waves are very difficult to extract in both, the model dependent as well as the model independent PWA. The 0^{-+} contribution however is found to be very stable, independent from the parameterizations of the scalar and tensor contributions. It is noteworthy, that most of the assumptions on contributing resonances discussed in Section 4.7.4 have been confirmed by the model dependent analysis.

Determination of Branching Fractions

Using the final fit result the product branching fractions $\mathcal{B}(J/\psi \to \gamma X \to \gamma(\omega\omega))$ of the individual fit contributions can be calculated (see Table 4.11). Additionally, also the value for $\mathcal{B}(J/\psi \to \gamma\omega\omega)$ is determined. The branching fraction is given by

$$\mathcal{B}(J/\psi \to \gamma X \to \gamma(\omega\omega)) = \frac{N_X}{N_{J/\psi}\mathcal{B}^2(\omega \to \pi^+\pi^-\pi^0) \cdot \mathcal{B}^2(\pi^0 \to \gamma\gamma) \cdot \epsilon}, \tag{4.36}$$

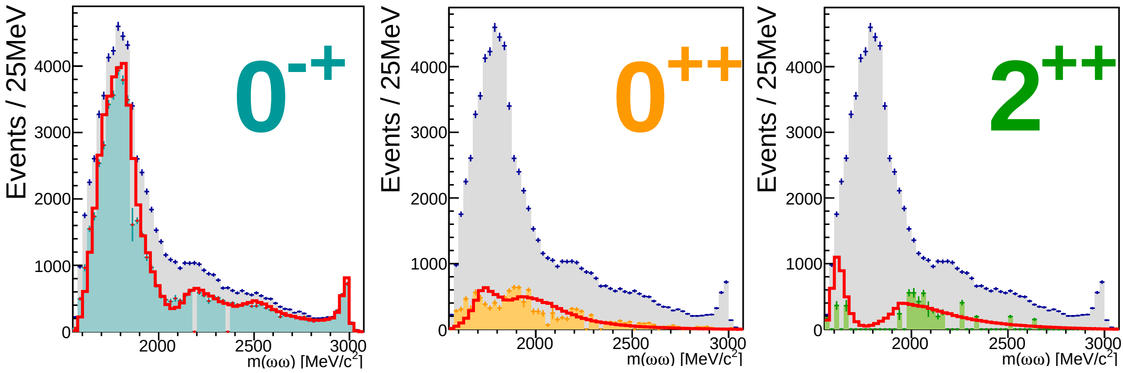

Fig. 4.19: Comparison of the contributions from different partial waves (colored histograms) extracted from the model independent PWA (cf. Figure 4.9) overlayed with the 0^{-+} (left), 0^{++} (center) and 2^{++} K-matrix (right) contributions from the best model dependent PWA fit (red line).

where N_X and $N_{J/\psi}$ denote the number of events assigned to the contribution X by the fit and the total number of recorded J/ψ events in the BESIII data set, respectively. Due to the usage of the K-matrix approach, the extraction of branching fractions for single resonances is not straightforward. Technically it is possible to extract single components by setting the parameters which are describing the production strength of all other resonances to zero, however due to possibly large interferences and effects like rescattering, the extracted values must be interpreted with caution. In the case presented here, all three matrices contain broad and partly overlapping contributions, so that only the product branching fractions $\mathcal{B}(J/\psi \to \gamma X \to \gamma(\omega\omega))$, whereas X denotes a complete J^{PC} contribution described by a K-matrix, are extracted here. Since these values are in general not comparable with the branching fractions for single resonances listed e.g. in [1], the mass region of the η_c is analyzed separately to extract its branching fraction into a pair of ω mesons (see Chapter 5).

The efficiency ϵ is determined by weighting a generated and a reconstructed MC sample using the probability density function obtained by the best fit. This method allows for a much more precise determination of the efficiency than the simple one-dimensional approximation that was performed in Section 3.2.8, since all angular distributions and decay dynamics are considered correctly. A more detailed description of the method can be found in 5.2.1. The systematic errors of the calculated branching fractions were determined from all sources listed in Table 4.12, whereas a description on the origin of the different systematic errors is given in Chapter 5. The difference of the extracted yield for the single components between a fit using hypothesis $\mathcal{H}_1$ and hypothesis $\mathcal{H}_0$ was used to estimate the systematic uncertainty arising from the PWA fit model and is also listed in Table 4.12.

The branching fraction for the decay $J/\psi \to \gamma\omega\omega$ was determined with unprecedented precision in this analysis and is listed in Table 4.11. The deviation between the value determined in this analysis and the world average value $\mathcal{B}_{\text{PDG}}(J/\psi \to \gamma\omega\omega) = (1.61 \pm 0.33) \cdot 10^{-3}$ [1] is about 2.7σ, which is regarded as not significant. The average listed in [1] is based on two low statistics measurements (120 and 412 events) from the late 1980s ([8],[9]) and a more recent measurement by BESII with very large uncertainties

($\mathcal{B}_{\text{BESII}}(J/\psi \to \gamma\omega\omega) = (6.0 \pm 4.8 \pm 1.8) \cdot 10^{-3}$) [53]. The uncertainties of the measurement presented in this work are a factor of two smaller than those of the PDG average.

	Number of events	$\mathcal{B} \pm \Delta\mathcal{B}_{\text{stat.}} \pm \Delta\mathcal{B}_{\text{syst.}}$
$\mathcal{B}(J/\psi \to \gamma\, 0^{-+} \to \gamma\omega\omega)$	52883 ± 291	$(1.76 \pm 0.01 \pm 0.12) \cdot 10^{-3}$
$\mathcal{B}(J/\psi \to \gamma\, 0^{++} \to \gamma\omega\omega)$	11431 ± 354	$(0.38 \pm 0.01 \pm 0.03) \cdot 10^{-3}$
$\mathcal{B}(J/\psi \to \gamma\, 2^{++} \to \gamma\omega\omega)$	10516 ± 460	$(0.35 \pm 0.02 \pm 0.05) \cdot 10^{-3}$
$\mathcal{B}(J/\psi \to \gamma\omega\omega)$	75245 ± 274	$(2.50 \pm 0.01 \pm 0.16) \cdot 10^{-3}$

Table 4.11: Branching fractions of the three fit contributions and the decay $J/\psi \to \gamma\omega\omega$

Source	Uncertainty
Number of J/ψ events	0.5%
Track reconstruction (4 pions)	4%
Photon reconstruction (5 photons)	5%
External branching fractions:	
$\omega \to \pi^+\pi^-\pi^0$	0.8%
$\pi^0 \to \gamma\gamma$	0.03%
Systematic error of Q-factor method	0.9%
PWA fit model:	0^{-+} : 2%, 0^{++} : 3%, 2^{++} : 13%
Quadratic Sum:	0^{-+} : 6.8%, 0^{++} : 7.2%, 2^{++} : 14.5%

Table 4.12: Summary of the systematic uncertainties

5 Measurement of the $\eta_c \to \omega\omega$ Branching Fraction

The extraction of the number of observed $\eta_c \to \omega\omega$ events and subsequently also the corresponding branching fraction was carried out in a dedicated analysis restricted to the mass range $m(\omega\omega) \geq 2.7\,\mathrm{GeV}/c^2$. The η_c signal was already excellently described by the best model dependent fit presented in Chapter 4, however it may be not straightforward to extract contributions of single resonances from a K-matrix parameterization (see "Review on Dalitz Plot Analysis Formalism" in [1]). In order to provide a number for the branching fraction that is comparable to others listed in [1], therefore a different parameterization was chosen. However, the η_c signal can not be described by a simple Breit-Wigner function and needs to be modified to account for the distortion of the line shape due to the radiative J/ψ decay. Details on the parameterization of the η_c signal, the PWA fit and the extraction of the branching fraction as well as the systematic uncertainties are discussed in the following sections.

5.1 Description of the Line Shape

When extracting the η_c signal yield from the reconstructed data, special attention must be paid to the line shape. CLEO-c first observed a distortion of the η_c line shape in radiative $\psi(3686)$ decays, which required a more sophisticated description than a simple Breit-Wigner function [54]. The observations show, that the signal of the η_c is obviously asymmetric, when it is produced in radiative decays. A strong tail towards lower masses is observed, while the signal drops rapidly on the high mass side, as can be seen in Figure 5.1a.

In Chapter 4.3.2 it was shown, that the helicity decay amplitudes of a resonance can be expanded into the radiative multipole basis. The radiative transition of the $\psi(3686)$ or the J/ψ into $\gamma\eta_c$ in this basis is described by an $M1$ transition. In this naming scheme, which is adopted from nuclear transitions, $M1$ designates a magnetic-dipole transition. In the case of the $\psi(3686) \to \gamma\eta_c$ decay, one speaks of a *hindered $M1$ transition*, while the $J/\psi \to \gamma\eta_c$ decay is described by a *pure $M1$-transition* [56]. CLEO-c took this transition into account by modifying the resonance shape with a term describing the energy dependence of the $M1$-transition matrix element. For the pure transition, the matrix element depends on the energy as $\propto E_\gamma^3$ [57]. In their analysis, CLEO-c fitted the energy spectrum of the radiative photon with a relativistic Breit-Wigner function, modified with the energy dependence of the matrix element. While this improves the fit at the peak, it automatically leads to a diverging tail towards higher photon energies. To avoid this unphysical behavior, a damping function of the form $E_{\gamma,0}^2/(E_\gamma E_{\gamma,0} + (E_\gamma - E_{\gamma,0})^2)$ is suggested in [58] by the KEDR collaboration. Here, E_γ denotes the energy of the radiative photon, while $E_{\gamma,0}$ is the most probable photon energy, which is corresponding to the peak position of the η_c and is calculated using the nominal PDG mass. It was found that by including this damping function the line shape of the η_c can be described very well. Thus the combination of the E_γ^3-term from the energy dependence of the matrix element, together with the damping function was used in this analysis. Figure 5.1a shows the *Q-weighted* invariant mass of

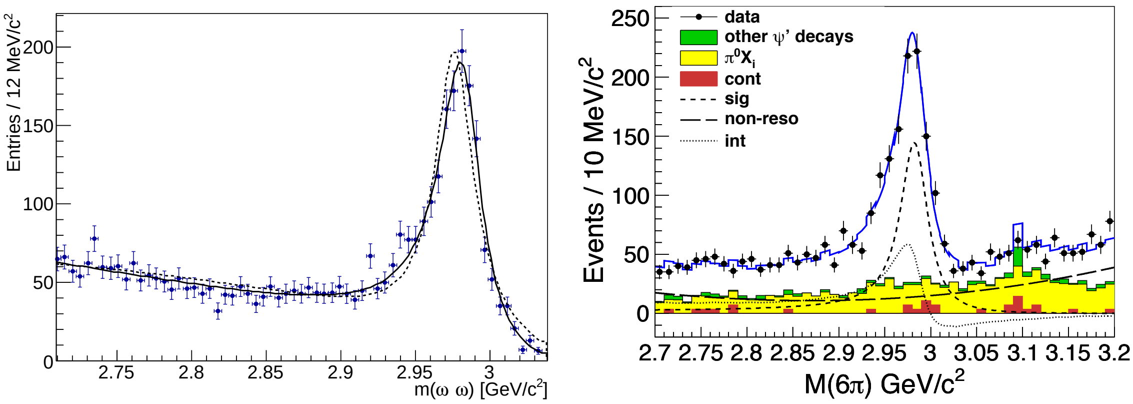

(a) **(b)**

Fig. 5.1: (a) Illustration of the difference between an unmodified relativistic Breit-Wigner function (dashed line) and the modified version (solid black line) as description of the η_c signal for the selected and *Q-weighted* data from this analysis.
(b) One dimensional fit to the $m(3(\pi^+\pi^-))$ spectrum from [55]. Here, interference between the η_c signal and the non-resonant background was allowed.

the $\omega\omega$ system in the region of the η_c from this analysis. To demonstrate the difference between a standard relativistic Breit-Wigner function and the modified version, two fits to this one-dimensional mass spectrum were performed and are displayed. For both fits, the non-resonant background is described with a second-order Chebychev-polynomial. The modified signal function describes the data much better in both the tails as well as around the peak position. It is noteworthy, that the peak position is shifted towards higher masses by the modifications, which brings the value of the observed η_c mass closer to the world average value.

In neither of the analyses from CLEO-c and KEDR, the possibility of interference between the non-resonant background and the η_c signal were considered. This was first taken into account by BESIII, where events from the radiative decay $\psi(3686) \to \gamma\eta_c$ were reconstructed using six exclusive decay modes of the η_c [55]. The line shape was described by a one-dimensional fit to the η_c mass spectrum, including the hindered-$M1$ matrix element as well as the damping function. Additionally, a free phase parameter was introduced to account for possible interference between the signal and the non-resonant background. In a combined fit it was found, that the interference is needed to adequately describe the line shape in all six exclusive modes. Figure 5.1b shows the invariant mass of $3(\pi^+\pi^-)$ from the earlier BESIII-analysis, where the strength of the interference is symbolized by the fine-dotted line.

The effect of this interference must be considered and has a significant impact on exclusively reconstructed events. Conclusively, for this analysis all findings were taken into account and finally a model dependent PWA in the region $2.65 \leq m(\omega\omega) \leq 3.05\,\mathrm{GeV}/c^2$ was performed. The chosen PWA model includes the description of the η_c signal with a relativistic Breit-Wigner function, modified with the energy dependence of the $M1$-transition matrix element as well as the damping function.

5.2 Model Dependent PWA in the η_c Mass Region

The main purpose of the PWA conducted in a restricted region of the $\omega\omega$ invariant mass is the extraction of the η_c signal yield, while allowing for quantum-mechanical interference between the η_c and other contributions and taking all phase space dimensions into account. In contrast to a one-dimensional fit, no additional fit parameters have to be introduced to account for the interference, as it was done e.g. in [55]. The interference is taken into account by the complex amplitudes already.

The strategy that was chosen here, is similar to that applied for the model independent study presented in Chapter 4.7. Also here, a number of hypotheses was tested independently and finally the best hypothesis was selected using the information criteria presented in Section 4.7.2. All hypotheses contain one contribution, that describes the η_c signal. The dynamical part of this amplitude is constructed from a relativistic Breit-Wigner function, multiplied with a factor describing the energy dependence of the $M1$-transition matrix element (E_γ^3) and a damping factor of the form $E_{\gamma,0}^2/(E_\gamma E_{\gamma,0} + (E_\gamma - E_{\gamma,0})^2)$, as introduced by the KEDR-collaboration [58]. Furthermore, the mass and width of the η_c have been left floating in the fits. Apart from the signal, one up to three different additional contributions were allowed. All of these "non-resonant" contributions are described without adding a dynamical part to the amplitude, thus no line-shape is parameterized and the contributions are describing the phase-space only. For the non-resonant contributions, the quantum numbers $J^{PC} = \{0^{-+}, 0^{++}, 1^{++}, 2^{++}\}$ were considered, according to the results of the model independent PWA. Using this strategy, one can construct 14 different hypotheses. It is also to be expected from the model independent PWA, that apart from the η_c signal, a strong (non-resonant) pseudoscalar contribution is found. Furthermore, contributions of 0^{++}, 1^{++} and/or 2^{++} components are likely to be found.

The results of the 14 fits with floating mass and width parameters were sorted using the $\Delta AICc + \Delta BIC$ model selection criterion and are listed in Table 5.1. This table also lists the single $AICc$ and BIC values, as well as the difference between these ranking criteria to that of the best hypothesis. The hypothesis yielding the best $\Delta AICc + \Delta BIC$ value, is given by

$$\mathcal{H}_0 = \{\eta_c,\, 0^{-+},\, 0^{++},\, 1^{++}\}, \tag{5.1}$$

which is therefore selected to be used for the determination of the nominal η_c yield. However, it is interesting to notice that the second best hypothesis yields a lower value of the $AICc$ criterion than the best hypothesis. If only the $\Delta AICc$ criterion had been considered, the hypothesis $\mathcal{H}_1 = \{\eta_c,\, 0^{-+},\, 0^{++},\, 2^{++}\}$ would have been selected as the best one. It should also be noted, that the third best hypothesis is a subset of the second best, in which the 0^{++} component is missing. This suggests, that the 0^{++} component in $\mathcal{H}_1$ is the least significant one. The hypothesis $\mathcal{H}_1$ is used to estimate the systematic error introduced by the procedure of selecting the best hypotheses (cf. Section 5.3).

Table 5.2 lists the most important parameters of the best fit, including the extracted yield of the η_c signal. A sample of 1076 $\eta_c \to \omega\omega$ signal events were reconstructed. The value of the total yield obtained from the fit is in very good agreement with the number of events present in the fitted data subsample, given by the sum over all event weights ($\sum_i Q_i$). However, adding up the yields of all single contributions delivers a value corresponding to only $\sim 83.7\%$ of the total yield. This means, that the integral interference in the selected mass range is on the level of $\sim 16.3\%$. It can be concluded that the interference, which

i	Hypothesis $\mathcal{H}_i$	$\log(LH)$	n.d.f.	BIC	ΔBIC	$AICc$	$\Delta AICc$	**ΔAICc +ΔBIC**
0	$0^{-+}0^{++}1^{++}$	-4182.68	13	-8255.71	0.00	-8339.27	0.00	**0.00**
1	$0^{-+}0^{++}2^{++}$	-4202.93	21	-8228.74	26.97	-8363.66	-24.39	**2.58**
2	$0^{-+}2^{++}$	-4189.89	17	-8236.39	19.32	-8345.64	-6.37	**12.95**
3	$0^{-+}1^{++}2^{++}$	-4188.02	21	-8198.93	56.78	-8333.84	5.43	**62.21**
4	$0^{-+}0^{++}$	-4128.05	9	-8180.19	75.52	-8238.06	101.21	**176.73**
5	$0^{-+}1^{++}$	-4048.57	9	-8021.23	234.48	-8079.10	260.17	**494.65**
6	2^{++}	-3969.40	15	-7812.28	443.43	-7908.69	430.58	**874.01**
7	$0^{++}2^{++}$	-3972.46	19	-7784.66	471.05	-7906.75	432.52	**903.57**
8	$1^{++}2^{++}$	-3953.96	19	-7747.67	508.04	-7869.75	469.52	**977.56**
9	$0^{++}1^{++}2^{++}$	-3958.18	23	-7722.37	533.34	-7870.12	469.15	**1002.49**
10	$0^{++}1^{++}$	-3845.96	11	-7599.15	656.56	-7669.87	669.40	**1325.96**
11	0^{++}	-3756.73	7	-7454.42	801.29	-7499.43	839.84	**1641.13**
12	1^{++}	-3675.89	7	-7292.75	962.96	-7337.76	1001.51	**1964.47**
13	0^{-+}	-3625.18	5	-7208.20	1047.51	-7240.35	1098.92	**2146.43**

Table 5.1: Results of model dependent PWA fits for 14 different hypotheses. The fits were performed for events in the region $2.65 \leq m(\omega\omega) \leq 3.05\,\mathrm{GeV}/c^2$ and the hypotheses were sorted ascending by their $\Delta AICc + \Delta BIC$ value.

Parameter	Value
Yield 0^{-+} contribution	2046 ± 130
Yield 0^{++} contribution	363 ± 39
Yield 1^{++} contribution	367 ± 44
Yield η_c contribution	1076 ± 49
Total No. of fitted events	4601 ± 68
$\sum_i Q_i$	4601.45
m_{η_c}	$(2982.7 \pm 0.9)\,\mathrm{MeV}/c^2$
Γ_{η_c}	$(27.6 \pm 1.4)\,\mathrm{MeV}/c^2$

Table 5.2: Extracted yield of all contributions and values of the η_c resonance parameters for the selected best hypothesis ($\mathcal{H}_0$)

here is respected by using a full partial wave analysis, is necessary to correctly describe the data and the observed η_c signal. Figure 5.2 shows various projections of the PWA fit for the $\mathcal{H}_0$ hypothesis and their decompositions into the fitted contributions.

Although the fit was performed as an unbinned maximum-likelihood fit, one can calculate a χ^2 value of any of the naturally binned histograms, to the fit result. For the invariant mass spectrum of the $\omega\omega$ system (bottom right plot in Fig. 5.2), a value of $\chi^2/\mathrm{n} \approx 45.35/43 = 1.05$ is obtained, where n denotes the number of bins. This shows a very good agreement between fit and data.

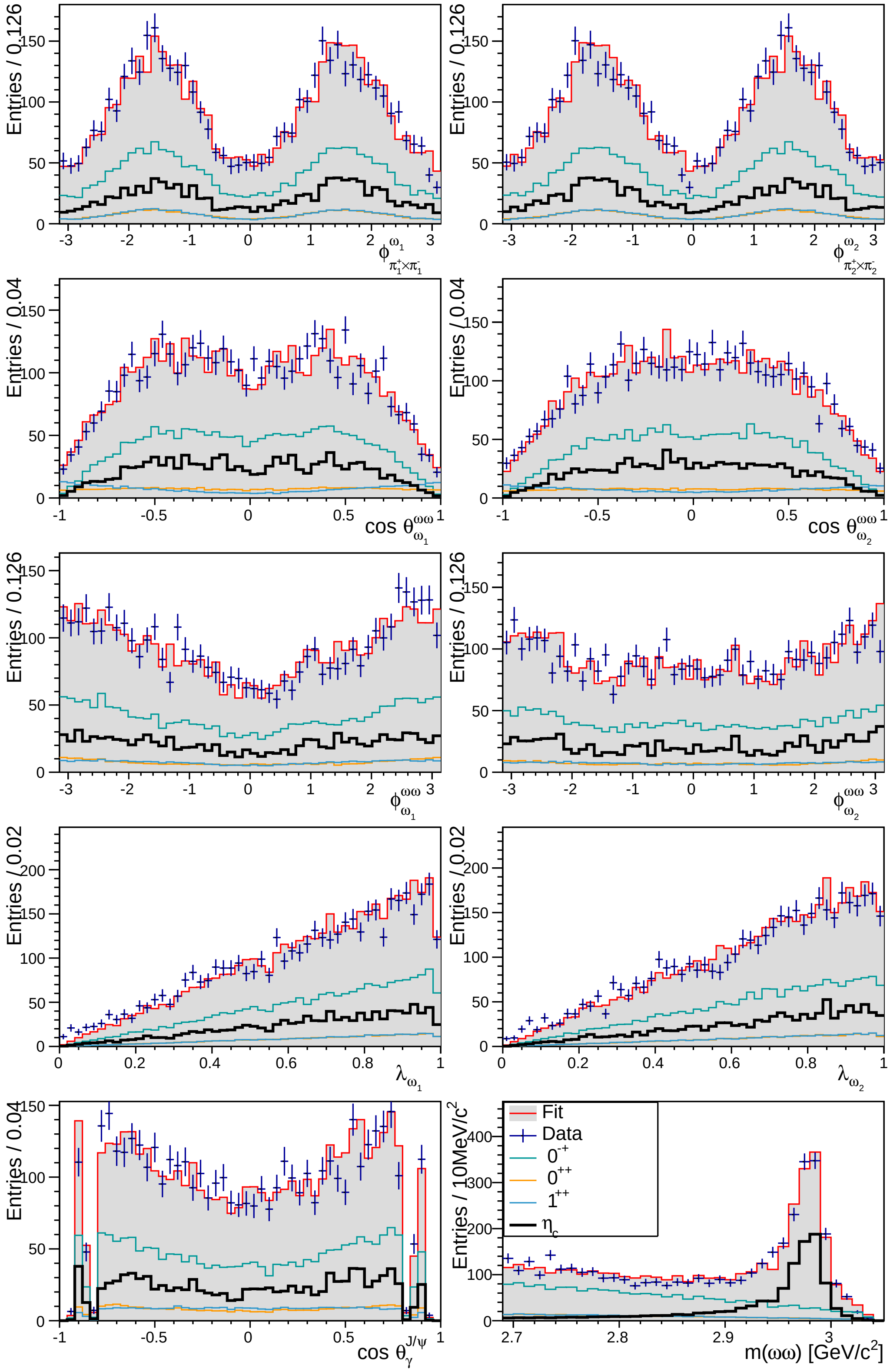

Fig. 5.2: Various projections of the model dependent PWA fit using hypothesis $\mathcal{H}_0$. All distributions show the data in the mass region $2.65 \leq m(\omega\omega) \leq 3.05\,\mathrm{GeV}/c^2$, together with the fit result and its decomposition into the four contributions.

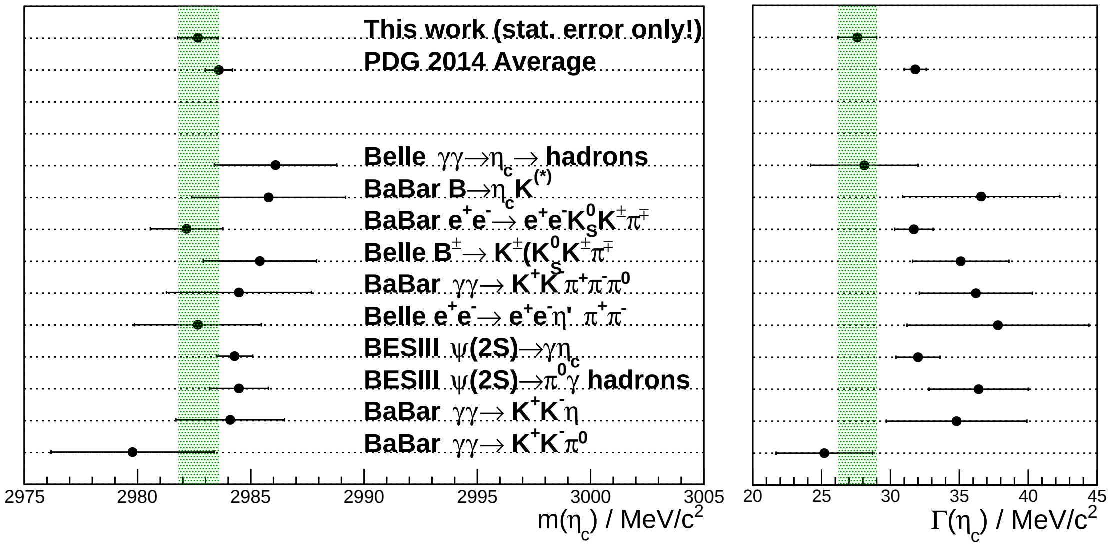

Fig. 5.3: Mass and width of the η_c obtained from the best fit in this work in comparison with the most up-to-date PDG value and results from previous measurements, that were used as an input for the PDG average [1]. The result from this work includes the statistical error only (green shaded area), while the error bars of all other results include statistical and systematic uncertainties.

Figure 5.3 shows the resulting mass and width of the η_c from this work in comparison with the value listed in the PDG. Additionally a list of results from previous experiments, that serve as input to the PDG average are listed. While the obtained value for the mass is compatible with many previous measurements and especially with the PDG average value within errors, the width is on the lower side of the world average value and only fully consistent with previous results from $\gamma\gamma$ fusion within their error bars. The deviations to other measurements are however all smaller than 2σ of the statistical uncertainty.

5.2.1 Reconstruction and Selection Efficiency

In order to calculate the branching fraction, apart from the extracted η_c yield, several external values must be known and the reconstruction and selection efficiency must be estimated from MC simulations. For a correct consideration in all dimensions of the phase-space, the partial wave analysis software is used to extract the efficiency. Therefore, the amplitude model obtained from the best fit is used, to weight a sample of phase space distributed MC events. This weighting is performed for the generated MC events, as well as for the same MC events after applying the reconstruction using the BOSS software. The resulting efficiency for the nominal result amounts to $\epsilon = 3.31\%$. For the determination of the total systematic uncertainty, different fits are performed and described in Section 5.3. For all fits, the efficiency was as well individually determined using the method described above.

5.2.2 Calculation of the Branching Fraction

For the determination of the η_c branching fraction, the extracted number of reconstructed η_c events has to be corrected with the previously determined efficiency. All intermediate resonances and the branching fractions of these, beginning with the J/ψ must also be considered. Using the number of J/ψ events present in the data sample, all external branching fractions, the efficiency calculated using the amplitude model and the yield of the fitted η_c signal, the branching fraction is derived as

$$\mathcal{B}(\eta_c \to \omega\omega) = \frac{N_{\eta_c}}{N_{J/\psi} \cdot \mathcal{B}(J/\psi \to \gamma\eta_c) \cdot \mathcal{B}^2(\omega \to \pi^+\pi^-\pi^0) \cdot \mathcal{B}^2(\pi^0 \to \gamma\gamma) \cdot \epsilon} \tag{5.2}$$

$$= (1.88 \pm 0.09) \cdot 10^{-3}. \tag{5.3}$$

with the values listed in Table 5.3.
The systematical uncertainties will be discussed in the following section.

Parameter	Value	Source
N_{η_c}	1076 ± 49	*this analysis*
ϵ	$3.31\,\%$	*this analysis*
$N_{J/\psi}$	$(1310.6 \pm 7.0) \cdot 10^6$	[59][22]
$\mathcal{B}(J/\psi \to \gamma\eta_c)$	$(1.7 \pm 0.4)\,\%$	[1]
$\mathcal{B}(\omega \to \pi^+\pi^-\pi^0)$	$(89.2 \pm 0.7)\,\%$	[1]
$\mathcal{B}(\pi^0 \to \gamma\gamma)$	$(98.823 \pm 0.034)\,\%$	[1]

Table 5.3: Summary of values required for the calculation of the $\eta_c \to \omega\omega$ branching fraction

5.3 Systematic Uncertainties

Number of J/ψ Events

The total number of J/ψ events in the J/ψ data sample has been determined by the BESIII collaboration from an analysis of inclusive hadronic events. The method as well as the result for the 2009 data sample were published in [59]. The corresponding numbers for the 2012 data sample have been determined using the same method. The combined total number of J/ψ decays amounts to $(1310.6 \pm 7.0) \cdot 10^6$ [22]. The error of this number translates to a systematic error on the $\eta_c \to \omega\omega$ branching fraction of 0.5%.

Track and Photon Reconstruction

A detailed study of the well understood decay channel $J/\psi \to p\bar{p}\pi^+\pi^-$ has been performed by the Data Quality group of the BESIII collaboration [60][61]. It was found, that for the BOSS release used in this analysis (6.6.4.p01), and in a general range of pion transverse momentum and angular distribution, a systematic error of 1% per track is a reasonable estimation. Thus, the corresponding systematic error for the four charged pions in this analysis amounts to 4%.

Also for the performance of the photon reconstruction, extensive studies were performed using the process $e^+e^- \to \mu^+\mu^-\gamma$ [62]. This initial-state-radiation process was studied using the full J/ψ dataset, and a systematic uncertainty introduced by the photon reconstruction efficiency of 1% per photon was found. The systematic uncertainty for the five photons in this analysis thus is taken to be 5%.

External Branching Fractions

The errors of all external branching fractions entering the calculation are treated as systematic uncertainties and are taken from [1]. The values of these uncertainties are listed in Table 5.7, while special attention should be paid to the branching fraction of the radiative decay $J/\psi \to \gamma\eta_c$. This branching fraction was measured by three different experiments, but the PDG only uses the results from CLEO as well as Crystal Ball. Although the CLEO measurement is a much more recent result, the error on the named branching fraction could not be improved with respect to the Crystal Ball measurement. This branching fraction is therefore listed with a relative error of 23.5%, which hence is the dominant contribution to the systematic error of this analysis.

Systematic Error of the Q-Value Method

Another source for a systematic error is the performance of the Q-factor method, which is used to suppress background of non-$\omega\omega$ events. The error introduced by this method influences the event weights directly, and therefore the observed yield of the η_c component. For a test utilizing a toy MC sample, only events in the region $2.65 \leq m(\omega\omega) \leq 3.05\,\mathrm{GeV}/c^2$, corresponding to the region in which the model dependent fits for the branching fraction determination were performed, were taken into account. No decomposition of the events into different components, especially the η_c component, was considered. This represents the worst-case-scenario, in which the full amount of wrongly assigned Q-factors changes the determined yield of the η_c component. Figure 5.4 shows the $\omega\omega$ invariant mass for the simulated signal and background distributions, as well as the corresponding Q- and $(1-Q)$-weighted events from the toy MC study presented in Appendix A with a zoom to

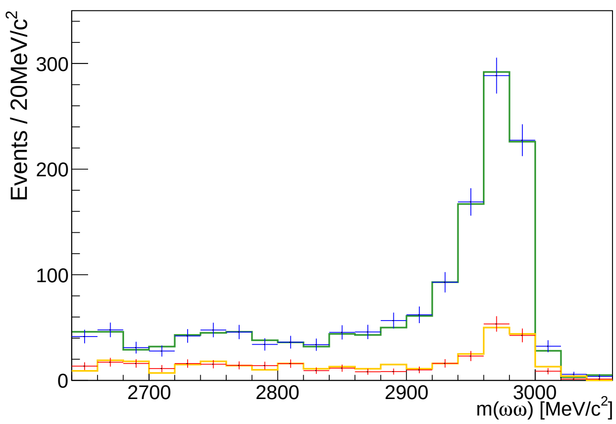

Fig. 5.4: Invariant $\omega\omega$ mass in the η_c region for toy MC data as presented in Figure A.1. The toy MC sample contains peaking and non peaking background contributions proceeding via $3\pi\omega$ or 6π decays.

the η_c fit region. The toy MC sample used for this study is similar to the one presented in Section 4.7.3, but additionally includes a peaking background contribution at the mass of the η_c. The systematic error of the $\eta_c \to \omega\omega$ branching fraction due to uncertainties of the Q-factor method was found to be 0.9%.

Systematic Uncertainty due to η_c Resonance Parameters

The best fit as described in Section 5.2 has been performed again, where mass and width have been fixed to the nominal values as listed in [1], namely

$$m_{\eta_c}^{\mathrm{PDG}} = (2983.6 \pm 0.6)\,\mathrm{MeV}/c^2 \quad \text{and} \quad \Gamma_{\eta_c}^{\mathrm{PDG}} = (31.8 \pm 0.8)\,\mathrm{MeV}/c^2. \tag{5.4}$$

The important key parameters of this fit are listed in Table 5.4 and the comparison of fit and data in the $\omega\omega$ invariant mass and the angular distribution of the radiative photon are shown in Figure 5.5. As expected, the observed η_c yield varies by a certain amount from the nominal value. The reconstruction and selection efficiency, as well as the resulting branching fraction are extracted for this fit in the same way as for the nominal result. The branching fraction was determined to be $\mathcal{B}(\eta_c \to \omega\omega) = (1.96 \pm 0.08) \cdot 10^{-3}$.
The deviation from this value to the nominal result is taken as a systematic uncertainty, which amounts to 4.3%.

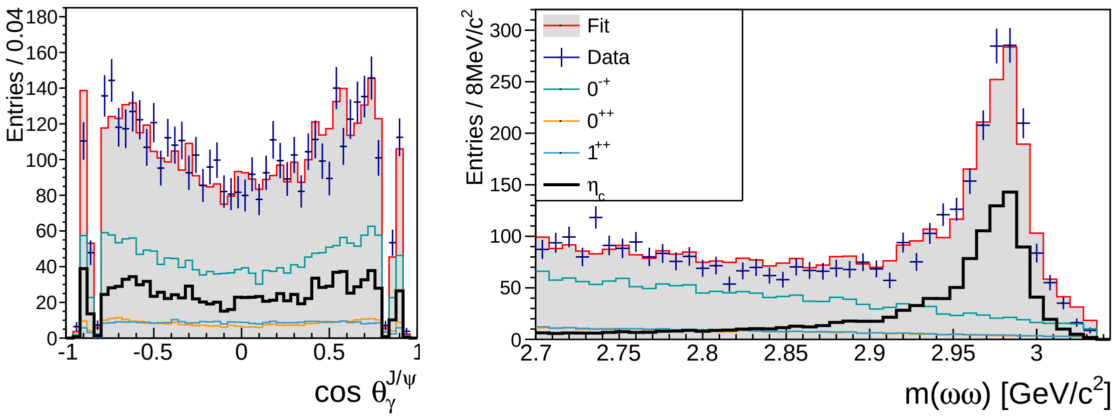

Fig. 5.5: Angular distribution of the radiative photon (left) and invariant $\omega\omega$ mass (right) for the fit with fixed values for the mass and width of the η_c.

Hypothesis	$\log(LH)$	n.d.f.	$m(\eta_c)$ MeV/c^2	$\Gamma(\eta_c)$ MeV/c^2	ϵ	N_{η_c}
$0^{-+}0^{++}1^{++}$	-4178.32	11	(2983.6)	(31.8)	3.31%	1125 ± 48

Table 5.4: Parameters of the best fit with fixed mass and width of the η_c.

Variation of the Fit Range

To determine the systematic uncertainty due to the choice of the $\omega\omega$ mass range, the fit for the nominal result, e.g. using the best hypothesis and floating parameters for $m(\eta_c)$

and $\Gamma(\eta_c)$, is performed again for a smaller and a larger mass range. While the nominal fit is performed in the mass range $2.65 \leq m(\omega\omega) \leq 3.1\,\mathrm{GeV}/c^2$, the lower boundary was varied by $\pm 50\,\mathrm{MeV}/c^2$ and the branching fractions were extracted in the same way as for the previously described fits. The branching fractions were calculated to

$$\text{Fit range } 2700 - 3050\,\mathrm{MeV}/c^2 : \ \mathcal{B}(\eta_c \to \omega\omega) = (1.96 \pm 0.10) \cdot 10^{-3}, \tag{5.5}$$

$$\text{Fit range } 2600 - 3050\,\mathrm{MeV}/c^2 : \ \mathcal{B}(\eta_c \to \omega\omega) = (1.80 \pm 0.08) \cdot 10^{-3}. \tag{5.6}$$

Table 5.5 lists the parameters for both fits. From the maximum observed deviation of the calculated branching fraction to the nominal result, a contribution to the systematic error of 4.3% was obtained.

Fit range MeV/c^2	$\log(LH)$	n.d.f.	$m(\eta_c)$ MeV/c^2	$\Gamma(\eta_c)$ MeV/c^2	ϵ	N_{η_c}
$2700 - 3050$	-3833.61	13	2983.6 ± 0.9	28.0 ± 1.4	3.30%	1124 ± 55
$2600 - 3050$	-4581.65	13	2982.0 ± 0.9	27.4 ± 1.5	3.35%	1044 ± 47

Table 5.5: Parameters of the fits with larger and smaller fit range, using the hypothesis of the best fit for the nominal result

Selection of Hypothesis

The ranking by the $\Delta AICc + \Delta BIC$ criterion only slightly preferred the best ranked over the second best hypothesis. To determine the systematic error introduced by the choice of the hypothesis, the branching fraction is extracted from the fit with the second best hypothesis, $\mathcal{H}_1 = \{\eta_c, 0^{-+}, 0^{++}, 2^{++}\}$, as well. Figure 5.6 shows the angular distribution of the radiative photon and the $\omega\omega$ invariant mass for this fit. Taking into account the parameters of the second best fit, which are listed in Table 5.6, the branching fraction was determined to be $\mathcal{B}_{\text{second}} = (1.92 \pm 0.08)\,\mathrm{MeV}/c^2$, which corresponds to a deviation of 2.1% from the nominal result. This deviation is taken as the systematic error due to the selection of the hypothesis.

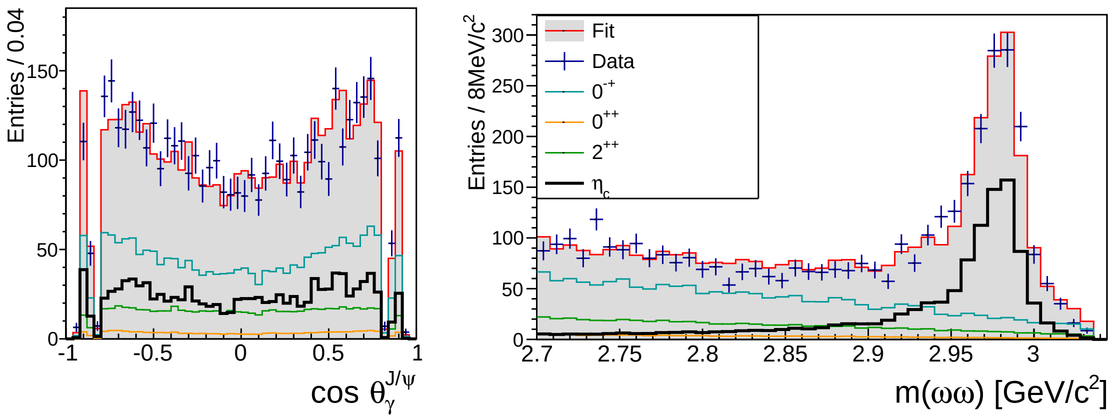

Fig. 5.6: Angular distribution of the radiative photon (left) and invariant $\omega\omega$ mass (right) for the second best fit

Hypothesis	$\log(LH)$	n.d.f.	$m(\eta_c)$ MeV/c^2	$\Gamma(\eta_c)$ MeV/c^2	ϵ	N_{η_c}
$0^{-+}0^{++}2^{++}$	-4202.93	21	2982.2 ± 0.8	27.5 ± 1.1	3.29%	1091 ± 46

Table 5.6: Parameters of the second best fit with the hypothesis $\mathcal{H}_1 = \{\eta_c, 0^{-+}, 0^{++}, 2^{++}\}$ in the η_c mass range

5.4 Final Result for the $\eta_c \to \omega\omega$ Branching Fraction

All contributions to the systematic error are listed in Table 5.7. This table also shows the quadratic sum of all systematic uncertainties, as well as the quadratic sum excluding the uncertainty of the branching fraction of the decay $J/\psi \to \gamma\eta_c$. The uncertainty in this branching fraction is dominating the total systematic uncertainty. Therefore, the final value of the branching fraction for the decay $\eta_c \to \omega\omega$ is given together with its statistical uncertainty, the uncertainty arising from the J/ψ decay branching fraction (labeled with "ext.") and the quadratic sum of all other systematic uncertainties.
The final value of the branching fraction is therefore given by:

$$\boxed{\mathcal{B}(\boldsymbol{\eta_c} \to \omega\omega) = (\mathbf{1.88} \pm \mathbf{0.09}_{\text{stat.}} \pm \mathbf{0.17}_{\text{syst.}} \pm \mathbf{0.44}_{\text{ext.}}) \cdot \mathbf{10^{-3}}} \tag{5.7}$$

Source	Uncertainty
Number of J/ψ events	0.5%
Track reconstruction (4 pions)	4%
Photon reconstruction (5 photons)	5%
External branching fractions:	
$J/\psi \to \gamma\eta_c$	23.5%
$\omega \to \pi^+\pi^-\pi^0$	0.8%
$\pi^0 \to \gamma\gamma$	0.03%
Systematic error of Q-factor method	0.9%
Fixed vs. floating $m(\eta_c)$,$\Gamma(\eta_c)$	4.3%
Variation of fit range	4.3%
Selection of hypothesis	2.1%
Quadratic Sum (all):	25.2%
Quadratic Sum (w/o $\mathcal{B}(J/\psi \to \gamma\eta_c)$):	9.2%

Table 5.7: Summary of the systematic uncertainties

6 Conclusion and Discussion of Part I

The radiative decay $J/\psi \to \gamma\omega\omega$ was studied using data recorded by the BESIII experiment within the scope of this thesis. The decay results in a highly complex final state of four charged pions and five photons, which were combined to select events containing two ω mesons accompanying the photon from the radiative decay of the J/ψ. The system under study in this analysis is the $\omega\omega$ vector meson pair, whereas no resonant structures are expected or observed in the $\gamma\omega$ system.

While the pion and photon mis-combination fraction was found to be negligible, a large contribution of background events containing only one ($\omega 3\pi$), or even none of the required ω resonances (6π) was observed. Further analysis steps greatly benefit from the application of an event based background subtraction method, based on probabilistic weights. The method and especially the choice of crucial normalization parameters were investigated and validated using toy Monte Carlo samples. After application of this method to the selected data set, a clean sample of 75245 ± 274 events was obtained and subjected to a full partial wave analysis.

In the first analysis stage, a model independent PWA in bins of the invariant mass of the $\omega\omega$ system was performed. The dominantly contributing partial waves could be determined by fitting the data under various different fit hypotheses for each bin individually. The best hypothesis for each bin was determined by exploiting two different information criteria from model selection theory, namely the BIC and the $AICc$ criterion. No condition on the continuity of the solution with respect to the $\omega\omega$ mass was required, so that this approach is regarded as unbiased. The model independent analysis revealed a dominant pseudoscalar (0^{-+}) contribution over the full mass range. Two enhancements at the beginning and at the end of the available phase space are observed and can be assigned a predominantly pseudoscalar character.

Furthermore, significant contributions are observed in the scalar (0^{++}) and tensor (2^{++}) partial waves. Various tests have shown, that although the differentiation between scalar and tensor contributions in single bins is not always unambiguously possible in this special case, the global behavior of both partial waves can be identified: Significant 2^{++} contributions are found in the direct vicinity of the $\omega\omega$ mass threshold ($m(\omega\omega) \approx 1.63\,\mathrm{GeV}/c^2$) as well as a rather broad contribution located around $m(\omega\omega) \approx 2\,\mathrm{GeV}/c^2$. A similar pattern is observed for the 0^{++} contribution, although here the two possible contributions located at $\sim 1.7\,\mathrm{GeV}/c^2$ and $\sim 1.9\,\mathrm{GeV}/c^2$ are not well separated and thus may be originating from broad and overlapping resonances. The contributions of other partial waves are found to be insignificant. It should be noted here, that especially the intensity of the dominant pseudoscalar contribution could be extracted with a very good stability regarding all systematic tests.

Based on the findings of the model independent analysis also a model dependent analysis was performed. Since it had to be expected that overlapping resonances contribute at least in the 0^{-+} and 0^{++} waves, a description utilizing the K-matrix formalism was chosen. The K-matrix parameterizations were restricted to describe the coupling to the $\omega\omega$ channel only. An iterative approach for the construction of various fit hypotheses based on all relevant states listed in [1] was employed. As an outcome of this strategy involving several hundred individual fits, a hypothesis was obtained for which a very good description of the data is achieved and which is additionally in very good agreement with the results of the model independent PWA. Especially the intensity of the 0^{-+} contribution could be excellently reproduced, while a reasonably good agreement for the scalar and tensor contributions is obtained.

In the final fit, the dominant pseudoscalar contribution was parameterized using five poles: The large enhancement at the $\omega\omega$ mass threshold is undoubtedly dominated by pseudoscalar contributions. This finding is consistent with the result of several previous experiments, where the enhancement was identified with the $\eta(1760)$, but stands in striking contrast to the results obtained by the Belle experiment in $\gamma\gamma$-fusion. Belle also observes a strong threshold enhancement in the invariant $\omega\omega$ mass, however their analysis suggests that the enhancement is dominated by 0^{++} and 2^{++} contributions. This could indicate, that the source of the pseudoscalar threshold enhancement shows only a relatively weak coupling to photons and thus could be assigned a gluonic content. However, with the approach utilized in this analysis, it was not possible to obtain a good agreement between fit and data when the enhancement is described by the $\eta(1760)$ alone. Especially the high-mass tail of the enhancement shows a rather sharp drop located at $1.86\,\mathrm{GeV}/c^2$ which coincides with the $\bar{p}p$ threshold. Allowing a coupling of the $\eta(1760)$ to the $\bar{p}p$ channel was investigated and found to be not sufficient to describe the data. Additionally, the possibility that the enhancement is dominated by two resonances was investigated. It was found, that the structure can be well described when an additional, slightly narrower, resonance is added, which could be identified with the $X(1835)$. This state is observed as a threshold enhancement in the $\bar{p}p$ channel [49]. The assumption of the presence of the $X(1835)$ is supported by [63], where the mixing angle between the $\eta(1760)$ and the $X(1835)$ is derived, and even a calculation for the mixing of both states in the $\omega\omega$ channel is given. In the higher mass region, the structure at $m(\omega\omega) \approx 2.98\,\mathrm{MeV}/c^2$ can be well described by the lowest lying charmonium state, the η_c, which has not been observed in its decay into a pair of ω mesons before.

Apart from the η_c, two additional states were necessary to describe the data in the mass region above $2\,\mathrm{GeV}/c^2$: A significant contribution located at an invariant mass of the $\omega\omega$ system of about $2134\,\mathrm{MeV}/c^2$ was identified with the $\eta(2225)$ meson, which was previously observed in the decay $J/\psi \to \gamma\phi\phi$ [48][52]. Additionally, another state with a mass of $2488^{+13}_{-14}\,\mathrm{MeV}/c^2$ and a width of $(215 \pm 15)\,\mathrm{MeV}/c^2$ was introduced. This state, called $X(2500)$, has so far only been possibly observed in a recent partial wave analysis of the $\phi\phi$ system produced in radiative J/ψ decays [52]. The observed mass and width of the $X(2500)$ are in very good agreement with those observed in the $\phi\phi$ channel. Including this state improves the fit quality significantly, however since this state is located in a region of low statistics in the invariant $\omega\omega$ mass, other explanations for the enhancement at about $2.5\,\mathrm{GeV}/c^2$ are possible (i.e. non-resonant processes).

As it was expected from the results of the model independent PWA, two resonances were identified to contribute to the 0^{++} and the 2^{++} waves each: The two scalar resonances were identified with the overlapping $f_0(1710)$ and the $f_0(2020)$ with a width of about $440\,\mathrm{MeV}/c^2$, while the tensor contribution can be described very well by the $f_2(1640)$ and the $f_2(1950)$ mesons. The latter of which has a relatively large width of approximately $470\,\mathrm{MeV}/c^2$. In fact, the $f_2(1950)$ is occasionally discussed as a candidate for a tensor glueball [64], since its decay pattern suggests a largely flavor-blind decay. Additionally, its

mass is close to the Lattice QCD prediction ($M_G \approx 2.39\,\mathrm{GeV}/c^2$) for the lightest tensor glueball [4]. Recent calculations based on an effective theory even suggest a broad tensor glueball state with a mass of $M \approx 2\,\mathrm{GeV}/c^2$, for which explicitly a significant coupling to the $\omega\omega$ channel is predicted [65].
Additionally, the branching fraction of the η_c into a pair of ω mesons was measured within the scope of this thesis. Therefore, a dedicated model dependent PWA was performed in the mass region of the η_c. The line shape of the η_c was parameterized under consideration of the energy dependent $M1$-transition matrix element for the radiative transition $J/\psi \to \gamma\eta_c$. The branching fraction was determined to be $\mathcal{B}(\eta_c \to \omega\omega) = (1.88 \pm 0.09_{\mathrm{stat.}} \pm 0.17_{\mathrm{syst.}} \pm 0.44_{\mathrm{ext.}}) \cdot 10^{-3}$, where the last uncertainty is due to the external branching fraction $J/\psi \to \gamma\eta_c$, which is only measured with large uncertainties. This is the first measurement of the $\eta_c \to \omega\omega$ branching fraction. The obtained value is well below the current upper limit of $\mathcal{B}(\eta_c \to \omega\omega) < 3.1 \cdot 10^{-3}$ listed in [1]. As for the previously measured decays of the η_c into pairs of vector mesons ($\rho\rho$, $\phi\phi$) also the branching fraction measured in this work is about one order of magnitude larger than the theoretical prediction given in [15].

Part II

Developments for the $\overline{\text{P}}$ANDA Electromagnetic Calorimeter

7 The $\overline{\text{P}}$ANDA Experiment

The second part of this thesis deals with hardware developments for the upcoming $\overline{\text{P}}$ANDA experiment (Antiproton ANnihilations at DArmstadt), which is a key project of the future accelerator facility FAIR, currently under construction near Darmstadt, Germany. $\overline{\text{P}}$ANDA will utilize a high precision antiproton beam impinging on a fixed target to perform various studies in the field of hadron physics. A brief overview over the envisaged physics program of the $\overline{\text{P}}$ANDA project as well as a description of the major detector components is given in this chapter. A more detailed description of the electromagnetic calorimeter (EMC) and especially the construction and developments for the forward endcap of the EMC are discussed in Chapter 8. Chapter 10 gives an overview over the construction and operation of the forward endcap prototype. Furthermore, the results of the analysis of test beam data recorded at the SPS (CERN) and ELSA (Bonn) accelerators are presented. Finally, the energy resolution for symmetric crystal matrices is extracted for the full energy range expected for the forward endcap.

7.1 Physics Program

The physics program of the future $\overline{\text{P}}$ANDA experiment is centered around investigations towards a better understanding of the strong interaction. While the mechanism responsible for the generation of the mass of elementary particles - the Higgs mechanism - has been confirmed by the discovery of the Higgs boson at the CERN LHC in 2012, the description of hadronic matter still largely remains unknown: The explanation for the origin of the mass of hadrons seems to be directly connected to the strong interaction, yet it is unknown how this process works. Similar examples are the confinement of quarks or the existence of exotic matter such as glueballs (gg, ggg) or hybrids ($q\bar{q}g$). As was discussed in the first part of this thesis, the BESIII experiment is one example for an experiment based on electrons and positrons as probes. In antiproton-proton annihilations however, particles with gluonic degrees of freedom are believed to be copiously produced directly - without any limitation on the accessible J^{PC} quantum numbers as in the case of e^+e^- annihilations. Despite all the advantages that the antiproton-proton annihilation provides for the study of hadrons, no hadron physics experiment utilizing this unique mechanism is running at the moment. This will change, when $\overline{\text{P}}$ANDA starts taking data in 2022. $\overline{\text{P}}$ANDA will be supplied with antiprotons by an accelerator (see 7.2.1) providing an unprecedented beam momentum resolution. The hadrons that can be produced at the $\overline{\text{P}}$ANDA experiment are shown in Figure 7.1 in dependence of antiproton beam momentum.
The spectroscopy of charmonia ($c\bar{c}$ mesons) and open charm mesons ($c\bar{q}$ or $\bar{c}q$ with $q \in \{u, d, s\}$) is a key part of the $\overline{\text{P}}$ANDA physics program and an important element towards the understanding of the strong interaction. Theoretical calculations and predictions, e.g. from Lattice QCD, are matching quite well the experimentally discovered charmonia below the $D\overline{D}$ threshold. However, above this threshold large discrepancies are observed. $\overline{\text{P}}$ANDA will be able to scan this high mass region and clarify the existence and properties of states that are poorly measured up to now or have not yet been observed,

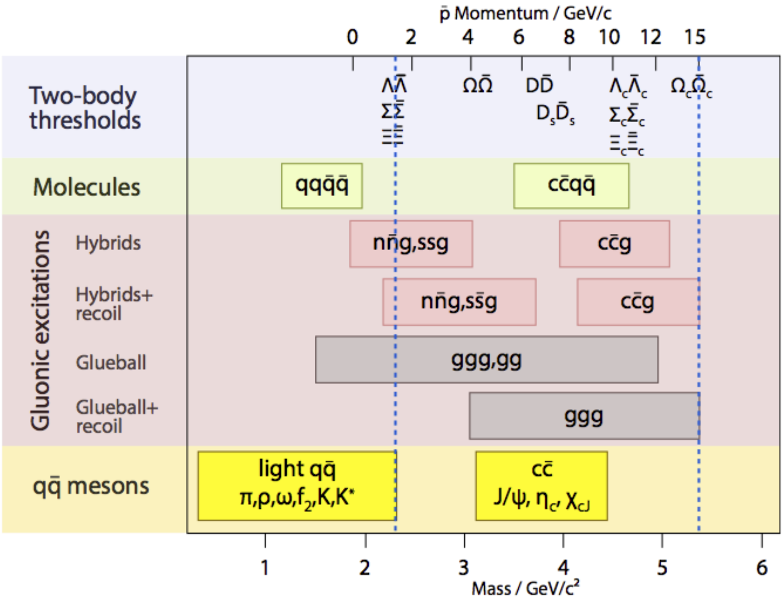

Fig. 7.1: Masses of hadrons that are accessible with the $\overline{\text{P}}$ANDA experiment

but predicted. Apart from charmonia, also hadrons with gluonic degrees of freedom such as hybrids or glueballs will be studied, which will be copiously produced in the gluon-rich environment of the antiproton-proton annihilation. Another goal of the diverse $\overline{\text{P}}$ANDA physics program is to obtain a better understanding of the nucleon structure by measuring i.e. the time-like electromagnetic form factor of the proton over a large momentum range via the reaction $\bar{p}p \to e^+e^-$. Furthermore, the origin of hadron masses can be addressed by the $\overline{\text{P}}$ANDA experiment by studying the process of embedding hadrons into nuclear matter. Previous measurements utilizing hadrons consisting of light quarks (u,d,s) have already been performed and have shown that the hadron mass changes in this process. $\overline{\text{P}}$ANDA will be able to perform such measurements with charmed hadrons for the first time. Another topic that will be addressed in a later stage of the $\overline{\text{P}}$ANDA experiment is the study of hypernuclei, which requires a modification of the detector hardware. Utilizing the antiproton beam, nuclei can be created that not only contain protons and neutrons, but also baryons containing a strange quark called hyperons. Nuclear spectroscopy can then be performed to investigate the interaction between the nucleons in the created hypernuclei.

7.2 The Facility for Antiproton and Ion Research (FAIR)

The FAIR facility is being built as an extension to the existing laboratories and accelerators of the GSI Helmholtzzentrum für Schwerionenforschung[1]. A sketch of the existing GSI and future FAIR facility is depicted in Figure 7.2. FAIR is a large-scale international project, which comprises experiments from different branches and disciplines: The two large experimental collaborations $\overline{\text{P}}$ANDA and CBM are performing studies towards a better understanding of quantum chromodynamics, while other pillars of research at FAIR include the investigation of nuclear matter (SPARC, FLAIR, ELISe, MATS), plasmas at

[1] Formerly known as Gesellschaft für Schwerionenforschung.

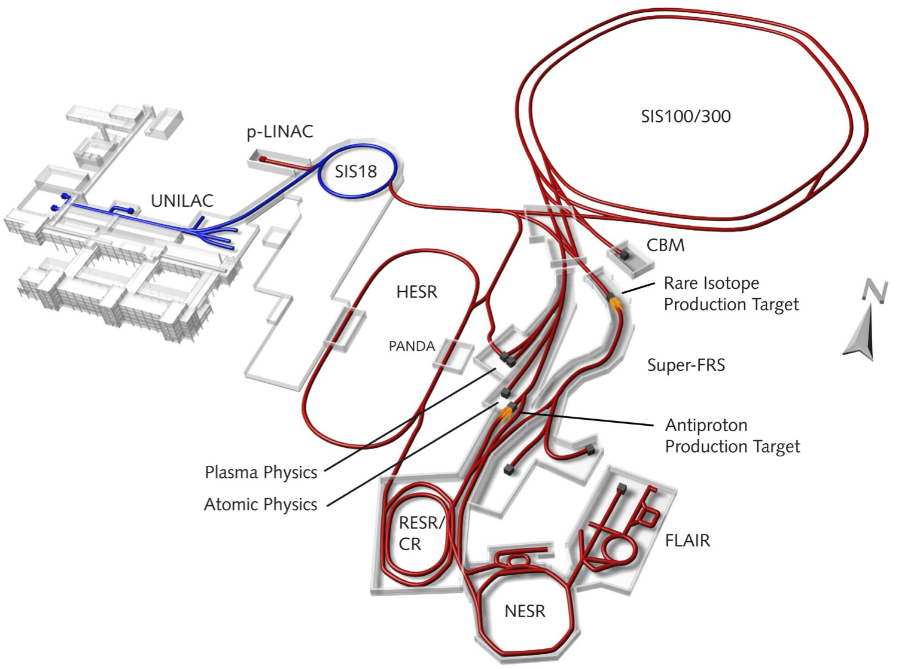

Fig. 7.2: Sketch of the future FAIR facility. The blue lines indicate the existing accelerators and beam lines of the GSI facility, while red lines shows the planned beam lines of FAIR. [66]

extremely high densities (HEDgeHOB, WDM) as well as experiments in the fields of biology and medicine (BIOMAT).

When the accelerator complex is finished, it will consist of two linear and eight circular accelerators. The largest of these will be the *Superconducting double-ring heavy Ion Synchrotron* SIS100, which will have a circumference of 1100 m. A special feature of this accelerator is its capability to accelerate two beams of different ion species at the same time, which are then fed into the subsequent storage rings. Protons can be accelerated up to an energy of 30 GeV in SIS100, while heavy ions reach energies of up to $35 - 45\,\mathrm{GeV/u}$. This feature allows for the parallel operation of multiple experiments. The protons which have been accelerated in SIS100 can either be delivered to the experiments that operate with a proton beam, or be fed to the antiproton production target. Here, the proton beam is impinging on a metal target (e.g. iridium) where inelastic collisions with the target material lead to the creation of particle-antiparticle pairs. For the creation of antiprotons this process can be written as $p + p \rightarrow p + p + p + \overline{p}$. The produced antiprotons are then collected and separated from other residue particles with a magnetic horn before they can be accumulated in the *Collector Ring* (CR). The antiprotons are then transferred into the *Recuperated Energy Storage Ring* (RESR), where they are cooled before they can be injected into the *High Energy Storage Ring* (HESR). This part of the FAIR beam line, which is marked with an orange dashed line in Figure 7.3, is the branch that is needed to operate the $\overline{\mathrm{P}}$ANDA experiment. As a consequence of a recent re-evaluation of the complete facility, FAIR will be realized in the so-called *modularized start version*, which means a staged construction. In this scenario, the RESR, in contrast to the CR and the HESR, will not be available in the initial phase of experiments, which puts a limitation to the initial performance of the $\overline{\mathrm{P}}$ANDA experiment (see Section 7.2.1). The start of the

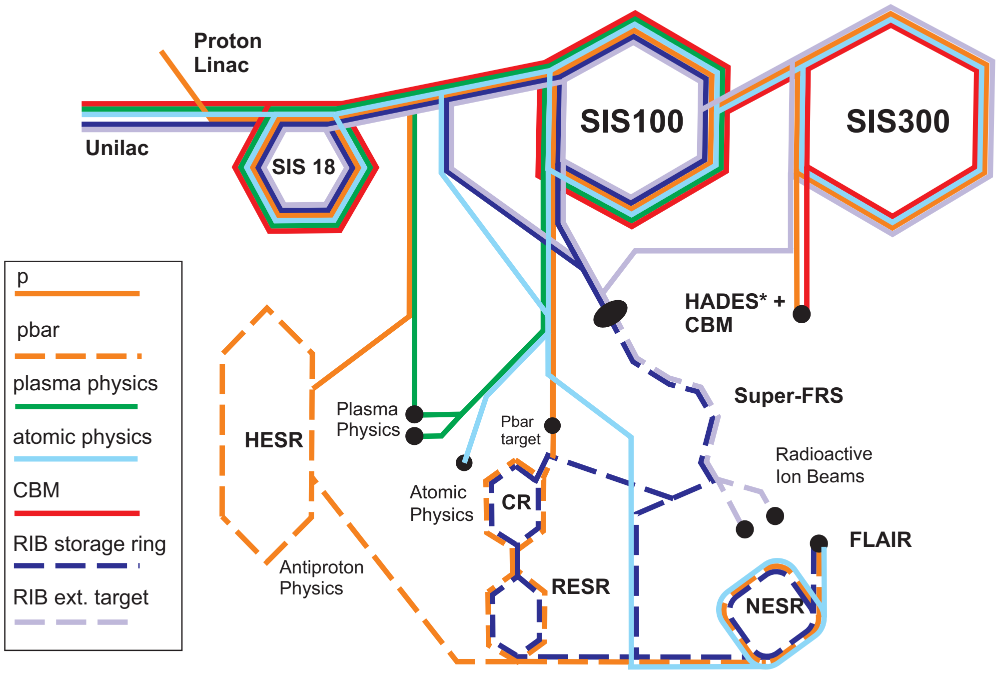

Fig. 7.3: Schematic overview of the different beam lines at the FAIR facility. The colors indicate the particle species and their intended use (see legend). [66]

experiments is foreseen for the year 2022. The HESR ring and the $\overline{\text{P}}$ANDA detector are discussed in more detail in the subsequent sections.

7.2.1 The High Energy Storage Ring (HESR)

The High Energy Storage Ring is the key component of the FAIR infrastructure required for the operation of the $\overline{\text{P}}$ANDA experiment. The detector will be placed in one of the two 132 m long straight sections of this slow ramping synchrotron storage ring, which has a total circumference of 574 m. The antiprotons that have been accumulated and cooled in the CR and RESR rings are injected into HESR at a momentum of 3.8 GeV/c and can then be decelerated down to 1.5 GeV/c or accelerated up to a maximum momentum of 15 GeV/c. This antiproton momentum translates to a center-of-mass energy $\sqrt{s}$ between 2.26 GeV and 5.48 GeV for collisions inside the $\overline{\text{P}}$ANDA detector with a proton target at rest. The proposed physics program of the $\overline{\text{P}}$ANDA experiment sets out stringent demands on the quality of the antiproton beam, especially in terms of the desired momentum resolution. To achieve the necessary performance, the ring will be equipped with a 4.5 MeV electron cooler[2], as well as a system for stochastic cooling. While the electron cooler is foreseen to be used for beam momenta up to 8.9 GeV/c, the stochastic cooling can be used for momenta larger than 3.8 GeV/c.

The ring can be operated in two distinct modes:

[2] In the first phase of the Modularized Start Version of FAIR, a 2 MeV electron cooler, which has recently been installed and tested in the COSY accelerator ring at Forschungszentrum Jülich will be used in HESR. [67]

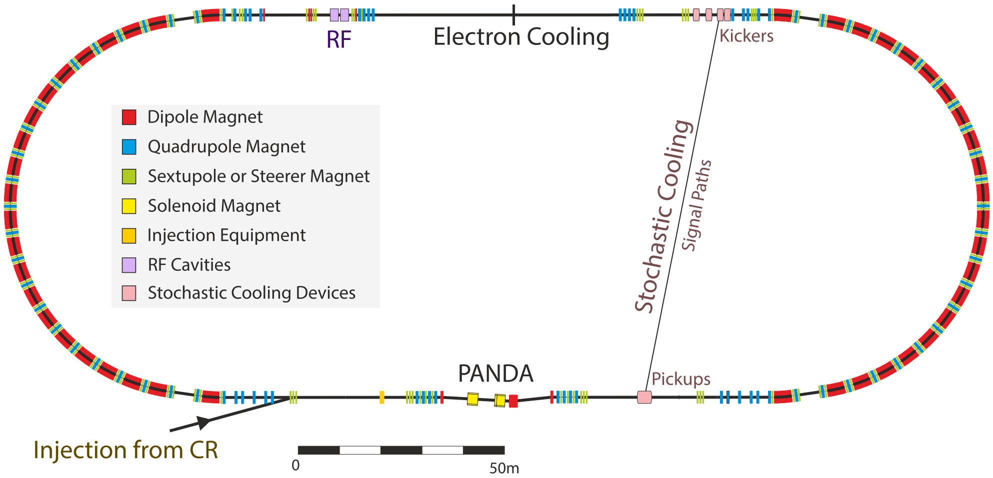

Fig. 7.4: Sketch of the High Energy Storage Ring. The $\overline{\text{P}}$ANDA detector is located in the middle of the lower straight section; the colored boxes indicate different types of magnets and technical components of the accelerator (see legend). [68]

- In the *High Luminosity Mode*, up to 10^{11} antiprotons can be stored in the HESR. A luminosity of up to $\mathcal{L} = 10^{32}\,\text{cm}^{-2}\text{s}^{-1}$ with a momentum resolution of $\Delta p/p \approx 10^{-4}$ can be achieved over the complete momentum range $(1.5 - 15\,\text{GeV}/c)$ in this mode.

- The *High Resolution Mode* can be used for antiproton beam momenta up to $8.9\,\text{GeV}/c$, to not exceed the operating range of the electron cooler. In this mode, only up to 10^{10} antiprotons can be stored in HESR, and the achievable luminosity is decreased by one order of magnitude ($\mathcal{L} = 10^{31}\,\text{cm}^{-2}\text{s}^{-1}$), but the momentum resolution can be improved to reach $\Delta p/p \approx 10^{-5}$.

7.3 Configuration of the $\overline{\text{P}}$ANDA Detector

The antiprotons delivered by the HESR collide with a fixed target inside the $\overline{\text{P}}$ANDA detector. This setup leads to an extremely asymmetric spatial distribution of the reaction products, since a large fraction of the particles created in the collision is moving in the direction of the beam, or with small angles to the beam axis. This phenomenon is called the *Lorentz-boost*, and leads to the separation of a fixed-target experiment into one detector part which surrounds the interaction point and a second detector part responsible for the precise measurement of particles under small angles with respect to the beam axis. In the case of the $\overline{\text{P}}$ANDA detector, these parts are called the *Target Spectrometer*, which incorporates the target system and thus surrounds the interaction point, and the *Forward Spectrometer*. Together, both parts of the detector cover almost the full solid angle. The complete detector setup has a length in beam direction of about 13 m and is depicted in Figure 7.5. The detector components of both sub-spectrometers will be shortly introduced in the following section.

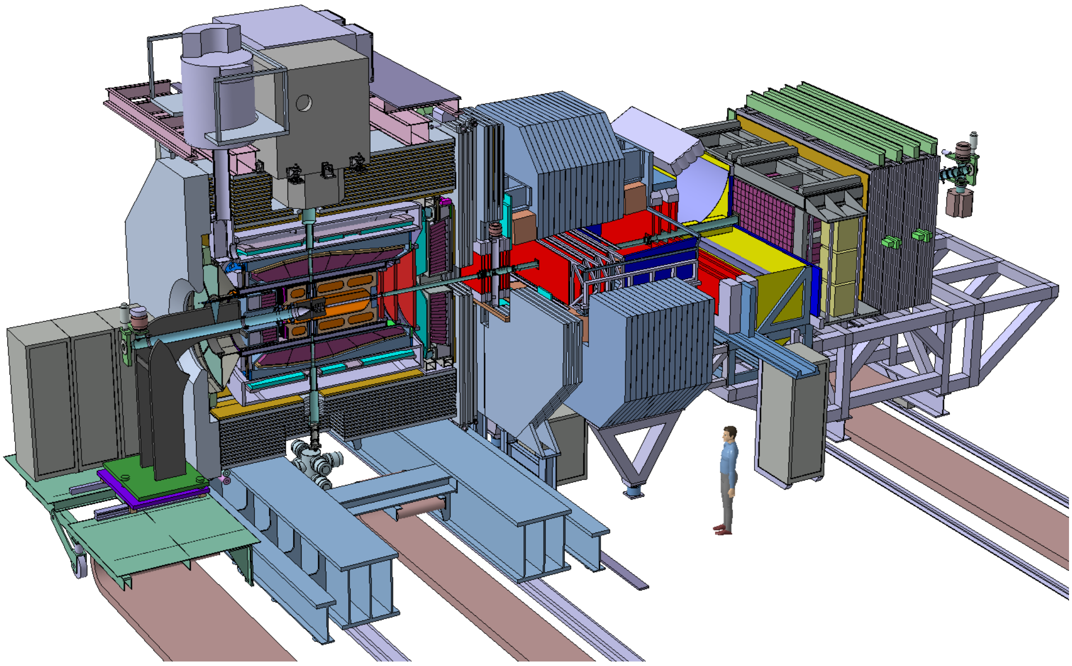

Fig. 7.5: Schematic view of the complete $\overline{\text{P}}$ANDA detector. The antiproton beam enters the detector from the left side.[69]

7.3.1 The Target Spectrometer (TS)

The *Target Spectrometer* (TS) has a cylindrically symmetrical form and surrounds the *Interaction Point* (IP), which is defined by the crossing of the beam pipe and the target pipe. Apart from the subsystem which is responsible for the detection and identification of muons, all other detector subsystems are placed inside a superconducting solenoid magnet, which will provide a magnetic field with a strength of 2 T. All components are shown in the schematic view of the TS in Figure 7.6.

Micro Vertex Detector (MVD)

The MVD is the innermost component of the $\overline{\text{P}}$ANDA tracking system. It is responsible for the precise measurement of tracks from charged particles in a close vicinity to the IP. Furthermore, this subdetector is essential for the detection of secondary (displaced) vertices, as e.g. the decay vertices of hyperons, which for the most part decay after they have left the interaction region and the beam pipe. The detector is composed of silicon pixel and strip sensor modules, arranged in a cylindrical pattern around the beam pipe and in the form of circular disks in beam direction. The thin silicon based sensors provide fast signals and an outstandingly good radiation hardness, while keeping a low profile in terms of the material budget. The signals generated by the strips and pixels of the MVD will be digitized by radiation hard front end *Application Specific Integrated Circuits* (ASICs) and read out using about 10M individual readout channels. The envisaged vertex resolution is in the order of 100 µm [70].

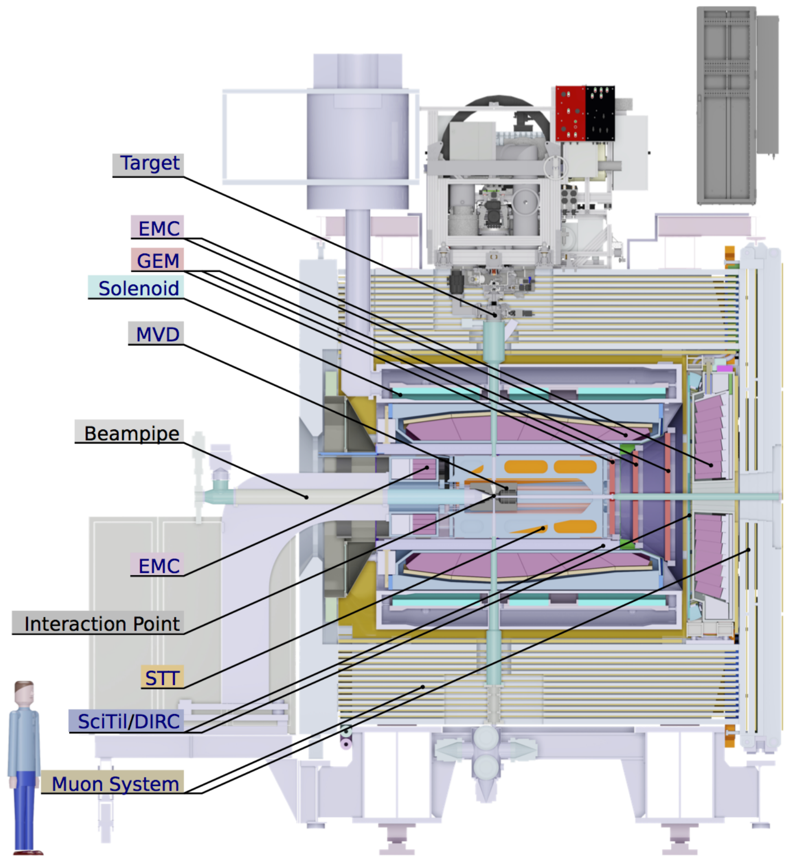

Fig. 7.6: Schematic view of the *Target Spectrometer* of the $\overline{\text{P}}$ANDA detector. The antiproton beam enters the detector from the left side. The interaction point is located approximately in the middle of the picture. [68]

The Straw Tube Tracker (STT)

Around the MVD, the central tracking detector of the TS, the *Straw Tube Tracker*, is located. It consists of ~ 4600 aluminized Mylar tubes (*straws*), which are operated at an overpressure of 1 bar to obtain a self-supporting rigid structure. The tubes have a diameter of 10 mm and a length of 150 cm each, while their wall thickness is only 27 µm. In the center of each tube, a 20 µm thick gold plated tungsten anode wire is placed, to which a high voltage is supplied. Charged particles traversing the tubes ionize the Argon-CO_2 gas inside the tubes, and the drift motion of the released electrons generates a signal at the anode wire. The tubes will be arranged in 27 planar layers around the MVD, whereas the innermost eight layers are skewed to achieve an acceptable resolution of ~ 3 mm in beam direction. The envisaged spatial resolution in the plane perpendicular to the beam is ~ 150 µm with this setup. Apart from their main purpose, both tracking detectors (MVD and STT) are capable of delivering valuable information for the identification of particles by measuring the differential energy loss (dE/dx) of traversing particles. [70]

The Gas Electron Multipliers (GEMs)

Since the geometrical acceptance of the STT is limited by its cylindrical design to angles larger than 22°, three additional disk-shaped tracking stations will be placed further downstream of the target. These stations are equipped with Gas Electron Multiplier (GEM) foils, which provide a position resolution in the order of 100 µm. Due to the Lorentz-boost, the hit rate in these detectors will be much higher than for the STT tubes. A particle flux of up to $3 \cdot 10^4\,\mathrm{cm}^{-2}\mathrm{s}^{-1}$ is expected. [70]

Čerenkov and Time Of Flight Detectors

The next layer of the $\overline{\text{P}}$ANDA detector comprises two subsystems which are mainly used for the identification of the particles (PID). The first of these subsystems, the DIRC detector (Detection of Internally Reflected Čerenkov light), consists of a barrel part and a disc shaped detector part placed further downstream perpendicular to the beam axis. The main components of the DIRC detectors are radiators made of fused silica. When a charged particle traverses this material with a velocity that is larger than the speed of light in this medium, it emits characteristic Čerenkov light. The light is reflected in the silica bars (barrel part) or the disc-shaped radiator parts until it is read out with Micro Channel Plate Photomultiplier Tubes (MCP-PMTs) at the outer edges of the radiators. By measuring the opening angle of the emitted Čerenkov light cone, the mass of the incident particle can be determined. Very slow particles cannot be identified with the help of the DIRC system because they do not emit Čerenkov light in the radiators, so that a second PID detector is placed directly adjacent to the barrel DIRC. This detector measures the time of flight of incident particles with a resolution of roughly 100 ps and consists of 5760 plastic scintillator tiles, which will be read out with two Silicon Photomultipliers (SiPMs) per tile.

The Electromagnetic Calorimeter (EMC)

The outermost subdetector inside the volume of the superconducting solenoid coil is a homogeneous crystal calorimeter. The energy of photons, electrons and positrons is measured with this detector, which is equipped with about 15500 scintillating lead-tungstate ($PbWO_4$) crystals. Since this thesis covers work related to test measurements and the construction of the EMC, this subdetector will be discussed in more detail in Chapter 8.

The Muon Detector

The muon detection system is the only subdetector of the TS that is placed outside the magnet coil, since muons will easily penetrate all inner detector components due to their extremely weak interaction with matter. The active detector elements of the muon system (Mini Drift Tubes) are placed inside the massive iron yoke of the solenoid magnet. In total 13 alternating layers of MDTs and iron with a thickness of 3 cm are foreseen for the barrel part of the detector, while due to higher particle energies the thickness of the iron plates is increased to 6 cm in forward direction. [70]

Target Systems

Two different target systems are under development for the $\overline{\text{P}}$ANDA detector. Apart from the operational parameters of the accelerator, the target density defines the achievable luminosity and is expected to reach $4 \cdot 10^{15}$ H_2 molecules per square centimeter. In the first phase of the experiment, a *Cluster Jet Target* will be used, for which the development is very far advanced. The second target option, a so-called *Pellet Target* is still under development and is foreseen as an upgrade option for a later stage of the experiment. In both target systems, cold hydrogen gas is used as the target material, which is pressed through a thin nozzle. In the case of the *Pellet Target*, the nozzle is oscillating at supersonic frequencies. By creating a lower pressure in the volume directly beneath the nozzle, it is ensured that the hydrogen leaves the nozzle in the form of small droplets (diameter: $24 - 40\,\mu$m), which then freeze while entering the vacuum system of the target/beam-pipe. The frozen droplets are then called pellets and resemble discrete, evenly shaped objects that traverse the antiproton beam. One downside of this technique is the large variation of the instantaneous luminosity, when a pellet crosses the beam. In the case of the *Cluster Jet Target*, small objects called *clusters*, which are consisting of $10^3 - 10^6$ hydrogen atoms, are created at the nozzle. These clusters can have very different shapes and form a cluster stream with a sizable lateral spread which crosses the antiproton beam. By this, an uncertainty in the definition of the interaction point in beam direction of several millimeters is introduced.

7.3.2 The Forward Spectrometer (FS)

Particles that are emitted under small angles to the beam axis in forward direction, namely $< 10°$ in horizontal and $< 5°$ in vertical direction, are outside the acceptance of the target spectrometer and are detected in the forward spectrometer, which is depicted in Figure 7.7. A central component of this part of the detector is a 2 Tm dipole magnet, which deflects the charged particles entering the FS, so that their momentum can be determined by measuring the tracks of the particles with straw tubes inside the dipole magnet. The beam antiprotons are deflected by this magnet by about 2.2° at the maximum beam momentum, so that additional correction magnets before and behind the $\overline{\text{P}}$ANDA detector are necessary.

Forward Tracking System

Apart from the straw tubes that are placed inside the dipole magnet, four additional tracking stations consisting of four double layers of straw tubes, each, are foreseen for the FS. Two stations will be located upstream of the FS dipole, while the other two will be placed downstream of the dipole and the RICH detector (see Figure 7.7). The outer layers of these stations will be equipped with vertically aligned straws, while for the inner layers the straws are inclined by $\pm 5°$ to provide a two-dimensional position measurement.

Forward Čerenkov and Time Of Flight Detectors

Similar to the setup in the TS, the FS will be equipped with two types of detectors for the identification of particles. Low momentum particles are identified by a time of flight detector based on plastic scintillator bars/tiles. One layer of plastic scintillators is integrated into the dipole magnet to measure particles that cannot leave the magnet due to their small momentum. A wall of scintillators placed further downstream will provide π/K and K/p separation for momenta up to 2.8 GeV/c and 4.7 GeV/c, respectively. Particles with higher momenta will be identified by a Ring Imaging Čerenkov detector (RICH), for which Aerogel and Decafluorobutan (C_4F_{10}) will be used as an active medium. With this

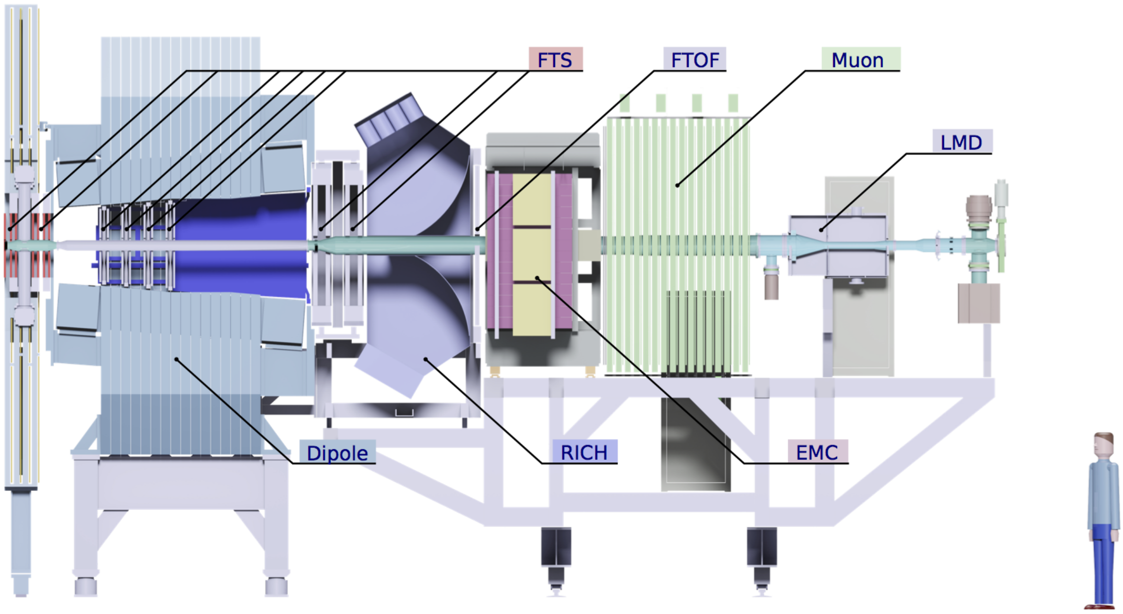

Fig. 7.7: Schematic view of the Forward Spectrometer of the $\overline{\text{P}}$ANDA detector. The antiproton beam enters the detector from the left side. [68]

detector, a good $\pi/K/p$ separation in a momentum range of 2 GeV/c up to 15 GeV/c will be possible. The Čerenkov light generated in the radiators will be focused by a lightweight mirror onto an array of photo tubes that are located outside of the active volume.

Forward Electromagnetic Calorimeter

The energy of photons and electrons is determined with a sampling type Shashlyk-calorimeter. In this design, sandwiches of lead plates and scintillator tiles are used, which are read out with wavelength-shifting fibers that are passing through each sandwich-block and are finally coupled to photo-multiplier tubes. Calorimeters of a similar design were able to achieve an energy resolution of $4\%/\sqrt{E[\mathrm{GeV}]}$.

Forward Muon Detectors

In about 9 m distance from the IP, the forward muon range system will be placed directly downstream of the forward EMC. The design of this subdetector is very similar to that of the muon detectors in the TS: It consists of absorbers which incorporate a number of drift tubes. These tubes are adapted for higher momenta for the use in the forward muon range system.

Luminosity Detector

Another component of the $\overline{\text{P}}$ANDA detector is situated downstream of the Forward Muon Detectors, just before the HESR correction magnet bends the beam back into the straight section of the accelerator. This detector is responsible for the precise determination of the online luminosity by measuring the angle of elastically scattered antiprotons under extremely small angles to the beam axis ($3-8$ mrad). The antiprotons will be detected with thin silicon based pixel detectors, which are arranged on four disks that are oriented perpendicular to the beam axis. The disks are placed as close as possible to the beam axis and the complete setup is operated in a vacuum chamber, to reduce scattering of the antiprotons before they hit the detector disks.

Trigger Concept and Data Acquisition

A novel concept for the realization of a trigger and data acquisition system will be employed for the $\overline{\text{P}}$ANDA experiment: When the experiment is running at the full design luminosity of $2 \cdot 10^{32}\,\text{cm}^{-2}\text{s}^{-1}$, an antiproton-proton collision rate of up to $2 \cdot 10^{7}\,\text{s}^{-1}$ is expected. Due to the complexity of the detector and the diverse physics program, a global monolithic trigger as it is and was used in many particle physics experiments, is not suited for the $\overline{\text{P}}$ANDA experiment. To allow for the desired flexibility in terms of event selection, all subdetectors are free-running autonomous entities. Each subsystem uses its own signals for triggering, before the data is preprocessed by the subdetector's frontend electronics. Only after relevant information has been extracted from the signals, a precise time stamp is added and the signals are transmitted to the compute nodes, where they are buffered. Flexible event selection algorithms that are running on the compute nodes can access these buffers and decide to retain or discard data in the buffer. With this approach, high-level trigger conditions can be implemented without changing the performance, its programming or even the hardware of any detector component.
Since the EMC of the target spectrometer is of importance for this thesis, the readout scheme and the frontend electronics for this detector subsystem will be explained in more detail in 8.5.2.

8 The Electromagnetic Calorimeter

This thesis deals in part with developments contributing to the construction of the forward endcap of the electromagnetic crystal calorimeter, which is located in the Target Spectrometer. The operating principle and details concerning the construction of this subdetector will be presented in this section.

The main purpose of an electromagnetic calorimeter is to precisely measure the energy of photons, electrons and positrons. To achieve this, the particle is stopped in a medium of high density, while at the same time a measurable signal is generated that allows to quantify the amount of energy that was deposited in the absorber medium. Usually, scintillating materials are used to generate these signals. Basically one can distinguish between *sampling* and *homogeneous* calorimeters: In sampling calorimeters, mostly layers of lead are used as absorber material, while thin plastic scintillators are placed in between them. This type of calorimeter is foreseen to be installed in the forward spectrometer. Alternatively, calorimeters consisting of just one single material that simultaneously serves as absorber and as active medium can be constructed. For this purpose optically transparent, inorganic crystals are used, which also generate scintillation light when traversed by a particle.

8.1 Energy Loss of Photons and Electrons in Matter

Independent of the type of calorimeter, the underlying mechanisms responsible for the energy loss of the particle are the same. In general, the interaction of a photon with a dense medium can be described by three processes, depending on the energy of the photon: For very low photon energies of less than 1 MeV, the *photoelectric effect* dominates. The incident photons are able to dislodge electrons from the atomic shells of the atoms in the crystal. The cross section for this process shows characteristic discontinuities (absorption edges) when the corresponding thresholds for the ionization of different atomic levels are reached. The complete energy of the incident photon is transferred to the electron that was hit. Figure 8.1a shows the fractional energy loss of photons in lead for the different contributing processes. The absorption edges are clearly visible in the region of photon energies below 1 MeV. The dominating effect in the energy range between 1 and 5 MeV is the *Compton Effect*. The incident photon is scattered elastically on an electron of the atomic shell of a crystal atom and thus only transfers part of its energy to the electron. The amount of energy that is transferred to the electron depends on the incident angle of the photon.

For photon energies larger than 5 MeV, the process of *pair production* becomes the dominant contribution to the cross section. In this process, an incoming photon creates an electron-positron pair, when it is in the vicinity of an atomic nucleus and can thereby interact with the Coulomb field of this nucleus. The photon energy threshold for the creation of an e^+e^- pair is given by $E_{\gamma,\mathrm{thr}} = 2m_e c^2 \cdot (1 + 1/m_N)$, with m_N being the mass of the nucleus.

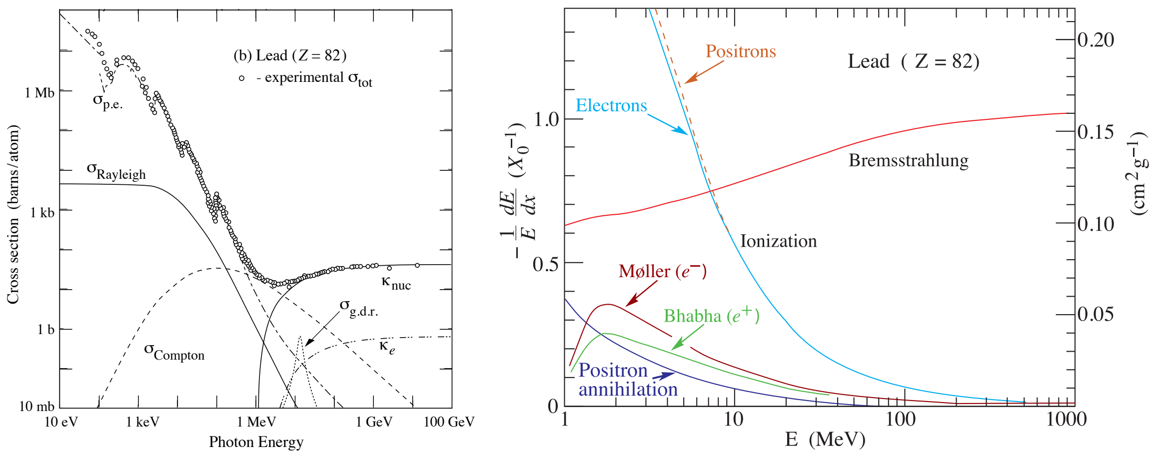

(a) **(b)**

Fig. 8.1: (a): Total cross section for the interactions of photons in lead vs. the incident photon energy. $\sigma_{\text{p.e.}}, \sigma_{\text{Compton}}$ and κ_{nuc} denote the contributions due to the photoelectric effect, Compton scattering and pair production in a nuclear field. (b) Fractional energy loss of electrons and positrons in lead [1]

In the case of light charged particles like electrons and positrons that are entering a dense material, the two effects of ionization and bremsstrahlung are the most important effects to be considered. For energies below 10 MeV, electrons and positrons predominantly lose energy due to collisions with electrons of the atomic shells of the material they enter, which are dislodged from the nucleus by the collision (ionization). At higher energies, losses due to bremsstrahlung become more important: When an electron or positron is decelerated in the Coulomb field of an atomic nucleus, the loss in kinetic energy leads to the emission of electromagnetic radiation. The fractional energy loss of electrons and positrons in lead due to both of these effects is shown in Figure 8.1b. It should be noted, that other particles, for which the energy loss is described by different processes, can also enter the EMC. The energy loss of heavy charged particles like protons or muons can be calculated with the Bethe-Bloch equation in a wide energy range. A detailed description of the corresponding phenomena is given in [1].

8.2 Electromagnetic Showers and the Scintillation Process

Electrons or positrons that were created in the process of pair production will lose energy in the medium due to the same processes as the incident light charged particles. When their energy is large enough, they will create bremsstrahlung photons, which themselves can create an e^+e^- pair again. This cascade of alternating processes of energy loss continues, until the energy of the contributing particles falls below the threshold for pair production. In summary, a single incident photon or electron/positron creates a large number of secondary particles in the medium. This is called an electromagnetic shower. The number of secondary particles in such a shower can be roughly estimated using the *radiation length* X_0: The radiation length is a characteristic property of the absorber material. It denotes the distance, after which the energy of an incident electron is reduced to $\frac{1}{e}$ of its initial value due to deceleration. For photons, the mean free path until pair production occurs, is given by $\frac{7}{9}X_0$. From this it can be estimated, that the number of secondary particles in an electromagnetic cascade roughly doubles per radiation length (see Figure 8.2a). The purpose of a calorimeter is to measure the complete energy of the incoming particles, thus it has to be ensured that the created shower is contained within the active volume of the EMC. For homogeneous crystal calorimeters usually a value of $\sim 20 \cdot X_0$ is chosen as the longitudinal dimension of the crystals. The second characteristic property of a shower is the size of its lateral extension, characterized by the *Molière radius* R_M. This property is defined as the radius of a cylinder, in which 90% of the energy of an incident particle are contained. A cylinder with a radius of $r = 3.5 \cdot R_M$ contains 95% of the initial energy of a particle. Mostly, the lateral granularity of calorimeter segments (e.g. crystals) is chosen to be in the order of one Molière radius. To reconstruct the initial energy of a particle entering the calorimeter the signals from several single crystals must be considered. Such a group of crystals that contribute to the measurement of the energy of a single incoming particle is called a *cluster*.

The processes described above are responsible for the energy loss of particles entering the calorimeter. However they do not explain how signals are generated that can be measured. The special characteristic of scintillating materials is, that the number of luminescence photons created by conversion is proportional to the energy that was deposited in the material. In the case of inorganic crystals, this effect can be explained with the help of the electronic band structure of a solid material: Due to ionization, electrons are energetically elevated from the valence to the conduction band. Electron-hole pairs are created, which are interpreted as bound states. In solid-state physics these states are often referred to as quasi-particles. These so-called *excitons* can move through the crystal lattice, until they dissociate. In most cases, this dissociation occurs due to a collision of the exciton with a phonon in the crystal lattice; However there is a small probability for the dissociation of an exciton via the emission of a (visible) photon. To increase the probability for the emission of scintillation photons, small amounts of impurities are introduced into the crystal at the time of production, which is called *doping*. By adding these impurities, additional metastable *activator* states are introduced in between the valence and the conduction band, via which an exciton can dissociate under the emittance of a photon (see Figure 8.2b).

The wavelength of the scintillation photons is mostly in the ultraviolet or visible range, which explains the necessity of optical transparency for scintillation crystals. The scintillation light can be measured with a photosensitive detector that transforms the light into an electrical signal.

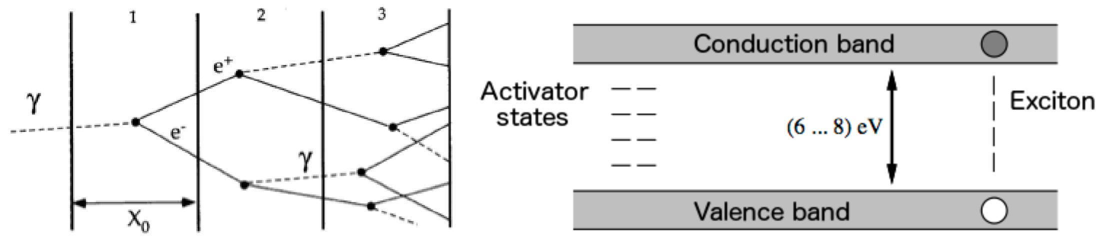

(a) (b)

Fig. 8.2: (a) Propagation of an electromagnetic shower [72].
(b) Band structure in doped inorganic scintillation crystals (adapted from [73])

8.3 Lead Tungstate Scintillation Crystals

The scintillator material that was chosen to be used for the $\overline{\text{P}}$ANDA EMC is called Lead Tungstate ($PbWO_4$, also short PWO). This material is very well suited to fulfill the requirements imposed by the operational parameters and design of the $\overline{\text{P}}$ANDA detector: Especially in the region of the forward endcap, high count rates per single calorimeter module are to be expected (up to $1 \cdot 10^6\,\text{s}^{-1}$), leading to an expected radiation dose of approximately $125\,\text{Gy}/a$ [74]. Furthermore, the size of the inner detectors of the target spectrometer, including the EMC, define the dimensions of the solenoid coil, which is a major cost factor of the detector and thus should be kept as compact as possible. PWO has very short decay times of 10 ns and 30 ns for the fast and the slow component of the scintillation light, respectively, as well as a comparably high density of $\rho_{\text{PWO}} = 8.3\,\text{g}\,\text{cm}^{-3}$, while at the same time providing a good radiation hardness. Already with a crystal length of 20 cm an equivalent of 22 radiation lengths (X_0) can be achieved, so that even particles with the highest energies to be expected at $\overline{\text{P}}$ANDA ($\sim 14.6\,\text{GeV}$) can be completely stopped. A disadvantage of this material is its comparably low light yield: The electromagnetic calorimeter of the CMS detector at the CERN Large Hadron Collider is equipped with lead tungstate crystals of the first generation (PWO-I), which only reach 0.3% of the light output of commonly used natrium iodide (NaI) crystals. It was possible to increase the light yield by decreasing the doping of the crystal material by about a factor of two, so that the material used for the $\overline{\text{P}}$ANDA EMC reaches 0.6% of the NaI light yield. The differences between the material used by the CMS experiment and the improved PWO-II material are listed in Table 8.1. Furthermore, the light yield of PWO can be significantly increased by cooling down the crystals: At lower temperatures the phonon density in the crystal decreases, so that the probability for the dissociation of an exciton via emission of a photon increases correspondingly. The $\overline{\text{P}}$ANDA EMC will be operated at a temperature of -25° C, which results in an increase of the light yield by a factor of ~ 4 when compared to the light yield at $+25^\circ$ C. Unfortunately, the new PWO-II material shows an even stronger dependency of the light yield with respect to the temperature than its predecessor PWO-I (cf. Table 8.1), so that it becomes necessary to monitor and regulate the temperature of the $\overline{\text{P}}$ANDA EMC crystals very precisely.

Characteristic	PWO-I (CMS)	PWO-II ($\overline{\text{P}}$ANDA)
La, Y doping concentration level (ppm)	100	40
Light yield of full size (20cm) crystal with PMT-readout at room temperature (photo electrons/MeV)	$8-12$	$17-22$
Light yield temperature coefficient at $T = +20°$C (%/K)	-2.0	-3.0
EMC operating temperature (°C)	$+18$	-25

Table 8.1: Characteristics of PWO-I and PWO-II crystals [75]

8.4 Design of the $\overline{\text{P}}$ANDA EMC

8.4.1 Requirements and Design Considerations

The broad physics program of the $\overline{\text{P}}$ANDA experiment sets strong limitations on the performance of the EMC: Signals corresponding to photon energies in the range of 10 MeV to 14.6 GeV at single crystal hit rates up to $10^6\,\text{s}^{-1}$ must be detected and processed by the subsequent electronics. Apart from the large dynamical range, the requirements on the expected performance of the EMC also include stringent limitations on the energy, time and spatial resolution as well as a high signal-to-noise ratio. A part of the $\overline{\text{P}}$ANDA physics program is to perform charmonium spectroscopy. It is of utmost importance for these studies to reconstruct all final state particles from the decays of heavier mesons. The light mesons π^0 or η are abundantly produced in various decays of heavier resonances and both are most commonly reconstructed in their decays into two photons. To ensure a high reconstruction efficiency of these light mesons, the photon detection threshold should be as low as possible and the EMC must cover a large part of the full solid angle to minimize the photon loss rate due to geometrical acceptance. Simulation studies have shown that already at a photon detection threshold of $E_{\gamma,\text{thr}} = 10\,\text{MeV}$ about $0.5 - 1.0\%$ of all π^0 mesons can not be reconstructed anymore [74]. Apart from the simple angular coverage, also the granularity, or segmentation, of the calorimeter is an important design parameter: For photons, the EMC is the only detector which can provide information on their direction of motion. Since high photon multiplicities per event are expected, a fine segmentation of the calorimeter modules is desirable to enable a clean separation of signals from single photons. Considering a π^0 meson with a momentum of 14.6 GeV, which is about the highest momentum achievable in $\overline{\text{P}}$ANDA, the corresponding opening angle between the two photons from the decay of the π^0 amounts to $0.5°$. A particle with a momentum as large as this will most likely impinge on the crystals of the forward endcap (or even leave the acceptance of the TS), which is located in a distance of approximately 2 m to the interaction point. The distance between the two points of impact on the endcap crystals is only about 20 mm in this case. These considerations define the required lateral segmentation of the calorimeter.

Further Monte Carlo simulations have shown that a single crystal threshold of $E_{\text{xtl}} = 3\,\text{MeV}$ and an energy equivalent of the electronic noise of a single readout unit of $\sigma_{\text{noise}} = 1\,\text{MeV}$ must be achieved in order to guarantee a clean reconstruction of photons with energies as low as 10 MeV. The targeted design value of the energy resolution is thus given as

$$\frac{\sigma_E}{E} = \frac{a}{\sqrt{E[GeV]}} \oplus b, \tag{8.1}$$

with $a \leq 2\%$ and $b \leq 1\%$ [74]. The first term in this parameterization of the energy resolution describes statistical effects like shower fluctuation and photo-electron statistics, while the second term is responsible for the description of inhomogeneities in the active material, calibration uncertainties and other systematic effects. In general, a third term ($\oplus\ c/(E[GeV])$) is part of the parameterization, which describes the part of the relative energy resolution that is created by electronic noise of the readout devices. However, this term has not been taken into account in the technical design report (TDR) of the EMC [74].

The energy resolution of a detector prototype equipped with PWO-II crystals has been determined in the scope of this work. Here, the parameterization given in 8.1 has been used to obtain parameters comparable to the design considerations given in the TDR. Together with the crystals, also the photo detectors and the first stage of the front-end electronics, the preamplifiers, must be operated at a temperature of $-25°$C in a high radiation environment - and even more constraining - inside the 2 T field of the solenoid magnet. The presence of the magnetic field and the spatial limitations render the use of common photomultiplier tubes impossible. For the largest part of the $\overline{\text{P}}$ANDA EMC silicon avalanche photo diodes have been chosen as photo sensors, while in the innermost part of the forward endcap small sized two-stage photo tubes have been selected. Both of these detectors will be described in more detail in Section 8.5.1.

8.4.2 Geometrical Design of the EMC

With regard to all the considerations and constraints mentioned in the previous section, the design of the $\overline{\text{P}}$ANDA EMC has been finalized and the production of single components has started recently. The calorimeter consists in total of 15744 lead tungstate crystals, which will be installed in three mechanically independent subdetectors: A cylindrically symmetrical *barrel* comprised of 11360 crystals will be concluded by a forward (3856 crystals) and a smaller backward endcap (524 crystals). Figure 8.3 shows the barrel and forward endcap parts. All crystals will have a length of 200 mm, which corresponds to $22 \cdot X_0$ of lead tungstate, while the tapering of the crystals differs with the position of the crystal in the calorimeter. The crystals in the endcaps are only slightly (forward endcap) or not tapered at all (backward endcap), while the crystals foreseen for the barrel part are produced in eleven different geometrical shapes. All crystals will be wrapped with a highly reflective foil (DF2000MA by 3M) to reflect light back into the crystal on all sides but the rear face, where the photodetectors will be attached. By using this specific foil, the light output can be increased by a factor of about 2.3 compared to no usage of reflective foil [76].

The barrel part of the EMC has a length of 2.5 m and an inner diameter of 1.14 m, covering the angular range of $22° \leq \vartheta \leq 140°$. The forward endcap was designed to be large enough to allow for a small overlap of its angular coverage given by $5° - 10° \leq \vartheta \leq 23.6°$ with the barrel part in order to avoid a gap in the geometrical acceptance in this important region of the detector. The backward endcap covers the angualar range between 151.4° and 169.7° which results in a total angular coverage of the TS EMC alone of about 93.4% of the full solid angle in the lab frame. Caution was taken to ensure that the symmetry axis of each crystal points off the target position in all three parts of the calorimeter, so that photons emerging from the interaction point cannot be lost by passing through a gap between two crystals. For the endcaps the off-points, to which the crystal axes are pointing are located 950 mm upstream (forward endcap), and 200 mm downstream (backward endcap) of the interaction point, while the barrel crystals are pointing towards an imaginary ring around the beam axis, located at a position of $z = +37$ mm along the beam axis.

In the following, the design, construction and development of the forward endcap will be discussed in more detail, since the studies presented in this thesis deal with the performance of this EMC subdetector. More details on the barrel and backward endcap subdetectors can be found in [74],[77] and [78].

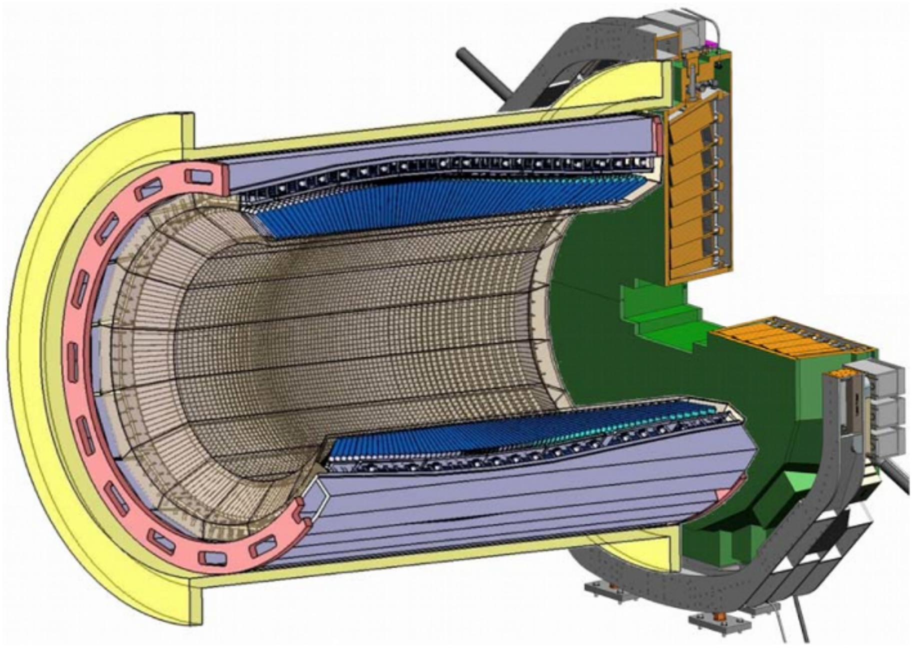

Fig. 8.3: CAD drawing of the $\overline{\text{P}}$ANDA EMC. The antiproton beam enters from the left side. This picture shows the barrel and forward endcap parts, while the backward endcap is omitted. [71]

8.5 The Forward Endcap of the EMC

In the past years until today, the design and realization of the forward endcap is being persued at the Institut für Experimentalphysik I at Ruhr-Universität Bochum in cooperation with the universities of Groningen (RUG/KVI, Netherlands), Bonn, Giessen (Germany) and Uppsala (Sweden). The geometrical shape of the endcap is that of a disc with an asymmetrical opening in the center, through which the beam pipe will be led. All particles passing through this opening will leave the acceptance of the target spectrometer and will be detected in the forward spectrometer instead. The mechanical core component of the forward endcap is the aluminum *backplate*, a disc shaped plate with a diameter of 2.1 m and a thickness of 30 mm. A variety of different holes, grooves and recesses are milled or drilled into this component. This backplate is the central support structure for the units containing the PWO crystals and their readout electronics. An additional aluminum structure is mounted to the outer (and inner) edges of the backplate to facilitate a spatial limitation of the inner, cold volume of the endcap. This structure, called the *stiffener ring*, increases the mechanical stability of the endcap, as required once the backplate is loaded with about 3800 crystals. The backplate and the mounted stiffener rings are depicted in Figure 8.4a (left).
The backplate also serves as the main component of the central cooling system of the endcap: A liquid cooling agent, e.g. a mixture of methanol and water, is pumped through long vertical holes running through the backplate. The subunits will be attached to the backplate using an aluminum mounting structure, while at the same time a good thermal coupling to the subunits will be ensured (shown in Figure 8.4b, right). The cooling agent can therefore drain the heat generated by the readout electronics (preamplifiers) and also cool down the crystals to their operational temperature. Two further cooling systems

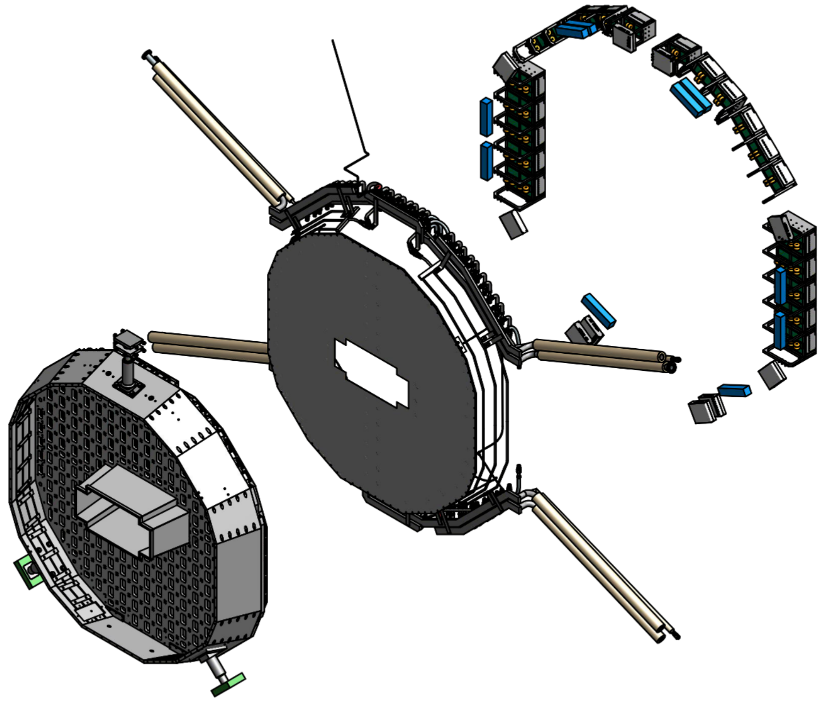

(a)

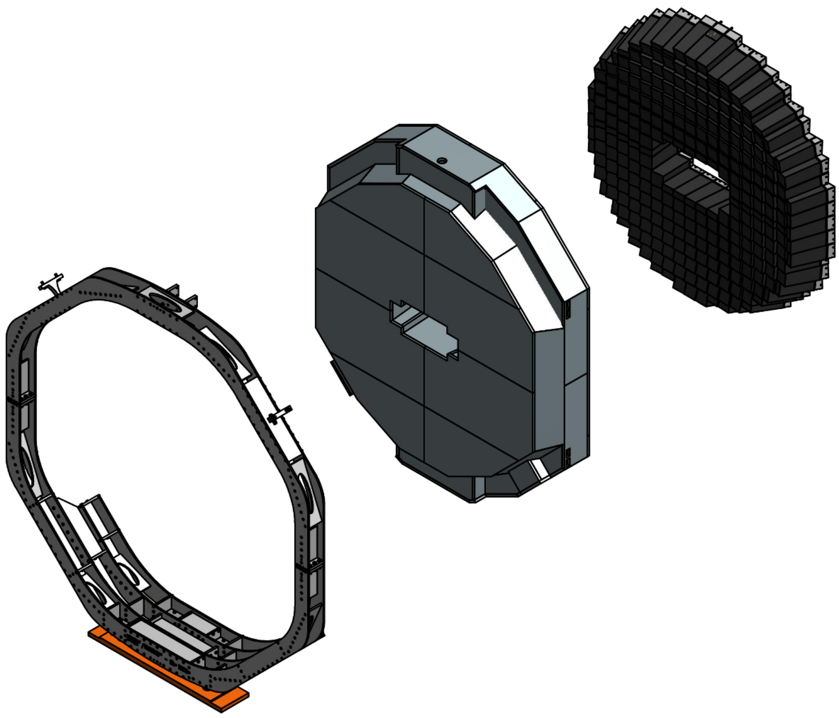

(b)

Fig. 8.4: Exploded view of the forward endcap components (left to right):
(a) Mechanical structure (backplate, stiffener ring), cooling systems, electronics components (light pulsers, temperature monitoring systems, ADCs)
(b) Support frame, vacuum-panel insulation, crystal subunits. [79]

are integrated into the endcap design: Easily bendable aluminum pipes are mounted into grooves at the inner side of the stiffener ring segments to provide cooling at the sides of the detector (cf. Fig. 8.5b). A thin ($d = 0.8$ mm) aluminum plate is attached to the end faces of the stiffener ring segments to close the volume of the endcap to the front. Thin hoses carrying a mixture of methanol and water are glued to this front plate from the inner side of the detector. This system is responsible for the front cooling of the crystals. To further enhance cooling and to prevent the formation of ice, the inner volume of the endcap will be flushed with cooled, dried air. The components of the main, side and front cooling systems are shown in Figure 8.4a (middle).

All cables necessary for the operation of a subunit, namely the supply voltage lines as well as signal output connections of the photosensors and preamplifiers, are fed through individual holes in the backplate for each subunit. The electrical connection and further cable routing to the warm volume will be discussed in Section 9.4. Four silica light fibers are routed to each single crystal for the distribution of light from an LED based light pulser system [80]. This light pulser system is used for tests of the readout chain and regular functionality checks of all subdetectors as also to monitor the optical transparency of the scintillation crystals, which is impaired by radiation damages in the experiment [80]. Downstream of the backplate, only 30 mm space are available for the routing of cables and fibers.

Another aluminum plate with a thickness of 3 mm finally closes the cold volume of the endcap in downstream direction, behind the cable and fiber layer. Since the calorimeter is operated at $-25°$C, a proper insulation is of utmost importance, however the available space is extremely limited. Therefore, vacuum insulation panels based on a fumed silica

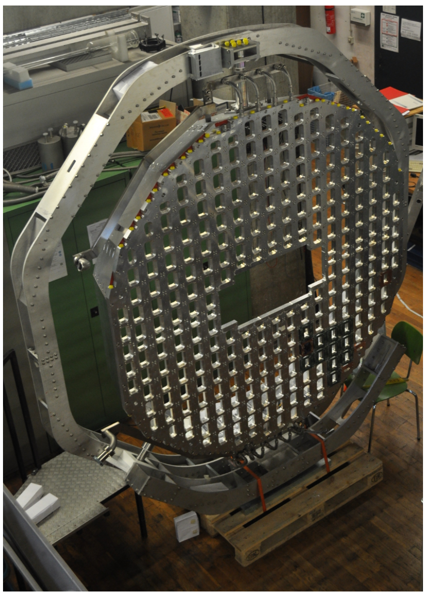

(a)

(b)

Fig. 8.5: (a) Mechanical components (backplate, stiffener ring, support frame) of the forward endcap assembled in the lab.
(b) Detailed view of the backplate and stiffener ring, where the grooves and one aluminum pipe of the side cooling system can be seen.

core are used, which provide a thermal conductivity of $(0.0043 - 0.02)\,\mathrm{W/(mK)}$. A sketch of the insulation is depicted in Figure 8.4b (middle). The complete assembly is affixed in the *support frame*, which can be seen in Figure 8.4b (left), using three massive bolts located at the top and lower left/right side of the stiffener ring. These bolts are made of two parts, between which a layer of PCTFE (a robust thermosoftening plastic) is placed to ensure a thermal insulation between the (cold) detector and the support frame. The backplate, the stiffener ring as well as the support frame have already been produced and assembled in the lab, as can be seen in Figure 8.5.

8.5.1 Photo Detectors

The $\overline{\mathrm{P}}$ANDA EMC will be equipped with two different kinds of photo sensors. The barrel, the backward endcap as well as the outer part of the forward endcap will be equipped with *Large Area Avalanche Photo Diodes* (LAAPDs), while in the inner region of the forward endcap small two-stage photomultipliers or *Vacuum Photo TeTrodes* (VPTTs) will be used. The latter are more suited to the extremely high radiation doses and single crystal hit rates that the detectors in the innermost part of the forward endcap will have to withstand.

Vacuum Photo Tetrodes (VPTTs)

The functional principle of a VPTT is very similar to that of a standard photomultiplier (PMT): A (scintillation) photon traverses the entrance window of an evacuated glass tube and impinges on the photo cathode. In most cases, the photo cathode is a very thin bi-alkali metal coating directly applied to the inner side of the entrance window. This technique has also been employed for the production of the VPTTs, but additionally to the coating, thin aluminum strips have been attached to the entrance window. These strips, which are arranged in a star-shaped pattern without being connected in the center of the tube (cf. Figure 8.6a), allow for a faster transport of electrons to the cathode. The incoming photon is absorbed by the photo cathode layer and can dislodge an electron from the cathode material due to the photoelectric effect. This occurs with a certain probability, called the *quantum efficiency* ($\sim 23\%$ for VPTTs). In conventional photomultiplier tubes, the primary electron is now accelerated towards the first solid dynode due to an electric potential between the photo cathode and the dynode. It impinges on the dynode and releases a number of secondary electrons. This process is repeated several times, so that a huge number of electrons is released for each incoming photon. Thus, the amplification factor (gain) of PMTs can reach values up to $10^5 - 10^8$, depending on the applied voltages and the specific model of the PMT. Due to this operational principle, PMTs are in general sensitive to external magnetic fields. Additionally, they have a much larger diameter than the size restrictions for a $\overline{\mathrm{P}}$ANDA PWO crystal allow for. To overcome the problem of the strict spatial limitation and in order to reduce the sensitivity to magnetic fields, the VPTTs have been designed exclusively for the $\overline{\mathrm{P}}$ANDA experiment by the Japanese manufacturer Hamamatsu.
In total 768 crystals of the forward endcap will be equipped with VPTTs of the type R11375-MOD, which have an active area of about $200\,\mathrm{mm}^2$ and a diameter of only 23.9 mm, so that they match the rear face of a $\overline{\mathrm{P}}$ANDA PWO crystal. The 40 mm long evacuated glass body of a VPTT contains two dynodes as well as the anode. All electrodes and dynodes are oriented in parallel to the entrance window of the tube, so that one dynode

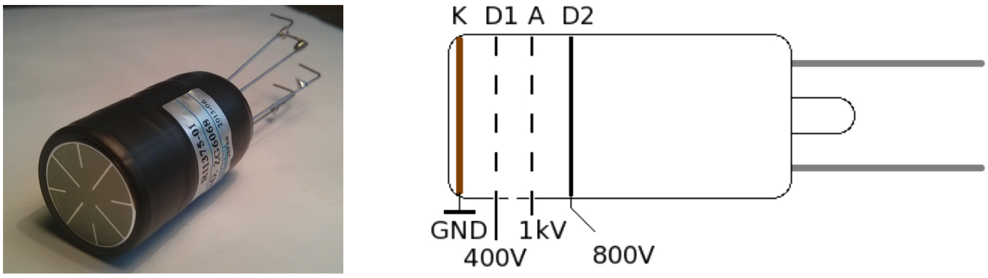

(a) (b)

Fig. 8.6: (a) Hamamatsu VPTT (R11375-MOD) for the $\overline{\text{P}}$ANDA Forward Endcap EMC
(b) Schematic view of the inner structure of a VPTT

as well as the anode had to be designed as a mesh, in contrast to solid electrodes. Figure 8.6b shows the arrangement of the electrodes in a VPTT as well as the voltages that are applied. The achievable gain is directly proportional to the number of dynode stages, thus the gain of a VPTT is much lower than that of a standard PMT. In total 800 VPTTs have been delivered, which is sufficient to equip the forward endcap as foreseen. The manufacturer determined several parameters for each tube, such as the amplification factor (gain) or the dark current. These properties were re-measured upon arrival, to ensure that all devices meet the specifications and to check the reproducibility of the manufacturer's values (see Figure 8.7a). The anode and cathode current were directly measured with pico-amperemeters, whilst the VPTT was illuminated with constant light (gain) or not illuminated (dark current). The measurements have shown that the dark current of all tubes is negligibly small, while the manufacturers' values for the gain can be reproduced on the order of a few percent. The VPTTs have an average gain of $M \approx 50$. Although the sensitivity towards an external magnetic field is significantly smaller than for a full-size PMT, the loss in amplification due to the B-field must be considered for the planned deployment in the forward endcap.

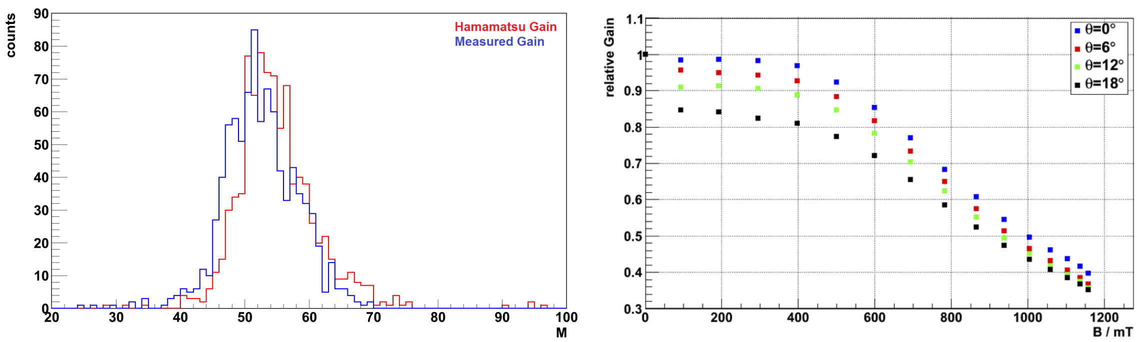

(a) (b)

Fig. 8.7: (a) Gain of all 800 VPTTs for the $\overline{\text{P}}$ANDA forward endcap (red: manufacturer values, blue: measured at RUB).
(b) Relative gain of a single VPTT under different angles in an external magnetic field of $B = 0 - 1.2\,\text{T}$ [81]

Depending on the exact position in the endcap, the angle of a certain VPTT to the magnetic field lines varies between 0° and 18°, which leads to a loss in amplification of about 50% at a magnetic field strength of 1 T. This is a realistic approximation of the field strength at the position of the VPTTs (see Figure 8.7b) [81].
Apart from their extremely good tolerance towards ionizing radiation, another key parameter of the VPTT is its detector capacitance of only $C_{\mathrm{VPTT}} \approx 22\,\mathrm{pF}$. The detector capacitance has a large influence on the noise level after the detector signal has been processed by a charge integrating preamplifier. For comparison it should be noted, that the capacitance of a VPTT is about a factor of ten lower than that of an APD.

Avalanche Photo Diodes (APDs)

The largest part ($\sim 95\%$) of the $\overline{\mathrm{P}}$ANDA EMC crystals will be read out with silicon based semiconductor detectors. The relatively low light yield of PWO crystals calls for a photo sensor with an intrinsic amplification, so that commonly used photo diodes (PIN-diodes) are not suitable and instead diodes providing an internal avalanche effect were chosen. As for the VPTTs, the APD model to be used in the EMC was developed by the manufacturer Hamamatsu exclusively for the $\overline{\mathrm{P}}$ANDA experiment (Model: S11048)[1]. The APDs are characterized by an exceptionally large active area of $(6.8 \times 14)\,\mathrm{mm}^2$ and have a rectangular shape, as can be seen in Figure 8.8b. This allows for two APDs to be attached to the rear face of one PWO crystal. Together, the two APDs have an active area of approximately $190\,\mathrm{mm}^2$, comparable to that of a single VPTT ($\sim 200\,\mathrm{mm}^2$).
The internal structure of these APDs is schematically shown in Figure 8.8a. A photon entering the APD through the optically transparent silicon nitride (Si_3N_4) window will be absorbed in the positively doped p^+ layer and create an electron-hole pair due to the photoelectric effect with a probability of more than 70%, which is the quantum efficiency of the APD. Since a reverse bias voltage is applied to the APD, the electrons begin to drift towards the pn-junction. On their path through the layers of the APD, the electrons reach a region with an extremely strong electric field, which massively accelerates them. When the electrons are fast enough, they will be able to create additional electron-hole pairs, which themselves again can contribute to the electron multiplication process (*avalanche effect*). The accelerated electrons will then pass the pn-junction and enter the negatively doped layer (n^{++}), which serves as an electrode (anode) of the APD. The accumulated charge will then be transported to the anode pin and constitutes the measurable signal.
The operational principle of an APD is largely unimpaired by the presence of an external magnetic field; However, the internal amplification depends on a variety of external conditions and operational parameters, which must be observed: Apart from the applied reverse bias voltage, the gain also critically depends on the temperature of the APD. To ensure a safe operation of all APDs at the same gain (M) in the experiment, a precise temperature measurement and regulation must be provided, while at the same time the characteristic of each single APD must be precisely known. This allows to select the correct bias voltage for a defined gain at a certain temperature. All APDs are therefore screened at various temperatures at the GSI APD Laboratory. A part of the data from these screening measurements has been analyzed in the scope of this work and shall be briefly presented here, to show the performance of the $\overline{\mathrm{P}}$ANDA APDs based on a large sample of about 1500 pieces.

[1] The design of the $\overline{\mathrm{P}}$ANDA APDs is a further development of quadratic diodes with a smaller active area that were produced for the calorimeter of the CMS experiment at CERN's LHC.

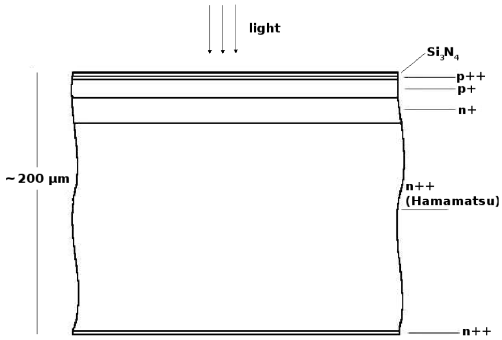

(a)

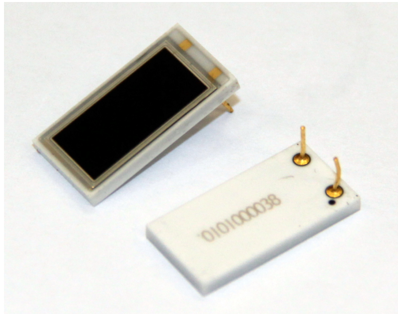

(b)

Fig. 8.8: (a) Schematic view of the internal structure of a $\overline{\text{P}}$ANDA APD [74]
(b) Two APDs as foreseen for installation in the forward endcap

8.5.2 Readout Chain of the EMC

The readout chain of the $\overline{\text{P}}$ANDA EMC is depicted in Figure 8.9. The single ended analog output signals of the preamplifiers have an impedance of 50 Ω and can vary in the voltage range (0 − 2.2) V. Once the thin coaxial cables are routed out of the cold volume of the forward endcap, they are connected to the backplanes of crates especially developed to fit into the support frame of the endcap and to accomodate up to 15 digitizer boards. It is planned, to perform at least a one-stage analog filtering and splitting of the analog signals. One branch of the splitted signal will be amplified (High Gain), while the other (Low Gain) is directly connected to a digitizer input. This drastically increases the resolution for very small signals, since they will be reconstructed from the High Gain branch, while for larger signals that exceed the input range of the digitizer in the High Gain branch, the corresponding output of the Low Gain branch digitizer channel will be used. The digitizer modules are based on Kintex-7 FPGAs, which are continuously sampling the output of 14-bit ADC chips at a rate of 80 MSamples/s. The signals of 32 photodetectors are connected to one digitizer board, where each board must supply 64

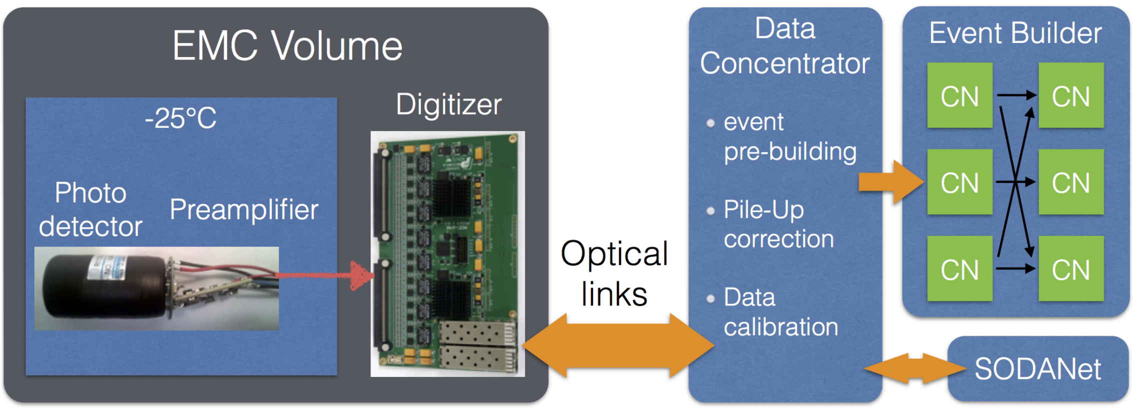

Fig. 8.9: Readout chain of the $\overline{\text{P}}$ANDA EMC. Starting from the photo detector, the signal is processed first by the digitizer, then transported to the Data Concentrator (DC) and from there to the event building network of Compute Nodes (CN).

analog input channels due to the High/Low Gain splitting. An online feature extraction will be performed by the firmware of the digitizer modules and the extracted information is finally transmitted via optical fibers out of the detector volume, which is enclosed by the solenoid magnet yoke. The signals are then further analyzed by *Data Concentrators*, where first algorithms for providing a fast trigger based on the EMC signals are executed. In the next step, the data is transferred further to a network of so called *Compute Nodes* (CN), where the event building based on the data received from many Data Concentrators is performed, before the events are transferred to the online computing farm and finally to a data storage facility. Already at the stage of the digitizers, precise time stamps will be attached to the recorded data. These time stamps are distributed throughout the complete $\overline{\mathrm{P}}$ANDA detector via the *SODANET* protocol [82].

9 Construction of Close-To-Final Forward Endcap Calorimeter Submodules

9.1 Assembly of Photo Detector Readout Units

The design and construction of readout units consisting of photo detectors and preamplifiers has been described in detail in [83] and [84]. However, different types of photo detectors were evaluated in the referenced theses and the production procedure for units that will finally be used in the $\overline{\text{P}}$ANDA detector had not yet been established. Thus, a short description of the final choice of components and the production process will be given here. Several APD as well as VPTT units have been produced and tested in the course of this thesis, including 16 units of each type which were assembled according to the procedure described below. These most recently produced units were finally tested during a test beam time, as described in detail in Section 10.4.
A charge integrating, low noise preamplifier (LNP) has been developed at the University of Basel specifically for usage in the $\overline{\text{P}}$ANDA EMC. The LNP is directly attached to the anode of the APD/VPTT; this connection between the photo sensor and the preamplifier has to be kept as short as possible. The LNPs are produced in two different geometrical shapes depending on the type of photo sensor, due to the different amount of space that is used up by VPTTs and APDs. Both types are displayed in Figure 9.1a. In the case of the VPTT units, a second printed circuit board (PCB), which carries the passive voltage divider, is used. The voltage divider board (see Figure 9.1b) was designed to match the outer dimensions of the VPTT and also allows to be mounted in the shortest possible distance from the glass tube. Therefore, it has a round outer shape with a circular opening in the middle, which has a diameter of 7 mm, so that the board can be fitted over the pump port of the tube. The LNP itself is subsequently connected to the voltage divider PCB via two small flexible leads for the connection of the anode and cathode to the tube. High and low voltage supply cables, as well as one coaxial signal cable are connected to each LNP before it is connected to the voltage divider board. A photograph of a VPTT unit at this stage of assembly is shown in Figure 9.1c. A shrinking tube with a wall thickness of only 150 µm is used to mechanically connect and cover the VPTT with the two PCBs attached to the tube base. The complete volume inside the shrinking tube, which contains the LNP as well as the voltage divider, is finally filled with a two-component silicone based casting compound (Elastosil RT601 A/B) to ensure mechanical stability and electrical isolation as well as protection against liquids. A piece of self-adhesive copper tape is wrapped around the shrinking tube at the position of the preamplifier. The copper tape is equipped with a copper strap which is electrically connected to the ground layer of the LNP to provide electrical shielding. A second shielding layer is created by wrapping the complete unit with self-adhesive aluminum foil. Here, a special type of foil was used, which is certified to provide a good conductivity also through the adhesive layer, so that an electrical connection to the GND layer of the preamplifier is maintained.
For APD units, the procedure described above is only slightly modified: Since two photo detectors are used in one unit, an additional mechanical component, called *capsule*, is

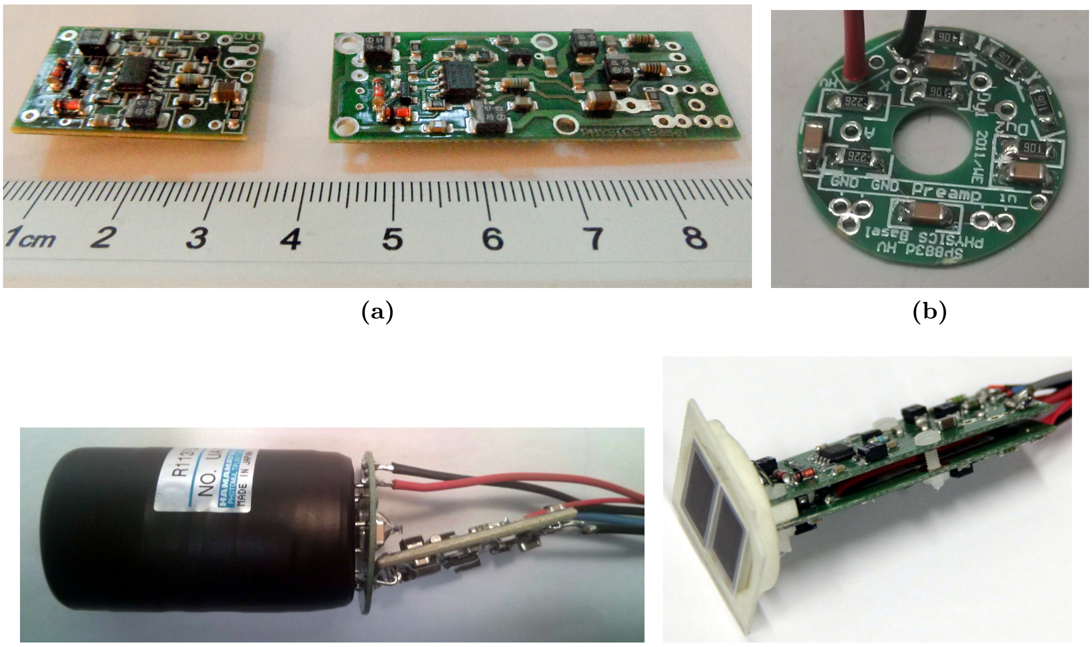

(a) (b)

(c) (d)

Fig. 9.1: (a) Low noise preamplifiers for VPTTs (left) and APDs (right)
(b) Round voltage divider PCB to be mounted directly to the VPTT tube base
(c) VPTT unit with voltage divider and LNP, before sealing
(d) APD unit with two LNPs. The APDs are glued into a nylon capsule.

Purpose	Material for VPTT unit	Material for APD unit
Photo detector	1× R11375-MOD VPTT	2× S11048 LAAPD
Preamplifier	1× SP883d_VPTT	2× SP883d_APD
Voltage divider	1× round PCB	n.a.
High voltage	2× 15 cm AWG24 cable w/ Molex Micro-Fit™ black: GND; red: HV	3× 15 cm AWG24 cable w/ Molex Micro-Fit™ black: GND; red/blue: HV APD1/2
Low voltage	3× 15 cm cable red/black/blue: +6 V/GND/-6 V	3× 15 cm cable red/black/blue: +6 V/GND/-6 V
Signal	1× 15 cm micro coaxial (U.FL)	2× 15 cm micro coaxial (U.FL)
Shielding	7 cm self-adhesive copper tape w/ soldered ground strap	5 cm solid copper tube w/ soldered ground strap
Isolation/Casting	70 × 42 mm shrinking tube ∼ 4.5 ml Elastosil® RT601 A/B	 ∼ 14 ml Elastosil® RT601 A/B
Outer shielding	Self-adhesive aluminum foil	Self-adhesive aluminum foil

Table 9.1: Material needed for the production of one VPTT/APD readout unit

needed for the assembly. These 3D-printed frames made of nylon are designed to accomodate two APDs with a fixed orientation to each other. Additionally, the capsules provide a fixation bar at their rear side, to which two LNPs can be attached. Two APDs are glued into a capsule and connected with very short leads (few mm) to the input soldering points on the respective LNPs, which are fixated on the capsule using M2 nylon screws (see Figure 9.1d). Each preamplifier is equipped with cables for the high voltage supply lines as well as a coaxial signal cable, while the low voltage supply lines are daisy-chained from one LNP to the second and thus only one set of low voltage cables is needed. Since a proper electrical shielding is absolutely necessary and in the case of APD units enough space is available, a solid copper tube with a length of 50 mm is placed around the LNPs. As for the VPTTs, the inner volume of the copper tube is filled with Elastosil. The rear end of the copper tube is sealed using the self-adhesive aluminum tape described above to provide electrical shielding to the back side.
Table 9.1 lists the material needed for the production of one VPTT, as well as one APD readout unit. In total 16 VPTT units and 16 APD units (one EMC-subunit each) were produced and tested for this thesis. After a unit has been tested electrically with illumination from a light pulser system, it was labeled with a unique bar code and information such as the tube and preamplifier serial number were stored in a database.

9.2 Screening of APDs

Similar to the measurements performed with the VPTTs, also the screening of the APDs serves as a quality check. Additionally, several parameters are measured to characterize the APDs at the operational temperature of $-25°$C, which are not provided by the manufacturer. At least in the forward endcap, about eight APDs will be supplied by the same high voltage line from a power supply located outside of the $\overline{\text{P}}$ANDA detector, due to spatial limitations. Therefore, the APDs need to be matched in groups of eight according to the bias voltage needed to achieve the operational gain of $M = 200$ at $-25°$C, as well as the slope of the APD response curves at that voltage.
The photo current of each APD is measured in dependence of the applied bias voltage at five different temperatures ($(+20, +10, +2, -10, -25)°$C). The dark current, which rises with the bias voltage, must be subtracted from the measured current to obtain the pure photo current. Therefore, the response curves are measured with and without illumination of the APD using a constant light source and the two curves are subtracted from each other. The APD screening measurements presented in this thesis have been performed at the *PhotoSensor Laboratory* (PSL) at GSI. The photo current is measured in steps of 5 V starting from 15 V up to a voltage of 100 V, then in steps of 10 V up to a voltage of 300 V and subsequently in steps of 2 V until the measured current exceeds 100 µA (breakdown).
The first step in the analysis procedure is to determine the photo current, which corresponds to an amplification of $M = 1$. This value is extracted from a linear extrapolation of the first few data points to $U = 0$ V after subtraction of the dark current and serves as a normalization for the response curve. Figure 9.2a shows typical response curves of one APD at all five temperatures.
Figure 9.2b shows the bias voltage that must be applied in order to achieve a fixed gain of $M = 200$ in dependence of the temperature. The values displayed correspond to the crossing points of the horizontal blue line with the response curves in Figure 9.2a. A linear correlation between the bias voltage and the temperature is apparent, while the gain in

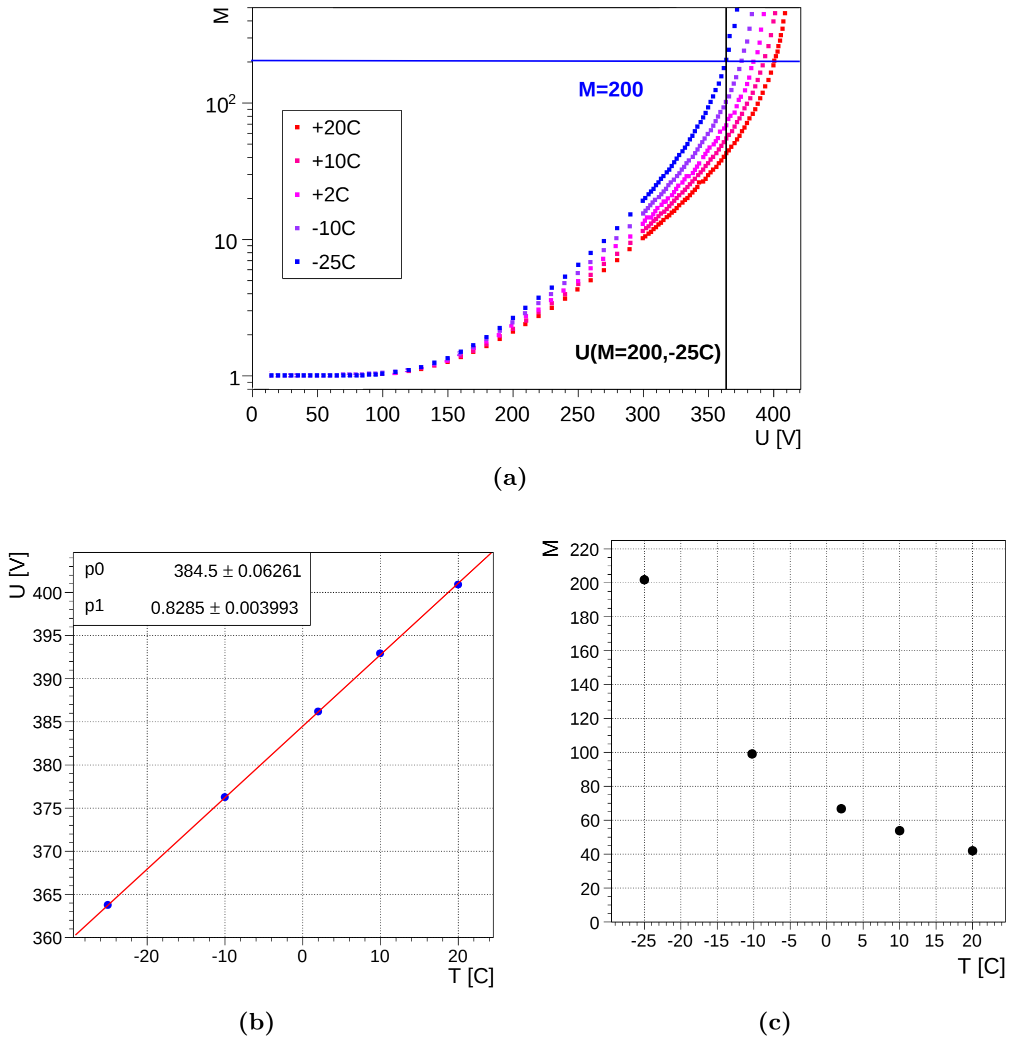

Fig. 9.2: (a) Typical response curves of one APD at all five temperatures
(b) Temperature dependence of the bias voltage for $M = 200$
(c) Temperature dependence of the gain for the bias voltage $U(M = 200, -25°\text{C})$

dependence on the temperature for a fixed bias voltage (see Figure 9.2c) shows a more complex behavior. In this case the values correspond to the intersections of the vertical black line with the response curves in Figure 9.2a. Both dependencies can be useful for the operation of the APDs in the $\overline{\text{P}}$ANDA detector: Knowing the correlation between the bias voltage and the temperature allows for a regulation of the voltage in order to keep the gain at a constant value. However, during normal operation, when the APD bias voltages are fixed, their actual gain can be estimated by using the temperature correlation.

An important purpose of the screening measurements is to provide a quality check for all delivered APDs. Therefore, the bias voltage for an amplification of $M = 100$ at a temperature of $+20°\text{C}$ is extracted for comparison with the values given by the manufacturer. In most cases it is necessary to interpolate between two measurement points. Therefore, a polynomial of third order is fitted to the data points in the vicinity of the desired value.

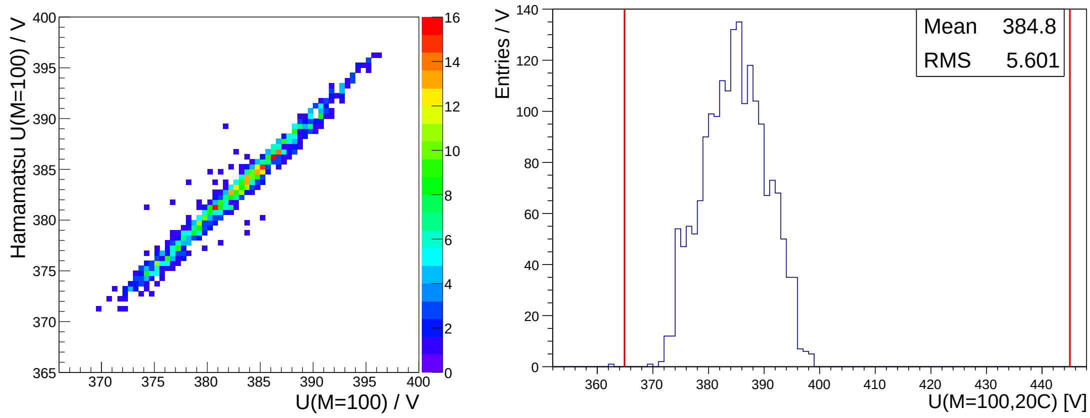

(a) **(b)**

Fig. 9.3: (a) Comparison of manufacturer's values (y-axis) and values obtained in this analysis (x-axis) of APD bias voltages for $M = 100$ at $T = +20°C$.
(b) APD bias voltage for $M = 100$ at $T = +20°C$. The red lines indicate the tolerances of the specification values.

Figure 9.3a shows the manufacturer's values of the bias voltage for $M = 100$ at $T = +20°C$, versus the value obtained in this analysis. All results shown here are obtained for a relatively small sample of about 1500 $\overline{\text{P}}$ANDA APDs from one of the first delivered batches. A strong correlation can be observed, while the standard deviation of the difference from the manufacturers values amounts to $\sigma_{\Delta U} \approx 0.6\,V$ which corresponds to about 0.2%. The values of all APDs analyzed here are within the tolerances given in the specification sheet, which are indicated by the red lines in Figure 9.3b.
Additionally the dark current as well as the slope of the response curve at $U(M = 100)$, $T = +20°C$ are extracted and displayed in Figures 9.4a and 9.4b. For both parameters no APD violating the specification values is found.

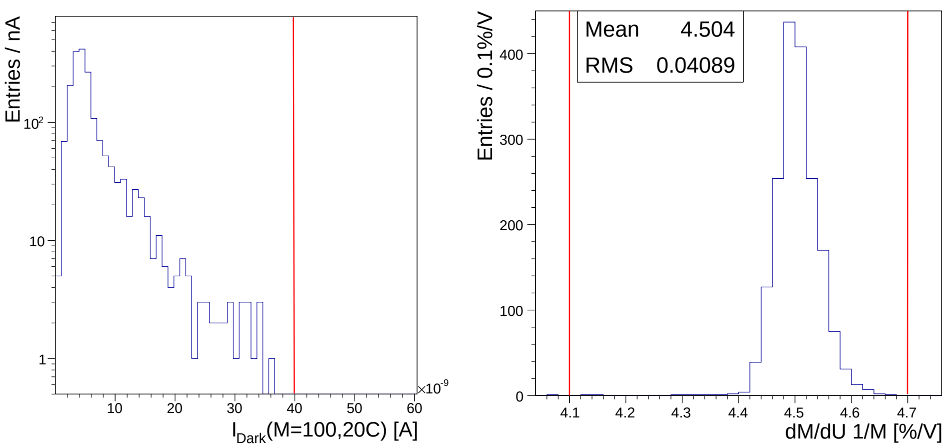

(a) **(b)**

Fig. 9.4: (a) Dark current of APDs for $M = 100$ at $T = +20°C$
(b) Slopes of the APD response curves at $M = 100$ and $T = +20°C$.

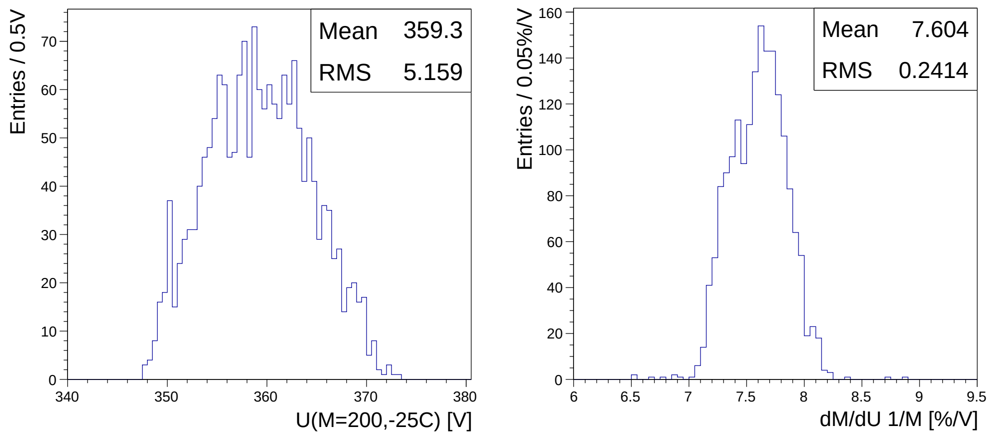

(a) **(b)**

Fig. 9.5: (a) APD bias voltages for $M = 100$ at $T = +20°C$
(b) Slopes of the APD response curves at $M = 200$ and $T = -25°C$.

The Figures 9.5a and 9.5b show the bias voltages and slopes of the response curves at $M = 200$ and $T = -25°C$, respectively. Based on these parameters, a matching of APDs can be performed to select groups which show similar operational characteristics.
It should be noted here, that apart from the screening measurements using a constant light source, also measurements utilizing the light pulser system are performed and are reported e.g. in [92]. The necessity for these additional measurements arises from the naturally pulsed behavior of the scintillation light during nominal operation of the EMC, which might have a non-negligible influence on the APD response curves.

9.3 Assembly of Forward Endcap Subunits

After the photo detector preamplifier units are tested, they are ready to be irreversibly glued to the scintillation crystals. In former tests and prototype setups, the optical coupling between the photo detectors and the PWO crystals was realized with optical grease or with the optically transparent casting compound Elastosil, which is also used to fill the volume containing the preamplifiers in the readout units. However, several photo detectors lost their coupling to the crystal due to mechanical stress while mounting or transporting the prototype assembly or during cooling down/heating up, so that for the production of the final subunits an irreversible connection was chosen. As for the optical couplings in the EMC of the CMS detector at CERN, a single component room temperature vulcanizing silicone based adhesive named Dow Corning® RTV-3145 was chosen. The crystals are stored in upright position in a dedicated glueing assembly, so that the photo detector can be attached from the upper side. Below the glueing assembly table, a camera can be positioned beneath each crystal and thus the connection between the detector and the crystal can be visually examined and adjusted, if necessary, before it cannot be removed anymore [85]. Finally, the crystal is covered with a prefabricated shell made out of highly reflective foil. As a last step, the unit is tested again in a light pulser driven test stand to ensure proper operation before mounting the unit. An assembled unit of photo detector, preamplifier and crystal is shown in Figure 9.6.

Fig. 9.6: Sealed VPTT preamplifier unit (left) after being glued to a PWO crystal wrapped in reflective foil.

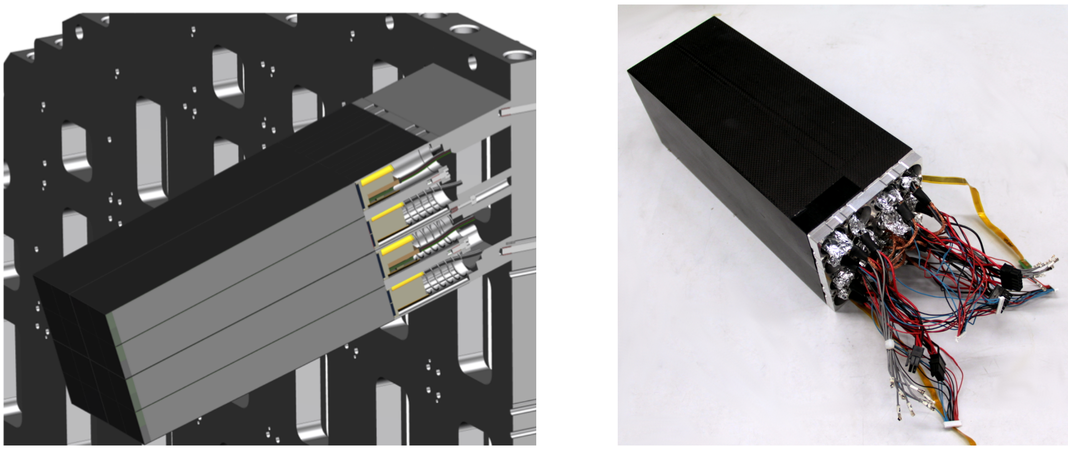

(a) **(b)**

Fig. 9.7: (a) CAD drawing of a subunit mounted to the backplate.
(b) Assembled VPTT subunit (view from back).

Once 16 (or eight, in case of half subunits) single crystal units have been produced, glued and tested, an EMC subunit can be produced. Figure 9.7a shows a CAD drawing of a subunit attached to the backplate, while in Figure 9.7b a readily assembled subunit is depicted. The subunits represent the mechanical holding structure for the crystals in order to attach them safely and precisely to the backplate.

The design of the forward endcap foresees full 4×4 crystal subunits, and half 4×2 crystal subunits in certain regions of the endcap to obtain best coverage of the available space. The primary component of each subunit is a carbon fiber shell, called *alveole*, which encloses the PWO crystal units. An alveole is constructed from four compartments of the same size, which resemble a truncated four-sided pyramid, and therefore reproduce the outer shape of the four slightly tapered PWO crystals that they contain. To ensure an equal distance between all crystals, two sheets of the carbon fiber material are assembled in a cross-like shape and positioned in between the four crystals in each compartment. The alveole, as well as the carbon fiber crosses are depicted in Figure 9.8. In earlier test setups and prototype subunits, the carbon fiber alveoles had an open front face, so that on the one hand a visual inspection of the crystals and also the optical couplings was possible at all times, while on the other hand plastic front-stoppers had to be installed, which kept the crystals from slipping or moving out of the alveole. In the final version, the design of the alveoli was slightly changed, so that the front is completely closed with a carbon fiber layer of the same thickness as chosen for the outer and inner walls of the alveole (180 µm). After the four carbon fiber crosses have been placed in between the four groups of crystals,

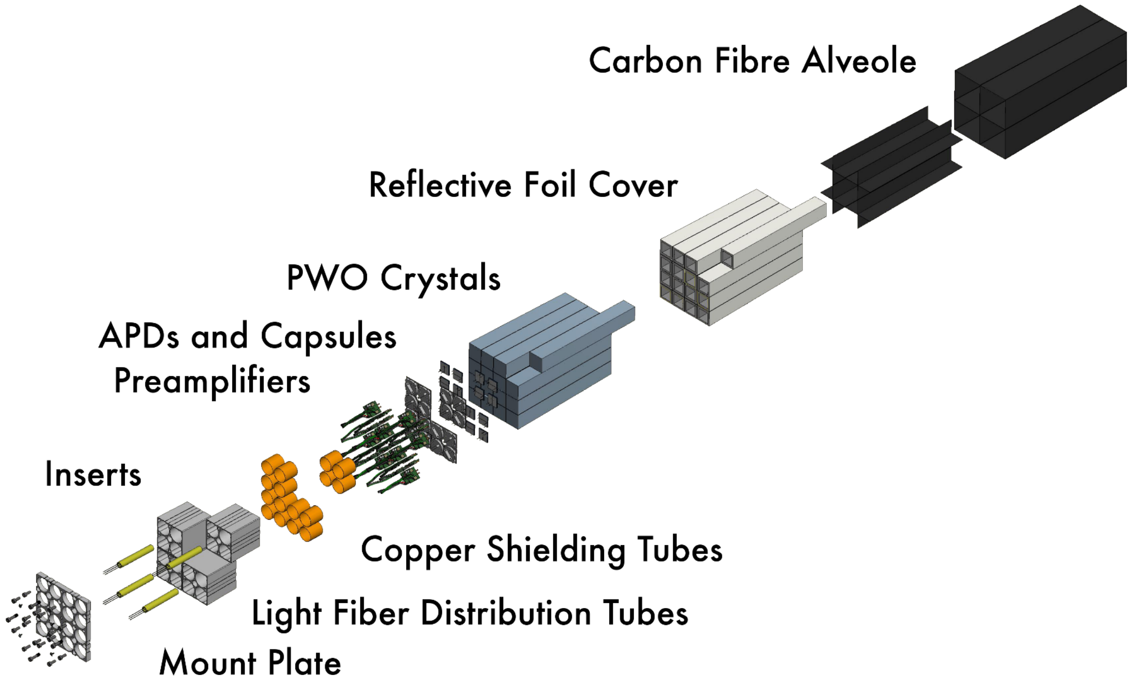

Fig. 9.8: Exploded view of an EMC subunit equipped with APDs as photo detectors.

all 16 units are simultaneously pushed into the alveole from the rear side until they get stuck in this tapered assembly. Subsequently, the first component of the aluminum holding structure is inserted into the compartments of the alveole. A precisely milled aluminum workpiece, called *insert*, with four holes, one for each photo detector preamplifier unit, is pushed into each compartment of the alveole. Additionally, each insert is produced with a smaller hole positioned centrally between those for the photo detector units, into which an aluminum tube can be inserted, carrying the fibers of the externally mounted LED light pulser system. The subunit is concluded by another aluminum piece, which is used to connect all four inserts to a robust and stiff mechanical unit. This 8 mm thick *mount plate* is shown in the lower left corner of Figure 9.8.

9.4 Electrical Connections of a Subunit

The length of all cables that are directly connected to the preamplifiers have been kept as short as possible, so that they are just long enough to fit through the hole foreseen for each subunit in the backplate. At this point, all cables are connected to a multilayer patch panel PCB, which serves as a kind of adapter board from the thin, single channel cable bundles to thicker supply lines and multichannel-coaxial cable bundles for the signals. Another reason for having only short cables irreversibly attached to each subunit is the mounting procedure and manageability of single subunits during production and test phases.
The patch panel PCB was designed at the University of Bonn [86] and has a quadratic shape with a rectangular opening in the center. The boards will be directly attached to the rear side of the backplate, so that the high and low voltage cable bundles from a subunit can be directly connected to receptacles placed on the rear side of the patch panel. The signal cables are fed through the opening in the PCB and are connected to receptacles

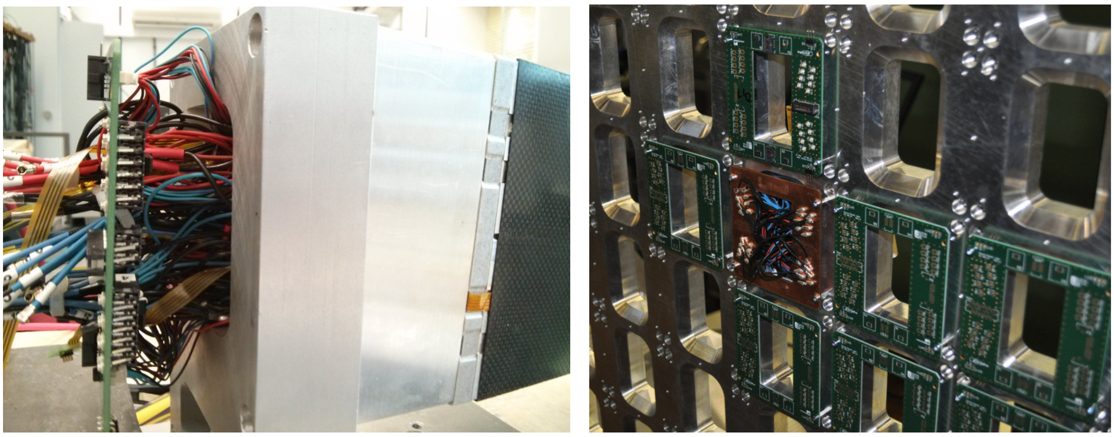

(a) (b)

Fig. 9.9: (a) Assembled APD subunit mounted to mockup mini backplate. High and low voltage cables are connected to a patch panel PCB (left).
(b) Several patch panel PCBs mounted to the forward endcap backplate.

mounted on the front side of the PCB. In total 32 analog signal cables can be connected to the board. Each of the two groups of signals are connected to one high-density connector, from where the signals are guided towards the ADC crates. The bundles of 16 signal cables are routed to the outer edge of the backplate, where they pass an insulated volume to reach the warm environment outside of the narrow electronics space downstream of the backplate. The support frame which carries the forward endcap also accommodates crates with digitizer boards, to which the signal cables are connected. The longest signal cable bundles are the ones connected to the subunits that are placed directly in the vicinity of the inner hole for the HESR beam pipe. Their length amounts to a maximum of approximately 2.5 m [79].
The connection of the analog signals to the digitizer boards is an essential part of the detector: The type of cable that is used for this delicate purpose is a miniature coaxial cable with one single conductor in its core with a diameter of only 0.2 mm (Nexans Filotex® 50VMTX). The conductor and the surrounding shielding are covered by an insulation made of PTFE (Teflon). The damping of this cable was measured to be approximately 0.18 dB/m. This measurement was performed using a charge injection circuit connected to a $\overline{\mathrm{P}}$ANDA LNP which was fed to a 9 m long cable, so that the attenuation could be evaluated for signals with a shape close to the signals expected in the forward endcap.
High voltage will be supplied to each subunit via up to four cables (Huber+Suhner® Enviroflex), which are then distributed to the 16 or 32 detectors. The connectors and supply cables for the low voltage are still under discussion.
Apart from the connections discussed above, the patch panel PCB accommodates four 0.5 mm pitch pin headers, which are routed on the board to connectors to which up to four ultrathin Pt100 temperature sensors can be connected. It is foreseen to supply every subunit with up to two of these sensors. A standard 0.5 mm pitch flat ribbon cable is used to lead the wires of the temperature sensors from the patch panel PCB to the warm volume, where they are connected to the temperature and humidity monitoring boards (THMP) which are placed in the support frame of the forward endcap [87].

10 Beam Tests with the Forward Endcap Prototype

A prototype resembling a cutout (see Figure 10.1a) of the forward endcap comprised of 216 PWO crystals, has been built at the Institut für Experimentalphysik I in the past few years. Design and construction have been described in detail in [88], [89], [83], and [84] before and will just be briefly summarized here. The first calorimeter subunits were built and tested under realistic conditions with this prototype not only in the lab, but also during various test beam times at different accelerators. These subunits were equipped with different types of photo sensors and one goal of the measurements was to select the photo sensor type to be used in the forward endcap. The choice was finally made and after several iterations of improvements to the mechanical parts and electronics components, the two close-to-final subunits described in the previous chapter were built. To ensure that all modifications were done properly and to perform a final gain matching of the readout chain, the two subunits were mounted to the prototype and test beam data at the ELSA accelerator was recorded. The results of the first three test beam times conducted with the forward endcap prototype were presented in [84], while the data recorded at the two most recent beam times is analyzed in the scope of this work.

The central mechanical component of the prototype is the aluminum backplate, which follows the design of the backplate of the full forward endcap. In total, the prototype can be equipped with 13 full subunits (4×4 crystals) and one half subunit (4×2 crystals). On the front side (upstream), the volume of the prototype is enclosed with a front hull made of aluminium sheets as well as PVC sheets in the region of the central hole for the HESR beam line and the opening towards the forward spectrometer. On the rear side, a frame made of 30 mm thick PVC creates a volume for the routing of light fibers and cables, which is covered by a 3 mm thick aluminum sheet.

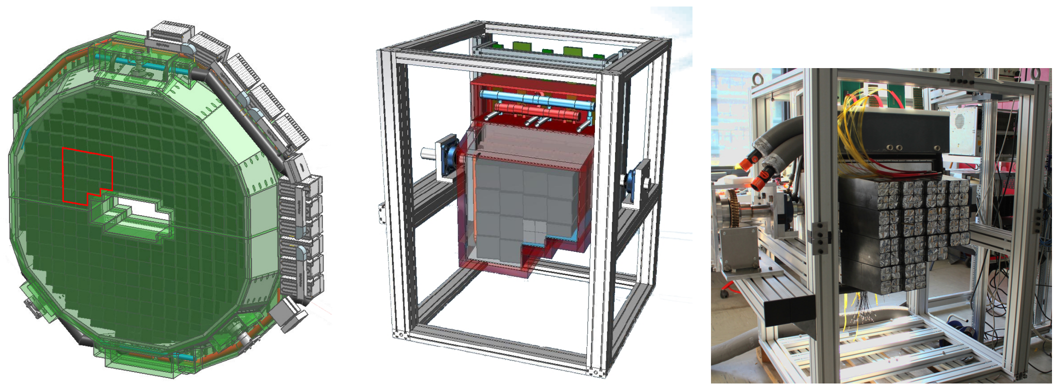

(a) (b) (c)

Fig. 10.1: (a) Red: area of the forward endcap resembling the prototype
(b) CAD drawing of the prototype in its holding structure
(c) Photograph of the prototype with all subunits mounted, but with front insulation and shielding removed

A mixture of 60% methanol and 40% water is pumped through long vertical holes drilled into the backplate, as well as through polyurethane hoses of 5 mm diameter, which are glued to the inside of the front hull to cool the inner volume of the prototype by external chillers. The aluminum enclosing of the assembly is covered by vacuum insulation panels, as foreseen for the forward endcap, to provide a thermal insulation against ambient temperature.

The complete prototype is mounted in a frame of aluminum profiles with just two rods made of glass fiber reinforced plastic, that are attached to the side faces of the backplate (see Figure 10.1b). These rods ensure a thermal insulation of the cold backplate from the aluminum frame and enable a rotation of the assembly by a worm drive mounted to the frame, so that the angle of the prototype towards the incoming beam can be adjusted. Furthermore, it is possible to adjust the height of the complete assembly in its frame by moving the bars up or down, to which the bearings that accommodate the plastic rods are mounted. This procedure is, however, only possible if the prototype is opened and a crane is available and thus the adjustments have to be made prior to transportation to an accelerator.

Front and back covers are attached with several screws to the backplate and O-rings between all components ensure an air-tight enclosure of the cold volume. An additional external chiller is used to cool dried pressurized air, with which the cold volume is constantly flushed at a rate of $\sim$ 100 l/hr. A photograph of the fully equipped prototype before attaching the front hull is shown in Figure 10.1c. All cables leading to and from the subunits, are led through one of the holes in the backplate and end shortly thereafter. At this point one patch panel PCB per subunit is mounted to the backplate and all cables are connected to it. The patch panel PCBs have been tested at the most recent beam time at the ELSA accelerator; However, they were not available during all previous beam times. Originally, the prototype was equipped with long multilayer PCBs, which carry the high and low voltage lines as well as the signals from the warm to the cold volume, however this solution was not feasible for application in the full forward endcap. A picture of the opened rear side of the prototype is shown for illustration in Figure 10.2.

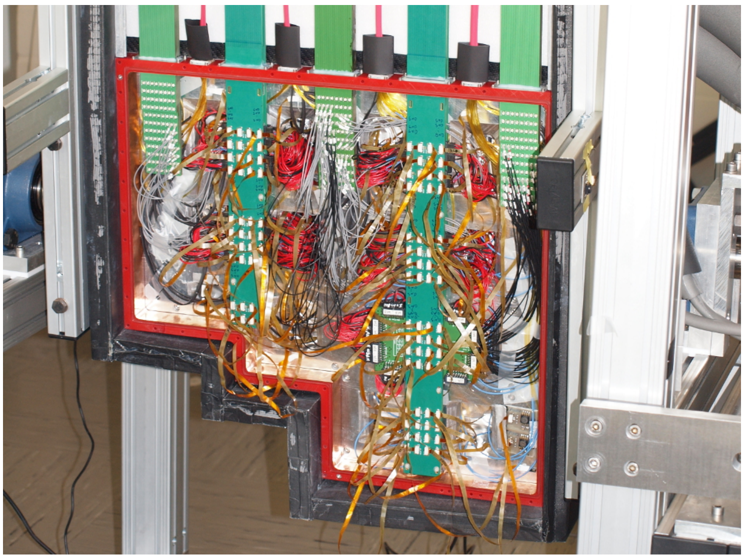

Fig. 10.2: Rear view of the opened prototype (vertical green bars are multilayer PCBs).

10.1 Overview of Test Beam Times

As many details as possible concerning construction and operation of the prototype were kept in line with the design of the full forward endcap to obtain a realistic test setup. However, several improvements were made over the course of the first four beam times. The first test beam time was conducted at the CERN Super Proton Synchrotron (SPS), where positrons with momenta of $10\,\mathrm{GeV}/c$ and $15\,\mathrm{GeV}/c$ as well as muons with a kinetic energy of 150 GeV were used. Dedicated tracking detectors consisting of a fiber-hodoscope and two silicon strip detector modules were installed in front of the prototype to provide a trigger signal and a precise position measurement for the particles impinging on the prototype crystals. Due to several issues with the preamplifier gain, the shaper boards and the digitizer modules, the noise and thus the corresponding single crystal threshold were rather high. Shortly after the first beam time, the prototype was installed downstream of the Crystal Barrel detector, which is located at the ELSA accelerator in Bonn. Here, tagged photons were used to measure response and energy resolution of the prototype at three energy points in the range between 1 and 3.1 GeV. Additionally, the rate of the beam photons could be varied at the ELSA facility, so that feasibility studies for the readout of photo detector-preamplifier units at rates comparable to those expected for the innermost crystals of the forward endcap could be performed. After several improvements and modifications of the hardware, a second test with a beam of tagged photons was performed at the MAMI accelerator in Mainz. At this beam time the response and the energy resolution for photons in the energy range of $20 - 415\,\mathrm{MeV}$ were studied and a single crystal threshold near to the design value was reached for the first time [84]. Since the results regarding the energy resolution at the highest energies were dominated by the partially bad performance of some hardware components, a second beam time at the CERN SPS accelerator was performed after especially the components of the readout chain (shapers, ADCs) were optimized. The results will be presented in the following section in further detail. As a last step, one close-to-final subunit equipped with VPTTs and one equipped with APDs were tested again at the ELSA accelerator, to verify the gain matching of the full readout chain. Some results of these measurements are reported in Section 10.4. An overview of all forward endcap prototype test beam times is given in Table 10.1.

	Beam particles	E_{Beam} or p_{Beam}	Characteristic feature
CERN/SPS	e^+	$10, 15\,\mathrm{GeV}/c$	Max. $\overline{\mathrm{P}}$ANDA energy
	μ^+	$150\,\mathrm{GeV}/c$	Energy deposit$\approx 230\,\mathrm{MeV}$
ELSA/Bonn	Tagged γ	1, 2.1, 3.1 GeV	Rates up to $2 \cdot 10^6\,\mathrm{s}^{-1}$
MAMI/Mainz	Tagged γ	20 - 415 MeV	Excellent beam energy resolution
CERN/SPS	e^-	$5 - 15\,\mathrm{GeV}/c$	Fiber / Si-strip
	$\pi^+, K^+, \overline{p}$	$15, 50\,\mathrm{GeV}/c$	Tracking Station
ELSA/Bonn	e^-	1.25, 2.4, 3.2 GeV	Fiber hodoscope

Table 10.1: List of beam tests with the forward endcap prototype. The first three listed test beam times are discussed in detail in [84], the fourth (CERN/SPS) in this work, and the last (ELSA) in this work as well as in [90].

10.2 Monte Carlo Simulation of the Prototype

For all beam times, the complete frame carrying the prototype was mounted onto an xy-positioning carriage. With the help of this device, the prototype could be moved in a plane perpendicular to the beam axis with an accuracy of $< 1\,\mathrm{mm}$, so that each instrumented crystal could be moved into the beam spot. This feature, in combination with a Monte Carlo simulation of the prototype, was used to obtain an absolute energy calibration for each single readout unit. As described in Section 8, the axes of all crystals of the forward endcap are directed towards a common off-point behind the nominal target position in the $\overline{\mathrm{P}}$ANDA detector. Since this geometry was also realized for the prototype, the angle between the test beam and a crystal in the prototype varies, when the detector is moved linearly in the xy-plane. The variation of this angle changes the most probable value of the energy that is deposited in a single crystal. A simulation of the energy deposition in three different crystals of the prototype for electrons with a momentum of $p_{e^-} = 10\,\mathrm{GeV}/c$ is shown in Figure 10.3b to illustrate the effect. For each beam time, the orientation of the complete prototype towards the beam was reproduced as realistically as possible in the simulation.

For the simulations, the detector model described in [84] was used. Figure 10.3a shows a visualization of the GEANT4 geometry model of the prototype. It includes all subunits containing the lead tungstate crystals (active material) as well as the carbon fiber alveoles, the reflective foils around the crystals, the air inside the prototype volume as well as the insulation hull in front of the crystals made of aluminum. Additionally also the poly-urethane hoses for the front cooling system and the vacuum insulation panels were included.

The *Single Particle Generator* of the *EvtGen* package was used to simulate the beam particles. In the context of this thesis, the setup described above was used to simulate and reconstruct the energy deposition in all instrumented crystals for all particle energies used during the two most recent beam times.

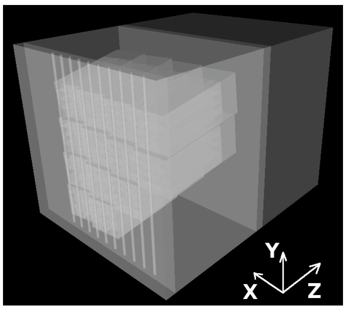

(a)

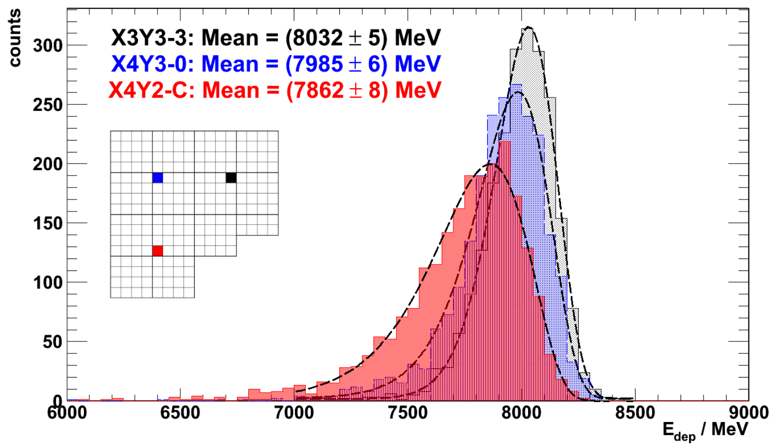

(b)

Fig. 10.3: (a) 3D-view of the prototype model as implemented in GEANT4.
(b) Energy deposition in three different crystals of the prototype by electrons ($p_{e^-} = 10\,\mathrm{GeV}/c$). The differences between the distributions are due to the different angles of the targeted crystals with respect to the beam axis. [84]

10.3 Beam Time at the CERN SPS

The forward endcap prototype was mounted at a test beam position in the H4 hall at the CERN Prévessin area, to which a tertiary beam from the SPS-C accelerator was delivered. The beam available in the experimental area is created by protons that are accelerated in SPS, which are then extracted and impinge on a beryllium production target. Downstream of this target a separation magnet and a tunable filter magnet are used to select the momentum and species of the particles that finally reach the test beam area. For this beam time electrons with momenta of $5.0, 7.5, 10.0, 12.5$ and $15\,\mathrm{GeV}/c$ were selected subsequently over the course of the beam time. Additionally, a beam consisting of mixed negatively charged hadrons ($\pi^-, K^-, \overline{p}$) with momenta of 15 and $50\,\mathrm{GeV}/c$ was used to study the response of the calorimeter to hadrons and the shapes of hadronic showers. For all electron momenta, the prototype was moved with the xy-carriage on which it was mounted to direct the beam centrally into each of the instrumented crystals. For each crystal position a dedicated run was recorded, with the goal to collect ~ 10000 events for each electron momentum. This data was used for the energy calibration as well as for a cluster reconstruction and the determination of the energy resolution, as described in the following sections.

10.3.1 Instrumentation of the Prototype

In total, 25 crystals of the prototype were instrumented with two LAAPDs each (see red marked boxes in Figure 10.4a). Nine crystals were read out using VPTTs (see green boxes in Figure 10.4a), since at the time of this test only a small batch of VPTTs from a pre-series production were available and this beam time marks their first test under realistic conditions.

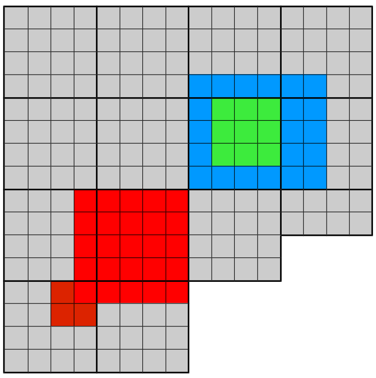

(a)

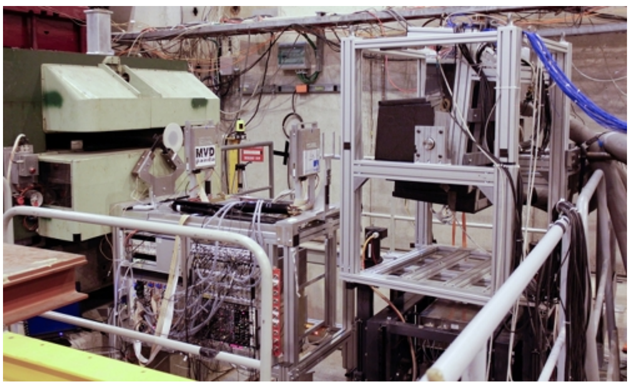

(b)

Fig. 10.4: (a) Instrumentation of the forward endcap prototype at the second CERN/SPS test beam time (front view). Red boxes mark crystals read out with LAAPDs, while green boxes stand for VPTTs and gray boxes mark uninstrumented crystals. The dark red and blue boxes denote other types of photo detectors and are not considered in this analysis.
(b) Photograph of the prototype at the test beam position in H4A at CERN. The beam is entering from the left side.

The nine VPTTs are surrounded by crystals instrumented with Hamamatsu Vacuum Photo Triodes (VPTs), a photo detector very similar to a VPTT containing only one instead of two dynode stages. These detectors were tested at earlier prototype test beam times and were used here to create a larger instrumented crystal matrix to obtain a better reconstruction efficiency for showers and minimize the shower leakage. However, for the determination of the energy resolution only the 3×3 matrix equipped with VPTTs was used. Pairs of LAAPDs were matched according to their characteristics while the APD-preamplifier units were assembled, so that a pair of APDs could be supplied by a common high voltage supply. At this beam time it was practiced for the first time, to tune the bias voltage of each APD pair during pre-calibration runs at a fixed beam momentum to obtain comparable signal yields for all APDs.

10.3.2 Readout and Data Acquisition

The analog signals of the photo detectors (preamplifier output signals) were routed via 7 m long coaxial cables (Huber+Suhner® Enviroflex) to electronics racks in which the shapers and digitizers were placed. Each analog detector signal was first passed to an analog shaping module, which performed an analog filtering of the input signal with a shaping time of 100 ns and which was also used to split the signal into two branches. In one branch the signal was shaped and left the module towards an input connector of a VME sampling ADC module. The second branch additionally featured an amplification of the shaped signal by a factor of approximately 15, so that signals with small amplitudes could be measured with a much better resolution. This measure was taken to ensure a good resolution over the complete dynamic range from a few MeV up to 15 GeV. All shaped signals were digitized using Wiener AVM/AVX-16 160 MHz, or SIS 3302 100 MHz sampling ADCs. Directly in front of the prototype, the *Bonn Tracking Station* was set up. Two crossed plastic scintillator paddles were used to deliver a trigger signal for both the tracking detectors as well as the prototype readout. The beam particles then traversed two double sided silicon strip detector modules and one fiber hodoscope. A schematic drawing of the readout chain is depicted in Figure 10.5.

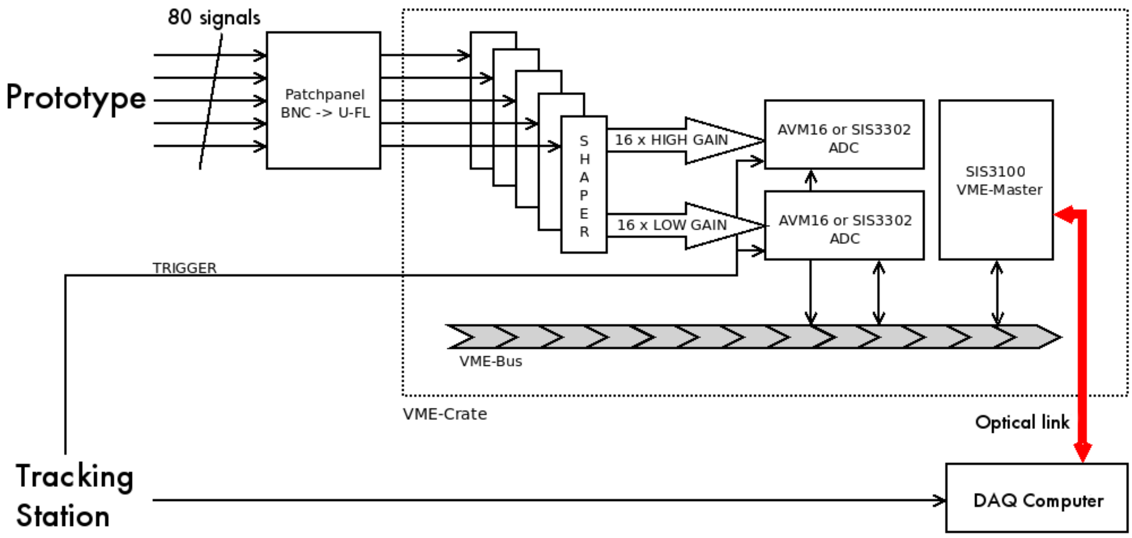

Fig. 10.5: Schematic diagram of the prototype readout during the CERN SPS beam time

10.3.3 Calibration

In the first step of the calibration procedure the signals from the low and high gain branches of a single analog detector signal are unified to provide only one digital value that will be calibrated using the Monte Carlo simulation data. For small signal amplitudes the high gain branch conversion is used for further analysis, while from a certain point on the response of the high gain branch becomes nonlinear and for even larger amplitudes clipping can be observed, so that the low gain signal must be used. In order to simplify the calibration procedure, a virtual high gain conversion is calculated for each signal in the low gain using a high gain to low gain calibration function. This calibration function is extracted for each photo detector by plotting the high gain versus the low gain conversion of each event and fitting the resulting curve in the region of linearity with a polynomial of first order. An example of such a high-low gain calibration function is shown in Figure 10.6a. The red line indicates the linear fit function, while the dashed red lines show the region in which a linear correlation is assumed. The nonlinearity towards large high gain conversions and the clipping beyond that region can be clearly seen. The red dashed line thus not only corresponds to the fit range of the linear function, but also marks the maximum amplitude up to which the high gain conversion can be used. After performing the high-low gain calibration, an absolute energy calibration is performed utilizing the Monte Carlo simulation data described above. For this simulation, the information from the fiber hodoscope of the *Bonn Tracking Station* is used to select events that impinge centrally onto the targeted crystal. The same cut is also applied to the MC data. Figure 10.6b shows the hit pattern of the hodoscope, which consists of 16×16 scintillating fibers with a diameter of 1 mm each. The elliptical shape of the 10 GeV/c beam can be clearly seen in the hit pattern. A cut to a region of 3×3 pixels in this hit map was performed to select the particles that centrally hit the crystal.

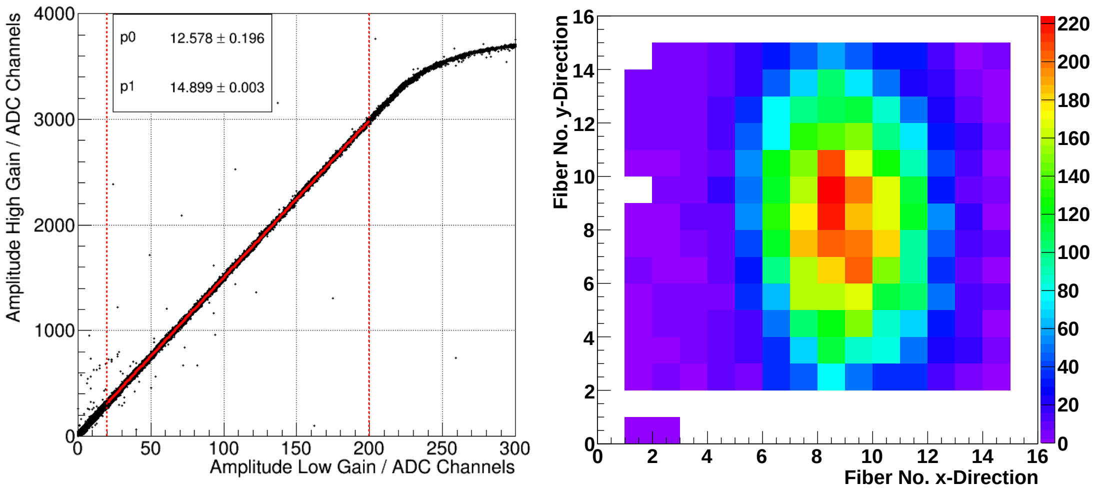

(a) **(b)**

Fig. 10.6: (a) High vs. low gain conversions for an APD. For events in the overlap region, marked with the dashed red lines, a linear fit to the data was performed (solid red line).
(b) Hit pattern of the fiber hodoscope for $p_e = 10\,\mathrm{GeV}/c$

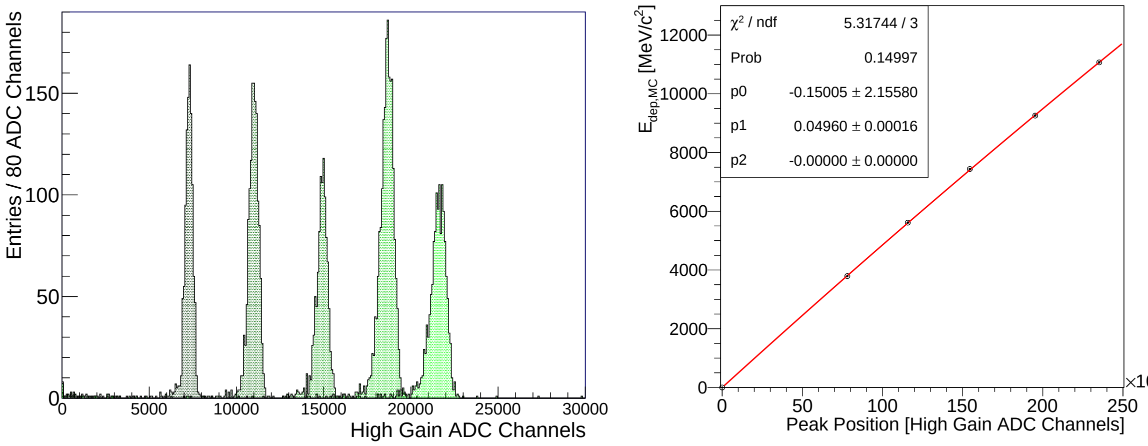

Fig. 10.7: (a) Uncalibrated response of a VPTT to 5, 7.5, 10, 12.5 and 15 GeV/c electrons (peaks from left to right) after applying a narrow cut on the fiber hodoscope hit pattern to select centrally impinging particles
(b) Exemplary energy calibration of an APD channel. The data points with error bars (inside the black circles) show the most probable energy loss for each beam momentum for centrally impinging particles from data (x-axis) and the Monte Carlo simulation (y-axis).

The raw spectra of the response of a single VPTT are shown for illustration in Figure 10.7a after application of this cut for all five electron momenta. The most probable value for the energy loss (i.e. the peak position) is extracted by fitting an asymmetrical function (*Novosibirsk function*) of the form

$$f(E) = A \cdot \exp\left[-\frac{1}{2}\left(\frac{\ln(1+\tau(E-\nu)\cdot\Lambda}{\tau}\right)^2 + \tau^2\right] \tag{10.1}$$

with $\Lambda = \frac{\sinh(\tau\sqrt{\ln 4})}{\sigma\tau\sqrt{\ln 4}}$ [91] to the spectra of both the data as well as the Monte Carlo simulated data for each crystal position and beam momentum. The parameter τ is called the *tail parameter* and describes the asymmetry of the function, while σ is the width and ν the peak position of the function. Finally, the correlation between the peak positions obtained from data and MC are fitted with a polynomial of second order and these calibration fit functions are from here on used to calculate the energy equivalent of a measured amplitude for a specific photo detector. The calibration function of an APD is shown exemplary in Figure 10.7b. In this case it can be seen, that the offset of the calibration function (p_0) is compatible with zero, and the quadratic term (p_2) vanishes.

10.3.4 Results on Noise and Energy Resolution

In contrast to the readout scheme foreseen for the full forward endcap, full-sized waveforms of the sampling ADCs were read out and stored to disk during all prototype test beam times. For the operation of the full detector, this option is not feasible due to the large amount of data that would need to be transmitted continuously. For the prototype studies this option enables the possibility to study the pulse shapes offline and perform several tests, e.g. digital filtering algorithms, with real data. Apart from the information contained in the signal pulse (see Figure 10.8a), as e.g. the amplitude, integral or the rise and fall time, about 100 samples prior to the beginning of the pulse are recorded. The data in this region is used together with the calibration functions to measure the energy equivalent of the noise level for each photo detector. Samples that lie within the region marked with red dashed lines in Figure 10.8a are histogrammed for all waveforms recorded for the same photo detector. The noise distributions are then fitted with a Gaussian function and their width (σ) is extracted. Using the calibration function, the energy equivalent of the width (given in ADC-channels) is calculated. The resulting values for all nine VPTTs and 50 APDs are displayed in Figure 10.8b. The mean values of the noise amount to

$$\langle\sigma_{\text{Noise}}\rangle_{\text{VPTTs}} = 1.9\,\text{MeV, and} \tag{10.2}$$
$$\langle\sigma_{\text{Noise}}\rangle_{\text{APDs}} = 1.8\,\text{MeV}, \tag{10.3}$$

when only the data from the CERN beam time described here is taken into account. Slightly better values could be achieved for measurements with VPTTs at the MAMI accelerator as described in [84]. Both mean values are close to the design value of $\sigma_{\text{Noise}} = 1\,\text{MeV}$ given in the technical design report of the EMC. It is a common practice to set the single crystal threshold to a value similar to $3 \cdot \sigma_{\text{Noise}}$, which in this case corresponds to $E_{\text{thr}} \approx 6\,\text{MeV}$. Under the assumption that the noise shows a purely gaussian distribution, the 3σ cut translates to a suppression of about 99.73% of all noise signals.

For this test beam time, the lowest beam momentum was $5\,\text{GeV}/c$, which means that even in the outer crystals of a 5×5 crystal matrix, in most cases more than 6 MeV are deposited. Thus, no proper threshold scan to verify that the best performance is achieved

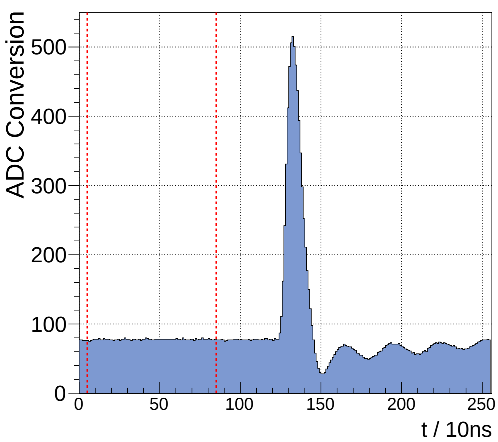

(a)

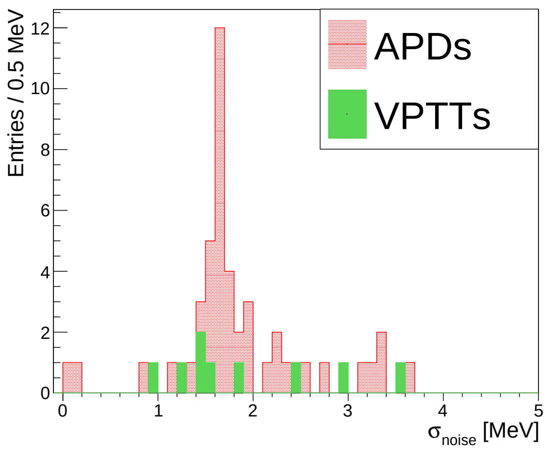

(b)

Fig. 10.8: (a) Typical waveform of an AVM/AVX-16 ADC showing a shaped signal from a connected APD. The region between the red dashed lines is used to determine the noise level.
(b) Width of the noise distributions for all VPTTs and APDs

when choosing the threshold as $3 \cdot \sigma_{\text{Noise}}$ can be performed and a threshold of 6 MeV was applied for all results presented here.

When an electron centrally hits a PWO crystal, about 80% of its energy is deposited in this "central" crystal. In order to fully reconstruct the energy of the incident particle, the deposition in the neighboring crystals has to be considered as well. The group of crystals that are considered for the calculation of the total energy is called a *cluster*. Once the EMC will be completed and operated as a part of the full the $\overline{\text{P}}$ANDA detector, an algorithm for finding clusters will be employed, which starts from the crystal with the largest energy deposit and stepwise moves outwards adding the deposited energy of surrounding crystals to the cluster as long as their signal exceeds the single crystal threshold. For the prototype studies symmetrical 3×3 and 5×5 crystal matrices were considered for the cluster reconstruction instead, due to the fact, that the position of the central crystal and the point of impact are precisely known. The energy deposited in the 9 or 25 crystals was then summed up and the resulting distribution was fitted with a Novosibirsk-function as given in equation (10.1). The energy resolution is defined as the ratio of the width σ_E and the peak position $\nu := E$ of this function. As an example, Figure 10.9a shows the distributions of deposited energy for the central crystal, the two surrounding crystal rings as well as the 3×3 and 5×5 matrix for crystals instrumented with APDs at a beam momentum of 5 GeV/c. The blue line indicates the fit function from which the resolution is extracted. Similarly, Figure 10.9b shows the corresponding distributions for the 3×3 matrix equipped with VPTTs at the highest available beam momentum of 15 GeV/c. A summary of all extracted values for the resolution is listed in Table 10.2 and visualized in Figure 10.10 together with the design values given in the technical design report of the EMC [74]. In general the envisaged design values can be easily reached if a 5×5 crystal matrix is used. The results for the 3×3 matrix are only slightly worse and also give results close to the design values.

It should be noted, that all results for the energy resolution measured with APDs are based on the signals of one photo detector per crystal. It is in principle possible to combine the signals of both APDs, which leads to an improvement of the signal-to-noise ratio by a factor of $\sqrt{2}$ and therefore also further improves the energy resolution.

	VPTT 3×3	APD 3×3	APD 5×5	TDR
p_{e^-} [GeV/c]	$\frac{\sigma_E}{E}$	$\frac{\sigma_E}{E}$	$\frac{\sigma_E}{E}$	$\frac{\sigma_E}{E}$
5.0	(1.48 ± 0.04) %	(1.27 ± 0.03) %	(1.19 ± 0.04)%	1.34%
7.5	(1.16 ± 0.02) %	(1.12 ± 0.03) %	(1.03 ± 0.03) %	1.24%
10.0	(1.12 ± 0.02) %	(1.19 ± 0.03) %	(1.10 ± 0.03) %	1.18%
12.5	(1.05 ± 0.03) %	(1.19 ± 0.04) %	(1.09 ± 0.04) %	1.15%
15.0	(1.00 ± 0.03) %	(1.24 ± 0.03) %	(1.13 ± 0.03) %	1.13%

Table 10.2: Relative energy resolution for all beam momenta and crystal matrix sizes together with the design values given in the TDR

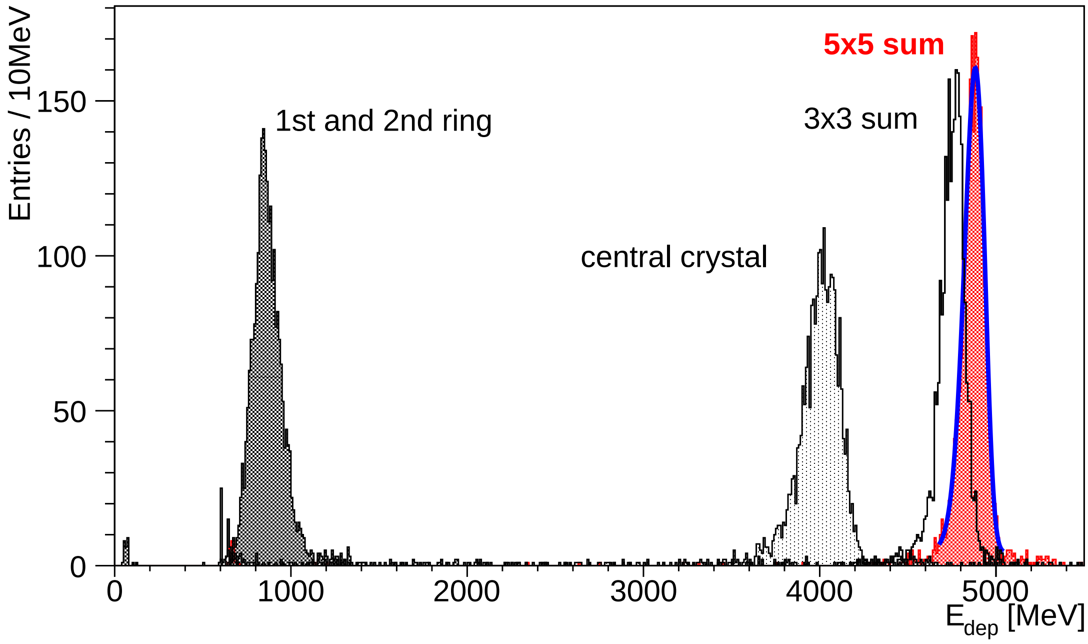

(a)

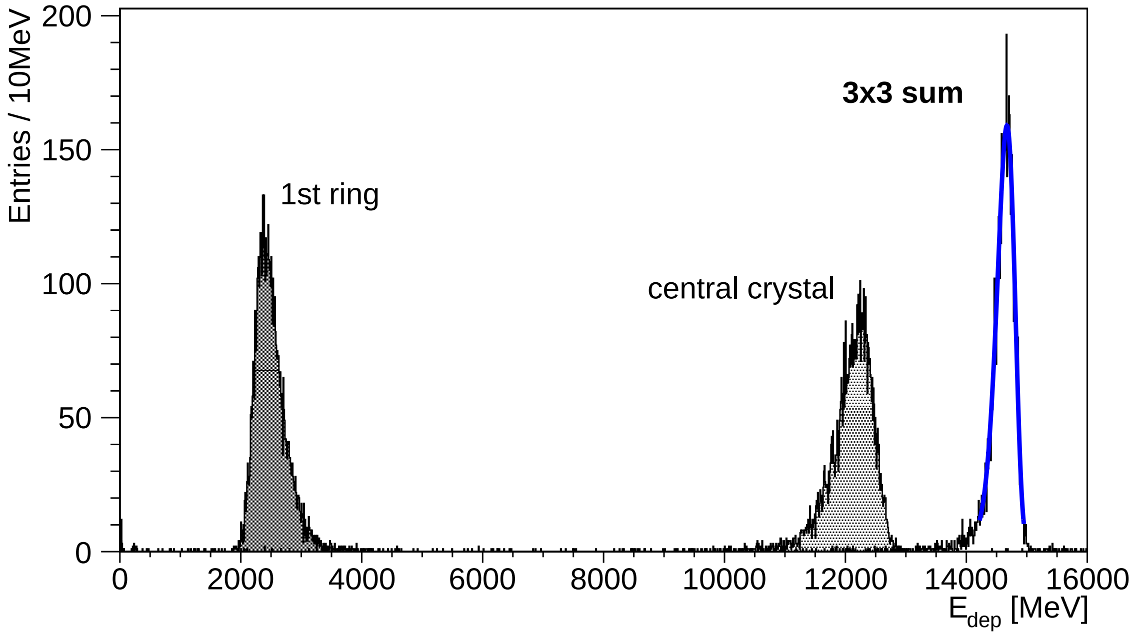

(b)

Fig. 10.9: Energy deposit in the central crystal, the surrounding crystal ring(s) and the complete 3×3 and 5×5 crystal matrix for (a) APDs at a beam momentum of $5\,\mathrm{GeV}/c$ and (b) VPTTs at a beam momentum of $15\,\mathrm{GeV}/c$.

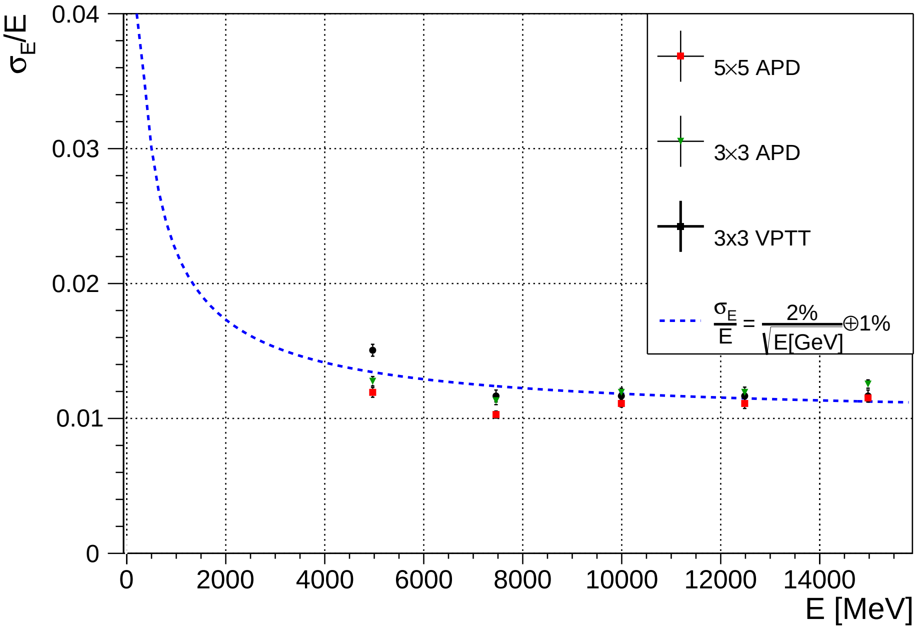

Fig. 10.10: Relative energy resolution versus incident particle energy for a 3×3 crystal matrix equipped with VPTTs (black) as well as a 3×3 (green) and 5×5 crystal matrix equipped with APDs for all five electron beam momenta. The blue curve shows the design values as given in the TDR.

10.4 Beam Time at the ELSA Accelerator

The main differences between the subunits produced for earlier beam tests and the final subunits are the permanent optical coupling between the photo detectors and the crystals, as well as the alveole structure, which in the newer version has a closed front. Before starting the mass production of subunits, a beam test with the two subunits described in Section 9.1 was performed at the electron stretcher facility ELSA at the University of Bonn. The ELSA accelerator provides a continuous electron beam that was directed towards the surfaces of the crystals in the prototype. As before, the prototype was mounted on an xy-carriage and was moved in a plane perpendicular to the beam axis, to direct the beam onto each of the 32 instrumented crystals. Measurements with electrons of three different energies were performed, namely 1.25, 2.4 and 3.2 GeV. Figure 10.11a shows the position of the two subunits in the prototype. During this beam time, the fiber hodoscope described in the previous section was used as well, in order to provide rudimentary tracking information. The same procedure concerning the calibration of the low- to the high-gain branch of the shaper modules as well as a cut on the impact position to select central hits was performed. Figure 10.12 shows the response of a VPTT for all three beam energies.

As foreseen for the instrumentation of the full forward endcap, a careful selection of the photo detectors placed in both subunits was performed during the assembly: The amplification of all VPTTs was measured upon arrival, as described in Section 8.5.1.

Based on these measurements, 16 tubes with a mean gain of $\langle M \rangle_{\mathrm{VPTT}} = 57.75$ for operation at an anode voltage of 1 kV were selected, whereas the maximum deviation from this mean value amounts to just 1.5% [81]. For the APDs it was necessary to measure

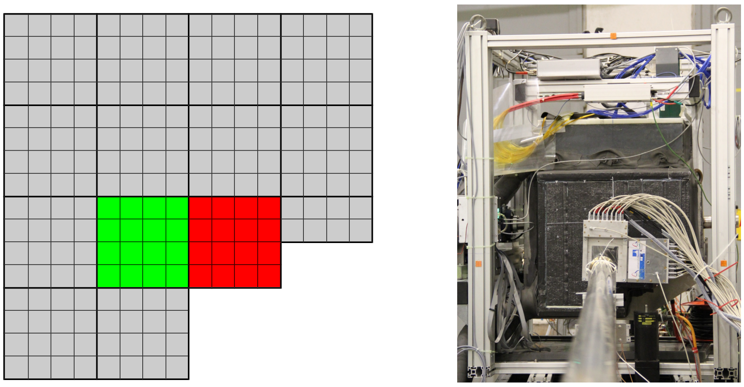

(a) **(b)**

Fig. 10.11: (a) Instrumentation of the forward endcap prototype at the second ELSA test beam time (front view). Red boxes mark crystals read out with LAAPDs, green boxes denote VPTTs and gray boxes mark uninstrumented crystals. (b) Photograph of the front face of the prototype. The fiber hodoscope box is visible between the end of the beam pipe and the prototype.

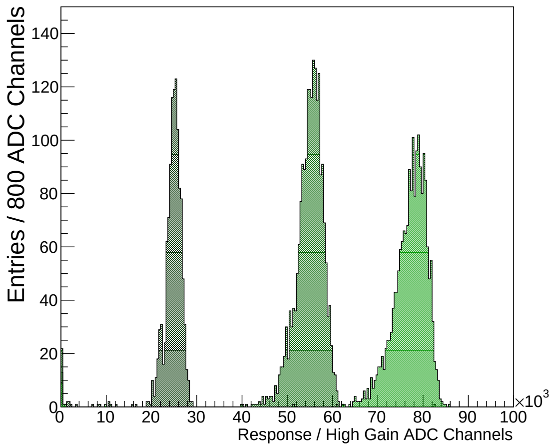

Fig. 10.12: Uncalibrated response of a VPTT to 1.25, 2.4 and 3.2 GeV electrons (peaks from left to right) after a narrow cut to the fiber hodoscope hit pattern was performed to select centrally impinging particles.

the response curve in dependence of the bias voltage at $-25°C$ with the same procedure as described in Section 8.5.1. The bias voltage needed to reach the operational gain of $M = 200$ at $-25°C$ was extracted, and groups of eight APDs were identified, for which similar values were obtained. The maximum deviation of the obtained APD gain from the envisaged gain of $M = 200$ amounts to 2% [92].

The main goal of the ELSA test beam time was to determine the response of the photo detector preamplifier units to check the matching of the voltage ranges of all electronic components, mainly that of the preamplifier. Since the available beam energy is much smaller than the maximum single crystal energy deposit expected in the forward endcap (approx. 12 GeV), an extrapolation had to be employed to estimate the output signal amplitude of the preamplifier at the maximum expected energy. After selecting centrally impinging particles by using data from the fiber hodoscope, the resulting energy distributions were fitted with a Novosibirsk-function as described in Section 10.3.3, and the value for the most probable energy deposition (the peak position) was extracted.

Signal Yield of VPTTs Figure 10.13a shows the uncalibrated peak positions for all 16 VPTTs versus the number of the crystal in the subunit. The diagram shows, that all VPTTs have comparable signal outputs. The standard deviation of the 16 values is on the level of a few percent. It should be noted here, that the variation of the light yield (number of scintillation photons per MeV) for the crystals in the VPTT subunit introduces deviations on the order of $\sigma_{\mathrm{LY}} \approx 3\%$. Possible deviations between individual shaper and ADC channels were investigated and found to be negligible. Taking into account the input and output impedances of all components in the readout chain (preamplifier, shaper, ADC), the output signal of the VPTT preamplifiers could be determined to be approximately 200 mV/GeV [81]. This value was cross-checked and finally confirmed after the end of the beam time with cosmic muons, measured with the same VPTT subunit after disassembly from the prototype in a test stand at the Universität Bonn. The output range of the preamplifier extends up to ~ 2.5 V, thus extrapolating from the value of 200 mV/GeV, no change in amplification of the preamplifier would be necessary, when no magnetic field is present. Due to the expected loss of about 50% of the VPTT signal in the magnetic field of the $\overline{\mathrm{P}}$ANDA solenoid, the preamplifier gain was optimized as a result of the test beam time: All VPTTs were sorted by their gain as well as their sensitivity to an external magnetic field and divided into three groups. Adapted versions of the preamplifier will be used for each of the these groups. While the preamplifiers that were used at the ELSA test beam time delivered a signal of 460 mV/pC, the modified versions are able to deliver 890, 820 and 700 mV/pC, respectively [81].

Signal Yield of APDs The same study was performed for the signal yield of the APD subunit; However, much larger deviations between the response of individual APD units were observed. Figure 10.13b shows the peak positions of all operational APD units for a beam energy of 1 GeV (units 6 and 15 were non-operational). Astonishingly, two well separated groups of signal amplitudes show up. These are not corresponding to APDs connected to the same high voltage supply line. Also the mechanical pairing of two APDs mounted in one capsule can not be correlated with the two groups.

As for the VPTT subunit, the deviations between the light yield of the crystals and the individual shaper/ADC channels were checked, and similar values were obtained, so that the differences in signal yield cannot be explained by either of these.

Various investigations into the cause of these large difference in signal yield between the two groups of APDs have been performed. These included *in-situ* measurements of the APD quantum efficiency, which are reported in [93]. The quantum efficiency was found to be almost independent from the operational temperature of the APD and furthermore the intrinsic differences between the APDs were on the level of $\sim 2.5\%$ and thus cannot explain the observed large deviations. During these studies however, a significant impact of varying pressure or tactile contact to the reflective foil in which all crystals are wrapped was noticed. Therefore, a dedicated study with the completely assembled APD subunit was performed, for which it was placed in a climate chamber at different orientations.

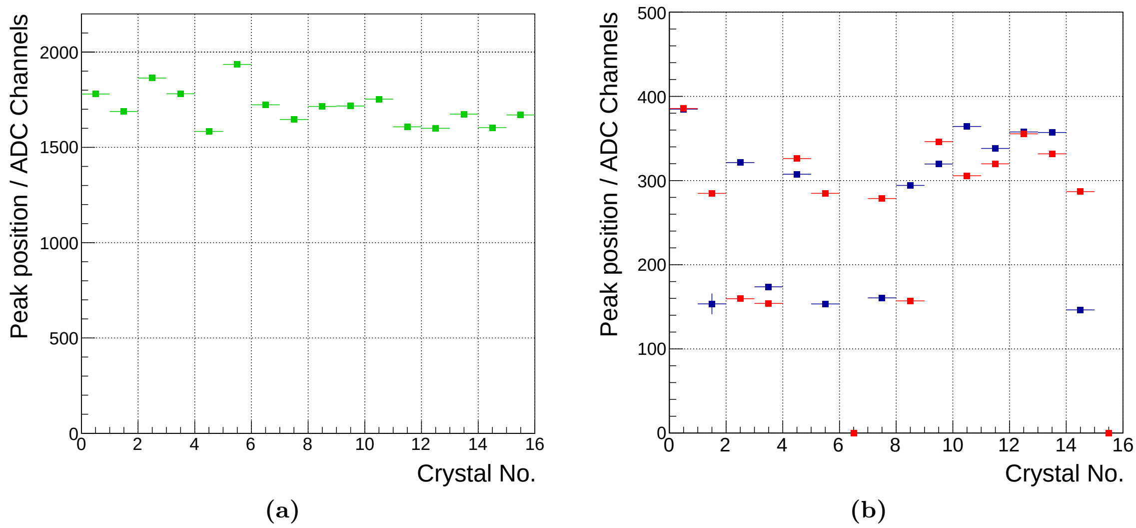

Fig. 10.13: Most probable value (peak position) for the response of VPTTs (a) and APDs (b) for centrally impinging electrons with a momenum of 1 GeV/c^2 versus the crystal number in the corresponding subunit. Blue and red markers are used to distinguish between the two APDs attached to each crystal.

Due to their weight, the crystals are slightly moving inside the carbon fiber alveole and the reflective foil is pressed to the crystal surface slightly differently for each orientation that was tested. These tests have shown that the yield of an APD unit varies on the level of $5-10\%$, if the subunit is moved and rotated [94]. However, also this effect cannot be the sole explanation for the observed deviations. During the investigations in the aftermath of the ELSA beam time, a few photo detectors (three APD and two VPTT units) unexpectedly lost their coupling to the crystal and had to be re-glued. Although the two subunits were heavily used, the silicone based coupling should not have failed. A new cleaning fluid based on methylsiloxane was introduced to clean the photo detector and crystal surfaces from potential residue e.g. of the Elastosil casting compound, which could possibly compromise the glueing surfaces, however this effect was never proven to occur.

The energy resolution based on a cluster reconstruction using four different 3×3 crystal matrices equipped with VPTTs was performed as a part of [90]. Table 10.3 shows the results for the resolution and the corresponding design values given in the TDR.

	$E = 1.25\,\mathrm{GeV}$	$E = 2.4\,\mathrm{GeV}$	$E = 3.2\,\mathrm{GeV}$
3×3 VPTT	$(2.3 \pm 0.15)\%$	$(1.76 \pm 0.11)\%$	$(1.46 \pm 0.11)\%$
TDR	2.05%	1.63%	1.5%

Table 10.3: Relative energy resolution for all three beam energies available during the ELSA test beam time [90] and the design values as given in the TDR

10.5 Determination of the Energy Resolution for the Full Energy Range

When combining the results for the energy resolution at low energies down to 23 MeV [84] (MAMI) with those obtained for medium energies [90] (ELSA) and the results presented in this work for energies up to 15 GeV (CERN), a parameterization for the energy resolution can be extracted for the full $\overline{\mathrm{P}}$ANDA energy range. A combined fit to all test beam data yields an energy resolution for symmetric 3×3 and 5×5 lead tungstate crystal matrices of

$$\frac{\sigma_E}{E} = \frac{(2.41 \pm 0.02)\%}{\sqrt{E[GeV]}} \oplus (0.86 \pm 0.02)\%, \qquad (10.4)$$

which is depicted in Figure 10.14. The parameterization given in equation (8.1) was used for this fit in order to compare the results with the envisaged resolution given in [74]. While the targeted resolution is well met for higher energies, a slightly worse resolution is obtained for energies below 1 GeV. In accordance to this observation, the parameter of the energy dependent term is somewhat larger than its design value of 2%, while the parameter for the constant term was even found to be smaller than the targeted value of 1%.

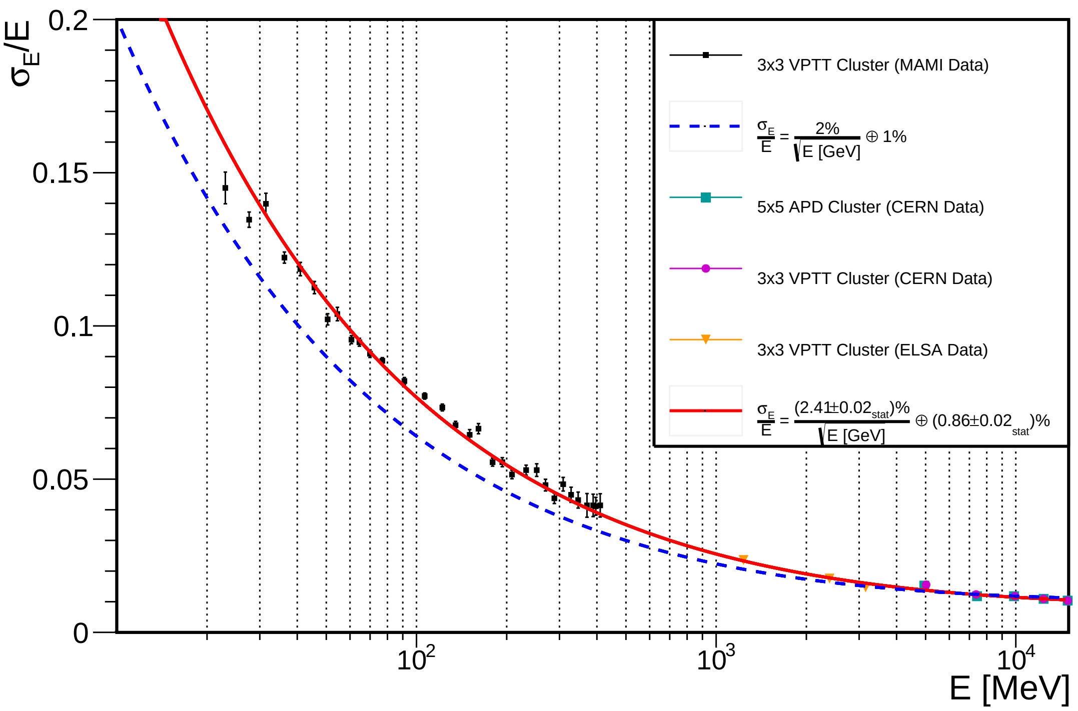

Fig. 10.14: Energy resolution in dependence of the incident energy for symmetric crystal matrices of the $\overline{\mathrm{P}}$ANDA forward endcap EMC prototype. The resolution was measured at different accelerators with tagged photon or electron beams.

11 Conclusion and Discussion of Part II

The readout of lead tungstate scintillation crystals of the forward endcap using both Vacuum Photo Tetrodes as well as Avalanche Photo Diodes was studied and further developed within the scope of this thesis. Several readout units utilizing charge-integrating preamplifiers were assembled and finally tested in the forward endcap prototype under realistic conditions at different accelerators (SPS/CERN, MAMI/Mainz, ELSA/Bonn). These tests included two close-to-final calorimeter subunits, one equipped with VPTTs, the other with APDs, for which for the first time a permanent coupling between the photo sensors and the crystals was employed. While the overall performance of the calorimeter was found to be more than satisfactory, a small fraction of photo sensors unexpectedly lost their connection to the crystal. This effect is being investigated further at the moment.
As a result of the test beam measurements, the final amplification factor for the VPTT preamplifiers was defined and all devices have been produced already. The photodetector-preamplifier units produced as a part of this thesis show a stable performance and thus mass production for this type of units can start right away.
Several APDs will be supplied with a common high voltage line in the forward endcap, which demands for a good matching of APDs to groups with similar characteristics. The key parameters for the matching of APDs are the bias voltage that is needed to achieve an amplification factor of $M = 200$ at a temperature of $-25°$C and the slope of the diode response curve with respect to the applied bias voltage. Although the final gain matching for all APDs for the forward endcap demands for a larger number of fully screened APDs and probably also the application of an advanced matching algorithm, the available data already enables the construction of first subunits.
The data recorded at the most recent test beam time revealed large differences in the obtained signal yield for some APD units. Differences in the quantum efficiency of single diodes, the optical coupling of the sensors to the crystals as well as differences in the mechanical assembly were excluded as possible reasons for the observed discrepancies. Although all APD units show a good performance with respect to the noise and energy resolution, the observed differences have to be further investigated.
As a result of the analyses of test beam data presented in this work, the energy resolution of symmetric (3×3 and 5×5) lead tungstate crystal matrices was studied for the full energy range expected for the forward endcap. A combined fit to data from all test beam times yields an energy resolution for which the energy dependent term ($\propto 1/\sqrt{E}$) was determined as $a = (2.41 \pm 0.02_{\text{stat.}})\%$, which is slightly larger than the envisaged value from the Technical Design Report of $a_{\text{TDR}} = 2\%$. The constant term however was found to be $b = (0.86 \pm 0.02_{\text{stat.}})\%$, which is even below the design value of $b_{\text{TDR}} = 1\%$. It is to be expected, that also the energy dependent term reaches the design value when larger or asymmetric crystal matrices and cluster reconstruction algorithms are used for the final detector. Additionally, the signal of the two APDs attached to one crystal can be combined, which will further improve the energy resolution especially for small energies.

12 Summary

The decay $J/\psi \to \gamma\omega\omega \to \gamma(\pi^+\pi^-\pi^0)(\pi^+\pi^-\pi^0)$, whereas both π^0 mesons were reconstructed via their decays into two photons, was analyzed in the scope of this thesis. The analysis is based on the world's largest data set of J/ψ decays, containing $1.31 \cdot 10^9$ events, which was recorded by the BESIII experiment located at the BEPCII electron-positron collider in Beijing, China.

A significant contribution of non-resonant background events containing just one ($\gamma\omega 3\pi$) or no ω meson ($\gamma 6\pi$) was observed in the $\omega\omega$ signal region. This type of background was removed by applying an event based background subtraction method utilizing probabilistic weights. The weights of the selected data set sum up to 75245 ± 274 events. Large enhancements are observed in the invariant $\omega\omega$ mass around $1.8\,\mathrm{GeV}/c^2$ as well as in the region of $2.98\,\mathrm{GeV}/c^2$. The latter is corresponding to the mass of the $\eta_c(1S)$. No resonant structures are observed in the $\gamma\omega$ system.

The data was subjected to a full partial wave analysis starting with the initial J/ψ system, down to the final state particles to determine the spin-parity of the enhancements and identify possibly contributing resonances in the $\omega\omega$ system. As a first step, a model independent PWA was performed by fitting the data with various hypotheses in slices of the invariant mass of the $\omega\omega$ system. This analysis revealed a dominant pseudoscalar (0^{-+}) contribution over the entire mass range as well as much smaller, but significant, scalar (0^{++}) and tensor (2^{++}) contributions, especially in the mass range $m(\omega\omega) \leq 2.3\,\mathrm{GeV}/c^2$. A pseudoscalar assignment is in particular also valid for the two enhancements observed in the $\omega\omega$ mass, so that the higher one can be identified with the lightest charmonium state, the η_c. Due to the complex structures observed in the contributions which were extracted with the model independent PWA, contributions of broad and overlapping resonances had to be expected. Therefore, the K-matrix formalism was used in the subsequent model dependent PWA. A very good description of the data was achieved utilizing parameterizations containing two poles for the 0^{++} as well as the 2^{++} contributions, and a five-pole parameterization for the dominant 0^{-+} contribution. The two resonances $f_0(1710)$ and $f_0(2020)$ were identified as possible contributions to the scalar partial wave, while the contributions to the tensor component were associated with the $f_2(1640)$ and the $f_2(1950)$. Two of these resonances, namely the $f_0(1710)$ and the $f_2(1950)$ are discussed as potential glueball candidates. Even though this association of the 0^{++} and 2^{++} contributions with the aforementioned resonances may be ambiguous due to the presence of many sometimes broad states of the same quantum numbers in this complex energy region, the presence of broad scalar and tensor components is confirmed by the model dependent PWA.

It was found that the pseudoscalar enhancement at the $\omega\omega$ mass threshold can be excellently described by a combination of the $\eta(1760)$ resonance and a second, slightly narrower resonance, which could be associated with the $X(1835)$. Furthermore, significant contributions of the $\eta(2225)$ and the η_c mesons were identified, as well as an additional broad structure, which was here associated with a pseudoscalar state called $X(2500)$. The resonance parameters of this state were determined to be $m = 2488^{+13}_{-14}\,\mathrm{MeV}/c^2$ and $\Gamma = (215 \pm 15)\,\mathrm{MeV}/c^2$, what is consistent with a recent observation in the $J/\psi \to \gamma\phi\phi$

channel by the BESIII experiment. The product branching fractions of the 0^{-+}, 0^{++} and 2^{++} contributions were determined together with the branching fraction for $J/\psi \to \gamma\omega\omega$, which amounts to $(2.5 \pm 0.16) \cdot 10^{-3}$. The uncertainties of this measurement are a factor of two smaller than those of previous measurements listed in [1]. The selection efficiency for this measurement was derived from the PWA fit, taking all dimensions of the phase space into account. The result shows a deviation of 2.7σ from the value listed in [1]; however, the result from the analysis presented here is based on a sample that is about a factor of 200 larger than that of the previous measurement.
The branching fraction $\eta_c \to \omega\omega$ was measured for the first time as a part of this thesis. A model dependent PWA fit was used for the description of the data. A value of

$$\mathcal{B}(\eta_c \to \omega\omega) = (1.88 \pm 0.09_{\text{stat.}} \pm 0.17_{\text{syst.}} \pm 0.44_{\text{ext.}}) \cdot 10^{-3}$$

was obtained, whereas the last uncertainty is due to the poorly measured external branching fraction $\mathcal{B}(J/\psi \to \gamma\eta_c)$.

Precision charmonium spectroscopy is also one of the key objectives of the upcoming $\overline{\text{P}}$ANDA experiment, where especially the mass region above the $D\overline{D}$ threshold will be accessible. As one of the key projects of the future accelerator facility FAIR, the $\overline{\text{P}}$ANDA experiment will significantly contribute to the understanding of the non-perturbative regime of QCD by exploring the nature of the strong interaction and the hadron spectrum. An accurate energy measurement of electrons and photons created in antiproton-proton annihilations inside the $\overline{\text{P}}$ANDA detector is an essential prerequisite for the envisaged studies. Due to the Lorentz-boost in fixed target experiments, the forward endcap of the EMC will experience high radiation doses and single crystal hit rates up to $10^6\,\text{s}^{-1}$. The readout of lead tungstate scintillation crystals utilizing two different types of photo sensors was studied as a part of this thesis. Readout units consisting of Vacuum Photo Tetrodes (VPTTs) as well as Avalanche Photo Diodes (APDs) combined with low-noise charge integrating preamplifiers were produced and tested in a prototype setup. The performance of the forward endcap prototype was tested during several test beam times, in which the crystals were irradiated with different particle beams in the energy range between 23 and 15000 MeV. Results of the two latest test beam times are presented in this thesis. The test beam time at the CERN/SPS accelerator has shown, that the envisaged energy resolution can be met at the highest energies to be expected in the region of the forward endcap. Two close-to-final calorimeter subunits comprised of 16 crystals and the corresponding readout units were produced and tested at the most recent beam time at the ELSA accelerator. As a result, the amplification of the preamplifiers for the use with VPTTs was determined, so that the production of all devices could be started and has been concluded in the meantime. Taking into account the data recorded at all test beam times, the energy resolution of the prototype setup over the full energy range to be expected in the forward endcap was determined as

$$\frac{\sigma_E}{E} = \frac{(2.41 \pm 0.02)\%}{\sqrt{E[GeV]}} \oplus (0.86 \pm 0.02)\%.$$

A Further Validation of the Q-Factor Method

Complementary to the toy MC study presented in Section 3.4.3, an even stronger test of the Q-factor method was performed involving a different model for background events. It is noted here, that no changes to the metric or the fitting procedure were made, the Q-factors are only calculated for a different MC data set. This second toy MC sample explicitly includes a peaking background component at the mass of the η_c, which is the subject of further studies in this analysis. Furthermore the way of generating the background sample was modified: The model obtained from a fit to the signal region was used in a slightly modified way to generate three distinct background sub-samples. Two sub-samples were generated, for which only one ω was removed and replaced by a phase-space-like description of the decay dynamics and one sub-sample for which both ω mesons were replaced in the same way. The three sub-samples and the signal sample were then mixed and subjected to the Q-factor method. The method was also applied for the different sub-samples before mixing. Figure A.1 shows the invariant mass of the $\omega\omega$ system (logarithmic y-scale) as well as the two 3π invariant mass spectra for generated signal and background events, and for the Q- and $(1-Q)$-weighted MC sample.
In the first scenario shown in Figure A.1a, all background events proceed via a direct decay into 6π, thus there is no ω signal present in the 3π mass spectra of the background sample, which is correctly identified by the Q-factor method. Also the peaking background component in the $\omega\omega$ mass distribution is well described. Figure A.1b shows a rather unrealistic scenario, in which the weighting method still performs quite well. Here, all background components decay into one ω and an associated 3π-system, which is not originating from an ω. Even here, the peaking background component is reasonably well identified. While these two plots just show the intermediate steps towards the final mixed MC toy sample, Figure A.1c shows the results for the combination of all scenarios. The peaking background contribution, as well as all other background contributions, contain decays via one or no ω resonance. Also here, the peaking background contribution is very well identified. The shape and total integral of the background below the two 3π mass distributions is well described. This study was performed, because decays of the η_c resulting in a final state of six pions are to be expected, while not all of them are decaying via two ω resonances. This study shows, that possible contamination under the η_c peak is clearly identified and removed by the Q-factor method.

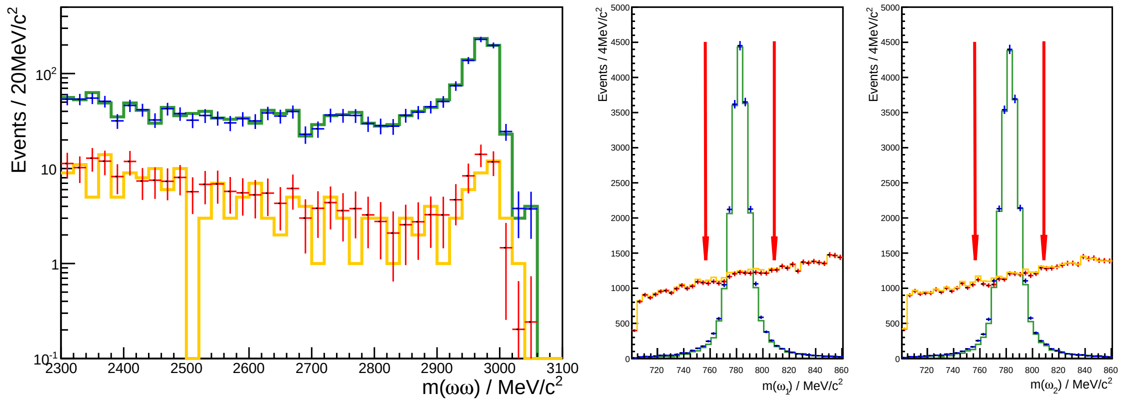

(a)

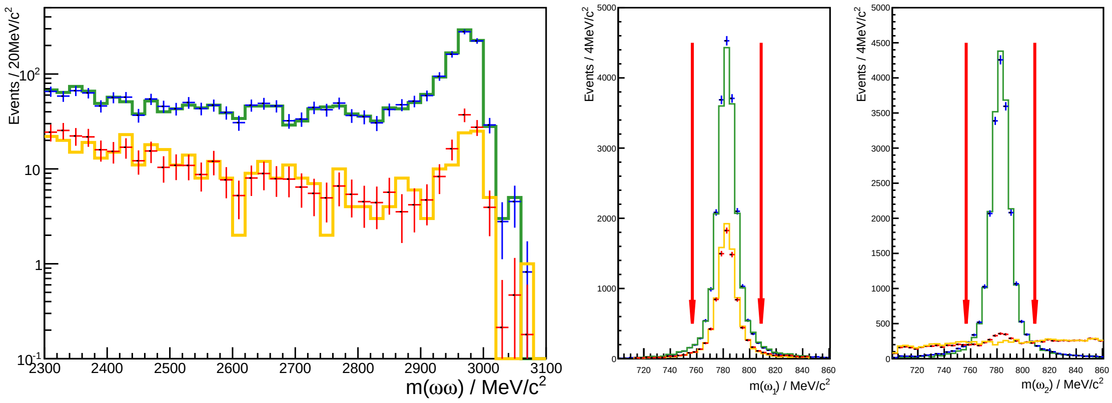

(b)

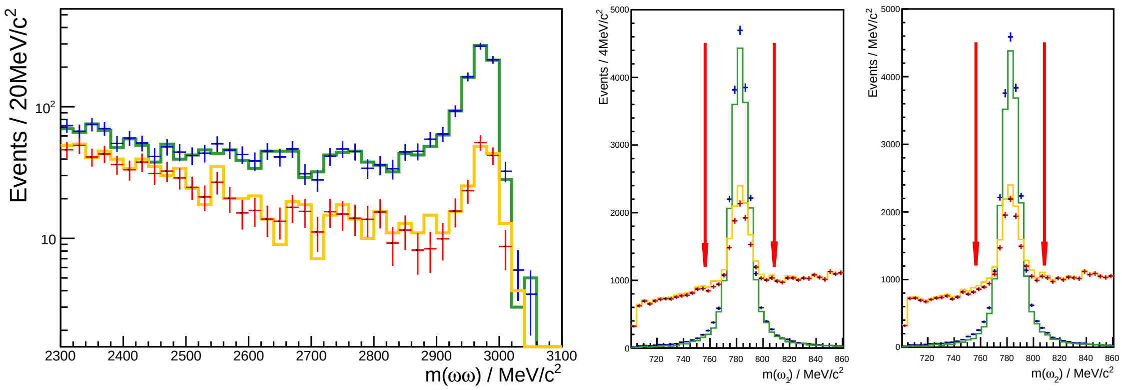

(c)

Fig. A.1: $\omega\omega$ (left) and both 3π invariant mass distributions (center, right). The left plot is shown after selection to the region marked with the red arrows in the middle and right plot. In (a) no ω is present in the background, (b) shows the $\omega 3\pi$ background and (c) the mixed sample. Generated signal and background are shown in green and orange colors, Q-weighted MC data in blue and $(1-Q)$-weighted in red, respectively.

B Results of the Systematic Survey Performed for the Model Dependent PWA

Hypothesis $\eta(1760) + \eta_c + ...$	$\log(LH)$	$n.d.f.$	BIC	$AICc$	Ranking
$\eta(1405)$	-49352.7	5	-98649	-98695	
$\eta(1475)$	-48925.4	5	-97794	-97840	
$\eta(2225)$	-52507.9	5	-104960	-105006	✓
$X(1835)$	-51442.5	5	-102829	-102875	
$f_0(1500)$	-71988.6	7	-143899	-143963	✓
$f_0(1710)$	-69668.9	7	-139259	-139324	✓
$f_0(2020)$	-72224.3	7	-144370	-144435	✓
$f_0(2100)$	-68019.4	7	-135960	-136025	
$f_0(2200)$	-66946.9	7	-133815	-133880	
$f_1(1510)$	-64044.0	7	-128009	-128074	✓
$f_2(1565)$	-71321.9	15	-142476	-142614	✓
$f_2(1640)$	-70826.5	15	-141485	-141623	
$f_2(1810)$	-71158.6	15	-142149	-142287	✓
$f_2(1910)$	-69799.7	15	-139431	-139569	
$f_2(2010)$	-68388.4	15	-136608	-136747	
$f_2(2150)$	-75558.1	15	-150948	-151086	✓
$f_2(2300)$	-62685.0	15	-125202	-125340	
$f_2(2340)$	-66066.0	15	-131964	-132102	

Table B.1: Results of model dependent fits using the base hypothesis combined with one additional resonance as listed in Table 4.5

Hypothesis $\eta(1760) + \eta_c + \ldots$		$\log(LH)$	$n.d.f.$	BIC	$AICc$	Ranking
$\eta(2225)$	$+f_0(1500)$	-72504.7	9	-144908	-144991	
	$+f_0(1710)$	-70591.6	9	-141082	-141165	
	$+f_0(2020)$	-73542.9	9	-146985	-147068	
	$+f_1(1510)$	-64503.5	9	-128906	-128989	
	$+f_2(1565)$	-71662.7	17	-143134	-143291	
	$+f_2(1810)$	-72314.9	17	-144439	-144596	
	$+f_2(2150)$	-66900.9	17	-133611	-133768	
$f_0(1500)$	$+f_0(1710)$	-72853.6	9	-145606	-145689	
	$+f_0(2020)$	-73847.7	9	-147594	-147677	
	$+f_1(1510)$	-72144.8	11	-144166	-144268	
	$+f_2(1565)$	-72730.0	19	-145247	-145422	
	$+f_2(1810)$	-74640.9	19	-149069	-149244	✓(#2)
	$+f_2(2150)$	-73668.4	19	-147123	-147299	
$f_0(1710)$	$+f_0(2020)$	-73862.3	9	-147624	-147707	
	$+f_1(1510)$	-71230.2	11	-142337	-142438	
	$+f_2(1565)$	-72607.0	19	-145001	-145176	
	$+f_2(1810)$	-72063.1	19	-143913	-144088	
	$+f_2(2150)$	-72309.4	19	-144405	-144581	
$f_0(2020)$	$+f_1(1510)$	-74001.9	11	-147880	-147982	✓(#4)
	$+f_2(1565)$	-75850.9	19	-151489	-151664	✓(#1)
	$+f_2(1810)$	-73558.4	19	-146903	-147079	
	$+f_2(2150)$	-72407.6	19	-144602	-144777	
$f_1(1510)$	$+f_2(1565)$	-71636.5	19	-143060	-143235	
	$+f_2(1810)$	-72672.7	19	-145132	-145307	
	$+f_2(2150)$	-69423.4	19	-138633	-138809	
$f_2(1565)$	$+f_2(1810)$	-74029.9	17	-147869	-148026	✓(#3)
	$+f_2(2150)$	-72715.5	17	-145240	-145397	
$f_2(1810)$	$+f_2(2150)$	-72996.3	17	-145802	-245959	

Table B.2: Results of model dependent fits using the base hypothesis and all possible combinations of two additional contributions from those marked in Table B.1.

Hypothesis $\eta(1760) + \eta_c + ...$			$\log(LH)$	$n.d.f.$	BIC	$AICc$	Ranking
$\eta(2225)$	$+f_0(1500)$	$+f_0(2020)$	-74716.8	11	-149310	-149412	
		$+f_0(1710)$	-73700.7	11	-147278	-147379	
	$+f_0(1710)$	$+f_0(2020)$	-74743.8	11	-149364	-149466	
	$+f_0(1500)$	$+f_1(1510)$	-72606.3	13	-145067	-145187	
	$+f_0(1710)$	$+f_1(1510)$	-71856.5	13	-143567	-143687	
	$+f_0(2020)$	$+f_1(1510)$	-74905.9	13	-149666	-149786	
	$+f_0(1500)$	$+f_2(1565)$	-73123.1	21	-146010	-146204	
		$+f_2(1810)$	-75266.4	21	-150297	-150491	
		$+f_2(2150)$	-74636.3	21	-149037	-149231	
	$+f_0(1710)$	$+f_2(1565)$	-73097.6	21	-145959	-146153	
		$+f_2(1810)$	-73121.6	21	-146007	-146201	
		$+f_2(2150)$	-73329.4	21	-146423	-146617	
	$+f_0(2020)$	$+f_2(1565)$	-76514.5	21	-152793	-152987	✓(#1)
		$+f_2(1810)$	-74815.2	21	-149395	-149588	
		$+f_2(2150)$	-73701.5	21	-147167	-147361	
	$+f_1(1510)$	$+f_2(1565)$	-71715.2	21	-143195	-143388	
		$+f_2(1810)$	-73509.3	21	-146783	-146977	
		$+f_2(2150)$	-69387.9	21	-138540	-138734	
	$+f_2(1565)$	$+f_2(1810)$	-74722.7	19	-149232	-149407	
		$+f_2(2150)$	-73867.6	19	-147522	-147697	
	$+f_2(1810)$	$+f_2(2150)$	-73719.2	19	-147225	-147400	
$f_1(1510)$	$+f_0(1500)$	$+f_0(1710)$	-73230.1	13	-146314	-146434	
	$+f_0(1710)$	$+f_0(2020)$	-74809.9	13	-149474	-149594	
	$+f_0(1500)$	$+f_0(2020)$	-74203.9	13	-148262	-148382	
$f_2(1565)$	$+f_0(1500)$	$+f_0(1710)$	-74464.8	21	-148694	-148888	
	$+f_0(1710)$	$+f_0(2020)$	-75864.1	21	-151492	-151686	✓(#5)
	$+f_0(1500)$	$+f_0(2020)$	-75577.1	21	-150918	-151112	✓(#6)
$f_2(1810)$	$+f_0(1500)$	$+f_0(1710)$	-74457.9	21	-148680	-148874	
	$+f_0(1710)$	$+f_0(2020)$	-74986.5	21	-149737	-149931	
	$+f_0(1500)$	$+f_0(2020)$	-75370.3	21	-150505	-150699	
$f_2(2150)$	$+f_0(1500)$	$+f_0(1710)$	-74384.2	21	-148533	-148726	
	$+f_0(1710)$	$+f_0(2020)$	-74058.6	21	-147881	-148075	
	$+f_0(1500)$	$+f_0(2020)$	-74693.3	21	-149151	-149345	
$f_1(1510)$	$+f_0(1500)$	$+f_2(1565)$	-72746.4	23	-145234	-145447	
		$+f_2(1810)$	-74754.1	23	-149250	-149462	
		$+f_2(2150)$	-73904.4	23	-147551	-147763	
	$+f_0(1710)$	$+f_2(1565)$	-72645.4	23	-145033	-145245	
		$+f_2(1810)$	-73267.4	23	-146277	-146489	
		$+f_2(2150)$	-75244.5	23	-146939	-147151	
	$+f_0(2020)$	$+f_2(1565)$	-75987.2	23	-151716	-151928	✓(#3)
		$+f_2(1810)$	-74844.7	23	-149431	-149643	
		$+f_2(2150)$	-74306.1	23	-148354	-148566	

Table B.3: Results of model dependent fits using the base hypothesis and all possible combinations of three additional contributions from those marked in Table B.1 (first part, continued in Table B.4).

Hypothesis $\eta(1760) + \eta_c + ...$			$\log(LH)$	$n.d.f.$	BIC	$AICc$	Ranking
$f_0(1500)$	$+f_2(1565)$	$+f_2(1810)$	-74627.8		-149020	-149214	
	$+f_2(1810)$	$+f_2(2150)$	-75225.2		-150215	-150408	
	$+f_2(1565)$	$+f_2(2150)$	-73653.4		-147071	-147265	
$f_0(1710)$	$+f_2(1565)$	$+f_2(1810)$	-74646.4		-149057	-149251	
	$+f_2(1810)$	$+f_2(2150)$	-73529.1		-146822	-147016	
	$+f_2(1565)$	$+f_2(2150)$	-73684.7		-147134	-147327	
$f_0(2020)$	$+f_2(1565)$	$+f_2(1810)$	-76081.1		-151926	-152120	✓(#2)
	$+f_2(1810)$	$+f_2(2150)$	-74251.9		-148268	-148462	
	$+f_2(1565)$	$+f_2(2150)$	-75886.4		-151537	-151731	✓(#4)
$f_1(1510)$	$+f_2(1565)$	$+f_2(1810)$	-74056.5		-147877	-148071	
	$+f_2(1810)$	$+f_2(2150)$	-74004.5		-147773	-147967	
	$+f_2(1565)$	$+f_2(2150)$	-72577.7		-144920	-145113	
$f_0(1500)$	$+f_0(1710)$	$+f_0(2020)$	-74940.0		-149757	-149859	

Table B.4: Results of model dependent fits using the base hypothesis and all possible combinations of three additional contributions from those marked in Table B.1 (second part, continued from Table B.3).

Hypothesis $\eta(1760) + \eta_c$ $+f_0(2020) + f_2(1565) + ...$		$\log(LH)$	$n.d.f.$	BIC	$AICc$	Ranking
$\eta(2225)$	$+f_2(1810)$	-76351.6	23	-152445	-152657	
	$+f_1(1510)$	-76555.4	25	-152830	-153061	
	$+f_2(2150)$	-76434.3	23	-152610	-152823	
	$+f_0(1710)$	-76548.1	23	-152838	-153050	
	$+f_0(1500)$	-76219.4	23	-152181	-152393	
$f_2(1810)$	$+f_1(1510)$	-76112.5	25	-151944	-152175	
	$+f_0(1710)$	-76216.6	23	-152175	-152387	
	$+f_0(1500)$	-75889.7	23	-151521	-151733	
$f_1(1510)$	$+f_2(2150)$	-75904.0	25	-151527	-151758	
	$+f_0(1710)$	-75881.1	25	-151482	-151712	
	$+f_0(1500)$	-75675.7	25	-151071	-151301	
$f_2(2150)$	$+f_0(1710)$	-75736.8	23	-151215	-151428	
	$+f_0(1500)$	-75550.6	23	-150843	-151055	
$f_0(1710)$	$+f_0(1500)$	-75374.9	23	-150491	-150704	

Table B.5: Results of model dependent fits using all possible combinations of the six best hypotheses from the second iteration, marked in Table B.3 and B.4.

List of Figures

List of Tables

Bibliography

[1] **Particle Data Group** Collaboration, K. A. Olive *et al.*, "Review of Particle Physics", *Chin. Phys.* **C38** (2014) 090001.

[2] G. S. Bali, "QCD forces and heavy quark bound states", *Phys. Rept.* **343** (2001) 1–136, `arXiv:hep-ph/0001312 [hep-ph]`.

[3] S. Bethke, "Experimental tests of asymptotic freedom", *Prog. Part. Nucl. Phys.* **58** (2007) 351–386, `arXiv:hep-ex/0606035 [hep-ex]`.

[4] Y. Chen *et al.*, "Glueball spectrum and matrix elements on anisotropic lattices", *Phys. Rev.* **D73** (2006) 014516, `arXiv:hep-lat/0510074 [hep-lat]`.

[5] L. Köpke and N. Wermes, "J/ψ decays", *Phys. Rept.* **174** no. 2, (1989) 67 – 227.

[6] D. L. Burke *et al.*, "Observation of the Decay $\psi \to \gamma\rho^0\rho^0$", *Phys. Rev. Lett.* **49** (1982) 632.

[7] **MARK-III** Collaboration, R. M. Baltrusaitis *et al.*, "A Study of the Radiative Decay $J/\psi \to \gamma\rho\rho$", *Phys. Rev.* **D33** (1986) 1222.

[8] **MARK-III** Collaboration, R. M. Baltrusaitis *et al.*, "Observation of J/ψ Radiative Decay to Pseudoscalar $\omega\omega$", *Phys. Rev. Lett.* **55** (1985) 1723.

[9] D. Bisello *et al.*, "Pseudoscalar $\omega\omega$ production at threshold in $J/\psi \to \gamma\omega\omega$ decay", *Phys. Lett. B* **192** no. 1–2, (1987) 239 – 244.

[10] **BES** Collaboration, M. Ablikim *et al.*, "Pseudoscalar production at $\omega\omega$ threshold in $J/\psi \to \gamma\omega\omega$", *Phys. Rev.* **D73** (2006) 112007, `arXiv:hep-ex/0604045 [hep-ex]`.

[11] **DM2** Collaboration, D. Bisello *et al.*, "Search of Glueballs in the $J/\psi \to \gamma\phi\phi$ Decay", *Phys. Lett.* **B179** (1986) 294.

[12] **MARK-III** Collaboration, Z. Bai *et al.*, "Observation of a Pseudoscalar State in $J/\psi \to \gamma\phi\phi$ Near $\phi\phi$ Threshold", *Phys. Rev. Lett.* **65** (1990) 1309–1312.

[13] N. Wermes, "Radiative J/ψ decays and the pseudoscalar puzzle", in *Physics in Collision V Autun, France, July 3-5, 1985.* 1985.

[14] **Belle** Collaboration, Z. Q. Liu *et al.*, "Observation of new resonant structures in $\gamma\gamma \to \omega\phi$, $\phi\phi$ and $\omega\omega$", *Phys. Rev. Lett.* **108** (2012) 232001, `arXiv:1202.5632 [hep-ex]`.

[15] P. Sun *et al.*, "Pseudoscalar quarkonium exclusive decays to vector meson pair", *Phys. Lett. B* **702** no. 1, (2011) 49 – 54.

[16] Q. Qin *et al.*, "Status and Performance of BEPCII", *Conf. Proc.* **C100523** (2010) .

[17] C. Zhang *et al.*, "Construction and Commissioning of BEPCII", in *Particle accelerator. Proceedings, 23rd Conference,PAC'09, Vancouver, Canada, May 4-8, 2009.* 2010.

[18] **BESIII** Collaboration, M. Ablikim *et al.*, "Design and Construction of the BESIII Detector", *Nucl. Instrum. Meth.* **A614** (2010) 345–399, `arXiv:arXiv:0911.4960 [physics.ins-det]`.

[19] Q. G. et al., "Particle identification using artificial neural networks at BES III", *Chin. Phys. C* **32** no. 1, (2008) 1.

[20] **BESIII** Collaboration, F. Feldbauer, "Current Status and Performance of the BESIII Electromagnetic Calorimeter", *Journal of Physics: Conference Series* **587** no. 1, (2015) 012046.

[21] G. Barrand *et al.*, "GAUDI - A software architecture and framework for building HEP data processing applications", *Comput. Phys. Commun.* **140** (2001) 45–55.

[22] "The total number of J/ψ events taken in 2009 and 2012 is determined to be $1310.6 \cdot 10^6$ with an uncertainty 0.8% with the same approach as that used in Ref. [59]", 2014.

[23] S. Jadach *et al.*, "The Precision Monte Carlo event generator $\mathcal{KK}$ for two fermion final states in e+ e- collisions", *Comput. Phys. Commun.* **130** (2000) 260–325.

[24] D. Lange, "The EvtGen particle decay simulation package", *Nucl. Instrum. Meth.* **A462** no. 1–2, (2001) 152 – 155.

[25] P. Rong-Gang, "Event generators at BESIII", *Chin. Phys. C* **32** no. 8, (2008) 599.

[26] S. Agostinelli *et al.*, "Geant4—a simulation toolkit", *Nucl. Instrum. Meth.* **A506** no. 3, (2003) 250 – 303.

[27] L. Yan *et al.*, "Lagrange multiplier method used in BESIII kinematic fitting", *Chin. Phys.* **C34** (2010) 204–209.

[28] M. Williams, M. Bellis, and C. A. Meyer, "Multivariate side-band subtraction using probabilistic event weights", *Journal of Instrumentation* **4** no. 10, (2009) P10003.

[29] C. Amsler *et al.*, "Spin density matrix of the ω in the reaction $\bar{p}p \to \omega\pi^0$", *The European Physical Journal C* **75** no. 3, (2015) .

[30] J. Pychy. `https://github.com/RUB-EP1/WiBaS`, November, 2015.

[31] B. Kopf *et al.*, "Partial wave analysis for $\bar{p}p$ and e^+e^- annihilation processes", *Hyperfine Interact.* **229** no. 1-3, (2014) 69–74.

[32] D. Griffiths, *Introduction to Quantum Mechanics.* Pearson International Edition. Pearson Prentice Hall, 2005.

[33] S. U. Chung *et al.*, "Partial wave analysis in K-matrix formalism", *Annalen der Physik* **507** no. 5, (1995) 404–430.

[34] K. Peters, "A Primer on partial wave analysis", *Int. J. Mod. Phys.* **A21** (2006) 5618–5624, `arXiv:hep-ph/0412069 [hep-ph]`.

[35] S. U. Chung, "Spin Formalisms", *CERN-71-08* (1971) .

[36] J. D. Richman, "An Experimenter's Guide to the Helicity Formalism", *CALT-68-1148* (1984) .

[37] M. G. Olsson and C. J. Suchyta, "Radiative angular distributions from $c\bar{c}$ states directly produced by $p\bar{p}$ annihilation", *Phys. Rev. D* **34** (Oct, 1986) 2043–2046.

[38] K. J. Sebastian, H. Grotch, and F. L. Ridener, "Multipole amplitudes in parity-changing one-photon transitions of charmonium", *Phys. Rev. D* **45** (May, 1992) 3163–3172.

[39] **CLEO** Collaboration, M. Artuso *et al.*, "Higher-order multipole amplitudes in charmonium radiative transitions", *Phys. Rev. D* **80** (Dec, 2009) 112003.

[40] **BABAR** Collaboration, B. Aubert *et al.*, "Amplitude analysis of the decay $B^{\pm} \to \pi^{\pm}\pi^{\pm}\pi^{\mp}$", *Phys. Rev. D* **72** (Sep, 2005) 052002.

[41] **BABAR** Collaboration, P. del Amo Sanchez *et al.*, "Evidence for the decay $X(3872) \to J/\psi\omega$", *Phys. Rev. D* **82** (Jul, 2010) 011101.

[42] S. U. Chung, "Formulas for Angular-Momentum Barrier Factors", *BNL-QGS-06-101* (2015) .

[43] I. J. R. Aitchison, "K-matrix formalism for overlapping resonances", *Nucl. Phys.* **A189** (1972) 417–423.

[44] A. M. Badalian, L. P. Kok, M. I. Polikarpov, and Yu. A. Simonov, "Resonances in Coupled Channels in Nuclear and Particle Physics", *Phys. Rept.* **82** (1982) 31.

[45] K. Schilling, P. Seyboth, and G. E. Wolf, "On the Analysis of Vector Meson Production by Polarized Photons", *Nucl. Phys.* **B15** (1970) 397–412. [Erratum: Nucl. Phys.B18,332(1970)].

[46] K. P. Burnham and D. R. Anderson, *Model Selection and Multimodel Inference - A Practical Information-Theoretic Approach.* Springer, New York, 2nd edition ed., 2002.

[47] **DM2** Collaboration, D. Bisello *et al.*, "Search of Glueballs in the $J/\psi \to \gamma\phi\phi$ Decay", *Phys. Lett.* **B179** (1986) 294.

[48] **BES** Collaboration, M. Ablikim *et al.*, "Partial wave analysis of $J/\psi \to \gamma\phi\phi$", *Phys. Lett.* **B662** (2008) 330–335, `arXiv:0801.3885 [hep-ex]`.

[49] **BESIII** Collaboration, M. Ablikim *et al.*, "Spin-Parity Analysis of $p\bar{p}$ Mass Threshold Structure in J/ψ and ψ' Radiative Decays", *Phys. Rev. Lett.* **108** (2012) 112003, `arXiv:1112.0942 [hep-ex]`.

[50] **BES** Collaboration, M. Ablikim *et al.*, "Observation of a resonance $X(1835)$ in $J/\psi \to \gamma\pi^+\pi^-\eta'$", *Phys. Rev. Lett.* **95** (2005) 262001, `arXiv:hep-ex/0508025 [hep-ex]`.

[51] **BESIII** Collaboration, M. Ablikim *et al.*, "Confirmation of the $X(1835)$ and observation of the resonances $X(2120)$ and $X(2370)$ in $J/\psi \to \gamma\pi^+\pi^-\eta'$", *Phys. Rev. Lett.* **106** (2011) 072002, `arXiv:1012.3510 [hep-ex]`.

[52] **BESIII** Collaboration, M. Ablikim *et al.*, "Observation of pseudoscalar and tensor resonances in $J/\psi \to \gamma\phi\phi$", `arXiv:1602.01523 [hep-ex]`.

[53] **BES** Collaboration, M. Ablikim *et al.*, "Search for the decays $J/\psi \to \gamma\rho\phi$ and $J/\psi \to \gamma\rho\omega$", *Phys. Rev.* **D77** (2008) 012001, `arXiv:0710.2979 [hep-ex]`.

[54] **CLEO** Collaboration, R. E. Mitchell *et al.*, "J/ψ and $\psi(2S)$ Radiative Transitions to η_c", *Phys. Rev. Lett.* **102** (Jan, 2009) 011801.

[55] **BESIII** Collaboration, M. Ablikim *et al.*, "Measurements of the mass and width of the η_c using the decay $\psi(3686) \to \gamma\eta_c$", *Phys. Rev. Lett.* **108** (May, 2012) 222002.

[56] J. Sucher, "Magnetic Dipole Transitions in Atomic and Particle Physics", *Rept. Prog. Phys.* **41** (1978) 1781.

[57] N. Brambilla, Y. Jia, and A. Vairo, "Model-independent study of magnetic dipole transitions in quarkonium", *Phys. Rev. D* **73** (Mar, 2006) 054005.

[58] V. V. Anashin *et al.*, "Measurement of $J/\psi \to \eta_c\gamma$ at KEDR", *Chinese Physics C* **34** no. 6, (2010) 831. `http://stacks.iop.org/1674-1137/34/i=6/a=035`.

[59] M. Ablikim *et al.*, "Determination of the number of J/ψ events with $J/\psi \to$ *inclusive* decays", *Chinese Physics C* **36** no. 10, (2012) 915. `http://stacks.iop.org/1674-1137/36/i=10/a=001`.

[60] W. Yuan and others (BESIII Data Quality Group), "Study of tracking efficiency from $J/\psi \to p\bar{p}\pi^+\pi^-$ (Talk at autumn 2014 Workshop)", 09, 2014.

[61] W. Yuan and others (BESIII Data Quality Group), "Study of tracking efficiency from $J/\psi \to p\bar{p}\pi^+\pi^-$ (BESIII Note)", 09, 2014.

[62] V. Prasad *et al.*, "Photon Detection Efficiency and Position Resolution of Electromagnetic Calorimeter at BESIII (Talk at spring 2014 Workshop)", 02, 2014.

[63] D.-M. Li and B. Ma, "$X(1835)$ and $\eta(1760)$ observed by BES Collaboration", *Phys. Rev.* **D77** (2008) 074004, `arXiv:0801.4821 [hep-ph]`.

[64] D. Parganlija, "Tensor Glueball in a Top-Down Holographic Approach to QCD", *Acta Phys. Polon. Supp.* **8** no. 2, (2015) 289, `arXiv:1506.03000 [hep-ph]`.

[65] F. Brünner, D. Parganlija, and A. Rebhan, "Glueball Decay Rates in the Witten-Sakai-Sugimoto Model", *Phys. Rev.* **D91** no. 10, (2015) 106002.

[66] I. G. Augustin, "BTR_Executive Summary", 12, 2006. `https://www-alt.gsi.de/documents/DOC-2006-Dec-94.html`.

[67] V. Kamerdzhiev *et al.*, "2MeV Electron Cooler for COSY and HESR – First Results", in *Proceedings, 5th International Particle Accelerator Conference (IPAC 2014)*, p. MOPRI070. 2014. `http://jacow.org/IPAC2014/papers/mopri070.pdf`.

[68] A. Herten, *GPU-based Online Track Reconstruction for PANDA and Application to the Analysis of $D \to K\pi\pi$* . Dissertation, Ruhr-Universität Bochum, 2015.

[69] **PANDA** Collaboration. `https://panda.gsi.de/oldwww/html/det/pictures/detector/Panda_1401_1_big.png`, January, 2016.

[70] **PANDA** Collaboration, W. Erni *et al.*, "Technical Design Report for the: PANDA Micro Vertex Detector", `arXiv:1207.6581 [physics.ins-det]`.

[71] **PANDA** Collaboration, M. Albrecht, "The Forward Endcap of the Electromagnetic Calorimeter for the PANDA Detector at FAIR", *J. Phys. Conf. Ser.* **587** no. 1, (2015) 012050.

[72] C. Amsler, *Kern- und Teilchenphysik.* vdf Hochschulverlag AG, 2007.

[73] K. Kleinknecht, *Detektoren für Teilchenstrahlung.* Teubner Studienbücher: Physik, 4te, überarbeitete Auflage ed., 2005.

[74] **PANDA** Collaboration, W. Erni *et al.*, "Technical Design Report for PANDA Electromagnetic Calorimeter (EMC)", `arXiv:0810.1216 [physics.ins-det]`.

[75] A. Borisevich *et al.*, "PWO-II scintillation crystals for the PANDA electromagnetic calorimeter", in *Nuclear Science Symposium Conference Record, 2008. NSS '08. IEEE*, pp. 2698–2700. Oct, 2008.

[76] J. Schulze, "Prototypenentwicklung für das elektromagnetische Kalorimeter des PANDA-EMC", Diplomarbeit, Ruhr-Universität Bochum, Institut für Experimentalphysik I, 2009.

[77] D. A. Bremer *et al.*, "Performance of prototypes for the PANDA barrel EMC", *Journal of Physics: Conference Series* **587** no. 1, (2015) 012052. `http://stacks.iop.org/1742-6596/587/i=1/a=012052`.

[78] L. Capozza *et al.*, "The backward end-cap for the PANDA electromagnetic calorimeter", *Journal of Physics: Conference Series* **587** no. 1, (2015) 012051. `http://stacks.iop.org/1742-6596/587/i=1/a=012051`.

[79] C. Schnier, "personal communication", 2016.

[80] C. Motzko, *Analyse des Zerfalls $\psi(2S) \to \chi_{c0}\gamma \to K_s K_s \pi^0 \pi^0 \gamma$ und Entwicklung eines Lichtpulsersystems für das PANDA-EMC.* Dissertation, Ruhr-Universität Bochum, Institut für Experimentalphysik I, 2012.

[81] T. Holtmann, "personal communication", 2015.

[82] I. Konorov, H. Angerer, A. Mann, and S. Paul, "SODA: Time distribution system for the PANDA experiment", pp. 1863–1865. 2009.

[83] M. Leyhe, *Analyse des J/ψ- und $\psi(2S)$-Zerfalls in $\gamma\pi^+\pi^-\eta$ bei BESIII und Entwicklungen zur Auslese des PANDA-EMC.* Dissertation, Ruhr-Universität Bochum, Institut für Experimentalphysik I, 2013.

[84] M. Albrecht, "Aufbau und Analyse der Testmessungen des Proto192 elektromagnetischen Kalorimeters", Master's Thesis, Ruhr-Universität Bochum, Institut für Experimentalphysik I, 2012.

[85] C. Schnier, "Aufbau und Test von Kalorimeter-Modulen für $\overline{\text{P}}$ANDA", Master's Thesis, Ruhr-Universität Bochum, Institut für Experimentalphysik I, 2014.

[86] C. Schmidt, "personal communication", 2015.

[87] M. Kümmel, "Investigations Concerning the Spatial and Energy Resolution of the $\overline{\text{P}}$ANDA Electromagnetic Calorimeter", Master's Thesis, Ruhr-Universität Bochum, Institut für Experimentalphysik I, 2014.

[88] J. Schulze, *Analyse des Zerfalls $\chi_{c0} \to K^+K^-\pi^0\pi^0$ bei BESIII und Entwicklung von mechanischen Komponenten für einen Prototypen des PANDA-EMC.* Dissertation, Ruhr-Universität Bochum, Institut für Experimentalphysik I, 2012.

[89] J. Becker, *Analyse des Zerfalls $\chi_{cJ} \to K^+K^-\eta$ bei BESIII und Entwicklung des Kühlsystems des Prototypen für das EMC des PANDA-Experiments.* Dissertation, Ruhr-Universität Bochum, Institut für Experimentalphysik I, 2012.

[90] M. Kuhlmann, "Messungen mit dem Prototypen des PANDA elektromagnetischen Kalorimeters", Master's Thesis, Ruhr-Universität Bochum, Institut für Experimentalphysik I, 2015.

[91] **BaBar** Collaboration, B. Aubert *et al.*, "Search for decays of B0 mesons into pairs of leptons", in *High energy physics. Proceedings, 31st International Conference, ICHEP 2002, Amsterdam, Netherlands, July 25-31, 2002.* 2002. `arXiv:hep-ex/0207083 [hep-ex]`.

[92] G. Kuhl, "Vermessung von Photodetektoren für das PANDA elektromagnetische Kalorimeter", Master's Thesis, Ruhr-Universität Bochum, Institut für Experimentalphysik I, 2014.

[93] Laura Rüß, "Messung zur Quanteneffizienz von Avalanche-Photodioden", Master's Thesis, Ruhr-Universität Bochum, Institut für Experimentalphysik I, 2015.

[94] A. Mustafa, "personal communication", 2015.

Acknowledgments

Finally (I used this word quite some times throughout this thesis, but now - I cant believe it myself - I in fact arrived at the final section, as it seems...), I would like to express my wholehearted gratitude to several people who supported me and made this work possible.

First, I would like to thank Prof. Dr. Ulrich Wiedner for the possibility to be a member of his group for more than six years to date, to participate in exciting experiments and - of course - to write this thesis! Thank you for your guidance, your support and confidence.

Dr. Marc Pelizäus and Dr. Bertram Kopf definitely deserve some special attention here: Thank you both for the endless discussions about our complicated life in light hadron physics, for introducing me to the world of partial wave analyses, for answering the tons of questions with which I came to your offices again and again and for your ongoing support, encouraging words when things wouldn't want to work out (again) and all the good ideas!

Now I want to come to the outstanding group of people that have worked or are still working at EP1: I want to thank you for all the fruitful discussions, your helpfulness and all the fun that we had together in the past years! I am especially grateful to PD Dr. Fritz-Herbert Heinsius, Dr. Thomas Held, Dr. Matthias Steinke, Dr. Torsten Schröder, Dr. Michael Leyhe and Dipl.Ing. Mario Fink. I have especially enjoyed working and travelling together with my office-mate M.Sc. Cathrina Sowa. Thank you for the nice company, all our sometimes heated discussions and for pushing me to finally sign up for the sailing class! I also want to thank all other EP1-minions that I did not explicitly mention here.

I want to acknowledge the support from RUB Research School$^{\text{PLUS}}$, which made it possible for me to visit Prof. Fred A. Harris and his group at the University of Hawai'i for a research stay. The trip to the Hawaiian islands became an everlasting memory for me. I learned a lot during this trip and enjoyed the seminars, meetings and discussions at the university a lot. As a by-product, I could see an incredibly impressive part of the world and met many calm and warm-hearted people. Mahalo, Fred, for your warm hospitality, your support and the unforgettable trip around O'ahu!

I also want to say thank you to all of my friends here in Bochum (or in Trier ;)) who accompanied me throughout the past years and always waited for me at the U71 when I was staying late at the lab or the office again. I think this is the place to express my gratitude especially towards M.Sc. Hendrik Vondracek. Thank you for your careful proof-reading of my manuscript, all our evening-discussions at the office and, of course, our trips that you organized!

I am deeply grateful for the support and understanding I received from my family, especially from my parents and my better half, Miriam. In fact, you, Miriam, should be named in many of the paragraphs above, as a colleague, friend, for proof-reading and for everything else. Thank you for being there for me during day and night times, especially in the last months. This work wouldn't have been possible without you.

Lebenslauf

Persönliche Daten	
Name	Malte Albrecht
Geburtsdatum	14.06.1987
Geburtsort	Essen
Eltern	Gudrun und Wilfried Albrecht

Berufserfahrung	
12/12 - heute	Wissenschaftlicher Mitarbeiter am Institut für Experimentalphysik I der Ruhr-Universität Bochum

Studium	
12/12 - heute	Promotionsvorhaben am Institut für Experimentalphysik I unter der Leitung von Prof. Dr. Ulrich Wiedner
10/14 - 12/14	Auslandsaufenthalt an der University of Hawai'i at Manoa, USA (Stipendium der RUB Research School$^{\mathrm{PLUS}}$ [DFG GSC 98/3])
01/11 - 07/11	Auslandssemester an der Universität Uppsala, Schweden. Projektarbeit (Thema: *Development of an FPGA-based readout system for hydrogen pellet tracking*) am *Department of Physics and Astronomy* unter der Leitung von Prof. Dr. Tord Johansson
10/10 - 10/12	Studium der Physik (M.Sc.) an der Ruhr-Universität Bochum Anfertigung der Masterarbeit mit dem Thema *Aufbau und Analyse der Testmessungen des Proto192 elektromagnetischen Kalorimeters* am Institut für Experimentalphysik I
10/07 - 07/10	Studium der Physik (B.Sc.) an der Ruhr-Universität Bochum Anfertigung der Bachelorarbeit mit dem Thema *Aufbau eines Messstands zur Charakterisierung von VPTs* am Institut für Experimentalphysik I

Zivildienst	
09/06 - 09/07	Zivildienstleistender in der Zentralen Notaufnahme, Kliniken Essen-Mitte, Huyssens-Stiftung anschliessende Weiterbeschäftigung

Schulbildung	
1997-2006	Helmholtz-Gymnasium, Essen Abschluss: Allgemeine Hochschulreife (Abitur)
1993-1997	Städtische Grundschule "Friedensschule", Essen

Weitere akademische	**Tätigkeiten**
12/09	Hochschuldidaktische Zertifizierung als Übungsgruppenleiter

Versicherung gemäß §7 Abs. 2 Nr. 6 PromO 2011

Hiermit versichere ich, dass ich meine Dissertation selbstständig angefertigt und verfasst und keine anderen als die angegebenen Hilfsmittel und Hilfen benutzt habe. Meine Dissertation habe ich in dieser oder ähnlicher Form noch bei keiner anderen Fakultät der Ruhr-Universität Bochum oder bei einer anderen Hochschule eingereicht.

Bochum, den

MALTE ALBRECHT

This page is not part of the dissertation by Malte Albrecht, which was submitted on April 5th, 2016 to the Department of Physics and Astronomy of the Ruhr-Universität Bochum, but has been added later.

Errata

Known mistakes and corresponding corrections as of June 26th, 2016:

- p.3:
  The fourth and third last sentences of the last paragraph on page 3 should read: When two electric charges are brought close to each other, the force between them gets stronger, while for larger distances the force weakens as $1/r^2$. The force between two quarks shows the same behavior at small distances, yet the potential unexpectedly increases for larger distances.

- p.64, equation (4.30):
  The first line of this equation should read:

  $$-\ln\mathcal{L} = -\sum_{i=1}^{n_{\mathrm{data}}} \ln(w(\vec{\Omega},\vec{\alpha})) \cdot Q_i + [...]$$

  instead of

  $$-\ln\mathcal{L} = -\sum_{i=1}^{n_{\mathrm{data}}} \ln(w(\vec{\Omega},\vec{\alpha}) \cdot Q_i) + [...].$$

  All fits have been performed with the correct likelihood function and the mistake only occurred in the dissertation.